OPTICAL ANALYSIS AND EXPERIMENTAL CHARACTERIZATION OF PEROVSKITE SOLAR CELLS AND COLOR SENSORS

Mohammad Ismail Hossain

PhD

The Hong Kong Polytechnic University

2020

The Hong Kong Polytechnic University

Department of Applied Physics

Optical Analysis and Experimental Characterization of Perovskite Solar Cells and Color Sensors

Mohammad Ismail Hossain

A thesis submitted in partial fulfillment of the requirements

for the degree of Doctor of Philosophy

May 2020

Certificate of Originality

I hereby declare that this thesis is my own work and that, to the best of my knowledge and belief, it reproduces no material previously published or written, nor material that has been accepted for the award of any other degree or diploma, except where due acknowledgement has been made in the text.

_____ (Signature)

MOHAMMAD ISMAIL HOSSAIN _____(Name of the candidate)

Abstract

Metal-halide perovskites are considered as one of the most exciting material systems due to their excellent optoelectronic properties. Notably, the multi-bandgap properties of perovskites have opened an emerging prospect for highly efficient tandem solar cell and color vision applications. So far, only perovskite-based tandem solar cells allow reaching energy conversion efficiencies exceeding 30% at low manufacturing cost. In this thesis, efficient solar cells and color sensors are studied based on metal-halide perovskite materials.

Charge transport/contact layers have a significant impact on the electrical and optical properties of perovskite solar cells. Particularly, the front contact, which is a part of the junction of the solar cell, has to be efficient for realizing high energy conversion efficiency. The front contact must provide a lateral charge transport to the terminals and should allow efficient light incoupling while maintaining low optical losses. Hence, In the first part of the thesis, metal-oxides, such as titanium oxide (TiO_2), nickel-oxide (NiO), zinc oxide (ZnO), etc., are investigated as potential front contacts for realizing efficient perovskite solar cells. High-quality metal oxide films are prepared by spray pyrolysis deposition (SPD), electron-beam physical vapor deposition (EBPVD), metal-organic chemical vapor deposition (MOCVD), and atomic layer deposition (ALD) techniques. As a first step, the study is carried out to investigate the planar perovskite solar cell performance with different front contacts, which is also used as a reference

device structure for future investigations. Subsequently, the study is progressed to the textured perovskite solar cells, which combines the benefit of reaching high short-circuit current densities and energy conversion efficiencies due to efficient photon management. Efficient photon management allows enhancing photon absorptions in perovskite solar cells through light incoupling and/or light trapping. Herein, light incoupling and light trapping are investigated with the integration of surface textures (e.g. moth-eye, pyramid, optical metasurfaces, etc.) on top of planar perovskite solar cells. A non-resonant optical metasurface is additionally studied as an alternative light-trapping structure for realizing efficient perovskite solar cells, where an array of ZnO nanowires is realized by the templated electrodeposition through a mask of resist. The complex requirements of perovskite solar front contacts and the effect of the front contact on the optics of perovskite solar cells are described in this part of the study. The optics of solar cells is investigated by 3D finite-difference time-domain (FDTD) optical simulations and the electrical effects of solar cells are inspected by the 3D finite element method (FEM). Detailed discussions for the realization of metal oxide films and the influence of photon management on the photovoltaic performance are provided.

The second part of this thesis deals with detailed balance calculations and photon management of perovskite-based tandem solar cells. An extended Shockley–Queisser model is used to identify fundamental loss mechanisms and link the losses to the optics of solar cells. The influence of free-carrier absorption of metal oxide films

on the optics of low bandgap and/or tandem solar cells is investigated. Herein, an optimized design is proposed for the perovskite/silicon tandem solar cell, which has the potential to reach energy conversion efficiency beyond 30% with a short-circuit current density exceeding 20 mA cm^{-2} while using realistic device geometry. A hybrid approach is used to investigate the optics of perovskite/silicon tandem solar cells by combining 3D finite-difference time-domain simulations with experimental measurements. Furthermore, multi-bandgap perovskites are employed as absorbers for investigating high-efficiency perovskite/perovskite tandem solar cells at low cost. Details on the nanophotonic design of perovskite-based tandem solar cells are provided.

In the final part of this thesis, multi-bandgap perovskite materials are considered for the realization of efficient vertically stacked color sensors. The vertically stacked color sensor consists of three different energy bandgap perovskite diodes (channels), which allows exhibiting excellent color separation without having any color aliasing or color moiré error. The complex material properties of multi-bandgap perovskites are determined by the energy shift modeling. The quantum efficiency of the proposed vertically stacked color sensor is 3 times higher than the conventional filter-based color sensors. The current study focuses on the perovskite color sensor for achieving the quantum efficiency approaching 100%. The quantum efficiency of the investigated sensor is calculated by 3D finite-difference time-domain simulations. The study is further advanced to the realization of the multi-channel color sensor for detecting multispectral imaging, where six individual perovskite diodes are used for the sensor construction.

The six-channel sensor outperforms all other characterized sensors. It enables the reconstruction of incident spectra that can be applied to a wide range of areas, such as health, communications, safety, and securities. The colorimetric characterization is performed based on the calculated spectral responsivities of the investigated color sensors. Details on the used materials, the device design, and the colorimetric analysis are provided.

List of Publications

Journal Publications Related to the Thesis

1. **M. I. Hossain**, AK Mahmud Hasan, W. Qarony, M. Shahiduzzaman, M. A. Islam, Y. Ishikawa, Y. Uraoka, N. Amin, D. Knipp, M. Akhtaruzzaman, Y. H. Tsang, Electrical and Optical Properties of Nickel-Oxide films for Efficient Perovskite Solar Cells, *Small Methods* (**2020**) 2000454.

2. **M. I. Hossain**, A. Mohammad, W. Qarony, S. Ilhom, D. Shukla, N. Biyikli, D. Knipp, Y. H. Tsang, Atomic Layer Deposition of Metal Oxides for Efficient and Stable Perovskite Solar Cells, *RSC Advances*, 10 (**2020**) 14856-14866.

3. **M. I. Hossain**, N. Yumnam, W. Qarony, A. Salleo, V. Wagner, D. Knipp, Y. H. Tsang, Non-resonant Metal-oxide Metasurfaces for Efficient Perovskite Solar Cells**,** *Solar Energy,* 198 (**2020**) 570-577.

4. **M. I. Hossain**, W. Qarony, S. Ma, L. Zeng, D. Knipp, Y. H. Tsang, Perovskite/silicon Tandem Solar Cells: From Detailed Balance Limit Calculations to Photon Management**,** *Nano-Micro Letter,* 11 (**2019**) 58.

5. **M. I. Hossain**, A. Hongsingthong, W. Qarony, P. Sichanugrist, M. Konagai, A. Salleo, D. Knipp, Y. H. Tsang, Optics of Perovskite Solar Cell Front Contacts, *ACS Applied Materials & Interfaces*, 11 (**2019**) 14693-14701.

6. **M. I. Hossain**, W. Qarony, V. Jovanov, Y.H. Tsang, D. Knipp, Nanophotonic design of perovskite/silicon tandem solar cells, *Journal of Materials Chemistry A,* 6 (**2018**) 3625-3633.

7. **M. I. Hossain**, W. Qarony, M. K. Hossain, M. K. Debnath, M. J. Uddin, Y. H. Tsang, Effect of back reflectors on photon absorption in thin-film amorphous silicon solar cells, *Applied Nanoscience*, 7 (**2017**) 489–497.

8. M. Shahiduzzaman, **M. I. Hossain**, S. Visal, T. Kaneko, W. Qarony, S. Umezu, K. Tomita, S. Iwamori, Y. H. Tsang, M. Akhtaruzzaman, T. Taima, and M. Isomura, Optimized Multi-layer Front Contact Design for Realizing High-efficiency Perovskite Solar Cells, *Nano-Micro Letters,* (**2020**). (major revision)

9. **M. I. Hossain,** H. A. Khan, M. Kozawa, W. Qarony, A. Salleo, J. Y. Hardeberg, H. Fujiwara, Y. H. Tsang, D. Knipp, Perovskite Color Detectors: Approaching to the Quantum Efficiency Limit, *ACS Applied Materials and Interfaces* (**2020**). (Accepted)

10. **M. I. Hossain,** H. A. Khan, M. Kozawa, W. Qarony, A. Saleo, J. Y. Hardeberg, H. Fujiwara, Y. H. Tsang, D. Knipp, Multispectral Imaging with Perovskite Three and Six Channel Sensors, (**2020**). (manuscript under preparation)

11. **M. I. Hossain**, W. Qarony, A. Tamang, A. Salleo, H. Fujiwara, K.T. Fountaine, H. Atwater, Y. H. Tsang, D. Knipp, Visibly Transparent Solar Cells Build from Optical Antennas, (**2020**). (manuscript under preparation)

12. **M. I. Hossain**, W. Qarony, A. Tamang, A. Salleo, H. Fujiwara, Y. H. Tsang, D. Knipp, Nano Concentrator Solar Cells Build from Optical Antenna-based Perovskite Tandem Solar Cells, (**2020**). (manuscript under preparation)

Other Journal Publications but not the Core Part of the Thesis:

13. W. Qarony, **M. I. Hossain**, J. Vladislav, A. Salleo, D. Knipp, Y. H. Tsang, Influence of Perovskite Interface Morphology on the Photon Management in Perovskite/silicon Tandem Solar Cells, *ACS Applied Materials & Interfaces,*12 (**2020**) 15080-15086.

14. W. Qarony, M. K. Hossain, **M. I. Hossain**, S. Ma, L. Zeng, K. M. Yu, D. Knipp, A. Salleo, H. Sun, C. T. Yip, Y. H. Tsang, Reversible Photochromic and Photoluminescence Behaviors in Iodide Perovskites, *Science China Materials,* (**2020**). (under review)

15. **M. I. Hossain**, A. M. Saleque, S. Ahmed, I. Saidjafarzoda, N. Biyikli, W. Qarony, Y. H. Tsang, Perovskite/Perovskite Tandem Solar Cells: a guideline for reaching energy conversion efficiency beyond 30%, Nano Energy (**2020**). (Accepted)

16. W. Qarony, **M. I. Hossain**, A. Tamang, V. Jovanov, D. Knipp, Y. H. Tsang, Enhancing the energy efficiency of low mobility solar cells by a 3D solar cell architecture, *Journal of Materials Chemistry C,* 7 (**2019**) 10289-10296.

17. W. Qarony, **M. I. Hossain**, A. Salleo, D. Knipp, Y. H. Tsang, Rough versus planar interfaces: How to maximize the short circuit current of perovskite single and tandem solar cells**,** *Materials Today Energy,* 11 (**2019**) 106-113.

18. W. Qarony, **M. I. Hossain**, R. Dewan, S. Fischer, V B. M.-Rochow, A. Salleo, D. Knipp, Y. H. Tsang, Approaching perfect light incoupling in perovskite and silicon thin film solar cells by moth eye surface textures, *Advanced Theory & Simulations,* 1 (**2018**) 1800030.

19. W. Qarony, **M. I. Hossain**, V. Jovanov, D. Knipp, Y. H. Tsang, Maximizing the short circuit current of organic solar cells by partial decoupling of electrical and optical properties, *Applied Nanoscience,* 8 (**2018**) 339-346.

20. W. Qarony, **M. I. Hossain**, M .K. Hossain, M. J. Uddin, A. Haque, A. R. Saad, Y. H. Tsang, Efficient amorphous silicon solar cells: characterization, optimization, and optical loss analysis, *Results in Physics*, 7 (**2017**) 4287-4293.

21. W. Qarony, M. Kozawa, H. Khan, **M. I. Hossain**, A. Salleo, Y. H. Tsang, H. Fujiwara, D. Knipp, Vertically Stacked Perovskite Detectors for Color Sensing and Color Vision**,** *Advanced Materials Interface* (**2020**) 2000459.

22. X. Wang, W. Qarony, P. K. Cheng, **M. I. Hossain**, Y. H. Tsang, Photoluminescence of Group-10 Transitional Metal Dichalcogenides (PtS2, PdS2, and PdSe2) Quantum Dots, *RSC Advances*, 9 (**2019**) 38077-38084.

23. S. Ma, W. Qarony, **M. I. Hossain**, Y. H. Tsang, Metal-organic framework derived porous carbon of light trapping structures for efficient solar steam generation, *Solar Energy Materials and Solar Cells,* 196 (**2019**) 36-42.

24. W. Qarony, M. K. Hossain, **M. I. Hossain**, S. Ma, L. Zeng, K. M. Yu, D. Knipp, A. Salleo, H. Sun, C. T. Yip, Y. H. Tsang, Excitation Wavelength Dependent Reversible Photoluminescence Peak in Iodide Perovskites, *arXiv preprint* arXiv:1812.10335 (**2018**).

25. W. Qarony, M.K. Hossain, **M. I. Hossain**, K. M. Yu, Y.H. Tsang, Photo-driven energy transformation phenomenon in CVD processed perovskite alloys for the

application of ultrafast and low-power multi-color luminescence photo pattern imaging. (Manuscript under preparation)

26. S. Ahmed, J. Qiao, P. K. Cheng, A. M. Saleque, **M. I. Hossain**, W. Qarony, L. Zeng, Y. H. Tsang*, SnTe Quantum Dots Saturable Absorber for Ultrafast Photonics. *(manuscript is ready to submit)*

27. A. M. Saleque, S. Ahmed, **M. I. Hossain**, W. Qarony, S. Ma, Y. H. Tsang*, *Biodegradable Luffa Sponge Derived Solar Steam Generator for Efficient and Cost-effective Water Purification*. *(manuscript is ready to submit)*

Conference Publications

Proceeding Papers

1. **M. I. Hossain**, J. Anowar, S. Ahmed, A. Saleque, A. Rahman, W. Qarony, Y. H. Tsang, Optics of Perovskite-based Highly Efficient Tandem Solar Cells, *IEEE TENSYMP 2020*, June 5-7 (**2020**) Dhaka, Bangladesh. (***In Press***)

2. **M. I. Hossain**, S. Ahmed, M. Shahiduzzaman, W. Qarony, A. M. Saleque, D. Knipp*, Y. H. Tsang, Influence of the TiO_2 Compact Electron Transport Layer on the Planar Perovskite Solar Cell Performance, 47th *IEEE Photovoltaic Specialists Conference (PVSC-47)*, June 15 – August 21 (**2020**) Calgary, Canada. (***In Press***)

Conference Presentations

3. **M. I. Hossain**, W. Qarony, S. Ahmed, A. M. Saleque, J. A. Zapien, D. Knipp*, Y. H. Tsang*, *Photon Management in Perovskite Solar Cells by Nanohole Front Contact*, SPIE. Optics + Photonics, Digital Forum, August 24 – 28 (**2020**) San Diego, USA. **(ORAL)**

4. **M. I. Hossain**, W. Qarony, H. A. Khan, M. Kozawa, A. Salleo, J. Y. Hardeberg, H. Fujiwara, Y. H. Tsang, D. Knipp*, Tsang, Color Imaging Sensors with Perovskite Alloys, *Nano-, Bio-, Info-Tech Sensors, and 3D Systems IV, SPIE Smart Structures + Non-destructive Evaluation*, Proceeding Volume 11378, April 27- May 1 (**2020**) California, USA. (**ORAL**)

5. **M. I. Hossain**, AKM Hasan, W. Qarony, M. Shahiduzzaman, M.A. Islam, N. Amin, D. Knipp, M. Akhtaruzzaman, Y. H. Tsang, On the Potential of metal NiO front contact for efficient perovskite solar cells, *Photonics for Solar Energy Systems VIII, SPIE Photonics Europe*, Proceeding Volume 11366, April 6-10 (**2020**) Strasbourg, France. (**ORAL**)

6. **M. I. Hossain**, W. Qarony, N. Yunman, V. Wagner, D. Knipp, Y. H. Tsang, The Energy Conversion Efficiency of Perovskite/perovskite Tandem Solar Cell Reaching 30% by Metal Oxide Optical Metasurfaces, *MRS Spring Meeting & Exhibition*, April 13-17 (**2020**) Phoenix, Arizona, USA. (postponed due to COVID-19, *to be presented*) (**POSTER**)

7. **M. I. Hossain**, W. Qarony, AKM Hasan, M. Shahiduzzaman, MA Islam, N. Amin, D. Knipp, M. Akhtaruzzaman, Y. H. Tsang, EB PVD grown NiO Films for Efficient Perovskite Solar Cells, *MRS Spring Meeting & Exhibition*, April 13-17

(**2020**) Phoenix, Arizona, USA. (postponed due to COVID-19, *to be presented*) (**POSTER**)

8. **M. I. Hossain**, J. Anowar, S. Ahmed, A. Saleque, A. Rahman, W. Qarony, Y. H. Tsang, Optics of Perovskite-based Highly Efficient Tandem Solar Cells, *IEEE TENSYMP 2020*, June 5-7 (**2020**) Dhaka, Bangladesh. (**ORAL**)

9. **M. I. Hossain**, S. Ahmed, M. Shahiduzzaman, W. Qarony, A. M. Saleque, D. Knipp, Y. H. Tsang, Influence of the TiO_2 Compact Electron Transport Layer on the Planar Perovskite Solar Cell Performance, 47th *IEEE Photovoltaic Specialists Conference (PVSC-47)*, June 15 – August 21 (**2020**) Calgary, Canada. (*to be presented*) (**ORAL**)

10. M. Shahiduzzaman, **M. I. Hossain**, W. Qarony, M. Akhtaruzzaman, K. Tomita, Y. H. Tsang, T. Taima, Spray Pyrolysis Deposition of TiO_2 for Efficient Planar Perovskite Solar Cells, *MRS Spring Meeting & Exhibition*, April 13-17 (**2020**) Phoenix, Arizona, USA. (*to be presented*) (**POSTER**)

11. **M. I. Hossain**, W. Qarony, S. Ilhom, N. Biyikli, D. Knipp, Y.H. Tsang, A route to Reach the Absorption Limit of Perovskite Solar Cells by using Metal-oxide Front Contacts, *International Conference of Material Science and Engineering, Materials Oceania*, September 16-18 (**2019)** Melbourne, Australia. (**ORAL**)

12. **M. I. Hossain**, W. Qarony, S. Ilhom, M. A. Islam, N. Amin, N. Biyikli, D. Knipp, Y.H. Tsang, Metal Oxide Front Contacts for High Efficiency Perovskite Solar Cells, *6th International Conference on Nanotechnology, Nanomaterials & Thin Film for Energy Applications, Nanoenergy*, July 27-29 (**2019**) Kuala Lumpur, Malaysia. (**ORAL**)

13. **M. I. Hossain**, S. Ilhom, W. Qarony, N. Amin, N. Biyikli, D. Knipp, Y.H. Tsang, Atomic Layer Depositions of Metal Oxides for Efficient and Stable Perovskite Solar Cells, *6th International Conference on Nanotechnology, Nanomaterials & Thin Film for Energy Applications, Nanoenergy*, July 27-29 (**2019**) Kuala Lumpur, Malaysia. (**POSTER**)

14. **M. I. Hossain**, S. Ilhom, W. Qarony, N. Biyikli, D. Knipp, Y.H. Tsang, Use of metal Oxide Front Contacts: An Approach to make Efficient Perovskite Single and Perovskite/Silicon Tandem Solar Cells, *IONS Exeter*, July 10-12 (**2019)** Exeter, UK. (**ORAL**)

15. **M. I. Hossain**, A. Mohammad, S. Ilhom, D. Shukla, N. Biyikli, D. Knipp, Y.H. Tsang, Atomic Layer Deposition for Efficient Perovskite Solar Cells, *CMOC 28th Annual Symposium,* March 25 (**2019)** Connecticut, USA. (**POSTER**)

16. **M. I. Hossain**, W. Qarony, D. Knipp, Y.H. Tsang, "Light trapping in Perovskite Solar Cells with Non-resonant Metasurfaces, *MRS Fall Meeting & Exhibition*, November 25-30 (**2018**) Boston, Massachusetts, USA. (**POSTER**)

17. **M. I. Hossain**, W. Qarony, D. Knipp, Y.H. Tsang, Perfect light incoupling in perovskite single junction and perovskite/silicon tandem solar cells, *SPIE/COS Photonics Asia*, October 11-13 (**2018**) Beijing, China. (**ORAL**)

18. **M. I. Hossain**, W. Qarony, Y.H. Tsang et al., Light Incoupling Enhancement in Perovskite Solar Cell using Nanostructured Transparent Contact**,** *The international Photovoltaic Science and Engineering Conference (PVSEC-27)*, November 12-17 (**2017**) Shiga, Japan. (**POSTER**)

19. W. Qarony, **M. I. Hossain**, H. A. Khan, M. Kozawa, A. Salleo, J. Y. Hardeberg, H. Fujiwara, Y. H. Tsang, D. Knipp, Optical Filter Free Color Imaging with Perovskite Alloys, *MRS Spring Meeting & Exhibition*, April 13-17 (**2020**) Phoenix, Arizona, USA. (postponed due to COVID-19, *to be presented*) (**POSTER**)

20. A. Saleque, **M. I. Hossain**, A. Safayet, I. Saidjafarzoda, N. Biyikli, W. Qarony, Y. H. Tsang, Optical Analysis of All-perovskite Planar Tandem Solar Cells, *MRS Spring Meeting & Exhibition*, April 13-17 (**2020**) Phoenix, Arizona, USA. (postponed due to COVID-19, *to be presented*) (**POSTER**)

21. W. Qarony, M. K. Hossain, **M. I. Hossain**, K. M. Yu, Y. H. Tsang, Reversible Photochromic and Photoluminescence in Iodide Perovskites, *MRS Spring Meeting & Exhibition*, April 13-17 (**2020**) Phoenix, Arizona, USA. (postponed due to COVID-19, *to be presented*) (**ORAL**)

22. S. Ma, W. Qarony, **M. I. Hossain**, Y.H. Tsang, MOF Derived Porous Carbon for Solar Driven Water Evaporation, *The 9th International Multidisciplinary Conference on Optofluidics (IMCO-2019)*, June 14-17 (**2019)** Kowloon, Hong Kong. (**POSTER**)

23. W. Qarony, M. K. Hossain, **M. I. Hossain**, K. M. Yu, C. T. Yip, Y. H. Tsang, Shifting of Excitation States in Iodine-based Lead Halide Perovskites Under Femtosecond Laser Excitation, *SPIE Photonics West*, 2-7 February (**2019**) San Francisco, California, USA. (**POSTER**)

24. W. Qarony, **M. I. Hossain**, D. Knipp, Y. H. Tsang, Influence of Perovskite Film Formation and Morphology on Textured Perovskite/Silicon Tandem Solar Cells,

MRS Fall Meeting & Exhibition, November 25-30 (**2018**) Boston, Massachusetts, USA. (**POSTER**)

25. W. Qarony, S. Ma, **M. I. Hossain**, C. T. Yip, Y. H. Tsang, Enlarging the Grain in Low-Temperature Solution-processed Perovskite Films Using Simple Annealing Method, *MRS Fall Meeting & Exhibition*, 25-30 November 2018, Boston, USA. (**POSTER**)

26. S. A. Shahahmadi, P. Chelvanathan, **M. I. Hossain**, W. Qarony, S. Z. Othman, H. Misran, M. Akhtaruzzaman, Y. H. Tsang, N. Amin, Investigation on Photovoltaic Properties of Nb-Doped MoS2 Thin Films Grown by Magnetron Sputtering, *MRS Fall Meeting & Exhibition*, November 25-30 (**2018**) Boston, Massachusetts, USA. (**POSTER**)

27. W. Qarony, **M. I. Hossain**, D. Knipp, Y. H. Tsang, Nanophotonic design of an optically rough and electrically flat perovskite/silicon tandem solar cell, *SPIE/COS Photonics Asia*, October 11-13 (**2018**) Beijing, China. ***(Invited Speaker)***

28. W. Qarony, **M. I. Hossain**, Y. H. Tsang, Optimum Perovskite Cell for Highly Efficient Perovskite/Silicon Tandem Solar Cell, *The international Photovoltaic Science and Engineering Conference (PVSEC-27)*, November 12-17 (**2017**) Shiga, Japan. (**ORAL**)

Acknowledgments

Alhamdulillah. All acclaims and gratitude to Allah SWT, the Almighty and most Merciful, who always guides me to the right path. I am immensely grateful to him for his shower of blessings, which give me strength, determination, and patience to complete this study.

Foremost, I would like to express my sincere and deep gratitude to my chief supervisor, an extraordinarily kind person, Associate Prof. Dr. Yuen Hong Tsang, for allowing me to do research and providing me the precious guidance from the early stage of my Ph.D. fellowship application. His patience, enthusiasm, motivation, immense knowledge, and continuous supports toward the accomplishment of this study have profoundly stirred me to do my best. I must be exceptionally grateful to him for his friendly behavior, empathy, mainly listening and appreciating my constructive comments. Besides being a tremendous supervisor, he is a great person who always emotionally support me during my crucial times.

I would like to show my most profound appreciation to my external advisor Prof. Dr. Dietmar Knipp, from Stanford University, USA, who was also my direct supervisor during my master's study at Jacobs University Bremen, Germany. I have been working with him for slightly over eight years. He motivated me to extend my research to the Ph.D. and encouraged me to study in Hong Kong with his grand project ideas. He is a man of novel ideas, and his continuous guidance, suggestions, and quick feedback on constructive comments were constructive to reach many research outputs. In general, I appreciate his extreme contributions to my Ph.D. research.

Thanks to the examiners for accepting the request and spend their valuable time to

review my thesis.

I must thank some experts, Prof. Fujiwara (Gifu University, Japan), Prof. Alberto Salleo (Stanford University, USA), Prof. Hardeberg (NTNU, Norway), Dr. Asman (Dalhousie University, Canada), Prof. Veit Wagner (Jacobs University Bremen, Germany), Prof. Makoto Konagai (Tokyo Institute of Technology, Japan), Prof. Necmi Biyikli (University of Connecticut, USA), Prof. Nowshad Amin (UNITEN, Malaysia), Dr. Md. Shahiduzzaman (Kanazawa University, Japan), for their esteemed collaborative supports which helped to finish my study effectively.

I am immeasurably thankful to my brotherly friend and colleague, Dr. Wayesh Qarony, currently at the University of California-Davis, USA. He accompanied and shared suffering with me during my study. We have been working together for more than a decade. His intense dedication, support, and continuous valuable suggestions made my Ph.D. journey comfortable. I must thank to my friend, Waqar Ahmed, Dept. of Industrial Engineering, PolyU, his brotherhood was extraordinarily good that helped me to overcome the crisis moments through my Ph.D. journey.

I also like to acknowledge the Hong Kong University Grant Commission (UGC) and Hong Kong government for giving me an opportunity and substantial financial support to pursue my Ph.D. at HK PolyU under a highly prestigious Hong Kong Ph.D. Fellowship Scheme (HKPFS).

I do not forget to thank my lab mates, Dr. Zeng, Dr. Longhui, Dr. Sainan, Dr. Wang, Dr. Zeng, Mr. Ahmed, Mr. Safayet, and entire teams; their optimistic attitudes helped me to learn never give up during difficulties.

My unique and insightful thanks and love to my beloved wife, Dr. Sabrina Sifat, who has been struggling with me for a long time to secure a brighter future. Her continuous supports, understanding, obligation, taking care of my children during my Ph.D. study all stand behind my success. Concurrently, I like to express my esteemed love to my children, Aariz and Azwar, who are the source of all my happiness and inspiration. I want to dedicate this thesis to my children. I owe everything to my family, my deep love for adored parents for their outstanding support, encouragement, and always keep faith in me. I also thank my parents in law and my adoring siblings. I shall never forget these beautiful people in my prayers.

Table of Contents

List of Figures

List of Tables

List of Symbols and Acronyms

AM1.5G	The Global standard Spectrum Air Mass 1.5G
Al	Aluminum
ZnO	Zinc Oxide
ZnO:Al or AZO	Aluminum-doped Zinc Oxide
AFM	Atomic Force Microscopy
BTCO	Back Transparent Conductive Oxide
ZnO:B	Boron-doped Zinc Oxide
ZnO:Ga	Gallium-doped Zinc Oxide
CIGS	Copper Indium Gallium Selenide
CZTS	Copper Zinc Tin Sulfide
CZTSe	Copper Zinc Tin Selenide
InP	Indium Phosphide
CIS	Copper Indium Diselenide
c-Si	Crystalline Silicon
D_2O	Deuterium Water
DEZ	Diethylzinc
EMA	Effective Medium Approximation
FDTD	Finite Difference Time Domain
FEM	Finite Element Method
FIT	Finite Integration Technique
FTCO	Front Transparent Conductive Oxide
GaAs	Gallium Arsenide
FWHM	Full Width at Half Maxima
a-Si:H	Hydrogenated Amorphous Silicon
IOH	Hydrogen-doped Indium Oxide (In2O3:H)

IR	IR Infrared
CIE	International Commission on Illumination
LPCVD	Low Pressure Chemical Vapor Deposition
MgF2	Magnesium Fluoride
MOCVD	Metal-organic Chemical Vapor Deposition
PECVD	Plasma Enhanced Chemical Vapor Deposition
PML	Perfectly Matched Layer
QE	Quantum Efficiency
RMS	Root mean square
SEM	Scanning electron microscope
SiO2	Silicon Dioxide
SR	Spectral Responsivity
Si	Silicon
sccm	Standard Cubic Centimeter per Minute
Ag	Silver
Au	Gold
ITO	Indium Tin Oxide (In2O3:Sn)
TE	Transverse Electric
TM	Transverse Magnetic
EQE	External Quantum Efficiency
IQE	Internal Quantum Efficiency
CE	Collection Efficiency
J_{SC}	Short-circuit Current Density
V_{OC}	Open-circuit Voltage
ECE	Energy Conversion Efficiency
FF	Fill Factor
J_0	Saturation Current Density

EBPVD	Electron Beam Physical Vapor Deposition
ALD	Atomic Layer Deposition
SPD	Spray Pyrolysis Deposition
$MAPbI_3$	Methylammonium Lead Halide
NiO	Nickel Oxide
TiO_2	Titanium Oxide
FTO	Fluorine-doped Tin Oxide

CHAPTER 1

INTRODUCTION

1.1 Motivation

Photovoltaic is the fastest-growing energy source in the electricity sector, which has great potential to overcome the world's energy crisis. However, record energy conversion efficiencies yet much lower than the theoretical upper limit of a solar cell. Different methodologies have been proposed to overcome the limits of conventional single-junction solar cells by applying novel physical principles, amongst, tandem solar cells have been the most promising approach, which can reach the energy conversion efficiency exceeding 40%. Furthermore, the color image sensor is a fundamental fragment of a multitude of technologies, including digital cameras, smartphones, optical mouse devices, camera modules, medical imaging equipment, sonar, radar, and many others. Hence, image sensing technology has an inordinate impact on our daily life; nevertheless, the conventional color image sensors based on color filter arrays (CFA) are not efficient due to sensor construction. However, designs of efficient tandem solar cells and color sensors are challenging, which demand optically matched materials with excellent electrical and optical properties. This thesis aims at realizing highly efficient tandem solar cells and optical color sensors based on perovskite material systems.

1.2 Introduction

In recent years, the perovskite material system has gained considerable research attention because of its excellent electronic and optical properties, particularly, its ability to tailor the bandgap and low deposition cost.(Bush et al., 2017a; Chung et al., 2017; Y. C. Kim et al., 2017; M. Liu, Johnston, & Snaith, 2013a) The low penetration or absorption depths of several tens to hundreds of nanometers in combination with the high diffusion lengths >1 μm allows for realizing thin-film solar cells with high energy conversion efficiency (ECE).(Castelli, García-Lastra, Thygesen, & Jacobsen,

2014; Green, Jiang, Soufiani, & Ho-Baillie, 2015; Jang et al., 2016; Jiang, Green, Sheng, & Ho-Baillie, 2015; Li et al., 2015; Shi et al., 2015; L. Wang et al., 2016) Single-junction perovskite solar cells (PSCs) with ECEs exceeding 20% have been demonstrated by several research groups.(Green, Dunlop, et al., 2019; Green et al., 2018; N.-G. Park, 2015a) This thesis initially focuses on the optics of PSC front contacts to realize an optimized single-junction PSC structure; later, the structure is applied to the implementation of perovskite-based high-efficiency tandem solar cells (TSCs). The photon management is studied through the improvement of light incoupling and/or light trapping in PSCs, which has a significant influence on the realization of high ECEs. Finally, the study is extended to the implementation of efficient optical color sensors with perovskite alloys. Further explanations are discussed in the following sub-sections.

1.2.1 Perovskite Solar Cell Front Contacts

In a simple PSC structure, the perovskite layer is sandwiched between two charge transport/contact layers. Hence, the qualities of the electron transport material (ETM) and/or hole transport material (HTM), such as energy level alignment, charge mobility, morphology, and its related interface properties are substantially valuable for the determination of PSCs with better photovoltaic performance.(Juarez-Perez et al., 2014; N.-G. Park, 2015b; Werner, Niesen, & Ballif, 2018) So far, PSCs with high ECEs are made from organic HTMs (e.g., PEDOT:PSS, Spiro-OMeTAD, PTAA, and P3HT) along with TiO_2 ETL. However, organic HTMs require additional dopant materials and adhesive ingredients (e.g., BCP) which degrade the device stability.(Burschka, Kessler, Nazeeruddin, & Grätzel, 2013; Conings et al., 2014; Heo et al., 2013; H.-S. Kim et al., 2012; Noh, Jeon, et al., 2013a; You et al., 2014) Recently, promising results have been demonstrated by using metal oxides (titanium oxide (TiO_2), zinc oxide (ZnO), and

Nickel oxide (NiO)) as charge transport layers for the implementation of efficient PSCs due to their extensive range of benefits, such as chemical stability, high mobility, low resistivity, low cost, and suitable energy level.(Mohammad I. Hossain, Qarony, Jovanov, Tsang, & Knipp, 2018a; Wakamiya et al., 2014; J.-Y. Wang et al., 2009a; Yongzhen Wu et al., 2014; Xu et al., 2015a; J. Zhou et al., 2017) Metal oxides can be prepared by several deposition techniques, including spin-coating, spray-pyrolysis, sol-gel, magnetron sputtering, atomic layer deposition (ALD), electron beam physical vapor deposition (EBPVD).(Abzieher et al., 2019; Aydin et al., 2018; Jin Cui et al., 2014; Jlassi, Sta, Hajji, & Ezzaouia, 2014; Ryu et al., 2000; Seo et al., 2016; Yongzhen Wu et al., 2014; Zardetto et al., 2017; Z. Zhu et al., 2014) Nevertheless, until now, most emphasis has been made on the optimization of absorber materials and the electronic properties of the contact layers of PSCs. Little attention has been on the optics of the solar cell and the influence of the contact layers on the optics of the solar cells. However, the optics of the contact layers has a distinct impact on the optics of the complete solar cells and the short-circuit current density (J_{SC}). The optics of the contact layers is essential for single-junction PSCs and even more critical for perovskite-based TSCs. The front contact of a PSC has four functions. Firstly, the front and back contacts together with the perovskite absorber form the junction of the solar cell. Hence, the work function of the materials must be selected accordingly. Secondly, the front contact must provide lateral conductivity, so that the charges can be transported to the solar cell terminals or a printed metallic front contact grid. Thirdly, the front contact must allow for an efficient incoupling of the light in the solar cell. It might be combined with the diffraction or refraction of the incident light to increase the optical path length of the light in the solar cell, which results in increased quantum efficiency (QE). Often this is achieved by texturing the contacts. Fourthly, the absorption loss of the contact layer should be as low as possible. The second point is closely linked to the fourth point. An increased doping concentration leads to increased

conductivity, but also the free carrier absorption is increased, and potentially the absorption loss of the contact layers is increased. The metal oxide contacts can fulfill all requirements for the implementation of efficient PSCs. The current study aims to propose a solar cell design that allows for reaching J_{SC} of more than 90% of its maximum J_{SC}. Such high values have been achieved for record silicon or gallium arsenide solar cells exceeds 90% of the theoretical limit.(Green, Emery, Hishikawa, Warta, & Dunlop, 2016; Shockley & Queisser, 1961b) In the case of PSCs with ~1.6 eV perovskite absorber, such high values have not been achieved yet. Hence, we inspect several transport materials as front contact of PSCs, which were realized from different deposition methods. As a first step, metal oxide films were prepared for the fabrication of planar PSCs to investigate the influence of front contacts on the PSC performance. In the second step, the photon management in PSCs is studied by improving light incoupling and/or light trapping in PSCs.

In the current study, the spray-pyrolysis deposition (SPD) technique was used for the preparation of dense TiO_2 films, which is one of the popular methods used in industries to deposit large area ceramic films.(Piegari & Flory, 2013) Then, NiO films were prepared by the EBPVD technique at low temperatures. A recent study has shown that an EB deposited NiO as charge transport material can exhibit excellent PSC performance.(Abzieher et al., 2019) Next, the ALD technique was utilized to prepare high-quality uniform ZnO films at low temperatures. Designated metal oxides were used as potential front contacts for planar PSC fabrications.

Additionally, the refractive index of the perovskite material system is comparable to the refractive index of the metal oxide films. Hence, reflections at the metal oxide/perovskite interface are low. The reflection of two materials forming a planar interface increases with increasing refractive index difference between the materials. Hence, the layer stack consisting of the metal oxide layers and the perovskite layer can be treated as one unit with almost equal refractive index. This simplifies the optical

design. However, performances of planar devices are still limited due to the higher reflection losses. Hence, we focus on the coupling of the incident light in PSCs. This can be achieved by integrating a pyramidal surface texture on top of the solar cell. Depending on the dimensions of the pyramidal texture the structure might as well diffract or refract the incident light, so that the optical path length is increased. Consequently, the electrical properties of the PSCs should be comparable to planar PSCs realized in substrate configuration. It is assumed that the modified optical design does not affect the electrical properties of the solar cells. Hence, it is expected that electrical parameters of the solar cell, the open-circuit voltage (V_{OC}) and fill factor (FF), are comparable to planar solar cells in substrate configuration. As a part of this study smooth and pyramid textured boron-doped ZnO films were prepared by a Metal-Organic Chemical vapor deposition (MOCVD) process, which is a standard process used in industry to coat several square meter large glass substrates. The PSC covered with pyramid textures, which is formed by a self-texturing process,(Mohammad I. Hossain, Hongsingthong, et al., 2019) allow increasing the J_{SC} with improved light incoupling and light trapping. As an alternative solution for the light trapping structure while maintaining the planar technology, a new process using optical metasurfaces is introduced, which gives an almost equal performance like pyramid texture. The investigated metasurfaces consist of an array of ZnO nanowires with subwavelength large edge length, which are used as fundamental building blocks in controlling the phase of the incident light. The nanowires are prepared in this study by a templated electrodeposition through an electron beam patterned resist, which will open a new gateway for the next-generation photovoltaic technology.

1.2.2 Perovskite-based Tandem Solar Cells

Current commercial solar modules are predominately based on crystalline silicon (c-

Si) single-junction solar cells. So far, laboratory solar cells with record ECEs of 26.3% have been demonstrated(Yoshikawa et al., 2017a) while an upper theoretical ECE of a solar cell with a bandgap of 1.15 eV (e.g. silicon) is ~33.5%.(Shockley & Queisser, 1961b) Detailed balance calculations reveal that the serial connected TSC can only reach ECE exceeding 40% if an ideal material combination is selected for the top and bottom solar cell.(Shockley & Queisser, 1961b; Vos, 1980) ECEs higher than 40% can be reached if $E_{G\_top}=0.5\times E_{G\_bot}+1.15$ eV, where E_{G_top} and E_{G_bot} are the bandgaps of the top and bottom diode absorbers. The relationship is valid if the bandgap of the bottom diode stays in a range from 0.85 eV to 1.2 eV. Hence, a variety of material combinations can be selected. The c-Si with a bandgap of 1.15 eV is well suited as a bottom solar cell. Consequently, a lot of research has been devoted to the development of TSCs using a c-Si bottom solar cell. In this case, the highest ECE can be reached if the bandgap of the top cell is equal to ~1.73 eV. Several aspects must be considered to combine the well-established c-Si solar cell technology with other material systems or fabrication processes. Amorphous silicon exhibits an ideal bandgap, but the tail states of the material prevent the realization of solar cells with high V_{OC}s, which is a prerequisite for the recognition of TSCs with high ECEs.(M. A. Green, 2003; Meier et al., 2004; Meillaud, Shah, Droz, Vallat-Sauvain, & Miazza, 2006; Qarony et al., 2017; Shah et al., 2002) Silicon oxide / c-Si based quantum dot and quantum well have been investigated as potential material of the top solar cell.(R. Lopez-Delgado et al., 2016, 2017; Rosendo Lopez-Delgado et al., 2018; Pi, Li, Li, & Yang, 2011) However, solar cells with high ECEs have not been realized using silicon-based quantum dots or quantum wells. Furthermore, compound semiconductors have been investigated as potential top solar cell absorber material. However, the high fabrication temperatures of compound semiconductors, the lattice mismatch between silicon and compound semiconductors, and the fabrication cost have so far prevented the successful realization. In recent years, the perovskite material system has been

investigated as potential material for single-junction solar cells or as material for perovskite/silicon TSCs.(Bush et al., 2017b; Leguy et al., 2015; Sahli et al., 2018a; Werner et al., 2018; Wolff et al., 2017; W.-J. Yin, Shi, & Yan, 2014a) So far, the perovskite material exhibits very encouraging results.(Fang et al., 2019; Jeon et al., 2013; M. Liu, Johnston, & Snaith, 2013b; H. Zhang, Wang, Chen, & Jen, 2017; Zuo et al., 2016, 2019; Zuo, Vak, Angmo, Ding, & Gao, 2018; Zuo & Ding, 2014) High ECEs have been achieved for single-junction PSCs with V_{OC}s close to the theoretical limit. Furthermore, the material system can be fabricated by a variety of deposition methods at low temperatures, which facilitates the integration of a perovskite top solar cell on a c-Si bottom solar cell. Up to now, single-junction PSCs with ECEs exceeding 20% have been achieved.(Burschka, Pellet, et al., 2013; Green, Hishikawa, et al., 2019; Hao, Stoumpos, Cao, Chang, & Kanatzidis, 2014; Lee, Seol, Cho, & Park, 2014; N.-G. Park, 2015b) Research on perovskite/silicon TSCs is still a new research topic. The number of teams working on the realization of record perovskite/silicon TSCs is still small. The realization of perovskite/silicon TSCs with record ECEs is only possible if the perovskite top solar cell and the silicon bottom solar cell operate very close to the theoretical limit. Nevertheless, perovskite/silicon TSCs with certified ECEs exceeding 27% have been demonstrated.(Oxford PV-The Perovskite Company, 2020) The realization of solar cells with higher ECEs approaching or even exceeding 30% can be expected soon. To close the gap between theoretical ECE limits and the performance of real solar cells a thorough investigation of the losses of a solar cell is required.

In the current study, we discuss a detailed balance approach and photon management to maximize the ECE of TSCs. We describe how optics and nanophotonics can be combinedly used to optimize not only the J_{SC} of a solar cell but also all other solar cell parameters. Herein, a nanophotonic design of the perovskite/silicon TSC is presented,

which can give an ECE over 30% with J_{SC} beyond 20 mA/cm^{-2}. By taking advantage of multi-bandgap perovskite material systems, we demonstrate efficient perovskite/perovskite TSC with the integration of optical metasurfaces which has the potential to deliver an ECE approaching 30%. The optics of solar cells was investigated by 3D FDTD optical simulations.

1.2.3 Color Imaging Sensors with Perovskite Alloys

A further extension of this study is the use of tunable bandgap properties of the perovskite material system for the realization of optical color sensors. In our modern life, all major optical devices, such as cameras, optical mouse, medical imaging, smartphones, etc. use image sensors. Hence, the image sensor has a high impact on the entire community. The conventional color image sensors, commonly used in different applications like smartphones and digital cameras, is usually performed by a side-by-side arrangement of an array of sensor elements as schematically shown in Figure 1(a). The sensor elements in this technology are covered by color filter arrays (CFA), consisting of a periodic arrangement of blue, green, and red color filters for a three-color channel sensor.(Bayer, 1976; Lukac & Plataniotis, 2005b) The use of CFA leads to color artifacts like color aliasing or color Moiré effect, resulting in poor sharpness and immunity in the captured images and videos.(Hubel, Liu, & Guttosch, 2004) For the case of black/white camera without using the CFA, the upper limit of the quantum efficiency ($QE_{BW}(\lambda)$) of the individual diodes is assumed to exhibit approx. 100%. However, in the case of a color camera with CFA, the upper limit of the QE of a color pixel is given by

$$\mathrm{QE}_{\mathrm{color}}(\lambda) \cong \frac{1}{\mathrm{N}} \times \mathrm{QE}_{\mathrm{BW}}(\lambda) \tag{1}$$

where N is the number of color channels. In this case of a conventional three-color

sensor with CFA, the QE exhibits an upper limit of 33%, since 2/3 of total incident photons are not converted into sensor signal.(Gunturk, Glotzbach, Altunbasak, Schafer, & Mersereau, 2005a) This is because only one color is detected by one channel at a time. In other words, when the red channel detects a red color image, the blue and green channels remain unused. As the red color covers 1/3 of the overall area of the color pixel, the resultant maximum achievable QE of the detection process is limited to 33%.(Palanchoke, Boutami, & Gidon, 2017) As a consequence, limits the image contrast and low-level light sensitivity of the sensors. Hence, the QE is limited by the side-by-side arrangement of the color filter, resulting in the reduction of the dynamic range by $20\times\log(N)\approx10$ dB and increase the signal to noise ratio (SNR).

The schematic diagram is shown in Fig. 1(b) is a vertically stacked color sensor used as an alternative to the conventional color sensor with CFA, where wavelength-dependent photon absorption and corresponding signals are collected at different depths of the device. The sensor consists of three vertically stacked semiconductor diodes. The design of the sensor device structure is made in such a way that high energy photons with blue colors are absorbed in the top diode. In contrast, relatively lower energetic photons with green and red colors are penetrated deep in the device and eventually absorbed by the middle and bottom diodes, respectively. This strong wavelength-dependent incident photon absorption strategy allows achieving good color-to-color separation. As all the incident photons are converted into sensor signals, this sensor can exhibit an upper limit of QE as 100%. Additionally, the vertically stacked color sensor does not require using color filters, allowing to capture images and videos without sampling artifacts like color aliasing or color Moiré. Such a vertically stacked color sensor technology was first deployed in the Sigma SD9 DSLR camera back in 2002, where the sensor principle is best known for the Foveon X3 sensor.(Hubel et al., 2004; Lyon & Hubel, 2002; Merrill, 1999) So far, the vertically stacked sensor has been

only demonstrated by using silicon alloys and c-Si materials. However, the use of indirect bandgap and low bandgap silicon materials in the conventional color sensors leads to poor color separation amongst red, green, and blue color spectral responsivities and high color detection error for the human vision system in the infrared region, respectively.(Hubel, 2005b) Moreover, the sensor is highly sensitive to lighting conditions, resulting in distinguishable image quality captured in the poor and bright light. However, such problems can be solved by developing a vertically stacked color sensor with tunable and direct bandgap semiconductor materials.

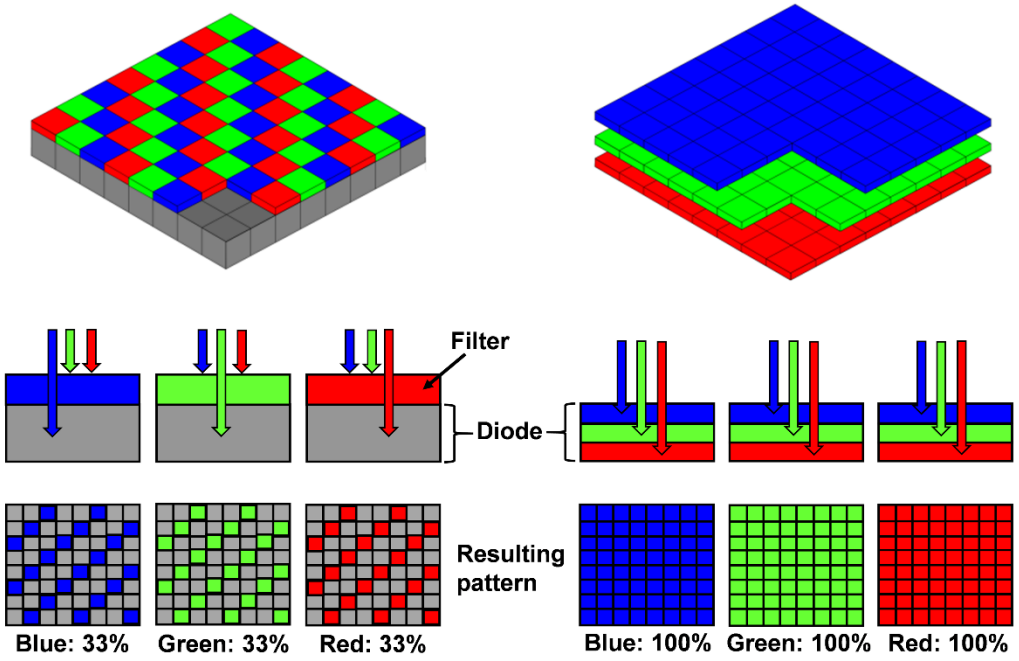

Figure 1.1: Schematic cross-sections of (a) conventional three-color sensor with the side-by-side arrangement of optical color filter arrays (CFA), where the upper limit of the resultant quantum efficiency of the detection process is limited to 33% and (b) vertically stacked three-color sensor consisting of three semiconductor diodes with three different bandgaps, resulting into 100% upper limit of quantum efficiency in the detection process.

In this study, mixed-halide perovskite materials are studied for the realization of highly efficient optical color sensors. Perovskites have recently gained substantial research attention in developing several high-performance optoelectronic devices due to their outstanding optical and electronic properties. In particular, unlike the silicon materials,

the mixed-halide perovskite materials exhibit excellent optical bandgap tunability with direct bandgap semiconductor properties. The electronic structure and bandgap can be nicely tuned only by changing the composition of the halide components in the mixed-halide perovskites. Additionally, the higher absorption coefficient and electron/hole diffusion length allow developing highly efficient devices. Hence, mixed-halide perovskites are proposed for developing vertically stacked color sensors as an alternative to the silicon-based color sensors in the current study. The study mainly focuses on achieving very high QE and spectral response of such vertically stacked perovskite color sensor by introducing textured interfaces in the devices. A very high QE of approaching 100% has been obtained from the proposed sensor device, allowing to detect images with high contrast and high-level of light sensitivity. However, 3-channel optical sensors are not able to identify beyond primary RGB colors. Hence, we study on the implementation of multispectral imaging with perovskite alloys. As we know, electromagnetic waves are carriers of energy and information, which propagate in time and space. An ideal electromagnetic sensor array would measure the light intensity and the wavelength of the electromagnetic wave as a function of time and position. The human vision system and digital cameras allow for detecting the light intensity of visible light as a function of time and position. The spectral information is measured in the form of “colors”, which represent an integral over a spectral range. Spectrometers are commonly used to measure the spectral characteristics of electromagnetic waves. However, spectrometers do not provide spatial information. Hence, a spectrometer can be seen as a single-pixel camera with high spectral resolution. Multispectral cameras provide spectral and spatial information as a function of time. Multispectral cameras capture images for many spectral channels so that the spectral information of the image can be reconstructed. The realization of such cameras is technically complex and expensive in comparison to classical digital cameras that mimic the human vision system. However, multispectral cameras allow for new applications in

Bio, health, and securities.

In this current study, we develop a basic RGB vertically stacked optical image sensor with multi-bandgap mixed halide perovskites, which can exhibit QE approaching 100%. Furthermore, mixed halide perovskites are utilized to realize the efficient six-channel multispectral image sensor, which has the potential to outperform all characterized color sensors. The investigated sensor can detect six distinct colors at a time. The optical properties of the mixed-halide tunable bandgap perovskites calculated by the energy shift model are discussed. The proposed sensor devices modeled by optical wave propagation simulations for QEs and spectral sensitivities for the color sensors are presented, where the calculated perovskite optical materials properties were used as input parameters. Herein, the calculated QE of the investigated sensor is compared with conventional color sensors. Sensors are colorimetrically characterized to determine the color error and compare with the traditional color sensor with CFA as well as the Foveon sensor based on the c-Si. The colorimetric characterization is described systematically, which allows realizing whether the investigated color sensors are suitable for the human vision system, which can also be used as a reference system.

1.3 Accomplished Milestones

a. The influence of front contacts and photon management for the realization of high-efficiency perovskite solar cells.
b. Realization of the energy conversion efficiency of perovskite/silicon tandem solar cells exceeding 30%.
c. A route to reach the efficient optical color sensors with perovskite alloys, which delivers a quantum efficiency approaching 100%.
d. A novel pathway to develop a visible transparent solar cell exhibiting

energy conversion efficiency over 20%.

1.4 Thesis Outline

This thesis focuses on the realization of highly efficient perovskite single-junction solar cells, perovskite-based tandem solar cells, and optical color sensors with multi-bandgap perovskite alloys. The optical and electronic properties are determined from the energy shift modeling. The optics of solar cells and color sensors are investigated by 3D FDTD simulations. The electrical effects of solar cells are investigated by the finite element method (FEM) simulations. Moreover, necessary material characterizations are performed to obtain the input parameters for optical and electrical simulations. For a clear insight, this thesis is arranged into seven chapters, whose insides are described below.

Chapter 1 "Introduction"

Chapter 1 includes the general introduction and motivation of the study. The thesis arrangement is also described in it.

Chapter 2 "Fundamentals"

Chapter 2 presents the basic theory of solar cells, photovoltaic performance parameters, losses in solar cells, thermodynamic limits, ultimate efficiency limit, detailed balance limit or Shockley-Queisser limit, and photodetectors. The chapter also describes the numerical modeling and methods. [*relevant publication: Nano-Micro Lett.,* 11 (**2019**) 58; *Applied Nanoscience, 7 (2017) 489-497*]

Chapter 3 & 4 "Optics of Perovskite Solar Cell Front Contacts"

In the Chapter 3, optics of flat-front contacts is discussed, where optics of textured front contacts is discussed in Chapter 4. Chapter 3 and 4 mainly describes the influence of front contact materials on short-circuit current densities and energy conversion efficiencies of perovskite solar cells. Furthermore, how efficient photon management can improve short-circuit current densities and energy conversion efficiencies is also discussed in this chapter. A potential pathway to reach photon absorption of single-junction perovskite solar cell approaching unity is systematically provided. [*relevant publications: Small Methods,* (**2020**) 200454; *RSC Advances*, 10 (**2020**) 14856-14866; *Solar Energy,* 198 (**2020**) 570-577; *ACS Applied Materials & Interfaces*, 11 (**2019**) 14693-14701; *Materials Today Energy,* 11 (**2019**) 106-113; *Advanced Theory & Simulations,* 1 (**2018**) 1800030]

Chapter 5 "Perovskite Tandem Solar Cells: From Detailed Balance Theory to Photon Management"

Chapter 5 covers the perovskite/silicon tandem solar cells from detailed balance calculations to photon management. The nanophotonic design of perovskite/silicon tandem solar cells is described, which can exhibit an energy conversion efficiency beyond 30%. A systematic explanation about the fabrication technique of perovskite/silicon tandem solar cells is also presented. A realization of the low-cost perovskite/perovskite tandem solar cell is additionally presented in this chapter. [*relevant publications: Nano-Micro Lett.,* 11 (**2019**) 58; *Journal of Materials Chemistry A,* 6 (**2018**) 3625-3633; *ACS Applied Materials & Interfaces*, 11 (**2019**) 14693-14701; *Solar Energy,* 198 (**2020**) 570-577; *ACS Applied Materials & Interfaces,*12 (**2020**) 15080-15086]

Chapter 6 "Color Image Sensors with Perovskite Alloys"

Chapter 6 describes how multi-bandgap mixed-halide perovskites can be used to implement efficient optical color sensors, which can deliver the quantum efficiency close to 100%. The investigated color sensors have a better color separation without

having color aliasing or color moiré error. All necessary optical analysis and colorimetric characterizations are performed for the investigated color sensors.

Chapter 7 "Summary and Outlook"

Chapter 7 summarizes the results demonstrated in all sections on perovskite single-junction solar cells, perovskite/silicon tandem solar cells, perovskite/perovskite tandem solar cells, and color imaging sensors with mixed-halide perovskites. Moreover, a short explanation of some ongoing and future projects is also presented in this chapter.

CHAPTER 2

FUNDAMENTALS

2.2 Fundamentals of Solar Cells

In general, a solar cell is an electronic device that converts sunlight into electricity. The basic device structure consists of a p-n or p-i-n junction.(Alharbi & Kais, 2015; Limpert, Bremner, & Linke, 2015) In a first step, the incident photons are absorbed, causing the creating of electron/hole pairs. In a second step, the photogenerated electron/hole pairs are separated and subsequently collected. The charge collection of the photogenerated charges occurs due to diffusion, drift, or the combination of both transport processes to the contacts of the solar cell. Figure 2.1 provides an overview of different solar cells. Figure 2.1(a) shows a schematic sketch of a crystalline silicon (c-Si) homojunction solar cell. Photons are absorbed throughout the complete p-n junction. The photogenerated electron/hole pairs are predominantly collected by charge diffusion. Figure 2.1(b) exhibits a heterojunction solar cell consisting of a c-Si absorber and amorphous silicon (a-Si:H) contact layers. In comparison to a classical silicon homojunction solar cells as shown in Figure 2.1(a), the heterojunction allows for minimizing optical loss (preferable in the emitter), leading to a high short-circuit current density (J_{SC}) and high open-circuit voltage (V_{OC}) due to the use of a heterostructure. Typically, amorphous silicon p- and n-layers are used to form the contacts. Due to the high diffusion length of c-Si, charge diffusion is the primary charge transport mechanism. Most thin-film solar cells consist of a p-i-n structure. An intrinsic absorber layer is introduced between the p- and n-regions. The charge collection process is mainly or partially dominated by the drift of the electron/hole pairs to the contacts. An example of an a-Si:H thin-film solar cell is shown in Figure 2.1(c). A heterojunction thin-film solar cell is shown in Figure 2.1(d). To increase the V_{OC}, hence, the energy conversion efficiency (ECE), a tandem solar cell (TSC) structure is introduced. As shown in Figure 2.1(e), a high bandgap material (e.g., perovskite) is used as a top absorber and a low bandgap material (e.g., c-Si) is considered as a bottom absorber for the implementation of a TSC. In this study, a heterojunction thin-

film solar cell structure is used for the investigation of perovskite solar cells (PSCs), where a perovskite layer is used as an absorber of the incident light. Perovskite material system is comparatively a new semiconducting direct bandgap material with excellent optoelectronic properties.(Green, Ho-Baillie, & Snaith, 2014; Kojima, Teshima, Shirai, & Miyasaka, 2009; Werner et al., 2018)

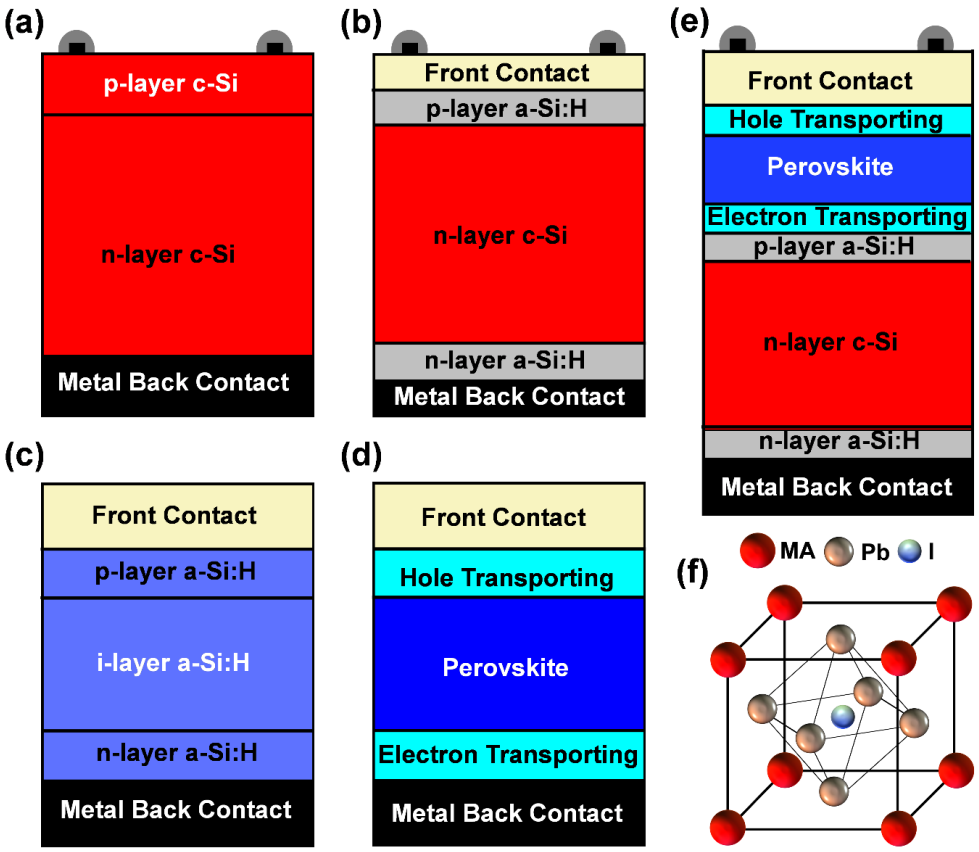

Figure 2.1: Schematics of (a) crystalline silicon homojunction solar cell, (b) silicon heterojunction solar cell consisting of a crystalline silicon absorber and amorphous silicon contact layers, (c) amorphous silicon homojunction thin-film solar cell, (d) perovskite heterojunction thin-film solar cell, and (e) perovskite/silicon tandem solar cell. (f) The schematic sketch of a perovskite crystal structure.

In general, the perovskite material system perovskite materials can be defined by the chemical formula ABX_3 where A is being organic/inorganic cations ($CH_3NH_3^+$ (MA^+), $NH_2CH_3NH_2^+$(FA^+), Cs), B is a divalent cation (Pb^+, Sn^+), and X is the monovalent halide anion (I^-, Cl^-, Br^-).(Green et al., 2014; Stranks & Snaith, 2015a) The crystal structure of a perovskite material is depicted in Figure 2.1(f). The perovskites are

considered as a very promising material due to its tunable bandgap ability, where only by changing the halide anion element (X), the bandgap of the perovskite materials can be changed from low to high. The multi-bandgap perovskites allow realizing high-efficiency tandem solar cells and efficient optical color sensors. In this study, methylammonium-lead(n)-iodide, $CH_3NH_3PbI_3$ ($MAPbI_3$) perovskite, which has a bandgap of ~1.6 eV, is used as a potential absorber for the investigation of single-junction perovskite and perovskite/silicon tandem solar cells. The complex optical constant of perovskite material used in this study is adapted from the published paper by Löper et al.(Loeper et al., 2015) In addition, multi-bandgap perovskites are used to realize the vertically stacked color sensors. However, in a typical PSC structure, the perovskite absorber is sandwiched between electron transporting / hole blocking and hole transporting / electron blocking layers, as depicted in Figure 2.1(d). A variety of electron transporting / hole blocking layers and hole transporting / electron blocking layers have been investigated as potential contact layers. In this study, we used transparent conductive oxides (TCO) as contact layers.

2.2.1 Photovoltaic Characteristic Parameters

In general, the most important parameter to characterize a solar cell is the ECE, which is given by the ratio of the electrical output power density to the optical input power. An Air Mass 1.5 spectrum is used as a standardized optical input power density.(“Reference Solar Spectral Irradiance: ASTM G-173,” n.d.) The electrical output power density is given by $V_{mp} \times J_{mp}$, where V_{mp} and J_{mp} are the voltage and current density at the maximal powerpoint. V_{mp} and J_{mp} are derived from the current-voltage characteristic, J(V), of the solar cell. To correlate the J(V) characteristics with the physics of a solar cell the parameters, short-circuit current density (J_{SC}), fill factor

(FF), and open-circuit voltage (V_{OC}) are introduced. The J_{SC} is given by $J(V=0)=J_{sc}$, while the V_{OC} is determined by $J(V=V_{OC})=0$. The ECE can be calculated by

$$\eta = \frac{V_{mp} \times J_{mp}}{P_{in}} = \frac{V_{OC} \times J_{SC} \times FF}{P_{in}} \tag{2.1}$$

Hence the fill factor can be computed by

$$FF = \frac{V_{mp} \times J_{mp}}{V_{OC} \times J_{SC}} \tag{2.2}$$

An ideal solar cell can be described by the following equation,

$$J(V) = J_0 \times \left(\exp\left(\frac{qV}{kT_{Cell}}\right) - 1\right) - J_{SC} \tag{2.3}$$

where q, V, k, T_{Cell}, and J_0 are an elementary charge, applied voltage, Boltzmann constant, the temperature of the solar cell, and saturation current density. The V_{OC} of the solar cell can be determined by

$$V_{OC} = \frac{kT_{Cell}}{q} \ln\left(\frac{J_{SC}}{J_0} + 1\right) \cong \frac{kT_{Cell}}{q} \ln\left(\frac{J_{SC}}{J_0}\right) \tag{2.4}$$

A graphical representation of solar cell J(V) characteristic curves along with photovoltaic characteristic parameters are shown in Figure 2.2.

In accordance with the optical conservation law, absorbance, transmittance, and reflectance for the solar cell can be defined by(Mohammad Ismail Hossain, 2013)

$$A(\lambda) + R(\lambda) + T(\lambda) = 1 \tag{2.5}$$

Where $A(\lambda)$, $R(\lambda) = \frac{P_{Refl}}{P_{Inc}}$, and $T(\lambda) = \frac{P_{Trans}}{P_{Inc}}$ are absorbance, reflectance, and transmittance of the solar cell at a given wavelength. P_{Inc} is the incident power. P_{Refl} and P_{Trans} are the portion of the incident power reflected by and transmitted through the solar cell, respectively.

One of the essential photovoltaic efficiency indicators is quantum efficiency (QE), which defines the ratio of the number of carriers contribute to the electricity under short-circuit conditions to the number of incident photons. Often, the external quantum efficiency (EQE) is termed as a QE.

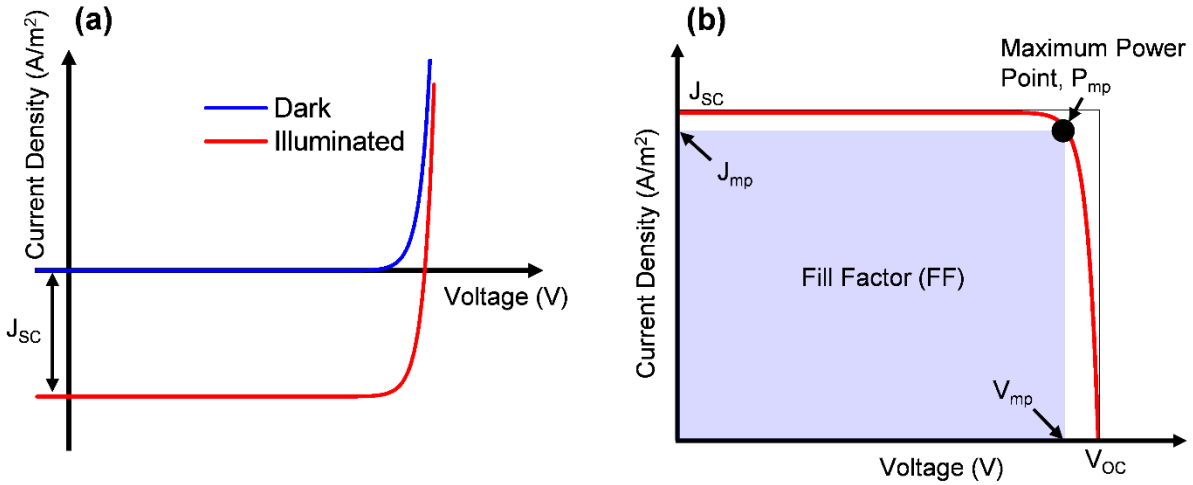

Figure 2.2: Schematics representation of (a) solar cell J-V characteristic curves under dark and illuminated conditions and (b) photovoltaic characteristic curve under only illumination condition along with performance parameters.

The internal quantum efficiency (IQE) is determined as the ratio of the number of carriers contribute to the output current at short-circuit condition to the total number of photogenerated electron-hole pairs within the absorber material.(Dewan, 2011; Luque & Hegedus, 2010a; Mohammad Ismail Hossain, 2013) In this thesis, the EQE is presented as the QE. The IQE and EQE can be expressed by

$$\mathrm{IQE}(\lambda) = \frac{\mathrm{EQE}(\lambda)}{1 - \mathrm{R}(\lambda)} \tag{2.6}$$

$$\mathrm{EQE}(\lambda) = \mathrm{QE}(\lambda) = \frac{\mathrm{J_{SC}}(\lambda)}{\mathrm{q}\phi(\lambda)} = \frac{\mathrm{J_{SC}}(\lambda)}{\mathrm{J_{in}}(\lambda)} \tag{2.7}$$

Where q is the elementary charge and Φ denotes the incident photon flux as a given wavelength. Hence, the overall collection efficiency can also be calculated by

$$CE(\lambda) = \frac{J_{SC}(\lambda)}{J_{in}(\lambda)} \tag{2.8}$$

However, The CE considers the total losses in the solar cell whereas QE exhibits only the losses by the absorber material.

2.3 Fundamentals of Photodetectors

Photodetectors are an essential element in the present technology, which is a semiconductor device that converts an optical signal into an electrical signal. Photodetectors have a wide range of applications, where almost all major sectors, e.g., telecommunications, biotechnology, medicine, monitoring systems, etc., use imaging devices that are based on photodetectors.

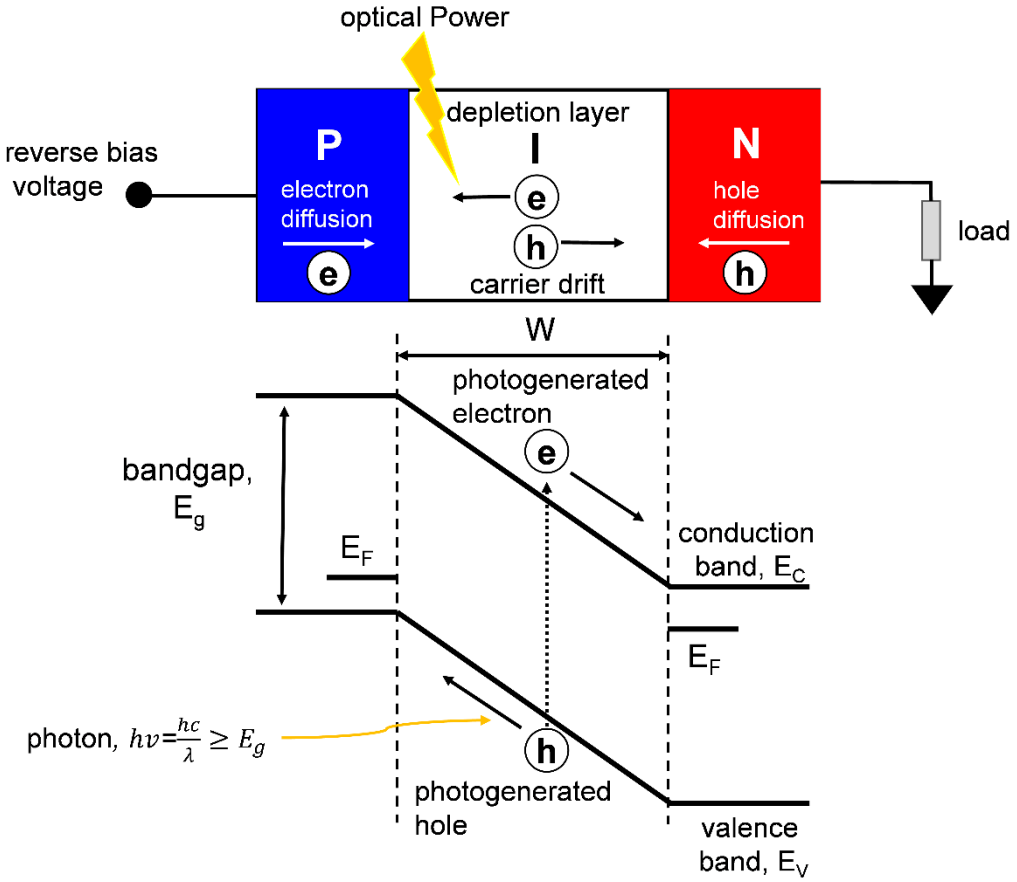

Figure 2.3: Schematic of a PIN structure of photodiode and corresponding energy band diagram.

Semiconductor photodetectors often termed as photodiodes used in the

communication industries, which have similar structures like light-emitting diodes, solar cells, or laser diodes. Nevertheless, unlike the conventional p-n diodes, which works in the forward bias, photodetectors operate in the reverse region so that a tiny saturation current flows through the diode terminals without an input signal.(Sze & Ng, 1995) In principle, to generate electron-hole pairs, the incident photons should have equal or higher energy than the bandgap of materials used in the photodetector as photoactive materials. Practically, many types of device structures are used to improve the performance of photodetectors; however, the underlying mechanism remains the same. A p-i-n structure is mostly used to build a photodetector, where a photoactive material is placed between two doped layers; hence, sometimes, it is called p-i-n diode.(Khosrow-Pour, D.B.A., 2009) The basic structure of p-i-n diode along with the corresponding energy band diagram is depicted in Figure 2.3.

The performance of the photodetector depends mostly on the used photoactive material (e.g., Si, 2D materials, perovskites, etc.) and device design, where only a few characteristic parameters are considered to evaluate the performance, those are responsivity, quantum efficiency, and spectral responsivity.

Responsivity (R) measures the photocurrents (J_{pc}) due to the incident optical power (P_{in}) which can be expressed mathematically by(Qarony, 2019)

$$R = \frac{J_{pc}}{P_{in}} \tag{2.12}$$

The quantum efficiency can be determined by

$$QE = \frac{Rhc}{q\lambda} \tag{2.13}$$

where h and c are Planck's constant and velocity of light in free space, respectively. q is the elementary charge. Then, the spectral responsivity of the photodetector can be calculated by the following formula

$$SR(\lambda) = \frac{q\lambda QE(\lambda)}{hc} \tag{2.14}$$

2.4 Thermodynamics and Detailed-balance Limits

Understanding the fundamental limits in the energy conversion process of solar cells and determining a potential upper limit of the ECE is essential in developing high-efficiency solar cells.(Hegedus & Luque, 2005; Kosyachenko, 2015; Luque & Hegedus, 2010b) The limit of the ECE of a solar cell can be derived by using the first and second laws of thermodynamics. In the first model, the solar conversion process is described as a heat engine, which converts the energy emitted by the sun in useable work. The energy is absorbed by a solar cell, which is described as an absorber at ambient temperature. The energy emitted by the sun is transferred to the solar cell and converted by the solar cell without creating entropy. Hence the conversion process is described by a reversible Carnot heat engine.(Curzon & Ahlborn, 1975; Peter T. Landsberg & Markvart, 1998) Landsberg expanded the model by taking reflection losses and entropy generation into account because of the conversion process. Shockley and Queisser were the first to apply thermodynamics to a solar cell described as a semiconductor device.(Shockley & Queisser, 1961b) They introduced the concept of an ultimate solar cell conversion efficiency. In this model, the solar cell is described by a semiconductor with a bandgap. Hence, large fractions of the incident light are lost due to thermalization and optical losses. Furthermore, it is assumed that the energy conversion process is free of recombination losses. In the next step, Shockley and Queisser expanded their model and took radiative recombination into account. The derived limit is commonly called the detailed balance or Shockley-Queisser limit. The solar cell is described as an ideal solar cell. Only the bandgap of the semiconductor is considered as parameter in description of the solar cell. Several authors expanded the

model of Shockley-Queisser to described special type of solar cells or consider charge transport and optical properties of materials. A brief introduction of different models is proved in the following sub sections.

2.4.1 The Carnot Conversion Efficiency Limit

The most fundamental energy conversion efficiency limit for a solar cell is the Carnot limit, which describes a solar cell as a heat engine as shown in Figure 2.4. The input parameters are E_{Sun} and S_{Sun}, where E_{Sun} and S_{Sun} are the heat flux and entropy flux coming from the sun. T_{sun} is the temperature of the sun which is assumed to be 6000 K. The entropy flux is given by E_{sun}/T_{sun}. The output parameters of the solar cell are represented by an energy flux in the form of useable work W and the heat flux Q emitted to the ambient. S_W is the entropy due to the generated heat energy and T_A is the ambient temperature. According to the first law of thermodynamics, the system can be described by

$$E_{Sun} = W + Q, \tag{2.15}$$

where E_{Sun} is the input radiation energy from the sun and W and Q are the output work and heat energy, respectively. Accordingly, the equation of the heat flux can be expressed as

$$S_{Sun} + S_G = S_W, \tag{2.16}$$

where S_{Sun} is entropies from the sun, while S_G is the entropy caused by transmission, absorption, and conversion of the sunlight. S_W is the entropy due to heat loss. It is assumed that no entropy is generated during the transmission, absorption or conversion of the sunlight. Hence, S_G is assumed to be zero and the process is a reversible energy conversion process. The ECE can be determined by

$$\eta_C = \frac{W}{E_{Sun}} = \frac{E_{Sun} - Q}{E_{Sun}} = 1 - \frac{Q}{E_{Sun}}. \quad (2.17)$$

Because S_G is equal to zero equation 5 can be rewritten by $E_{sun}/T_{sun}=Q/T_A$, so that the ECE can be express only by the input and output temperature.

$$\eta_C = 1 - \frac{T_A}{T_{Sun}} \quad (2.18)$$

Equation (8) defines the upper limit of the energy conversion process using the Carnot model.

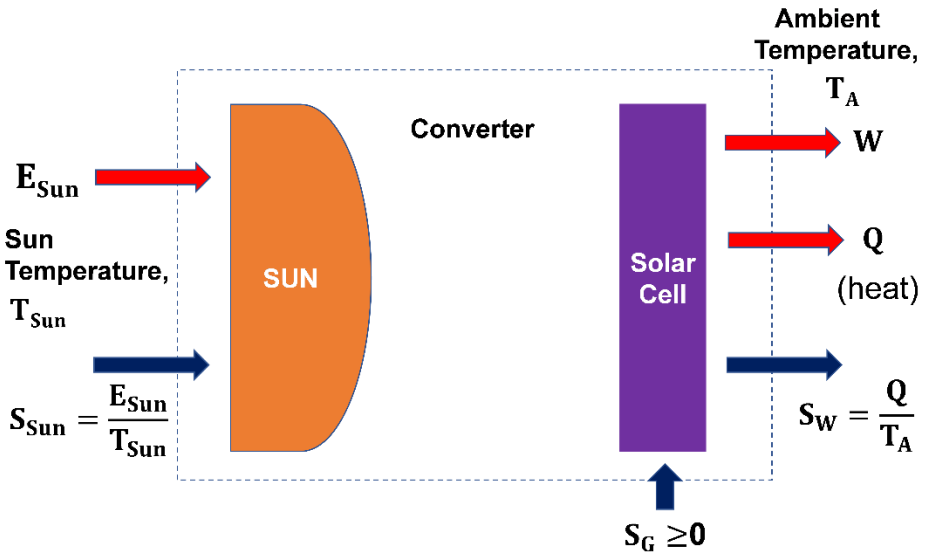

Figure 2.4: Schematic sketch of a solar cell represented by a Carnot reversible heat engine.

The final expression of the ECE does not require or provide any information about the potential realization of such a converter. Furthermore, the calculations assumed that no entropy generation occurs during the transmission, absorption or conversion of the sunlight. However, Planck showed already at the beginning of the 20th century, that an energy transfer between two blackbodies involves unavoidable entropy generation.(Alharbi & Kais, 2015; Kosyachenko, 2015; Planck, 1901) Landsberg tried to account for these entropy losses.

2.4.2 The Landsberg Conversion Efficiency Limit

Landsberg calculated an ECE limit assuming that the sun and the solar cell are described as blackbodies with entropy losses, which means that the transmission, generation, and conversion lead to an entropy loss.(Kosyachenko, 2015) Furthermore, the input and output heat fluxes are replaced by input and output radiation energies. The schematic sketch of the Landsberg solar converter is illustrated in Figure 2.5.

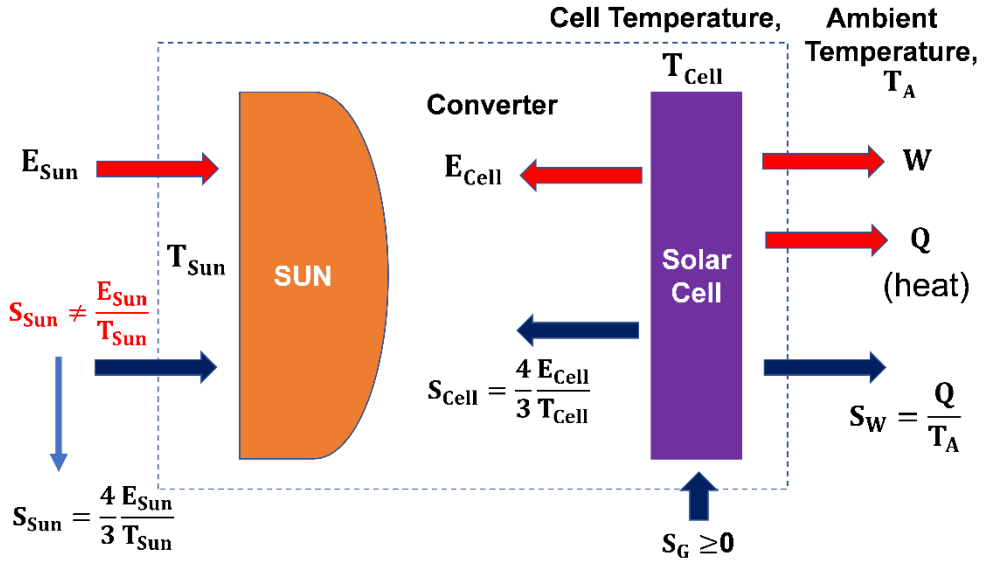

Figure 2.5: Schematic diagram of the Landsberg model for a solar converter.

The emission of an ideal blackbody is described by the Stefan Boltzmann law. According to the Stefan Boltzmann law, the radiation energy is given by

$$E = \sigma_{SB} T^4 \tag{2.19}$$

where T is the temperature of the blackbody and σ_{SB} is the Boltzmann constant. The entropy of the system can be calculated by solving the fundamental equation of thermodynamics TdS=dE, which leads to S=4×E/3/T, so that the entropy of the sun and the solar cell is given by

$$S_{Sun} = \frac{4}{3}\frac{E_{Sun}}{T_{Sun}} \tag{2.20}$$

and

$$S_C = \frac{4}{3}\frac{E_{Cell}}{T_{Cell}} \tag{2.21}$$

where E_{Cell} and S_{Cell} are the energy and entropy due to radiation, respectively. Now, equations (5) and (6) become

$$E_{Sun} = W + Q + E_{Cell} \tag{2.22}$$

$$S_{Sun} = S_W + S_{Cell} - S_G \tag{2.23}$$

If we assume that the solar cell temperature, T_{Cell}, is equal to the ambient temperature, T_A, so that the following expression can be derived.

$$\eta_L = \frac{W}{E_{Sun}} = \frac{E_{Sun} - Q - E_{Cell}}{E_{Sun}} = 1 - \frac{Q}{E_{Sun}} - \frac{E_{Cell}}{E_{Sun}} = 1 - \frac{Q}{E_{Sun}} - \frac{T_{cell}^4}{T_{Sun}^4} \tag{2.24}$$

The general solution of the Landsberg conversion efficiency is given by(De Vos, Landsberg, Baruch, & Parrott, 1993; Markvart & Landsberg, 2002)

$$\eta_L = 1 - \frac{T_{cell}^4}{T_{Sun}^4} - \frac{4}{3}\frac{T_A}{T_{Sun}} - \frac{4}{3}\frac{T_A}{T_{Cell}} \times \left(\frac{T_{cell}^4}{T_{Sun}^4}\right) \tag{2.25}$$

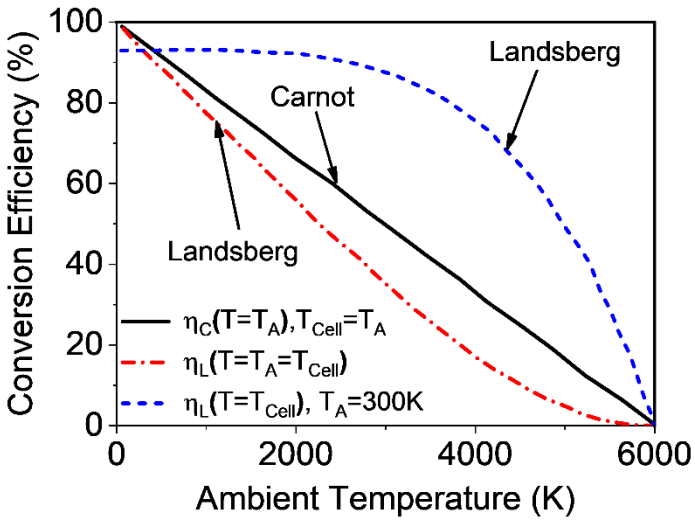

Figure 2.6: Temperature-dependent Carnot and Landsberg efficiencies for solar

energy conversion.

The Landsberg conversion efficiency is plotted in Figure 2.6 together with the Carnot limit. The Landsberg limit is plotted for two cases. In the first case, it is assumed that the temperature of the solar cell and the environment are equal and $T_{Cell} \approx T_A$. This is realistic for low solar cell temperatures, while the assumption is not realistic for high solar cell temperatures. In a second case, it is assumed that the ambient temperature is constant at T_A=300 K, while the conversion temperature is varied. The conversion efficiency as a function of the temperature is illustrated in Figure 2.6. According to the Carnot model, the upper conversion efficiency is limited to 95% assuming an ambient temperature of 300 K. The Landsberg model provides an upper limit of is to 93%. The ECE is zero if the converter and ambient temperature is equal to the sun temperature.(De Vos et al., 1993; P. T. Landsberg & Tonge, 1980; Rawat, Lamba, & Kaushik, 2017)

2.4.3 The Ultimate Solar Cell Conversion Efficiency Limit

So far, the solar cell has been described by a general blackbody. Now we will assume that the solar cell is described by a single-junction solar cell, which consists of a semiconductor with a constant bandgap. The ultimate conversion efficiency represents a theoretical ECE limit of a semiconductor-based solar cell. Photons with photon energies larger than or equal to the material bandgap are absorbed. Photons with energies smaller than the bandgap are not absorbed. It is assumed that photogenerated electron/hole pairs are collected. The recombination of electron/hole pairs is not considered. Only thermalization and absorption losses are considered. Absorption losses occur for photon energies smaller the bandgap and thermalization losses occur for energies larger than the bandgap.(Kosyachenko, 2015) The photon

flux of the sun, which is absorbed by the solar cell is given by.(Kosyachenko, 2015; Shockley & Queisser, 1961b)

$$F_{Cell}(T = T_{Sun}) = \frac{2\pi}{h^3c^2}\int_{E_g}^{\infty}\frac{E^2dE}{\exp\left(\frac{E}{kT_{Sun}}\right)-1} \tag{2.26}$$

where h, c, k, and E_G are Planck's constant, speed of light, Boltzmann constant, and energy bandgap of the photovoltaic material. The photon flux can be approximated by

$$F_{Cell}(T = T_{Sun}) \cong \frac{2\pi}{h^3c^2}\int_{E_g}^{\infty}\exp\left(-\frac{E}{kT_{Sun}}\right)E^2dE = \int_{E_g}^{\infty}\phi_{Sun}dE \tag{2.27}$$

where ϕ_{sun} is the blackbody radiation flux of the sun, which is given by

$$\phi_{Sun} = \frac{2\pi}{h^3c^2}\times E^2\times\exp\left(-\frac{E}{kT_{Sun}}\right) \tag{2.28}$$

The photocurrent density of the solar cell is given by $J=q\times F_{Cell}(T=T_{sun})$. The electrical output power density of the solar cell is calculated by

$$P_{Out} = J\times V = q\times F_{Cell}(T = T_{Sun})\times\frac{E_G}{q} = F_{Cell}(T = T_{Sun})\times E_g \tag{2.29}$$

The input sun power density is given by(Kosyachenko, 2015)

$$P_{in} = \frac{2\pi}{h^3c^2}\int_{0}^{\infty}\frac{E^3dE}{\exp\left(\frac{E}{kT_{Sun}}\right)-1} \cong \frac{2\pi^5(kT_{Sun})^4}{15h^3c^2} \tag{2.30}$$

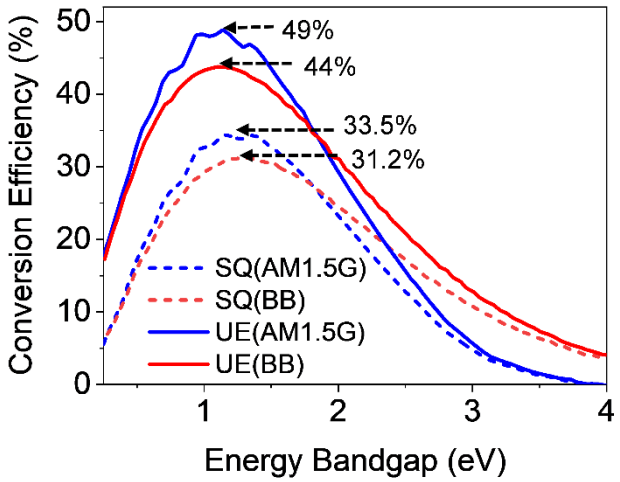

Figure 2.7: Temperature-dependent Carnot and Landsberg efficiencies for solar energy conversion.

Finally, the energy conversion efficiency of a solar cell is calculated by $\eta=P_{out}/P_{in}$. By using the blackbody spectrum (T=6000 K) and AM 1.5 global spectrum, the solar cell exhibits a maximum of the ultimate conversion efficiency of 44% and 49%, respectively for a bandgap of 1.1 eV as shown in Figure 2.7. These ECEs are significantly lower than the Carnot and Landsberg limits because of the two losses, absorption losses and thermalization losses, which are large for single-junction solar cells.(Kosyachenko, 2015)

2.4.4 Detailed Balance Limit or Shockley-Queisser Limit

The ultimate ECE limit derived by Shockley and Queisser does not consider radiative emission by the solar cell. Hence, the ultimate conversion efficiency limit violates the Kirchhoff law. Shockley and Queisser expanded their model commonly called detailed balance limit or Shockley-Queisser (SQ) limit, by taking radiative recombination into account. Thermal generation and non-radiative recombination are not considered. The photon flux emitted by the solar cell can be described by blackbody radiation. The

emission energy is given by E-qV, where V is the voltage applied to the solar cell.(Kosyachenko, 2015; Shockley & Queisser, 1961b)

$$F_R(V) = \frac{2\pi}{h^3c^2}\int_{E_G}^{\infty}\frac{E^2}{\exp\left(\frac{E-qV}{kT_{cell}}\right)-1}dE \tag{2.31}$$

The applied voltage is equal to the splitting of the Fermi levels $qV=E_F^n-E_F^p$, where E_F^n and E_F^p are the majority of quasi-Fermi levels in the p- and n-region of the p-n junction. The quasi-Fermi levels are determined by the free carrier concentration, which is again determined by doping concentration, generation, and recombination of charges. With increasing photogeneration, the quasi-Fermi levels shift closer to the conduction and valence bands, and the V_{OC} is increased. In contrast, for recombination, the quasi-Fermi levels away from the conduction and valence bands and the V_{OC} are reduced. The photon flux emitted by the solar cell can be approximated by

$$F_R(V) \cong \frac{2\pi}{h^3c^2}\int_{E_g}^{\infty}\exp\left(-\frac{E-qV}{kT_{Cell}}\right)E^2dE = \exp\left(\frac{qV}{kT_{Cell}}\right)\int_{E_G}^{\infty}\phi_{Cell}dE \tag{2.32}$$

The equation can be simplified and the blackbody radiation flux ϕ_{cell} of the solar cell can be described by

$$\phi_{Cell} = \frac{2\pi}{h^3c^2}E^2\exp\left(-\frac{E}{kT_{Cell}}\right) \tag{2.33}$$

So that the photon flux at zero applied voltage is given by

$$F_{R0} = \int_{E_G}^{\infty}\phi_{Cell}dE \tag{2.34}$$

Combining 22-24 allows for describing the photon flux as a function of the applied voltage.

$$F_R(V) = F_{R0} \times \exp\left(\frac{qV}{kT_{Cell}}\right) \quad (2.35)$$

The expression for the total current density is given by(Rühle, 2017; Shockley & Queisser, 1961b)

$$J(V) = q \times [F_{cell} - F_R(V)] \quad (2.36)$$

The J_{SC} and V_{OC} can be calculated by.

$$J_{SC} = q \times [F_{cell} - F_{R0}] \quad (2.37)$$

and

$$V_{OC} = \frac{kT_{Cell}}{q} \times \ln\left(\frac{F_{cell}}{F_{R0}}\right) \quad (2.38)$$

The FF and ECE of the solar cell is given by

$$FF = \frac{\max[J(V) \times V]}{J_{SC} \times V_{OC}} \quad (2.39)$$

and

$$\eta = \frac{\max[J(V) \times V]}{P_{in}} \quad (2.40)$$

The J_{SC}, V_{OC}, FF, and ECE as a function of the bandgap are shown in Figure 2.8 for blackbody radiation and an AM 1.5G sun spectrum.

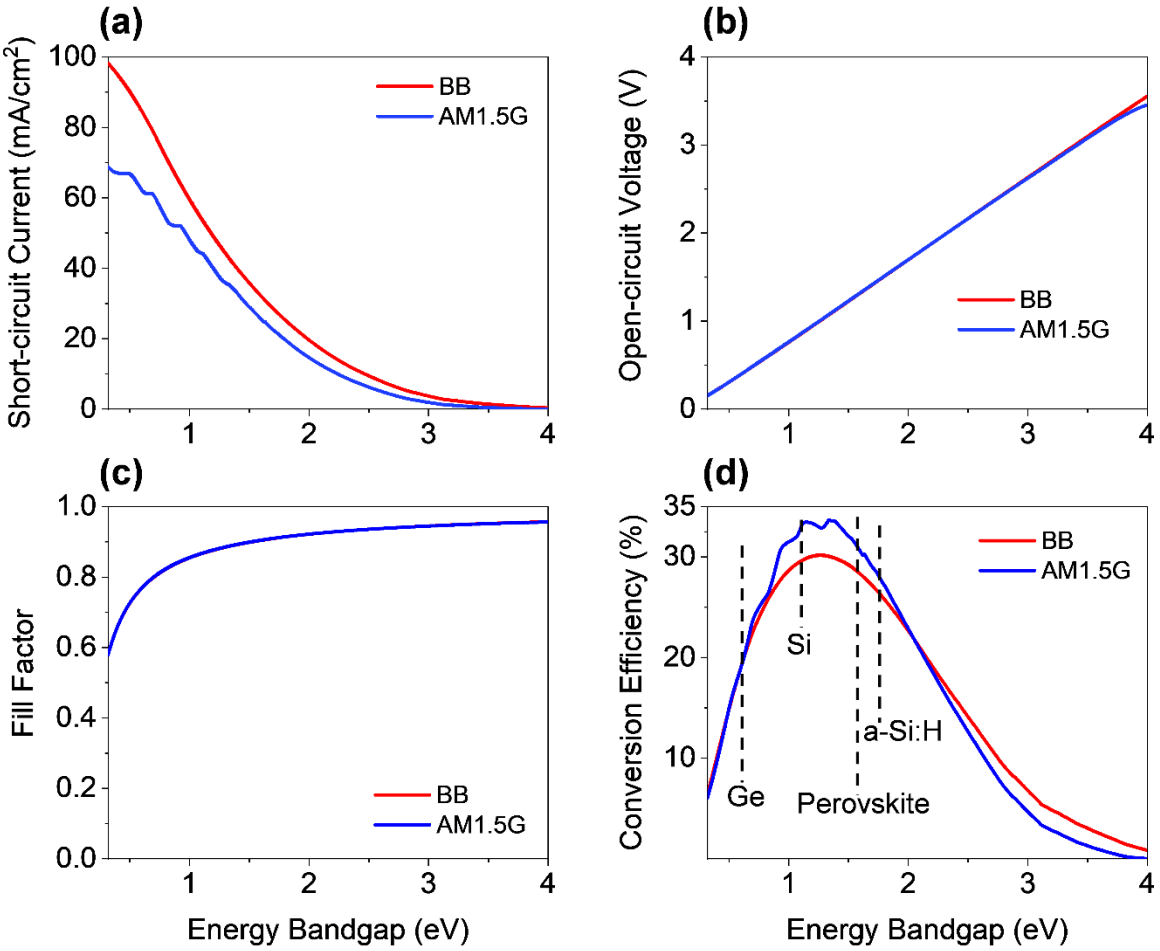

Figure 2.8: Detailed Balance limit or Shockley–Queisser limit for (a) short-circuit current density, (b) open-circuit voltage, (c) fill factor, and (d) conversion efficiency under AM 1.5G spectrum with blackbody spectrum at 6000 K.

The J_{SC} increases, while the V_{OC} decreases as a function of the bandgap. The optimal bandgap represents a trade-off between the J_{SC} and the V_{OC}. The ECE as a function of the bandgap is provided in Figure 2.8(d). The ECE reaches a maximum value of approx. 33.5%. The maximum ECE is observed for a bandgap of 1.2-1.4 eV. A comparison of the ultimate energy conversion efficiency and the Shockley-Queisser conversion efficiency limit is plotted in Figure 2.7. The additional loss in the ECE caused by radiative recombination and charge transport. The ultimate conversion efficiency exhibits its maximum for 1.1 eV, while the SQ limit exhibits a maximum at 1.2-1.4 eV. The difference is approximately equal to E_G-q×V_{OC}, where V_{OC} is the open-circuit voltage according to the SQ limit (equation 2.38). In other words, considering

radiative recombination losses leads to a shift of the optical bandgap to larger bandgaps. Hence, materials with appropriate bandgap can be selected. The electronic and optical properties of the materials will determine if the material allows for reaching ECEs close to the detailed balance limit.(Shockley & Queisser, 1961b)

2.5 Numerical Modeling Theory and Method

Numerical modeling and simulations are an essential part of realizing efficient optoelectronic devices by providing a reliable prediction on device performance. The optical performance of devices is determined from the optical wave propagation or the field distributions within the device structure, where the optical wave propagation is directly associated with the electromagnetic (EM) wave. In 1865, James Clerk Maxwell introduced a set of four equations, which are called Maxwell's equations, which can explain any electromagnetic wave propagation phenomena.("VIII. A dynamical theory of the electromagnetic field," 1865) As compared to the simple analytical methods (e.g., Transfer Matrix Method), Maxwell's equations can solve an extensive range of complex device structures with precision. Several mathematical approaches, e.g., Fourier modal method (FMM), finite element method (FEM), finite-difference time-domain (FDTD) method, finite integration technique (FIT), method of moments (MoM), rigorous coupled-wave analysis (RCWA), etc., is employed to solve Maxwell's equations.(Chandezon, Maystre, & Raoult, 1980; Inan & Marshall, 2011; Moharam, Pommet, Grann, & Gaylord, 1995; Sadiku, 2015; Saleh & Teich, 2007) In this thesis, the optics of solar cells and color sensors is investigated by FDTD-based Maxwell's equations solver. A further discussion on Maxwell's equations and device modeling theories is provided in the following subsections.

2.5.1 Electromagnetic Theory

The electromagnetic theory starts with Maxwell's equations, which describe a complete method of optical wave propagation. The shorter wavelength or low-level light cannot be explained by the classical wave theory, where Maxwell's equations solve such problems accurately.(Dewan, 2011; Sadiku, 2015; Saleh & Teich, 2007; "VIII. A dynamical theory of the electromagnetic field," 1865) Maxwell's equations in the following provide the relationship between electric and magnetic field quantities.(Dexter, 1958; Mohammad Ismail Hossain, 2013; Staelin, 2011; Steen, 2000)

$$\nabla \times \mathbf{E} = -\frac{\partial \mathbf{B}}{\partial t} = -\mu \frac{\partial \mathbf{H}}{\partial t} \tag{2.52a}$$

$$\nabla \times \mathbf{H} = \frac{\partial \mathbf{D}}{\partial t} + \mathbf{J} = \varepsilon \frac{\partial \mathbf{E}}{\partial t} + \mathbf{J} \tag{2.52b}$$

$$\nabla . \mathbf{D} = \rho \tag{2.52c}$$

$$\nabla . \boldsymbol{B} = 0 \tag{2.52d}$$

where **E** and **H** are electric field intensity and magnetic field intensity, respectively. **D** and **B** are electric flux intensity and magnetic flux intensity, respectively. J is the current density. ρ is being the charge density. ε and μ are electrical permittivity and magnetic permeability of the material.

Maxwell's equations have to be satisfied with the condition of the electric and magnetic field to realize wave equations. Hence, Maxwell's curl equation is taken for linear isotropic, homogeneous, and source-free medium (ρ=0, **J**=0), and added a curl of both sides of equation 2.52a.(Dewan, 2011; Mohammad Ismail Hossain, 2013; Qarony, 2019)

$$-\nabla \times \nabla \times \mathbf{E} = \mu \frac{\partial}{\partial t} (\nabla \times \mathbf{H}) \tag{2.53}$$

Since **J**=0,(Sadiku, 2015) equation 2.53 becomes

$$-\nabla \times \nabla \times \mathbf{E} = \mu\varepsilon \frac{\partial^2 \mathbf{E}}{\partial t^2} \tag{2.54}$$

By applying an identity vector to equation 2.54, it is found

$$\nabla(\nabla . \mathbf{E}) - \nabla^2 \mathbf{E} = -\mu\varepsilon \frac{\partial^2 \mathbf{E}}{\partial t^2} \tag{2.55}$$

Since ρ=0,(Sadiku, 2015) the equation 2.55 can be written as

$$\nabla^2 \mathbf{E} - \mu\varepsilon \frac{\partial^2 \mathbf{E}}{\partial t^2} = 0 \tag{2.56}$$

Equation 2.56 is called the time-dependent vector Helmholtz equation or simply wave equation. Moreover, it is possible to get the equation for **H**. If the same above procedure is applied to equation 2.52b, we can get

$$\nabla^2 \mathbf{H} - \mu\varepsilon \frac{\partial^2 \mathbf{H}}{\partial t^2} = 0 \tag{2.57}$$

These two equations (2.56 and 2.57) are the motion of electromagnetic waves that travel in a medium with a velocity of(Dewan, 2011; Mohammad Ismail Hossain, 2013; Qarony, 2019)

$$v = \sqrt{\mu\varepsilon} \tag{2.58}$$

In free space, with electromagnetics constants $\mu_0 = 4\pi \times 10^{-7}$ H/m and $\varepsilon_0 = 8.854 \times 10^{-12}$F/m, the speed of light is 3×10^8 m/s. Detailed information is provided in the literature.(Hecht, 2010; Popovic & Neff, 2000; Saleh & Teich, 2007; Steen, 2000)

2.5.2 Finite-Difference Time-Domain (FDTD) Method

In practice, Maxwell's equations deal with partial differential equations, which is non-linear by analyzing mathematical approaches. As mentioned earlier, several numerical

methods, such as FEM, FDM, FDTD, and MoM, are used. In finite difference methods, Maxwell's equations are discretized by replacing differential equations by finite difference equations.(Chandezon et al., 1980; Inan & Marshall, 2011; Moharam et al., 1995; Sadiku, 2015; Saleh & Teich, 2007) Amongst, FDTD is a very efficient method due to the requirement of fewer grids, which can be applied to the wide optoelectronic areas.(Dewan, 2011; Mohammad Ismail Hossain, 2013) In 1966, Kane S. Yee first introduced FDTD.(Yee, 1966) The optics of solar cells and color sensors are investigated by FDTD optical simulations in the current study. Electromagnetic wave elements in FDTD always denoted by not only time also a space and stability conditions depend on the size of the mesh. The wavelength of the incident light has substantial impact on the effectiveness of FDTD results.(Dewan, 2011; Mohammad Ismail Hossain, 2013; Qarony, 2019) Electromagnetic waves are rigorously calculated by the FDTD method, which strongly depends on the spatial distribution of the sample (sampling factor and time steps).(Yee, 1966) Maxwell's curl equations are realized from the Yee algorithm, which calculates all potential capacities of samples for a certain limit. The sampling in space has a further influence on the stability of the FDTD, thus, sampling time has to be properly defined to ensure stability in FDTD domain.(Yee, 1966)

Hence, the FDTD method can be started with the expansion of equations 2.52a and 2.52b with Faraday's and Ampere's laws in component form.

$$\mu \frac{\partial \mathbf{H}_x}{\partial t} = \left(\frac{\partial \mathbf{E}_y}{\partial z} - \frac{\partial \mathbf{E}_z}{\partial y}\right) \tag{2.59}$$

$$\mu \frac{\partial \mathbf{H}_y}{\partial t} = \left(\frac{\partial \mathbf{E}_z}{\partial x} - \frac{\partial \mathbf{E}_x}{\partial z}\right) \tag{2.60}$$

$$\mu \frac{\partial \mathbf{H}_z}{\partial t} = \left(\frac{\partial \mathbf{E}_x}{\partial y} - \frac{\partial \mathbf{E}_y}{\partial x}\right) \tag{2.61}$$

Similarly,

$$\varepsilon \frac{\partial \mathbf{E}_x}{\partial t} + \sigma \mathbf{E}_x = \left(\frac{\partial \mathbf{H}_z}{\partial y} - \frac{\partial \mathbf{H}_y}{\partial z}\right) \tag{2.62}$$

$$\varepsilon \frac{\partial \mathbf{E}_y}{\partial t} + \sigma \mathbf{E}_y = \left(\frac{\partial \mathbf{H}_x}{\partial z} - \frac{\partial \mathbf{H}_z}{\partial x}\right) \tag{2.63}$$

$$\varepsilon \frac{\partial \mathbf{E}_z}{\partial t} + \sigma \mathbf{E}_z = \left(\frac{\partial \mathbf{H}_y}{\partial x} - \frac{\partial \mathbf{H}_x}{\partial y}\right) \tag{2.64}$$

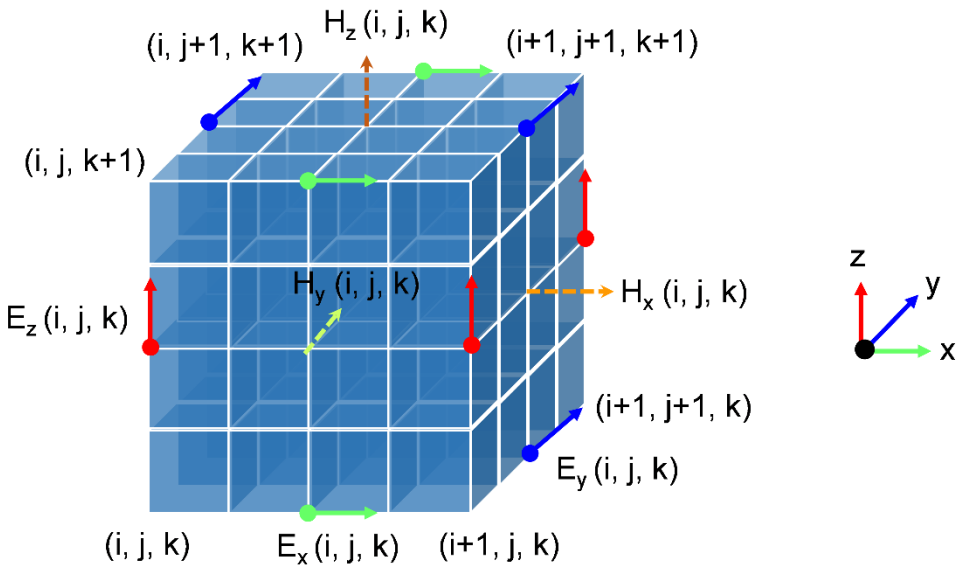

Figure 2.9: Unit cell of the Yee's lattice with the positions and directions of the electric field (E) and magnetic field (H) components.

Equations 2.59 to 2.61 are the expanded form of equation 2.52a, and equations 2.62 to 2.64 are the expanded form of equation 2.52b for a rectangular coordinate system. The following expanded equations can be discretized with central finite difference approximation as long as they lie on a staggered grid with representing a cubic box,

which is called Yee Cell.(Yee, 1966) All electric and magnetic field components are placed in a cubic or unit cell are shown in Figure 2.9.

By expanding the equation 2.59 in term of central finite difference, we obtain

$$\mu\frac{\mathbf{H}_x^{n+\frac{1}{2}}(i,j,k)-\mathbf{H}_x^{n-\frac{1}{2}}(i,j,k)}{\Delta t}=\frac{\mathbf{E}_y^{n}(i,j,k)-\mathbf{E}_y^{n}(i,j,k-1)}{\Delta z}-\frac{\mathbf{E}_z^{n}(i,j,k)-\mathbf{E}_z^{n}(i,j-1,k)}{\Delta y} \tag{2.65}$$

Solving for $\mathbf{H}_{x(i,j,k)}^{n+\frac{1}{2}}$, we have

$$\mathbf{H}_x^{n+\frac{1}{2}}(i,j,k)=\frac{\Delta t}{\mu_0\Delta z}(\mathbf{E}_y^{n}(i,j,k)-\mathbf{E}_y^{n}(i,j,k-1))-\frac{\Delta t}{\mu_0\Delta y}(\mathbf{E}_z^{n}(i,j,k)-\boldsymbol{E}_z^{n}(i,j-1,k))+H_x^{n-\frac{1}{2}}(i,j,k) \tag{2.66}$$

With the same procedure, the other two components of the magnetic field (**H**) can be determined. Next, by expanding the equation 2.62 in term of central finite difference again, we get

$$\varepsilon\frac{\mathbf{E}_x^{n+1}(i,j,k)-\mathbf{E}_x^{n}(i,j,k)}{\Delta t}+\sigma\mathbf{E}_x^{n+\frac{1}{2}}(i,j,k)=\frac{\mathbf{H}_z^{n+\frac{1}{2}}(i,j+1,k)-\mathbf{H}_z^{n+\frac{1}{2}}(i,j,k)}{\Delta y}-\frac{\mathbf{E}_z^{n}(i,j,k)-\mathbf{E}_z^{n}(i,j-1,k)}{\Delta y} \tag{2.67}$$

Solving for $\mathbf{E}_{x(i,j,k)}^{n+1}$, we have

$$\mathbf{E}_x^{n+1}(i,j,k)=\frac{1}{a\Delta y}(\mathbf{H}_z^{n+\frac{1}{2}}(i,j+1,k)-\mathbf{H}_z^{n+\frac{1}{2}}(i,j,k)) \tag{2.68}$$

$$-\frac{1}{a\Delta z}\left(\mathbf{H}_y^{n+\frac{1}{2}}(i,j,k+1)-\mathbf{H}_y^{n+\frac{1}{2}}(i,j,k)\right)+\frac{b}{a}\mathbf{E}_x^n(i,j,k)$$

By repeating the same procedure, the other two electric field (**E**) components can be determined. More details can be found in the literature.(Qarony, 2019; Yee, 1966) To investigate the optics within an optoelectronic device, the evolution of the electromagnetic fields are computed as follows.(Yee, 1966)

a) Setting initial conditions, let n=0, hence, $H^{-1/2}=0$ and $E^0=0$.
b) Computing values for sources at n.
c) Computing $H^{n+1/2}$.
d) Computing E^{n+1}.
e) Check for convergence of the solution. If not finished, let n=n+1 and go to step 2.
f) Performing post-processing.

In this study, Maxwell's equations solver is used in the three-dimensional (3D) environment, where the incident plane wave is circular, which is the combination of transverse electric (TE) and transverse magnetic (TM) to z-direction. Hence, to have the 3D FDTD equations, it is necessary to determine equations for 2D FDTD. By considering a structure that is infinite in the z dimension, so that $\frac{\partial}{\partial t}=0$, from equations 2.59 to 2.61, 2.62 to 2.64, we get.

$$\mu\frac{\partial \mathbf{H}_x}{\partial t}=-\frac{\partial \mathbf{E}_z}{\partial y} \tag{2.69}$$

$$\mu\frac{\partial \mathbf{H}_y}{\partial t}=\frac{\partial \mathbf{E}_z}{\partial x} \tag{2.70}$$

$$\varepsilon \frac{\partial \mathbf{E}_z}{\partial t} = \frac{\partial \mathbf{H}_y}{\partial x} - \frac{\partial \mathbf{H}_x}{\partial y} \tag{2.71}$$

Equations 2.69 to 2.71 are called the transverse magnetic to z (TM_z): $\mathbf{E}_z$, $\mathbf{H}_x$, $\mathbf{H}_y$. Similarly,

$$\varepsilon \frac{\partial \mathbf{E}_x}{\partial t} = \frac{\partial \mathbf{H}_z}{\partial y} \tag{2.72}$$

$$\varepsilon \frac{\partial \mathbf{E}_y}{\partial t} = -\frac{\partial \mathbf{H}_z}{\partial x} \tag{2.73}$$

$$\varepsilon \frac{\partial \mathbf{H}_z}{\partial t} = \left(\frac{\partial \mathbf{E}_x}{\partial y} - \frac{\partial \mathbf{E}_y}{\partial x}\right) \tag{2.74}$$

Equations 2.72 to 2.74 are called the transverse electric to z (TE_z): $\mathbf{H}_z$, $\mathbf{E}_x$, $\mathbf{E}_y$.

The stability of FDTD is a crucial part of any optical simulations. FDTD contains a spatial distribution means it includes both time and space. Hence, to achieve an accurate calculation, mesh cell size should be 1/100 or less at the shortest wavelength. The relation can be presented by the following formula

$$\text{Maximum grid size} = \text{minimum}(\Delta x, \Delta y, \Delta z) \leq \frac{\lambda_{min}}{10 n_{max}} \tag{2.75}$$

where, n_{max} is the maximum refractive index. Δx, Δy, and Δz are the step size. The stability of FDTD can be analyzed by using von-Neuman method, hence, we obtain the maximum time-step

$$\text{3D:}\quad \Delta t \leq \frac{\sqrt{\varepsilon_r^{min}}}{\varepsilon_0}\left(\frac{1}{\Delta x^2} + \frac{1}{\Delta y^2} + \frac{1}{\Delta z^2}\right)^{-1/2} \tag{2.76}$$

$$\text{2D:}\quad \Delta t \leq \frac{\sqrt{\varepsilon_r^{min}}}{\varepsilon_0}\left(\frac{1}{\Delta x^2} + \frac{1}{\Delta y^2}\right)^{-1/2} \tag{2.77}$$

Where, ε_r and ε_0 relative and vacuum permittivity of the material or medium, respectively.

2.5.3 Simulation Method

The numerical simulation always plays a vital role in realizing efficient solar cells, where the characteristic parameters often determine from the optical and electrical simulations without carrying complex experiments. In the following, both simulation methods used in this thesis are shortly explained.

Optical simulation

Three-dimensional FDTD optical simulations are performed to study the influence of the device design on the J_{SC} and derive an optimal device design. The complex refractive index of the materials and the geometry of the devices are used as input parameters. The optical constants of materials are determined either by ellipsometry measurement of the deposited film or adapted from the published works. Simulations are carried out for the wavelengths range from 300 nm to 800 nm for single-junction PSCs and 300 nm to 1200 nm for TSCs. A circularly polarized plane wave is considered as an incident wave, which has an amplitude of 1 V/m. The collection efficiency of solar cell absorbers is assumed to be 100%. This assumption is valid if the charge carrier diffusion length is larger than the thickness of the absorber. The measured diffusion length is large enough for $MAPbI_3$ (1.7 μm for electrons and 6.3 μm for holes), while the thickness of our perovskite solar cells is smaller than 400 nm.(Li et al., 2015). The calculated QE of the solar cell represents an upper limit of the QE. The total generation rate can be calculated by

$$GR_{Total}(\lambda) = \varepsilon'' \int \frac{|E(x,y,z)|}{2 \times h} d\lambda \tag{2.78}$$

where, ε'' is the imaginary part of the relative permittivity, $\varepsilon_r=(n-ik)^2$, where n is the refractive index and k is the extinction coefficient of the perovskite absorber. And, h is

the Planck's constant. The absorption coefficient of the absorber can be computed by $\alpha=4\pi k/\lambda$. The optical simulation provides the electric field distribution within the solar cell structure. The time-averaged power density within the solar cell is given by

$$Q(x,y,z) = \frac{1}{2} c\varepsilon_0 n\alpha |E(x,y,z)|^2 \tag{2.79}$$

where c and ε_0 are the speed of light in free space and permittivity of free space. α is the absorption coefficient. n and E are the refractive index of the material and electric field distribution, respectively. Based on the power density, the quantum efficiency (QE) of the solar cell is calculated by

$$QE(\lambda) = \frac{1}{P_{Opt}} \int Q(x,y,z)dxdydz \tag{2.80}$$

where P_{Opt} is the optical input power of the sun. The calculated QE of the solar cell represents an upper limit of QE. The QE is defined as the ratio of photons absorbed by the absorber layer divided by the total photons incident to the solar cell. Furthermore, the short-circuit current density can be calculated by

$$J_{SC} = \frac{q}{hc} \int \lambda \times QE(\lambda) \times S(\lambda)d\lambda \tag{2.81}$$

where h is the Planck's constant and $S(\lambda)$ is the solar spectral irradiance (AM 1.5G). Photons absorbed by the absorber layer contribute to the J_{SC}, and photons absorbed by all other layers do not contribute to the J_{SC}.

Electrical Simulation

To estimate the realistic photovoltaic performance, electrical parameters play an additional critical role; however, optical simulations do not allow determining electrical parameters of the solar cell. Therefore, electrical simulations are performed thoroughly of investigated solar cells by the finite element method (FEM), which allows determining the current-voltage (J-V) characteristic curve of the solar cell. In the FEM

approach, non-linear Poisson's, continuity, and drift-diffusion equations are engaged for the calculations. The charge (ρ) and the current density (J) can be expressed by

$$\rho = q(n - p + N_D + N_A) \quad (2.82)$$

$$J_n = -q\mu_n n\nabla\phi + qD_n\nabla n \quad (2.83a)$$

$$J_p = -q\mu_p p\nabla\phi - qD_p\nabla p \quad (2.83b)$$

where, n and p are electron concentration and hole concentration, respectively. N_D and N_A are donor density and acceptor density, respectively. μ_n and μ_p are electron and hole mobilities. D_n and D_p are electron and hole diffusion constants. Φ is the electrostatic potential.

Further detail of the numerical calculation can be found in the literature.(Da, Xuan, & Li, 2018) The electron-hole pair (EHP) generation was used as an optical input for the FEM simulation, which was realized from the FDTD optical simulation. The generation rate for electron and hole is kept constant to the total generation rate ($GR_{Total}=GR_n=GR_p$). Furthermore, both radiative recombination (R_{rad}) and non-radiative recombination, which are auger recombination (R_{auger}), Shockley-Read-Hall recombination (R_{SRH}), and surface recombination ($R_{surface}$), were considered for the investigation. Furthermore, a wide range of essential electronic properties of the material is used in the calculation. The close boundary conditions are applied to the simulation environment, where front contact and metal contact are designated as anode and cathode, respectively. For attaining the JV curve, a range of the voltage swipe is considered.

CHAPTER 3

OPTICS OF PEROVSKITE SOLAR CELL FRONT CONTACTS (Flat)

This chapter describes the influence of the front contacts on the photovoltaic performance of planar perovskite solar cells. Metal oxide contacts are used for the fabrication of the solar cells, where several deposition techniques are adapted to prepare high-quality metal oxide films. Detailed explanations are provided in the following sections.

3.1 Electron Beam Physical Vapor Deposition of NiO Films

Efficient hole transport materials (HTLs) are crucial for realizing improved short-circuit current density (J_{SC}) and energy conversion efficiency (ECE) of perovskite solar cells (PSCs). PSCs with high ECEs use organic HTMs that are highly responsive to humid due to enhanced hydrophilicity, affecting device stability.(You et al., 2016b) Currently, nickel-oxide (NiO), a direct bandgap inorganic material, has attracted considerable attention to the research community because of its better chemical stability, high hole mobility, low resistivity, low cost, and suitable energy level. NiO films can be used as a potential HTM for efficient and stable PSCs.(W. Sun et al., 2016; J.-Y. Wang et al., 2009a; X. Yin et al., 2017) In this study, NiO films were investigated as potential HTL for the fabrication of planar PSCs, where the films were prepared by electron-beam physical vapor deposition (EBPVD) at low temperatures. EB deposition is a comparatively new and less reported technique, which can produce high-quality films with more exceptional smoothness and compactness. As compared to solution-processed methods, the EVPVD-grown NiO film exhibits excellent reproducibility while utilizing for the fabrication of PSCs.(Abzieher et al., 2019; Singh, Quli, Wolfe, & Schriempf, 1999) In this current study, optics and electrical effects of PSCs are investigated, where NiO acts as an HTL. Further details are provided in the following sections.

3.1.1 Material Properties and Perovskite Solar Cell Structure

A superstrate configured planar PSC was fabricated experimentally to realize the potential use of NiO film as an HTL. A ~300 nm thick methylammonium lead-iodide ($MAPbI_3$) perovskite absorber with a bandgap (E_g) of ~1.6 eV was placed between hole-transport/electron-blocking layer (HTL) and electron-transport/hole-blocking layer (ETL). The best performance PSC consists of a 50 nm NiO HTL, where 50 nm PCBM and a 20 nm BCP were used as the ETL. Similar combinations of transport materials are used to realize contacts of highly efficient PSCs.(Abzieher et al., 2019) The solar cell was deposited on a thick FTO substrate, where a 100 nm silver (A_g) was used as a back reflector. The planar PSC exhibit a significant reflection loss due to the flat surface, which limits J_{SC} and ECE of the device. In this study, the front contact (FTO/NiO) and perovskite have almost a comparable refractive index, which reduces the optical losses due to front reflections. However, the J_{SC} can be increased by improving light incoupling and light trapping while the reflection losses are minimized.

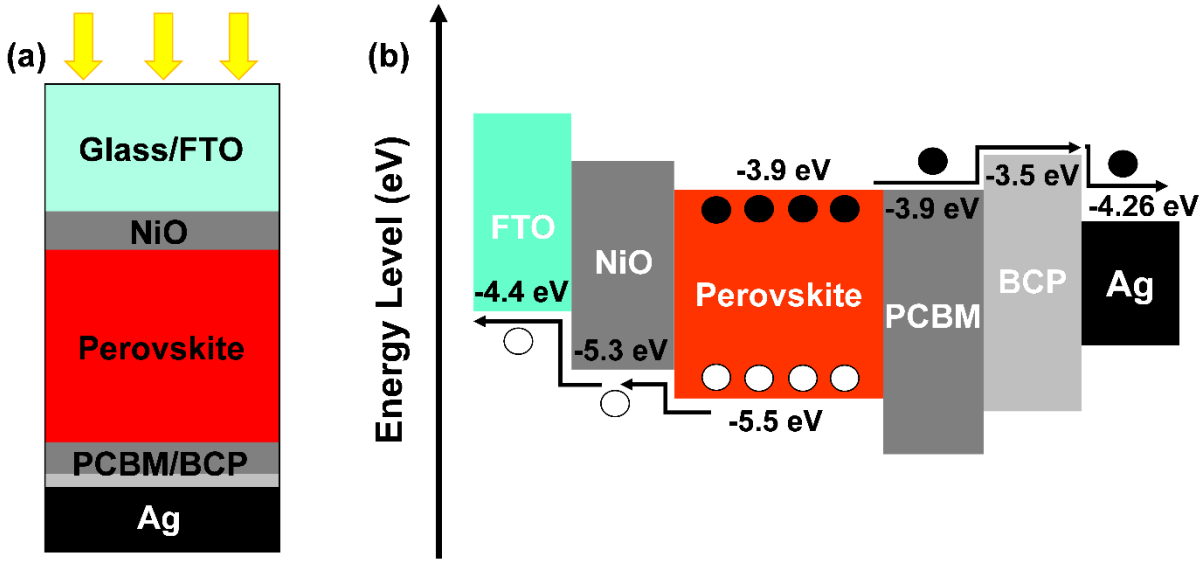

Figure 3.1: (a) The schematic diagram of the inverted planar perovskite solar cell. (b) Corresponding energy level structure of perovskite solar cell.

3.1.2 Results and Discussions

As a first step, NiO films were prepared on glass substrates with thicknesses ranging from 25 nm to 100 nm.

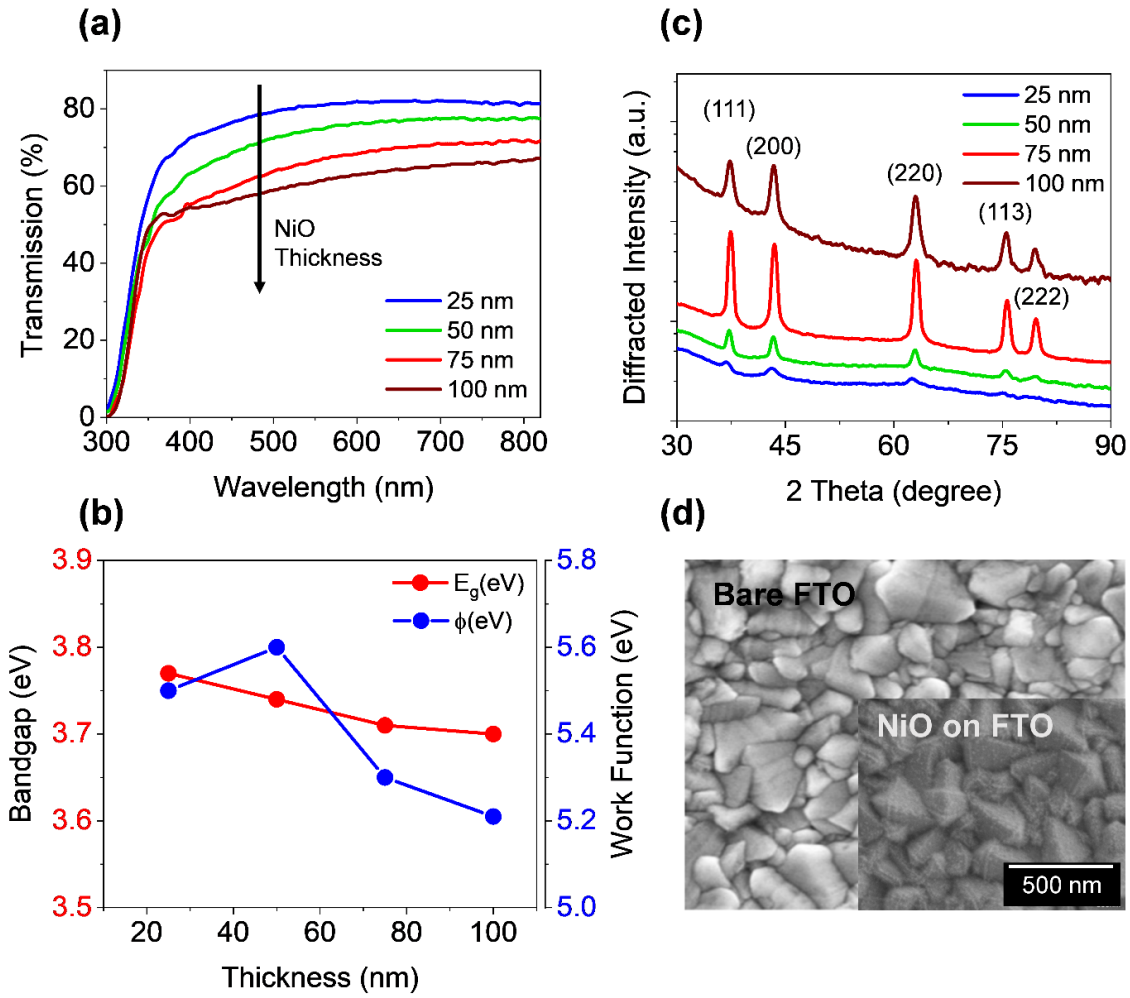

Figure 3.2: Thickness dependent (a) optical transmittance, and (b) energy bandgap and work function of EBPVD grown NiO films deposited on FTO substrates. (c) X-ray diffraction patterns of different thicknesses of NiO films. (d) Top-view SEM micrographs of NiO film on FTO substrates.(Mohammad Ismail Hossain et al., 2020)

The transmission spectra of the NiO films are shown in Figure 3.2(a). 25 nm NiO films exhibit transparency in the spectrum ranging from 300 nm to 800 nm of almost 80%, while a glass substrate without the NiO exhibits a transmission of 90%. With increasing film thickness, the absorption of the NiO film increases, while the transmission

decreases down to 60% for films with a thickness of 100 nm.(Jassim, Zumaila, & Al Waly, 2013) The optical transparency of NiO films for a wavelength range 300-1200 nm is provided in Appendix A (Figure A1).

The optical bandgap of the films was determined by analyzing the absorption of the NiO films. A thickness-dependent bandgap of the NiO film is shown in Figure 3.2(b), where the bandgap varies from 3.75 eV to 3.7 eV with the NiO film thickness from 25 nm to 100 nm, respectively.(Paulose, Mohan, & Parihar, 2017) Besides, the work functions of the deposited films are presented in Fig. 2(b), where the work function varies from 5.2 eV to 5.6 eV for the thickness range 25 nm to 100 nm. An HTL with a high work function is required to realize an increased open-circuit voltage (V_{OC}) of the PSC.(Yan et al., 2016) In this study, the peak of the work function is found for the 50 nm case. XRD measurements provide a good crystallinity of the deposited NiO films with necessary diffracted peaks.(Wei, Qiao, Yang, Zhang, & Yan, 2009) Figure 3.2(c) illustrates the XRD patterns of the NiO films for the angular region from 30° to 90°. Three major peaks are available in the XRD spectra. At 37.2º, a powerful diffraction peak appeared, corresponding to the (111) crystal plane.

Table 3.1: Thickness dependent resistivity of NiO films**.**

Thickness (nm)	Resistivity, (kΩ.cm)
25	4.97
50	4.05
75	2.89
100	3.16

In addition, at 43.2º and 62.8º, diffraction peaks for (200) and (220) crystal planes are also found. Increasing the thickness of the NiO film, corresponding diffraction peak

intensities are also increased, resulting in the improvement of the crystallinity of the materials.(H.-L. Chen, Lu, & Hwang, 2006) Furthermore, peaks between 75º to 90º are corresponding to the crystal planes (113) and (222), respectively, are strengthened by increasing the NiO thickness. The high-resolution SEM image of the NiO film surface is shown in Figure 3.2(d), where the film was prepared on the FTO substrate. At high magnification, the film shows a great uniformity and a very smooth surface. NIO film on the FTO substrate shows a pyramid-shaped structure that is mainly pronounced from the FTO properties. The influence of film thickness on the resistivity can be understood from Table 3.1.

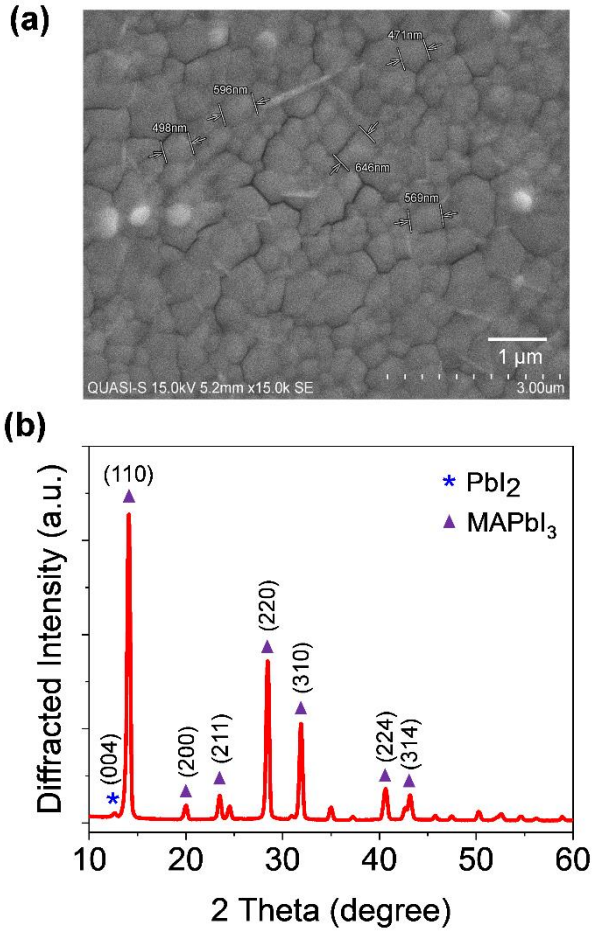

Figure 3.3: (a) SEM topography and (b) XRD patterns of $MAPbI_3$ perovskite films on NiO/FTO substrate.

As shown, the resistivity of the NiO film decreases from 4.97 to 2.89 kΩ.cm, with

increasing the thickness from 25 nm to 75 nm. However, the resistivity increases slightly for the 100 nm thick NiO film. In this study, 50 nm NiO film thickness was used to fabricate the PSCs with reasonable resistance to improve the conductivity of the device. As a second part, planar PSCs were fabricated in superstrate configuration with NiO HTL. A detailed procedure on how to fabricate the planar PSC with NiO HTL is explained in the Materials and Methods subsection. A schematic explanation of the PSC fabrication is shown in Appendix A (Figure A1.1).

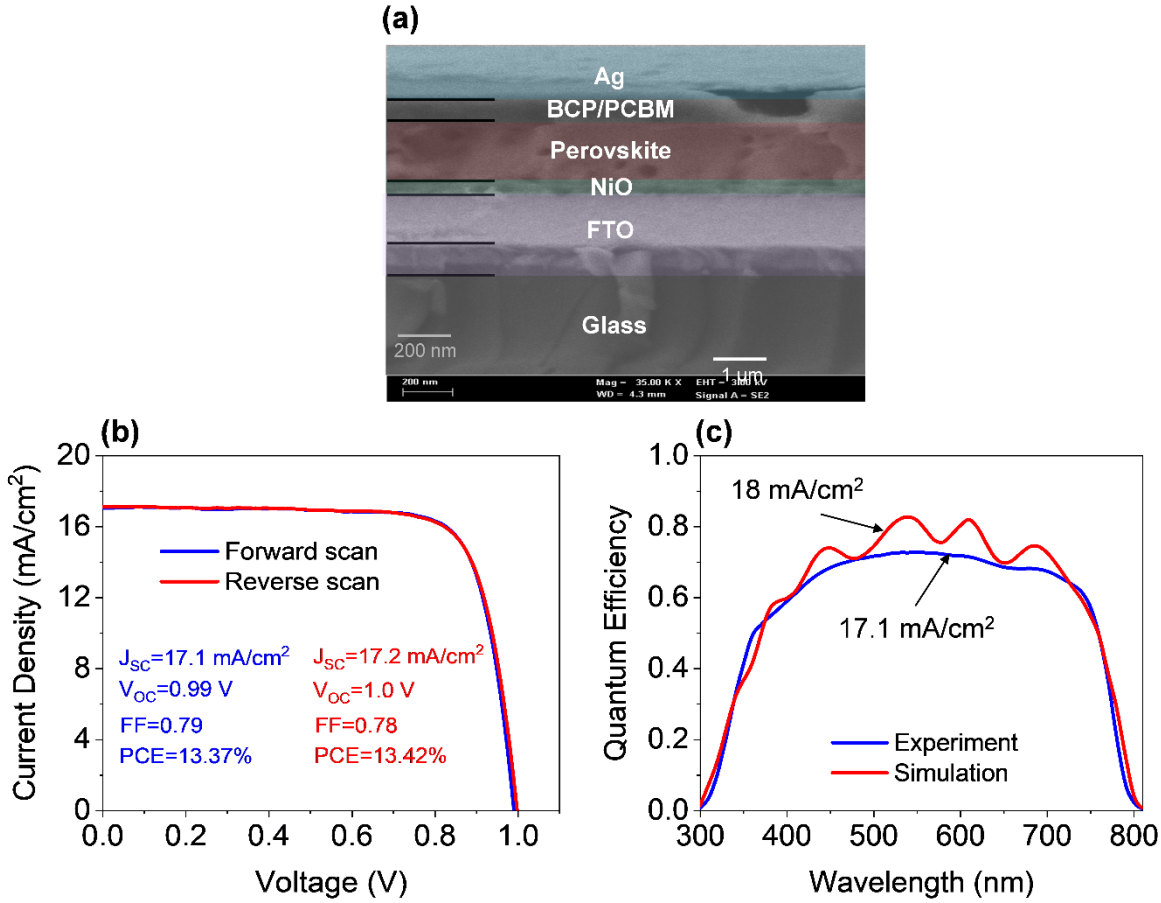

Figure 3.4: (a) Cross-sectional SEM image of the fabricated planar perovskite solar cell. A comparison of (b) current-voltage characteristics, and (c) quantum efficiencies of the fabricated planar perovskite solar cell deposited on FTO substrate of the champion device.(Mohammad Ismail Hossain et al., 2020)

Figure 3.3(a) displays the top-view SEM image of the $MAPbI_3$ perovskite/NiO on the FTO substrate, where an average grain size of perovskite was found over 500 nm.

The XRD patterns of the $MAPbI_3$ perovskite/NiO on the FTO substrate are shown in Figure 3.3(b). The spectra include major seven peaks at 14.08º, 19.9º, 23.3º, 28.42º, 31.85º, 40.28º, and 43.21º, which correspond to the (110), (200), (211), (220), (310), (224), and (314) crystal planes for the $MAPbI_3$ perovskite, respectively. Nevertheless, the peak located at 12.58º corresponds to the (004) plane for the PbI_2. The strongest signal was found from the (110) plane, and the morphology of the FTO substrate influences the formation of the crystalline $MAPbI_3$. Several experimentally realized devices were studied to investigate the role of NiO in PSC performance. A cross-sectional FESEM (Field emission scanning electron microscopy) image of the fabricated PSC is depicted in Figure 3.4(a). (Glass/FTO/NiO/$MAPbI_3$/PCBM/BCP/Ag), where the interface between $MAPbI_3$ perovskite and NiO formed the heterojunction. Measured thicknesses of $MAPbI_3$ and NiO were approximately 300 nm and 50 nm, respectively, where the thickness of PCBM/BCP is accounted to be ~70 nm. Figure 3.4(b) shows the current-voltage (I-V) characteristics of a champion device under an AM 1.5 spectrum along with the photovoltaic parameters. The photovoltaic parameters were extracted for forward and reverse voltage sweeps. Almost no hysteresis was observed during the measurements. ECEs of 13.37% and 13.42% were measured for forward and backward scans. J_{SC}, V_{OC}, and FF of the fabricated device with the reverse scan are 17.1 mA/cm^2, 0.99 V, and 0.79, respectively, whereas, the forward scan exhibits J_{SC} of 17.2 mA/cm^2, V_{OC} of 1.0 V, and FF of 0.78. A summary of the photovoltaic parameters for different NiO thicknesses is provided in Appendix A (Table A1.1). The measured QE under short-circuit conditions is provided in Figure 3.4(c). A maximal QE of 70% is observed in the wavelength range of 450 nm to 650 nm. The solar cell exhibits a J_{SC} of 17.10 mA/cm^2. J_{SC} and QE of the solar cell are limited by several factors. We used FDTD optical simulations to quantify the losses and to discuss optimization strategies. The optical constants of the materials used for the simulations are provided in Figure A1.2. The optical constants were determined by

spectroscopic ellipsometry of films prepared on glass substrates. The simulated QE, along with QE of the experimentally realized solar cell, is provided in Figure 3.3(e). A good agreement is found between experiment and optical simulation. The simulated J_{SC} was calculated to 18.0 mA/cm^2 with a maximum QE of 80% at ~530 nm wavelength. The optical simulations are characterized by the formation of optical fringes, which is caused by fringes that occurred from the FTO substrate. The influence of NiO film on QE and J_{SC} is provided in Appendix A (Figure A1.3). The experimentally realized solar cell is primarily limited by the optical absorption losses of the NiO layer and reflection losses of the solar cell. The refection can be minimized by using an anti-reflection coating; however, an anti-reflection coating minimizes the reflection for a narrow spectral region. An efficient broadband incoupling of light in a solar cell can be achieved by using a surface texture. We have shown that how a moth-eye surface texture could be used to improve the light incoupling of PSCs.(Qarony, Hossain, Dewan, et al., 2018)

3.1.3 Experimental Details

3.1.3.1 Materials

All chemicals with high purity were used as received in the absence of any further purification. Major solvents such as gamma butyrolactone (GBL), dimethyl sulfoxide (DMSO), chlorobenzene, hydrochloric acid (HCL), acetone, bathocuproine (BCP), and zinc (Zn) powder were purchased from Wako Pure Chemical Industries, Ltd., Japan.

3.1.3.2 Substrate Preparation

Before using Fluorine doped tin oxide (FTO, Pilkington, 14 Ω.cm) substrates (2.5 cm × 2.5 cm) for the fabrication, FTO conductive glasses were patterned with Zn powder and 2M HCL solution. Next, substrates were cleaned by ultrasonic treatment in

detergent, deionized water, acetone, and isopropyl alcohol in a sequence for 10 min at each step, and consecutively dried with pure nitrogen (N_2) blower. Substrates were then exposed to Ultraviolet-ozone (UV-O_3) treatment for 15 mins at 115°C before getting ready for the perovskite solar cell fabrication.

3.1.3.3 Precursor Solution Preparation

The perovskite solution was prepared by dissolving the 461 mg of PbI_2 (99%, Sigma-Aldrich) and 159 mg of MAI (>98%, Tokyo Chemical Industry Co., Japan) into the solution of DMSO (78 mg) and GBL (700 mg), which leads to a clear solution of $MAPbI_3$. The solution was stored in a glass container and stirred overnight at 55ºC before spin coating. Next, phenyl-C_{61}-butyric acid methyl ester ($PC_{61}BM$, 99.5%, Lumtec Co., Taiwan) solution was prepared by using chlorobenzene (20 mg/mL) as a solvent. The whole process of solution preparations was carried out inside the glove box.

3.1.3.4 Device Fabrication

NiO as a hole transporting material (HTM) was deposited on a clean and patterned FTO from a 99.99% pure NiO_x target pallet (1 cm^2, Kujondo Chemical Laboratories Co., Japan) by EBPVD technique. The pressure of the deposition chamber was approx. 4.62 × 10^{-6} Torr. Substrates were dispossessed from any purposeful heating (room temperature) during the deposition process, and the deposition rate was adjusted to 0.10 nm/s to reach an HTL thickness of ~50 nm. Then, HTM coated FTO substrates were immediately taken into the glove box for further fabrication. Next, the perovskite layer was deposited onto the NiO substrates from a 50 µL of $MAPbI_3$ precursor solution by spin coating. The spin coater was set into two different rotations and a time interval with a 2-sec slope. In a first step, spin coater rotated for 10 sec at 1000 rpm. In a second step, the spin coater was set for 30 sec at 5000 rpm immediately after 2 sec slope time in between. After 14 sec of spin coating, 500 µL of anhydrous toluene was

dripped onto spin-coated substrates and annealed. The annealing process was distributed into two sections. First, films were thermally treated for 10 min at 50°C onto a hot plate; later, films were moved to another hot plate for annealing at 100°C for 10 mins. As a next step, 50 µL of PCBM solution was spread over the perovskite deposited substrates and spin-coated for 30 sec at 1000 rpm. And, PCBM deposited substrates were thermally treated for 10 mins at 80°C. And, 150 µL of BCP solution was dropped onto the substrate and rotated for 30 sec at 6000 rpm. After completing the spin coating, deposited substrates were annealed at 80°C for 10 mins. Finally, a 120 nm thick silver (Ag) metal contact was deposited on the top of the BCP deposited substrates by a resistive thermal evaporator under a vacuum chamber with a pressure of 4.65×10^{-6} Torr. A customized patterned mask was used to attain the expected device structure of final PSCs. A detailed procedure is schematically shown in Figure A1.1.

3.1.3.5 Measurement and Characterization

A UV/VIS/NIR spectrometer (PerkinElmer UV/VIS/NIR Spectrometer Lambda 1050) was used to determine the optical transmittance, which allows measuring absorption, transmittance, and reflection of deposited films for the wavelength range from 200 nm to 4000 nm. The complex refractive indices of deposited films were analyzed by the spectroscopic ellipsometry (J.A. Woollam Co. Inc. Spectroscopic Ellipsometer) measurements where wavelength ranged from 371nm to 1000 nm at three incident angles of 60°, 65°, and 70°. The crystal structures of deposited films were examined by using X-ray diffraction (XRD, Ragaku SmartLab) measurements with CuK_{α} radiation (λ=0.154 nm) at room temperature. The XRD spectra were measured on all samples in the two-theta (2θ) angular region between 20° to 90°. The work function was measured by AC-3 with 2.0 nW light intensity and 0.05 interval (RIKEN KEIKI, JAPAN). The resistivity of the deposited NiOx films was measured by the Hall Effect

measurement tool 'ECOPIA 3000. The magnetic field was 0.57 Tesla, and the probe current was set to 4 mA for all the samples. A Van-Der-Pauw structure was made for a four-point probe resistivity measurement, where a small sample (1 cm × 1 cm) was prepared for the measurement. Field emission scanning electron microscopy (FESEM, JEOL JSM-6335F) was used to observe the morphological characteristics of deposited samples, which allows realizing the image at high resolution. The surface roughness of the deposited samples was determined by using atomic force microscopy (AFM, NT-MDT). All these measurements were performed under ambient environmental conditions. The photovoltaic parameters and performance of the fabricated device were investigated by a solar simulator (Newport solar simulator +EQE) under simulated AM 1.5G sunlight, which allows realizing current density-voltage (JV) characteristic. The computer-controlled solar illumination was set to 100 mA/cm^2 in air. Both forward and reverse scans were set to start from -0.2 V to 1.2 V and vice versa. Next, the quantum efficiency spectra were measured from 300 nm to 850 nm by using the EQE system. The photo-illuminated active area of the fabricated device was 0.16 cm^2 (0.4 cm × 0.4 cm) without further measures. The actual thicknesses of the deposited films were determined by the Dektak Veeco surface profiler.

3.2 Spray Pyrolysis Deposition of TiO_2 Films

In perovskite solar cells (PSCs), hole-blocking/electron-transport layer (ETL) plays a significant role in transporting the photogenerated electrons and blocking holes, avoiding the electrical shunt between the transparent electrode/perovskite and transparent electrode/hole transport material (HTM) interfaces.(Juarez-Perez et al., 2014; Moehl et al., 2014) The qualities of the ETL, such as energy level alignment, charge mobility, morphology, and its related interface properties are substantially valuable for the determination of PSCs with better photovoltaic performance.(Juarez-Perez et al., 2014; N.-G. Park, 2015b; Werner et al., 2018) In addition, the preparation of a hole-blocking layer has to be simple so that it reduces production costs and enables future commercialization of PSCs. So far, TiO_2 is considerably a popular material as an ETL due to its potential simple deposition, favorable energy level, tunable electronic properties, and surface uniformity.(Möllmann et al., 2019; Paek et al., 2017; Yongzhen Wu et al., 2014) Resulting in TiO_2 reduces hysteresis and improves charge transfer with the PSC. In this study, the spray pyrolysis technique was used for the deposition of dense TiO_2 layer, which is one of the popular methods used in industries to deposit large areas of ceramic films.(Piegari & Flory, 2013) Next, high-performance planar PSCs were fabricated by employing a spray-pyrolyzed TiO_2 compact ETL. The influence of TiO_2 layer thickness on the photovoltaic performance of the resulting devices was investigated by varying the precursor solution concentration from 0.15 M to 0.40 M. 3D optical simulations were utilized to study the mechanism of device operation from the optical point of view. Optical simulations were precisely used to model, design, and optimize the PSCs. A detailed discussion is provided in the following sections.

3.2.1 Device Design and Material Properties

In this study, planar PSCs were investigated experimentally for realizing the potential

of using a compact TiO_2 layer as an ETM, which was further validated by 3D FDTD optical simulations.(Mohammad I. Hossain, Qarony, et al., 2019; Qarony, Hossain, Salleo, Knipp, & Tsang, 2019) Spray-pyrolysis deposition was used to prepare the pin-hole free TiO_2 ETM. Herein, the most commonly used methylammonium lead-iodide ($MAPbI_3$) perovskite material was used as a photo-absorber, which has a bandgap of 1.55 eV. In the current PSC design, TiO_2 ETL is deposited on a thick FTO substrate where the thickness of the ETL was tuned by changing the TiO_2 precursor solution concentration. However, the champion cell has a TiO_2 thickness of 70 nm. Spiro-OMeTAD was used as a potential HTM for the fabrication of PSCs, which has a thickness of 250 nm. A 300 nm perovskite absorber is placed between electron and hole transport layers, where the only perovskite contributes to the quantum efficiency and short-circuit current density. A 100 nm gold metal contact was used as a back reflector to complete the device. Similar combinations of electron and hole transport layers have been used to realize contacts of highly efficient planar PSCs. A schematic of the investigated planar PSC structure is depicted in Figure 3.5(a), and the corresponding energy band diagram is shown in Figure 3.5(b).

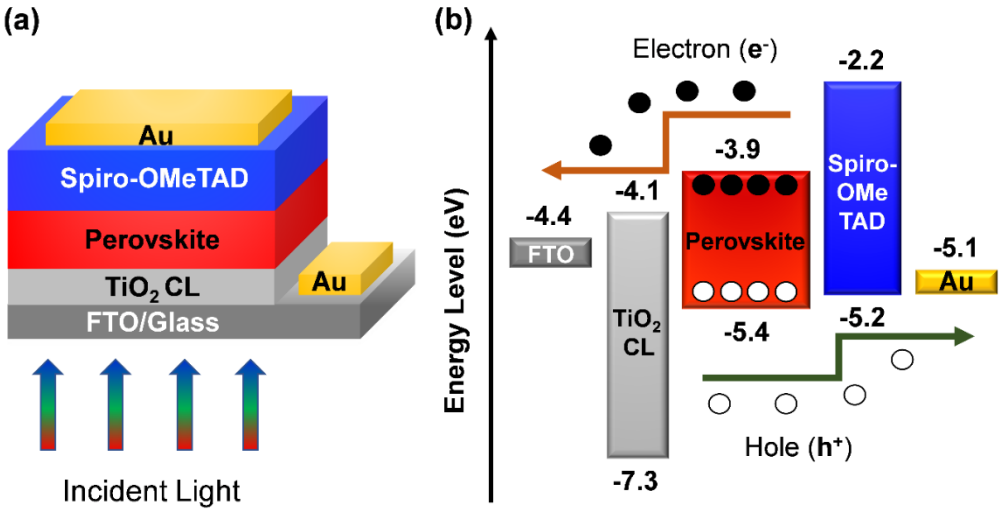

Figure 3.5: (a) The schematic diagram and (b) Corresponding energy level structure of planar perovskite solar cell.

3.2.2 Results and Discussions

Smooth morphology and higher crystallinity are highly required to produce highly efficient planar PSCs. Hence, the investigation started from the deposition of TiO_2 film on FTO substrates by using the spray-pyrolysis method. In the spray-pyrolysis method, the titanium precursors were brought to the FTO substrates, where the TiO_2 precursor solution concentration was tuned from 0.15 M to 0.40 M to obtain optimum performance. In this study, the optimum thickness of uniformly distributed TiO_2 ETL is ~70 nm, which was fabricated from the 0.35 M TiO_2 precursor solution concentration. Figure 3.6(a) shows the surface morphology of the TiO_2 compact layer on the FTO substrate. It is noted that the surface of the FTO substrate is rough, and grain size varies from tens to hundreds of nanometers. The resultant TiO_2 film shows a smooth surface, which predominantly imitates the basic FTO morphology, except some small crinkles. Such ETL compact layers are very suitable for the fabrication of continuous perovskite film. Figure 3.6(b) illustrates the SEM top-view of perovskite film deposited on the TiO_2/FTO through spin-coating. The SEM image shows a standard surface morphology with densely packed perovskite crystals where grain size varies from approximately 200 nm to 500 nm. It can be clearly observed that gaps between crystals are low, which ensures a high-quality perovskite film, where a more massive gap/crack minimizes the shunt-resistance of solar cells, which leads a leakage. The leakage will reduce both fill factor and short-circuit current density of the device, resulting in, the photovoltaic performance will be lowered. The effect of TiO_2 ETL on the crystallization of perovskites was further studied by the XRD spectra, which are shown in Figure 3.6(c). XRD patterns of perovskite film on the TiO_2/FTO exhibit a set of diffraction peaks of perovskite tetragonal phase located between 10º and 50º two-theta. At 14.2º, an extreme diffraction peak is appeared, corresponding to the characteristic peak of $MAPbI_3$ perovskite of lattice plane (110), which confirms a better crystallinity. In addition, some significant peaks are also discovered at 26.8º, 28.7º,

and 38º from XRD spectra that correspond to (220), (310), and (440) crystal planes. The UV-vis absorption spectra of perovskite films on TiO_2 deposited FTO were also measured to investigate the effect of crystallinity on the absorption, which is presented in Figure 3.6(d). High absorptions can be observed throughout the spectral range (300 nm to 900 nm), where the absorbance goes zero after reaching 800 nm wavelength, and it proves the perfect perovskite material properties. Absorptions from 300 nm to 350 nm wavelengths correspond to the TiO_2 ETL.

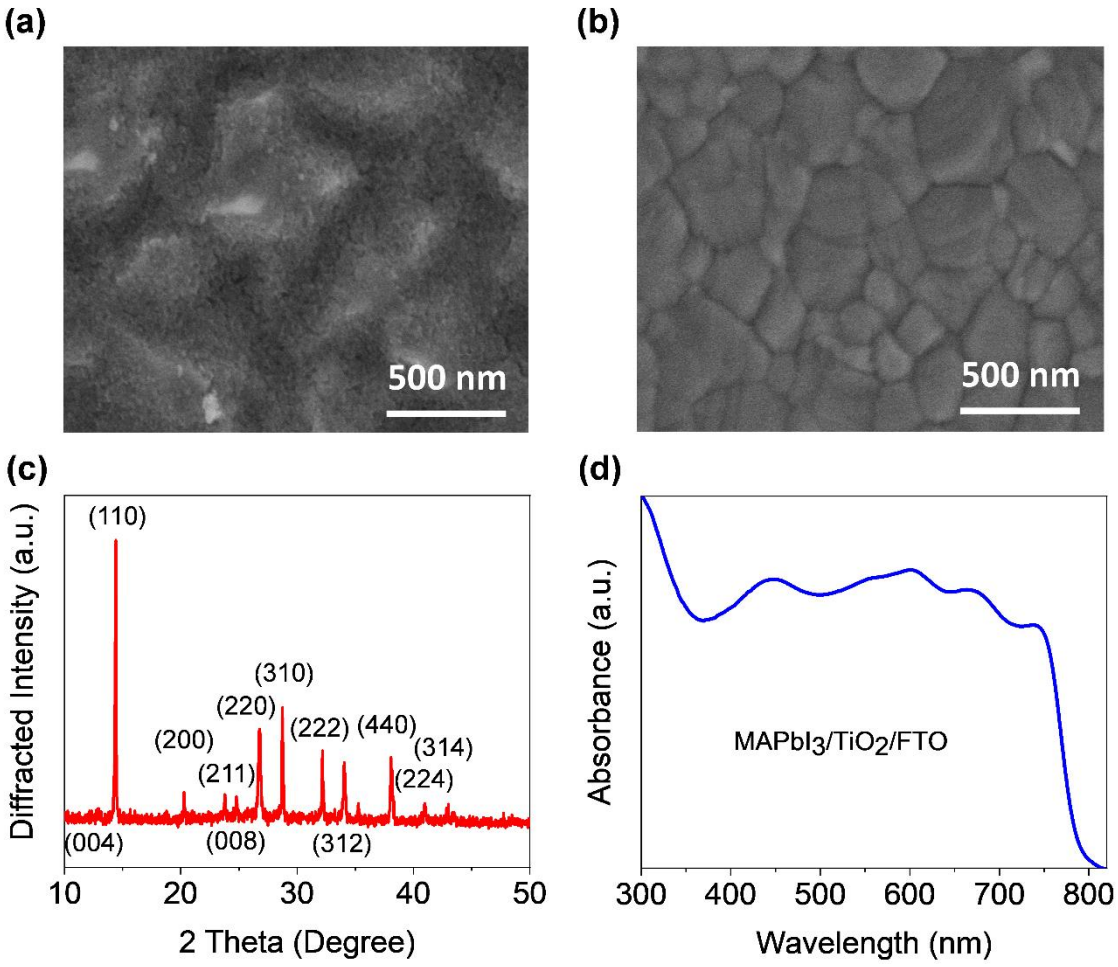

Figure 3.6: Top-view SEM micrographs of (a) spray-pyrolysis deposited TiO_2 and (b) perovskite film on the TiO_2 compact layer. (c) The X-ray diffraction patterns and (d) the UV-vis absorption spectrum of the perovskite film fabricated on a compact TiO_2. The TiO_2 precursor solution has a concentration of 0.35 M and a thickness of 70 nm.

Moreover, high and smooth absorbance confirm the crack-free morphology and excellent crystallinity, which enhances the J_{SC} and device performance. To study the influence of TiO_2 ETL on the photovoltaic performance, a group of PSCs was

fabricated with the structure FTO/TiO_2 CL/Perovskite/Spiro-OMeTAD/Au under identical conditions, where the concentration of TiO_2 precursor solution was varied from 0.15 M to 0.40 M. A cross-sectional SEM image of the best performing planar PSC is shown in Figure 3.7(a), which confirms a nice crystallinity within the perovskite layer; however, a number of cracks can be seen between perovskite and contact interfaces that will be further investigated through optics. The current-density versus voltage (J-V) characteristics at a scan speed of 0.05 V/s with reverse scan (RS; from 1.2V to -0.1 V) of the fabricated PSCs against different TiO_2 precursor solution concentrations are presented in Figure 3.7(b). The J-V curves with the forward scan (FS; from -0.1 V to 1.2 V) with the same scan rate are given in Appendix A (Figure A2.1).

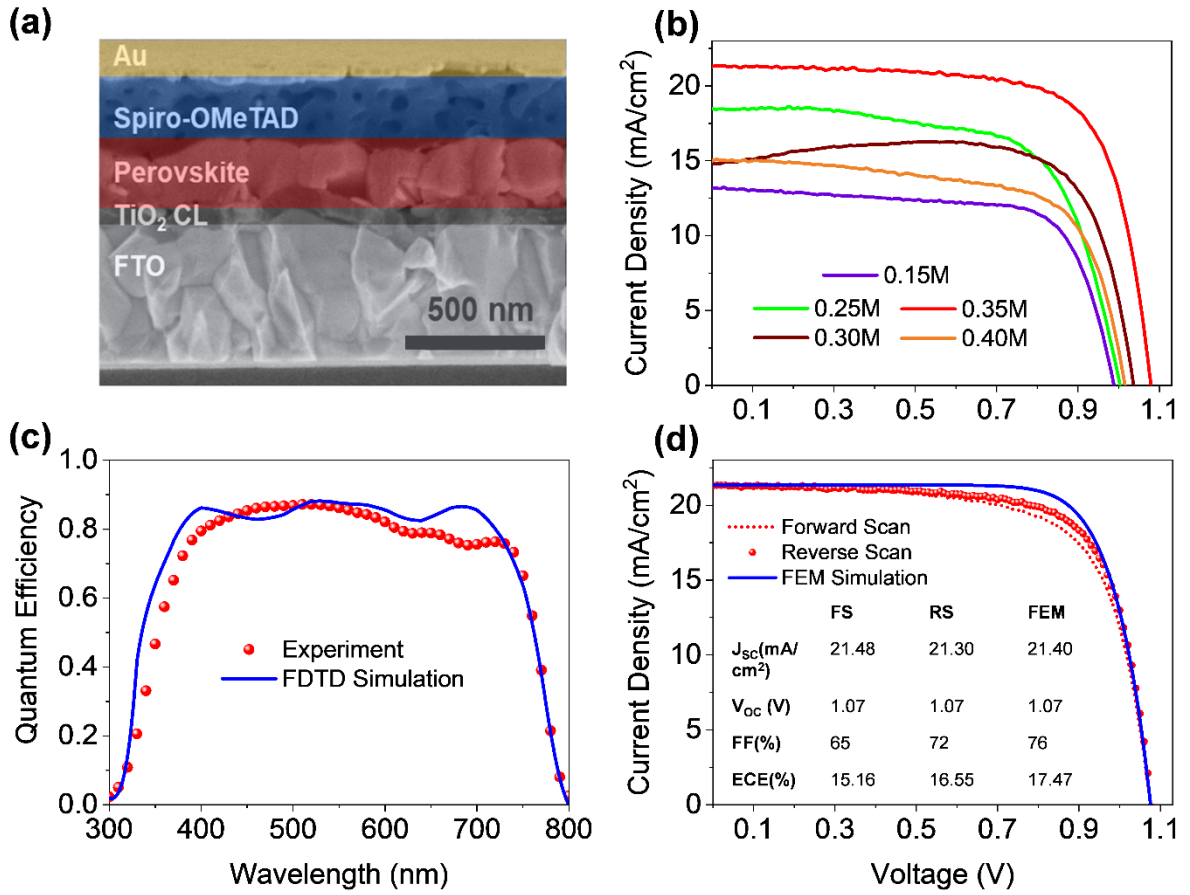

Figure 3.7: (a) The cross-sectional FESEM image of the fabricated champion PSC. (b) Current-voltage (J-V) curves of the reverse scan (from 1.2 V to -0.1 V) for the fabricated planar PSCs with different TiO_2 precursor solution concentration (from 0.15 m to 0.40 M). (c) A comparison of quantum efficiencies between experiment and 3D FDTD optical simulation. (b) Forward scan (from -0.1 V to 1.2 V) and reverse scan (1.2 V to 0.1 V) J-V curves of the fabricated best-performing PSC along with the J-V curve realized from the 3D FEM electrical simulation.

A wide variation of J-V curves can be observed by changing the TiO_2 precursor solution concentration. The photovoltaic performance of fabricated devices with different TiO_2 precursor solution concentrations was compared by using parameters extracted from J-V curves and QEs, which are illustrated in Figure A2.2. With varying the TiO_2 precursor solution concentration, J_{SC}, V_{OC}, and FF are varied from 13.3 mA/cm^2 to 21.3 mA/cm^2, 0.99 V to 1.08 V, and 65.8% to 72%, respectively with the RS. On the other hand, J_{SC}, V_{OC}, and FF are changed from 15.07 mA/cm^2 to 21.4 mA/cm^2, 0.99 V to 1.075 V, and 50.4% to 69%, respectively with the FS. In all cases, J_{SC} and V_{OC} are maximized only when the concentration of the TiO_2 precursor solution is 0.35 M, FF is maximized for 0.30 M (RS) case. However, the hysteresis effect is quite high in the case of 0.30 M, where 0.35 M case shows a very low hysteresis problem. Still, both incremental and decremental trends are noticeable in ECEs against different TiO_2 precursor solution concentrations, where the highest ECE (16.56%) was achieved for the 0.35 M case. J-V characteristic and QE of the best-performing PSC (0.35 M) are shown in Figure 3.7(b) and Figure 3.7(c), respectively, along with rigorous optical and electrical simulation results. The complex refractive indices of used materials were used as input parameters for optical simulations, which are shown in Appendix A (Figure A2.3). A detail description on the simulation method is provided in Chapter 2 (Section 2.3). Experimental results show a very nice agreement with the results from the simulations. However, experimental performance parameter values are slightly lower than the simulation values. In addition, experimental QE is marginally lower than the simulated QE, which leads to a reduction of the J_{SC}, such drop was occurred due to the slight degradation of the sample while transferring from J-V measurement to QE measurement, and this is due to the limitation of our laboratory facility. It should be noted that the thickness of TiO_2 ETL depends on its precursor solution concentration. The thickness-dependent QE and absorption in the ETL are shown in Appendix A (Figure A2.4).

To examine the reproducibility, 13 fabricated devices were investigated in each group (total 6 groups), where the TiO_2 precursor solution concentration was varied from 0.15 M to 0.40 M. The photovoltaic parameters were obtained from each J-V curve and displayed in Figure 3.8. Figure 3.8(a), Figure 3.8(b), Figure 3.8(c), and Figure 3.8(d) reveal the average values of V_{OC}, J_{SC}, FF, and ECE of resultant PSCs as a function of TiO_2 precursor solution concentration, respectively.

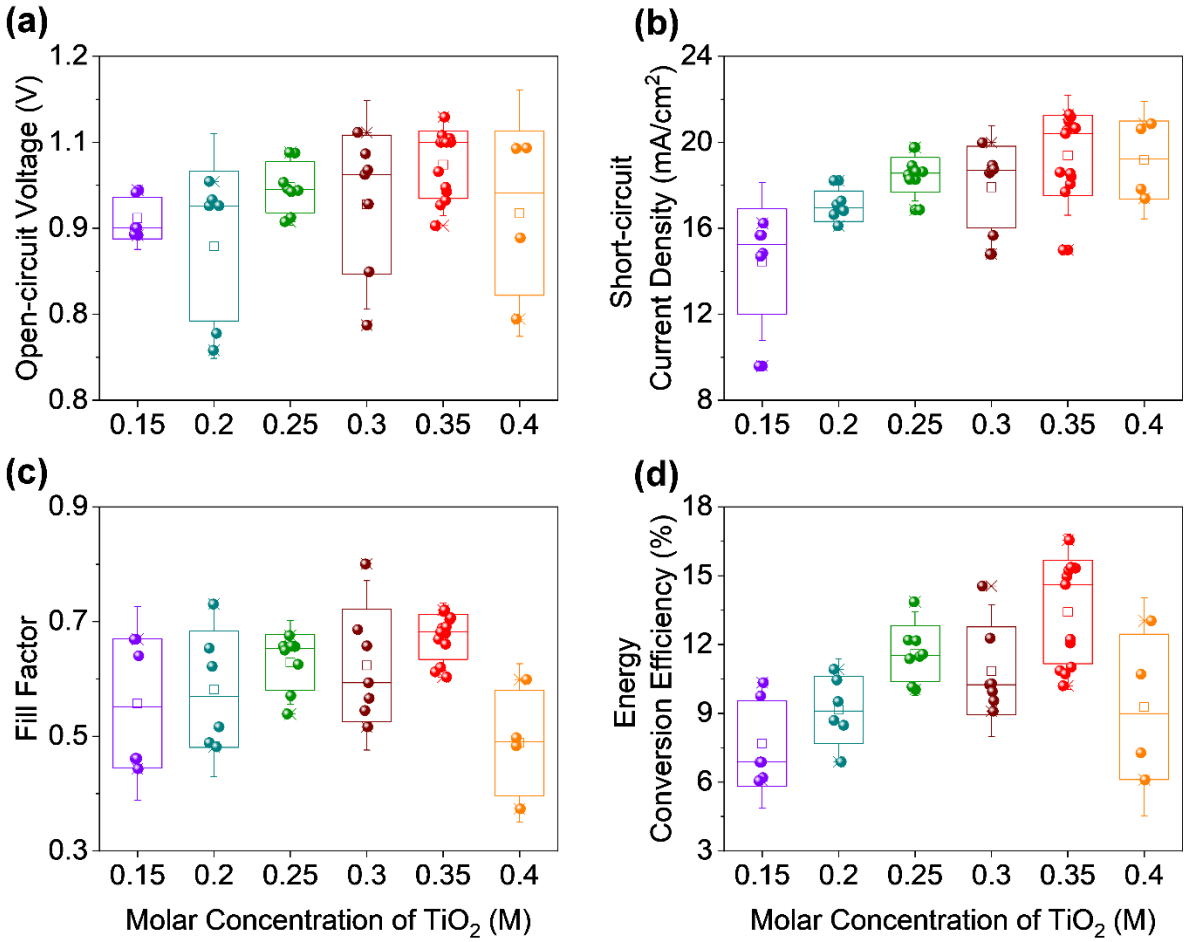

Figure 3.8: Average values of (a) V_{OC}, (b) J_{SC}, (c) FF, and (d) ECE obtained in terms of varying the molar concentration of TiO_2 solution based resultant 13 devices with a scan from 1.2 V to -0.1 V and a scan rate of 0.05 V/s.

Error bars indicate plus or minus the standard deviation from the mean value. The best-optimized performance with excellent reproducibility was obtained for the 0.35

TiO_2 precursor solution concentration. As expected, 0.35 M case exposed a superior performance than other cases (0.15 M, 0.20 M, 0.25 M, 0.30 M, and 0.40 M). The 0.35 M TiO_2 precursor solution concentration ETL-based devices yield better reproducibility and average V_{OC}, J_{SC}, FF, ECE of 1.02±0.06 V, 19.37±1.93 mA/cm^2, 67±5%, 13.5±3.05%, respectively. The statistics of PSC performances of 13 devices are summarized in Table 3.2, where the results can be attributed to the enhanced morphology and crystallinity of perovskite films using optimized TiO_2 precursor solution concentration. The best-performance PSC has an optimized TiO_2 ETL thickness of approx. 70 nm, which shows a maximum ECE of 16.55% with a J_{SC} of 21.3 mA/cm$_2$, a V_{OC} of 1.08 V, and an FF of 72%. Moreover, the integrated currents from QE also agree within 10% of the measured J_{SC} from the J-V curve.

Table 3.2: TiO_2 precursor solution concentration-dependent performance statistics of fabricated PSCs with a structure of FTO/TiO_2/perovskite/Spiro-OMeTAD/Au. Statistical analysis (average ± standard deviation) based on 13 devices for each round of device fabrication as a function of TiO_2 concentration.

TiO_2 Precursor Solution Concentration	Open-circuit Voltage (V)	Short-circuit Current Density (mA/cm^2)	Fill-Factor (%)	Power Conversion Efficiency (%)
0.15 M	0.96±0.03	14.35±5	56±11	7.3±3
0.20 M	0.93±0.07	16.94±1.2	58±12	9.1±1.7
0.25 M	1.0±0.04	18.45±1.3	63±5	9.1±1.7
0.30 M	0.98±0.07	17.9±2.2	68±12	11.6±2.3
0.35 M	1.02±0.06	19.37±1.93	67±5	13.5±3.05
0.40 M	0.97±0.09	19.1±1.7	48±12	9.3±3.7

To understand further the device optimization and performance, it is necessary to investigate the optics along with the experiment, which can demonstrate layer by layer

loss analysis through electric field distribution and ensure the total charge collection efficiency 100%. In this study, 3D FDTD optical simulations were used to model and optimize PSCs. The optical simulation allows determining electric field distributions, which further utilized to calculate power density, reflectance, transmittance, parasitic absorption losses, absorption in the perovskite layer that leads to obtaining QE and J_{SC}. Herein, the perovskite layer thickness was kept constant to 300 nm, while the thickness of TiO_2 ETL was varied from 50 nm to 130 nm. An excellent agreement was found between simulated results and experiment results, where the J_{SC} is varied from 19.75 mA/cm^2 to 21.35 mA/cm^2, J_{SC} was maximized when TiO_2 ETL thickness is 70 nm which can be seen in Figure 3.7(b) and Figure A2.4. Simulated power densities of the optimized PSC under monochromatic illumination of 300 nm, 400 nm, 500 nm, 600 nm, 700 nm, and 800 nm are revealed in Figure 3.9(b-e) along with a cross-section of the device (Figure 3.9(a)). For shorter wavelengths (<400 nm), most of the incident photons are absorbed by the TiO_2 ETL, and a fraction of photons are absorbed by the perovskite absorber, where at 400 nm, photons are absorbed by the vicinity of TiO_2/Perovskite and start propagates to the perovskite layer. As wavelength increases, the absorption in the perovskite absorber layer gets higher, as observed in Figure 3.9(d-f). At 700 nm, a significant portion of the incident light reaches the back contact and gets reflected and forms a standing wave pattern, a minor portion of lights are absorbed by the TiO_2 ETL and the Spiro-OMeTAD/Au interface. This is due to constructive and destructive interfaces, as shown in Figure 3.9(f). Furthermore, the absorptions get zero while wavelengths go beyond 800 nm, as illustrated in Figure 3.9(g), where a particular portion of incident photons is only absorbed by TiO_2 and Au layers. These optical phenomena are also supported by the QE plots presented in Figure 3.9(c). It can be realized that the most considerable portion of incident lights either gets reflected or considers as the parasitic optical losses. Hence, interface engineering and light incoupling strategies must be introduced so that such losses can

be minimized, and QE and J_{SC} can be maximized, which further supports to boost ECE of PSCs.

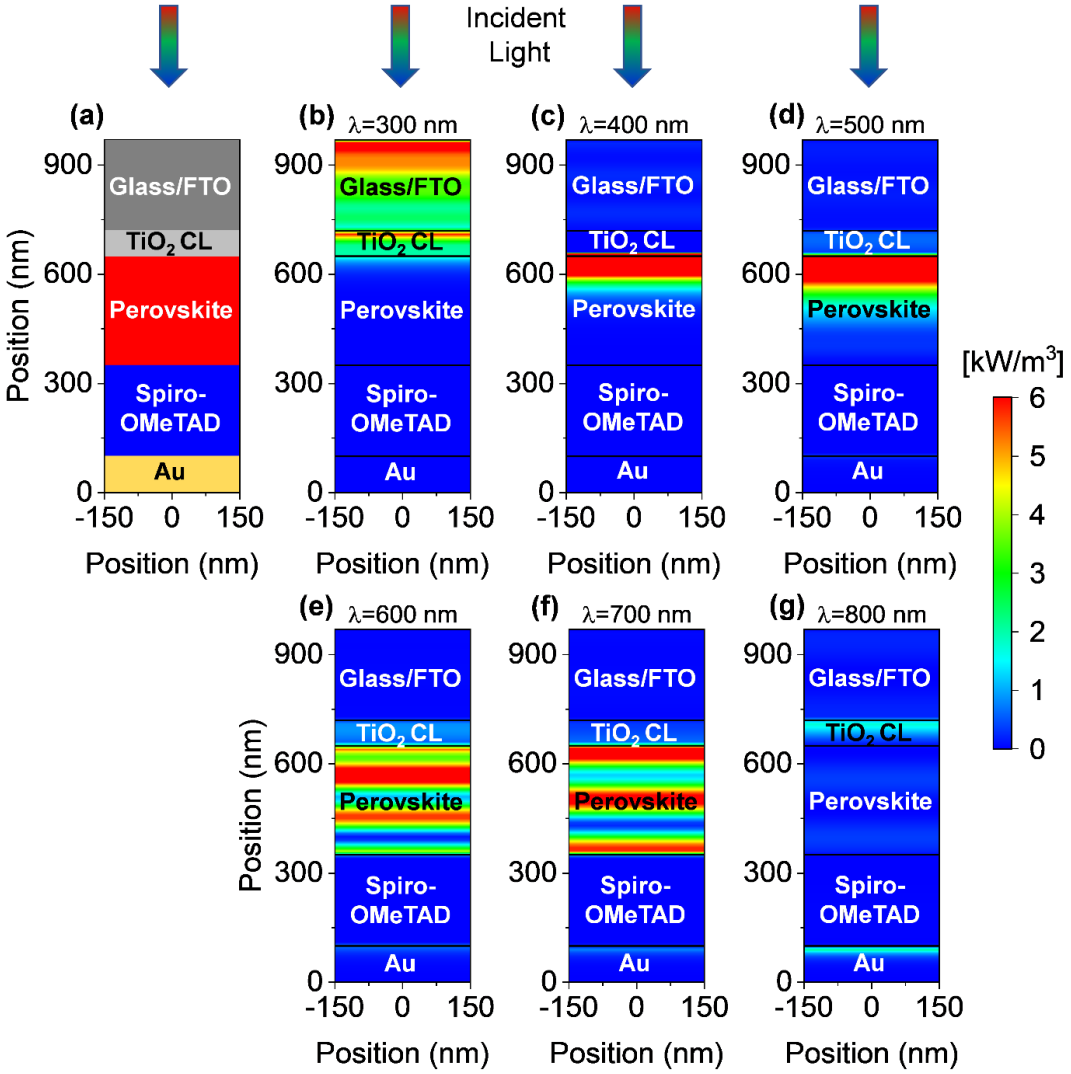

Figure 3.9: (a) The schematic cross-section of a planar PSC with optimized TiO_2 ETL. Power density map of the pyramid textured perovskite solar cell for monochromatic illumination of (b) 300 nm, (c) 400 nm, (d) 500 nm, (e) 600 nm, (f) 700 nm, and (e) 750 nm. The TiO_2 ETL has a thickness of 70 nm.

3.2.3 Experimental Section

3.2.3.1 Materials and Characterization

Lead iodide (PbI_2) and methylammonium iodide (CH_3NH_3I) was purchased from Tokyo

Chemical Industry (Tokyo, Japan). In addition, titanium diisopropoxide bis (acetylacetonate; Aldrich, 75 wt%) in isopropanol was bought from Wako chemical. *N,N*-dimethylformamide (DMF, purity 99.5%) and Dimethyl sulfoxide (DMSO, purity 99.5%) were also purchased from Wako Chemical (Tokyo, Japan). The field emission scanning electron microscopy (FE-SEM; S-4800, Hitachi High-Tech, Tokyo, Japan) was used to analyze the resulting surface morphologies. The ultraviolet-visible near-infrared spectrophotometer (UV-Vis-NIR; V-670, Jasco Corporation, Tokyo, Japan) absorption spectra from the samples were measured using a spectrophotometer. The X-ray diffraction (XRD) patterns of perovskite films were measured using an X-ray diffractometer (D8 Discover, Bruker AXS Co. Ltd, Tokyo, Japan) with an X-ray tube (Cu Kα radiation, λ = 1.5406 Å). The current density *versus* voltage (*J-V*) characteristics at a scan speed of 0.05 V/s with forward-scan (FS; from -0.1V to 1.2V) and reverse-scan (RS; from 1.2V to -0.1V) of the resultant devices were analyzed under simulated (100 mW/cm^2, AM1.5, 1 sun intensity) by a solar simulator using a Keithley 2401 digital source meter. The incident photon-to-electron conversion efficiency (IPCE) of the resultant devices was tested using a monochromatic xenon arc light system (Bunkoukeiki, SMI-250JA). All the devices were characterized in air, humidity ranging from 40% to 50%, and temperature 20°C. The active area of the device was 0.09 cm^2.

3.2.3.2 Device Fabrication

The transparent conducting fluorine-doped tin oxide FTO/patterned glass substrates with sheet resistance 10 Ωsq^{-1} were cleaned with soap solution, distilled water, acetone, ethyl alcohol, and again distilled water then cleaned by UV-ozone treatment for 15 min. Then, a compact TiO_2 layer was deposited on the FTO-glass via spray pyrolysis deposition at 450 °C from a precursor solution of from 0.15 to 0.0.40 M titanium diisopropoxide bis(acetylacetonate) in isopropanol according to the procedure

described by Wakamiya et al.(Wakamiya et al., 2014) As deposited substrates were left at 450 °C for 30 min in a muffle furnace and let to cool down to room temperature. The perovskite precursor solution (1M PbI_2 and 1M CH_3NH_3I in DMF and DMSO mixed solvent) was coated on the resulting substrates. A mix solution of 1M PbI_2 and 1M CH_3NH_3I was dissolved in a mixed solvent of DMF and DMSO (4V DMF: 1V DMSO), followed by at 60 °C for 1h. The perovskite film was prepared by spin-coating the precursor solution at 6000 rpm for 60 s with dripping 500 µl of chlorobenzene (CB) just 8 s after the spin-coating started. The precursor coated substrates were then allowed to anneal at 100 °C on a hot plate for 1 h to crystallize perovskite in a glove box under an inert environment. We tuned the thickness of compact TiO_2 by changing the concentration (0.15, 0.20, 0.25, 0.30, 0.35 M, and 0.40 M) of TiO_2 solution. The optimized thickness of spray pyrolysis TiO_2 was measured ~70 nm. The HTL was spin-coating at 3000 rpm for 30 s from a solution of 2,2',7,7'-tetrakis(N,N-di-p-methoxyphenylamine)-9,9'spirobifluorene (spiro-OMeTAD) in CB (0.058 M) with 4-tert-butylpyridine (0.19 M), lithium bis(trifluoromethylsulfonyl)imide (0.031 M) and tris[2-(1H-pyrazol-1-y1)-4-tert-butylpyridine]cobalt(III) tris[bis(trifluoromethysulfonyl)imide] (5.6×10^{-3} M).(Dualeh et al., 2014; Wakamiya et al., 2014)The resulting thin-films were annealed at 70 °C for 20 min on a hot plate. After that, 60-nm-thick gold (Au) electrodes were deposited on HTL layer at 6.5×10^{-3} Pa.

3.3 Atomic Layer Deposition of ZnO Films

ALD is a unique deposition technique for the precision-controlled deposition of high-quality metal oxide films for optoelectronic device applications.(Seo, Jeong, Park, Shin, & Park, 2019; Zardetto et al., 2017) ALD is a specific pulse-mode CVD method which allows for self-limiting film growth. Recently, ALD films have gained considerable interest in the solar cell community because of its large-area uniformity, high film conformity, sub-monolayer atomic precision thickness control, pinhole or defect-free films over large substrate areas, and most importantly it allows low-temperature depositions.(Keun Kim, Seong Hwang, Ko Park, & Jin Yun, 2005; Lim & Lee, 2007; Seo et al., 2019; Zardetto et al., 2017) In this study, Aluminum-doped and undoped zinc oxide (ZnO) films were investigated as potential charge transporting/blocking layers for planar perovskite solar cells (PSCs), where the films were prepared by atomic layer deposition (ALD) at low (<200°C) substrate temperatures. Herein, ZnO refers to ALD films without nominal aluminum doping, while AZO refers to intentionally aluminum-doped ZnO films. The deposited films were crystalline with a single-phase wurtzite structure and exhibit excellent uniformity and low surface roughness, which was confirmed by XRD and SEM measurements. Necessary optical and electrical characterizations were performed on the deposited films, which allow for realizing high-quality films with low resistivity and high optical transparency at the standard growth rate. Spectroscopic ellipsometry measurements were carried out to extract the complex refractive index of the deposited films, which was used to study the optics of PSCs. Guidelines are provided on how to realize PSCs exhibiting high short-circuit current densities (J_{SC}s).

3.3.1 Materials and Device Geometry

The crystal structure of perovskites is depicted in Figure 3.10(b). The hybrid organic-

inorganic metal halide-based perovskite materials can be defined by the chemical formula ABX_3 where A and B are being cations, and X is an anion.(Green et al., 2014) In this study, methylammonium lead-iodide ($MAPbI_3$) perovskite material (bandgap of ~1.6 eV). In a typical PSC structure, the perovskite absorber is sandwiched between an electron transport layer (ETL) and the hole transport layer (HTL), as depicted in Figure 3.10(a). Herein, metal oxides are used as potential HTL and ETL. In the current study, we used high-quality AZO and ZnO as potential front and rear contacts, which were prepared by ALD at low growth temperatures of less than 200°C.

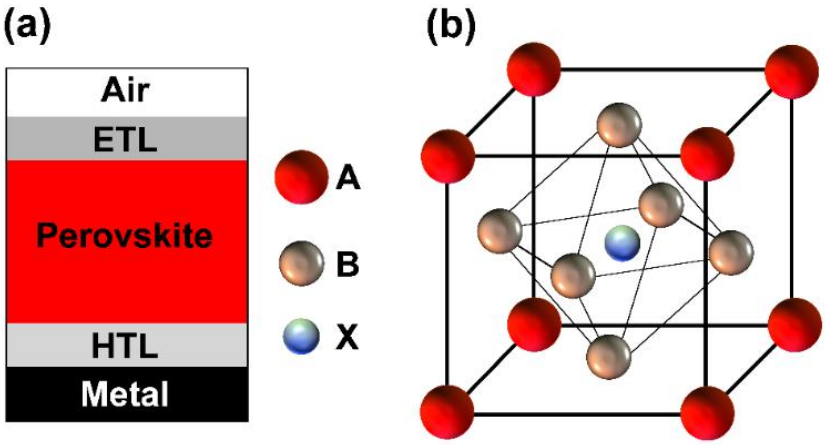

Figure 3.10: Schematic sketch of (a) a planar perovskite solar cell structure and (b) a perovskite crystal structure.

Perovskite and metal oxides have a comparable refractive index, which helps to minimize the reflection loss. The optical constants used for the simulations are provided in Appendix A (Figure A3.1), where the complex refractive index of $MAPbI_3$ was adapted from the literature.(Löper et al., 2015b) A planar PSC structure is investigated in the current study as depicted in Figure 3.16(a), where a 50 nm thick ALD-grown AZO is used as an electron transport/hole blocking layer (ETL). A $MAPbI_3$ perovskite absorber is sandwiched between the front and back contact, where the thickness of the perovskite absorber is varied from 100 nm to 400 nm. A double NiO/ZnO layer is used as a hole transport or an electron blocking layer (HTL), where a 50 nm thick ALD-grown ZnO is combined with a very thin NiO. The NiO/ZnO double

layer acts as a tunneling junction.(Mohammad I. Hossain, Hongsingthong, et al., 2019; Qarony et al., 2019) The double NiO/ZnO layer exhibits a suitable work function, high lateral conductivity, and low absorption losses.(Mohammad I. Hossain et al., 2018a; J.-Y. Wang et al., 2009a) Similar combinations of metal oxides have been used to realize contacts of highly efficient PSCs.(An et al., 2017; Mohammad I. Hossain et al., 2018a; W. Zhang, Ren, Guo, He, & Li, 2018; J. Zhou et al., 2017) A thick aluminum (Al) is utilized as a back reflector. All investigated PSC structures are assumed to be realized in substrate configuration, which allows further for integrating the solar cell on top of a crystalline silicon bottom solar cell to form a perovskite/silicon TSC.

3.3.2 Experimental Details

ALD technique allows realizing a wide range of metal oxide depositions such as TiO_2, ZnO, SnO_2, NiO, etc. for optoelectronic applications.(Zardetto et al., 2017) For the ALD process of a metal oxide compound, the gaseous vapor from a chemical precursor usually in liquid or solid form is used in conjunction with an oxidizing co-reactant such as H_2O, O_2, or O_3, for the periodic surface reactions separated by purging cycles, so that film growth reactions occur only on the film surface in a self-limiting manner.(Iqbal et al., 2016; Mohammad et al., 2019; Seo et al., 2019) A repetitive supply of precursors leads to the deposition of the desired film at a growth rate less than a single monolayer, which ensures the formation of a pinhole defect-free film on the substrate surface. The optoelectronic properties of deposited films mainly depend on the deposition temperature, pressure, choice of precursors, and the total number of utilized ALD cycles.(Iqbal et al., 2016; Keun Kim et al., 2005; Zardetto et al., 2017) In this study, a thermal ALD system (*Okyay Technologies, Inc.*) is utilized to prepare ZnO and AZO films on silicon and glass substrates. Description of the used ALD system and substrate loading is illustrated in Figure 3.11(a). Detailed explanations of the

deposition process and film characterizations will be discussed in the following sections.

3.3.2.1 Deposition of Metal Oxides

In this study, ZnO and AZO films were deposited thermally by ALD, where silicon (100) and glass (Corning 7059) were used as substrates. Throughout the experiments, Diethylzinc ($(Zn(C_2H_5)_2)$, DEZ, *Sigma-Aldrich*), Trimethylaluminum (TMA, 99.999%, *Strem Chemicals*, Inc.), and Deionized (DI) water (H_2O) were used as precursors and oxidant. Nitrogen (N_2, 99.999% purity, *Airgas*) was used as both carrier and purging gas. In all experiments, precursors and water oxidants were kept at room temperature (22-24ºC) in the lab.

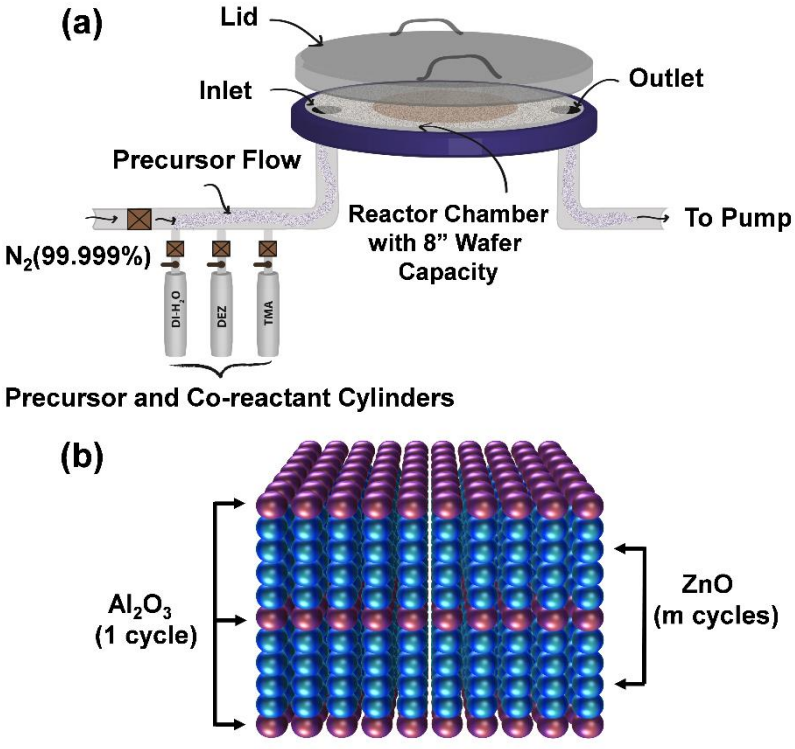

Figure 3.11: (a) ALD thermal system description and substrate arrangement, and (b) schematic of the deposition process for the growth of AZO.

The substrate temperature was varied from 100ºC to 200ºC with an interval of 50ºC. The base pressure of the chamber was kept below ~100 mTorr throughout the

experiments. Up to 500 ALD cycles were performed to investigate the layer by layer film growth in the self-limiting growth regime. Before loading the substrates into the ALD chamber, silicon and glass substrates were ultrasonically cleaned with solvents (acetone and isopropanol) and deionized water in a sequence for 2 minutes, next dried with nitrogen flow. Prior to start, the deposition of zinc-oxide films, standard alumina (Al_2O_3) film was grown as a reference sample, where TMA and water were used as precursors and co-reactant. The deposited alumina films exhibited excellent uniformity and high quality in terms of their optical properties (refractive index) and surface morphology.

Deposition of Zinc-oxide (ZnO) Film

DEZ and DI water were selected as precursor and oxidant for the deposition of ZnO films on silicon and glass substrates. The precursor and oxidant were alternately supplied into the ALD reactor by using external intrinsic vapor pressures. The ALD reaction mechanism for the ZnO film growth can be defined by the following equation:

$$Zn(CH_2CH_3)_2 + H_2O \rightarrow ZnO + 2C_2H_6 \quad (3.1)$$

The deposition of ZnO film is a quite straight forward process, where a single ALD reaction cycle consists of a 15 ms exposure to DEZ, followed by a 10 s for N_2 purge, a 15 ms exposure to H_2O, and then another 10 s N_2 purge to remove reaction by-products and an excess amount of precursor vapor entirely. The total number of ALD reaction cycles ranged from 50 to 500, allowing us to choose the film thickness within ~9 to 90 nm.

Deposition of Al-doped Zinc Oxide (AZO) Film

Similar substrates (silicon and glass) were used to deposit AZO films, where the substrate temperature was kept constant to 150ºC. DEZ and DI water vapor served

as zinc and oxygen precursors, where they alternatively introduced in the ALD reactor through the chamber inlet using N_2 carrier gas at a flow rate of 20 sccm. TMA and DI water were selected as aluminum and oxygen precursors for the Al_2O_3 growth, which is used to dope the ZnO film. In this experiment, the pulsing time of precursors (DEZ and TMA) and oxidant (H_2O) was kept constant at 15 ms, where purging flow time was 10 s for all cases. The ALD growth of AZO can be described by the following expression (equation 3.2).

$$[A \times (DEZ + H_2O) + B \times (TMA + H_2O)] \times C \quad (3.2)$$

where $[A \times (DEZ + H_2O) + B \times (TMA + H_2O)]$ represents one supercycle, and C is the number of supercycles for the AZO film deposition. The supercycle was repetitively performed until obtaining the expected film thickness, where multiple (m) ZnO cycles repeated for one (1) Al_2O_3 cycle, as illustrated schematically in Figure 3.11(b). Henceforth, the number of DEZ/H_2O cycles carried out for the AZO film deposition depends on the deposition cycle ratio ZnO:Al_2O_3. In this experiment, the deposition cycle ratio varied from 15:1 to 50:1 to realize the better AZO film having low resistivity (high conductivity) and high transparency. A similar number of ALD cycles (up to 500) was performed for the AZO deposition, where the total number of ALD cycles was determined by adding individual ZnO and Al_2O_3 cycles. It is noted that the pulse time of individual precursor flow has been optimized to the minimum value (15 ms) which is notably lower than the reported value in the literature.(Iqbal et al., 2016; Seo et al., 2019; J. Zhou et al., 2017) Hence, the proposed deposition process might result in high quality and, at the same time low-cost device layers.

3.3.2.2 Materials Characterization

As a part of this study, different physical properties of the deposited films have been characterized by using several techniques, which lead to realizing the better contact

layers for PSCs. The electrical and optical characterizations were performed on the films deposited on silicon substrates, where films deposited on glass substrates were used for the morphological and structural analyses. All measurements were performed at room temperature (22-24°C). To begin the characterization process, we started to study the growth mechanism of undoped ZnO films for multiple ALD reaction cycles, which were deposited at 150ºC. The growth property of deposited films was determined by the ex-situ multi-wavelength ellipsometry measurement (*FS-1 Multi-wavelength Ellipsometer, Film Sense, LLC*). This ellipsometry allows determining the wavelength-independent refractive index, where we have obtained the expected refractive index (~2) for deposited ZnO films. The film thickness varies with changing the number of ALD cycles, where ZnO film thickness ranged from ~9 nm to ~88 nm for 50 to 500 ALD cycles. The growth per cycle (GPC) for individual ZnO films varies from ~0.177 nm to ~0.175 nm. The thickness of the deposited film is increased linearly due to an almost constant GPC, which demonstrates the self-limiting behavior of the ALD growth process.

Additionally, we also measured the growth rate (~0.1 nm/cycle) and refractive index (~1.6) of previously deposited Al_2O_3 film, which will be used as a reference to determine the doping percentage. Next, we studied the growth of AZO film for different deposition cycles. In general, the growth rate of AZO films is relatively lower than the growth rate of ZnO, which might occur due to the insufficient energy of chemical reactions. The growth rate of deposited AZO films decreases with the increase of the Al percentage up to 25:1 deposition cycle and then starts to increase with a further increase of dopant. Typically, the minimum growth rate is useful to achieve a uniform and good quality film. Figure 3.12(a) shows the growth per cycle of AZO for different deposition cycles along with undoped ZnO, where the total number of ALD cycles was 300 considered. The corresponding film thickness is varied from ~50 nm to ~54 nm, with an average growth rate of ~0.18 nm/cycle. Our calculated GPC has a comparable

value, which was determined by other research groups.(Geng et al., 2011; Guziewicz et al., 2008; Iqbal et al., 2016) The nominal Al percentage in the AZO film can be determined by the following formula (Eq. 3).(Y. Wu et al., 2013)

$$\%\mathrm{Al}_{\mathrm{Nom}} = \frac{\mathrm{GPC}_{\mathrm{Al_2O_3}}}{\mathrm{GPC}_{\mathrm{Al_2O_3}} + \mathrm{GPC}_{\mathrm{ZnO}} \times \mathrm{N}} \times 100\% \tag{3.3}$$

where $\mathrm{GPC}_{\mathrm{Al_2O_3}}$ and $\mathrm{GPC}_{\mathrm{ZnO}}$ represents the growth rates of Al_2O_3 and ZnO, respectively, where N indicates the number of supercycles.

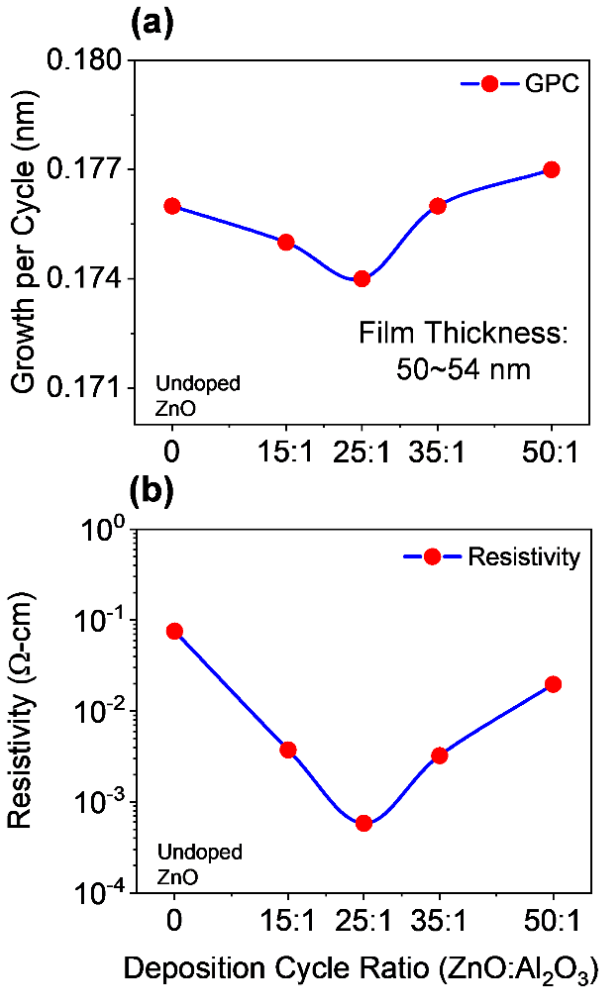

Figure 3.12: (a) Growth per ALD cycle and (b) measured resistivity as a function of the deposition cycle. ZnO and AZO films on silicon substrates were used to determine the GPC, whereas films on glass substrates used for the determination of resistivity.

According to the equation (3.3), the nominal Al percentage of AZO film, which has a

comparatively low GPC (25:1 deposition cycle), was calculated to 2.14%. One of the major optoelectronic applications of ZnO films is to use as a transparent contact, where both high conductivity (low resistivity) and high transparency are required. In PSC, the front contact should be thin enough to minimize series resistance so that optical losses are minimized. The thinner front contact should also provide an efficient charge injection. Since deposited AZO and ZnO films will be used as potential front and back contacts in this study for the implementation of PSCs, it is necessary to evaluate the performance as a contact layer by understanding the electrical properties of deposited films. The electrical characterization of deposited AZO and ZnO films was carried by means of four-point probe measurements by using the *Alessi CPS system* at room temperature. The system allows determining the sheet resistance of the film, which can be further multiplied with film thickness for the realization of a resistivity. To avoid spatial resistivity distribution, films were deposited on glass substrates, which patterned in squared-shaped (1 cm × 1 cm) following the van der Pauw geometry. Figure 3.12(b) shows the measured resistivity of AZO and ZnO films as a function of the deposition cycle ratio. In the case of undoped ZnO, the resistivity is 7.56×10^{-2} Ω-cm. As aluminum incorporated into ZnO films, the resistivity of AZO decreases and reaches to the lowest value of 5.84×10^{-4} Ω-cm for 25:1 deposition cycle ratio. Further doping of Al leads to slight increase the resistivity to 3.74×10^{-3} Ω-cm for 15:1 deposition cycle ratio. The lowest resistivity was achieved for 25:1 AZO which is lower than the results reported in the literature.(Iqbal et al., 2016; Keun Kim et al., 2005; Y. Wu et al., 2013) The deposition was carried by controlling the number of supercycles consisted of DEZ/H_2O:TMA/H_2O cycle ratio 25:1, as explained in the deposition process.

To start with the optical characterization, the spectroscopic ellipsometry (*J.A. Woollam Co. Inc. Spectroscopic Ellipsometer*) measurements were performed on AZO and ZnO

films deposited on silicon substrates. The wavelength ranged from 371nm to 1000 nm at three incident angles of 60°, 65°, and 70° for the measurements. The ellipsometry techniques allow determining complex dielectric constants and refractive index of deposited films. Figure 3.13 shows the measured optical constants of AZO films, where it is found that complex dielectric constant and refractive index of 50:1 AZO is almost like undoped ZnO. Hence, only the optical constants of AZO films are shown in Figure 3.13, where the deposition cycle ratio is varied from 15:1 to 50:1. A blue or UV shift is observed in the optical constants by increasing the Al doping percentage since Al impurity can act as effective n-type donors for generating free carriers.

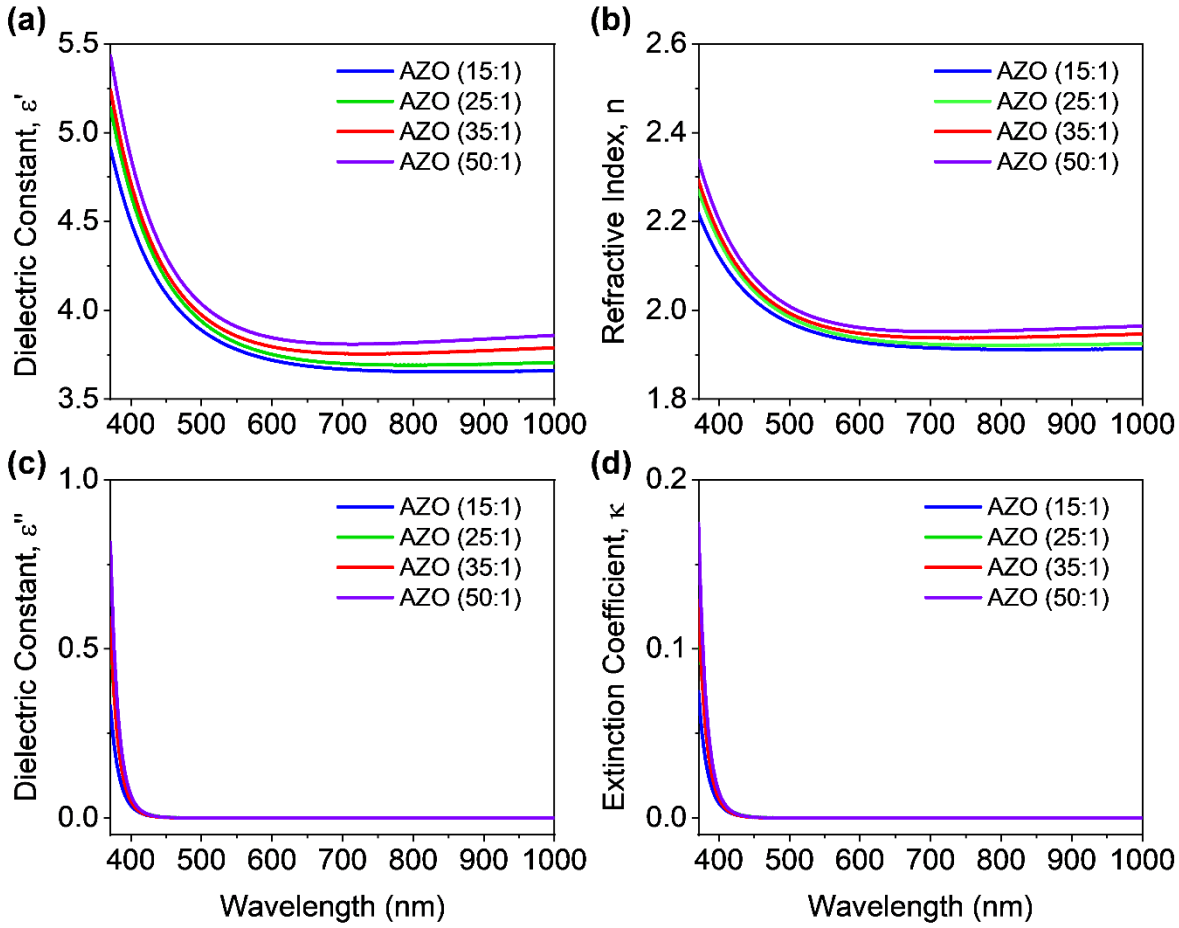

Figure 3.13: (a) real and (b) imaginary part of the complex dielectric function of AZO films as a function of the incident wavelength. (c) Real and (d) imaginary part of the complex refractive index of AZO films as a function of the incident wavelength. Films were grown on silicon substrates for the optical measurement.

The doping concentration of DEZ/H_2O can increase the free carrier concentration that reduces the refractive index of AZO film. Figure 3.13(d) shows the extinction coefficient of AZO films for various deposition cycle ratios. It can be seen that all the extinction coefficients are close to zero for the entire wavelength range 400-1000 nm, which indicates the transparency within this wavelength range. The absorption coefficient, α can be determined from the following formula (equation 3.4), which further allows calculating the bandgap of the film. The bandgap of the deposited AZO films is approx. 3.1 eV.

$$\alpha = \frac{4\pi\kappa}{\lambda} \tag{3.4}$$

where, κ is the extinction coefficient of the film.

To investigate the transparency of deposited films, a UV/VIS/NIR spectrometer (*PerkinElmer UV/VIS/NIR Spectrometer Lambda 1050*) was used to analyze the optical transmittance of both AZO and ZnO films. The system allows measuring absorption, transmittance, and reflection of deposited films for the wavelength range from 200 nm to 4000 nm. Since deposited films will be used in PSC, therefore, we studied the transmission for the wavelength range 300 nm to 800 nm.

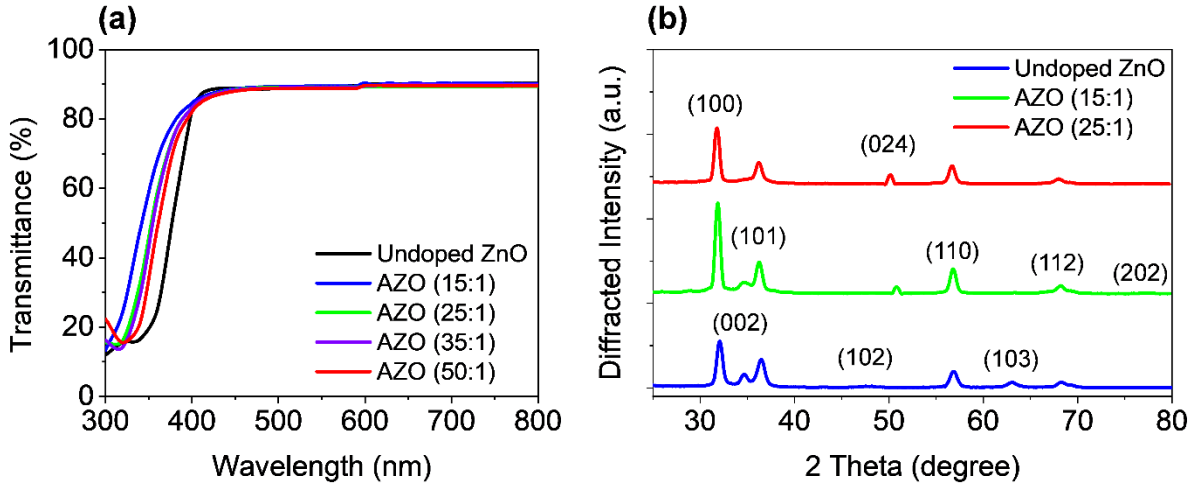

Figure 3.14: (a) Optical transmittance spectrum of ZnO and AZO films with various deposition cycles, grown on glass substrates. (b) X-ray diffraction patterns of ZnO and AZO films with various deposition cycles, grown on Si substrates.

Figure 3.14(a) illustrates the transmittance spectrum for AZO and ZnO films, where the deposition cycle ratio of AZO is varied from 15:1 to 50:1. Moreover, films on glass substrates were used for the transmission measurement. It can be seen that the average transmission of the deposited samples is approximately 90 % in the visible wavelength region (400-700 nm). The UV shift of absorption edge (300-400 nm) has been found with increasing Al doping level, which is very consistent with the results measured by the spectroscopy ellipsometry. Such ALD growth films exhibit great potential as a transparent conductor for PSC applications, which can be further applied to the implementation of transparent solar cells.

For the structural analysis, x-ray diffraction (XRD) measurements were done on deposited ZnO and AZO films. The crystalline structures were performed for the deposited films by using *Ragaku SmartLab* automated multi-purpose X-ray Diffractometer with CuK_{α} radiation (λ=0.154 nm) at room temperature. The XRD spectra were measured on all samples in the two-theta (2θ) angular region between 25° to 80°. The XRD patterns of ZnO and AZO with the deposition cycles of 15:1 and 25:1 is shown in Figure 3.14(b), where comparison of XRD pattern of only AZO films for various deposition cycle ratios are presented in Appendix A (Figure A3.2). In addition, temperature-dependent XRD patterns for the 25:1 (optimal cycle ratio) AZO film is shown in Appendix A (Figure A3.3). All XRD patterns clearly exhibit the polycrystalline structure with orientation along different planes. These planes are (100), (002), (101), (102), (110), (103), and (112) of undoped ZnO, which confirm that films are polycrystalline wurtzite structure. Major diffraction peaks ((100), (002), (101), and (110)) are observed at 31.8°, 34.5°, 36°, and 56.5° in the undoped ZnO film. Nevertheless, at 34.5° diffraction peak (002) has a less intensity, which disappears by Al doping, where (002) is completely missing in 15:1 AZO case. On the other hand,

peak (100) at 31.8° becomes more dominant after increasing the Al doping level, which is similar to the results reported in the literature. Moreover, increased doping causes to introduce new peaks, which are (024) and (202).

In order to check the uniformity of deposited films, surface morphologies of AZO and ZnO films grown on a silicon substrate were studied by using optical microscopy (*Leica DM 2700M*) and field emission scanning electron microscopy (*FESEM JEOL JSM-6335F*). Surface morphologies were first investigated with optical microscopy where all films exhibit a good uniformity and no significant difference is observed between AZO and ZnO films. Figure 3.15(a,b) shows optical microscopic images of 25:1 AZO and ZnO films for a large area.

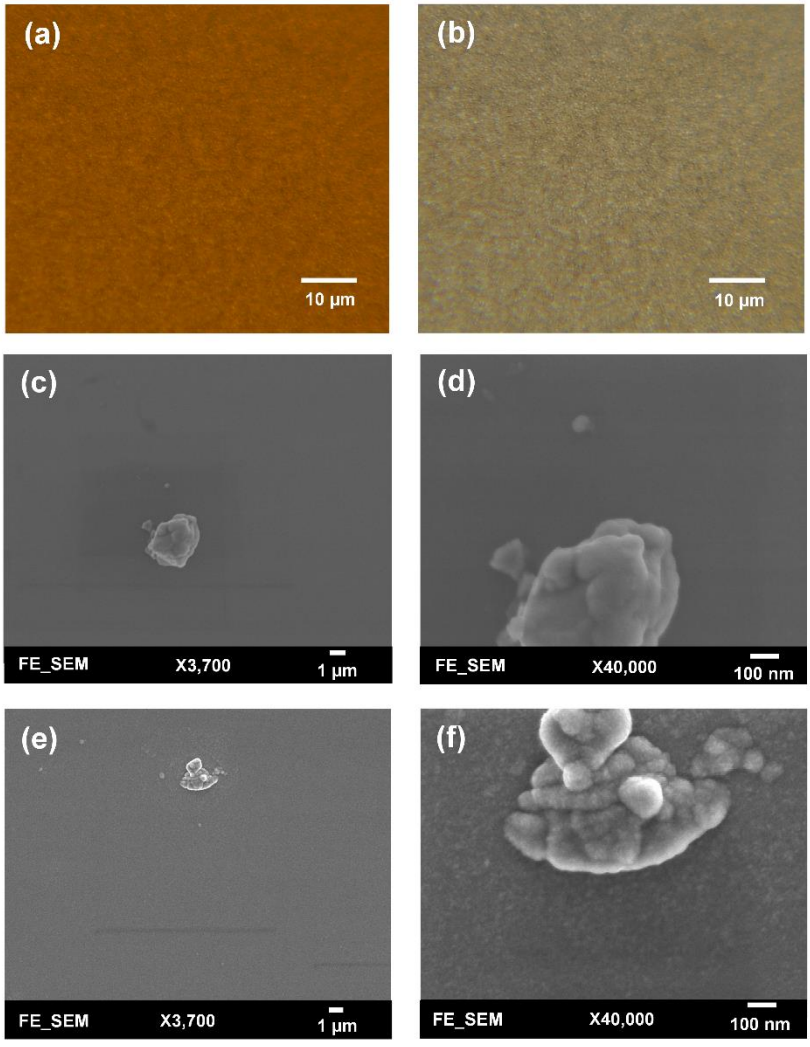

Figure 3.15: Optical microscopic images of (a) 25:1 AZO and (b) undoped ZnO. Top

view of SEM micrographs of (c,d) 25:1 and (e,f) undoped ZnO. All films were grown on silicon substrates at 150°C deposition temperature.

Next, surface morphologies were investigated by using FESEM, where typically all films exhibit good uniformity over the scanning area. High-resolution SEM images of ZnO and 25:1 AZO are depicted in Figure 3.15(c-d), where film thickness varies between 50-54 nm. In low magnification images, it has been seen that all films show a great uniformity, which is highly dense. For higher magnification, AZO film demonstrates a relatively smoother than undoped ZnO film. The influence of Al doping makes the ZnO film more uniform, which leads to prepare a high-quality film. Generally, it is clear that all samples show a smooth surface with low surface roughness, which will help to improve the stability and performance of PSCs.

3.3.3 Realization of Optimum Front Contact for PSCs

In the current study, we have investigated the influence of the front contact on the QE and J_{SC} of perovskite single-junction solar cells. The sheet resistance of the front contact was kept constant to 80 Ohms, while the doping concentration was varied. Hence, the AZO film thickness has to be adjusted to keep the sheet resistance of the front contact constant. The charges are collected by a metal front contact grid printed on the solar cell. For the given sheet resistance, the thickness of the AZO film was varied from 50 nm to 1690 nm. Figure 3.16(b) exhibits the power density profile of a solar cell with an AZO thickness of 50 nm under monochromatic illumination of 420 nm, 550 nm, and 700 nm. At 420 nm wavelength, most of the incident photons are absorbed within the first 150 nm of the perovskite film. At 700 nm, a large fraction of the incident light reaches the back contact, where it is reflected, and a standing wave is formed inside the solar cell due to constructive and destructive interference, as shown in Figure 3.16(b). The QE of solar cells with equal sheet resistance but different

doping concentration and thickness is shown in Figure 3.17(a). The solar cell with a front contact thickness of 50 nm exhibits the highest QE. An increased QE is observed for short wavelengths due to the low absorption of the thin AZO layer.

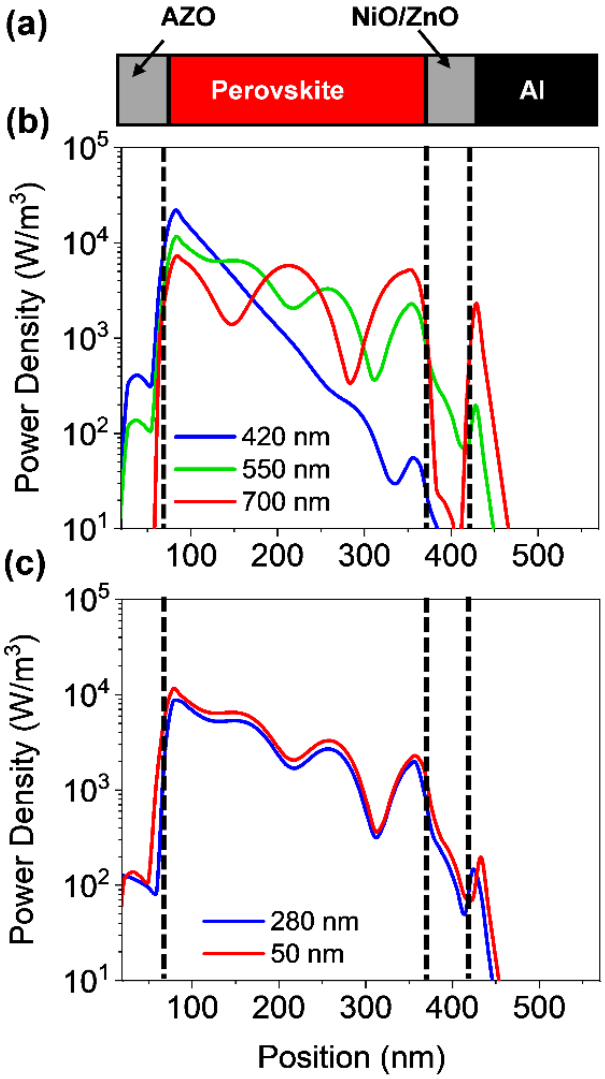

Figure 3.16: (a) Schematic cross-section of a perovskite planar solar cell with AZO front contact. (b) Power density profile of perovskite solar cell with an AZO front contact (deposition cycle ratio 25:1) for different incident wavelengths. (c) Power density profile of perovskite solar cell with an AZO front contact for different front contact thicknesses at an incident wavelength of 550 nm.

Furthermore, an increased QE is observed for the spectral range from 400 nm to almost 600 nm. The front contact acts as a quarter wavelength thick anti-reflection coating for an incident wavelength of 500 nm. The thickness of an anti-reflection

coating is commonly given by $\lambda/(4\times n_{ARC})$, where λ is the wavelength at which the reflection is minimized, and n_{ARC} is the refractive index of the anti-reflection coating. In our case, the thickness of the anti-reflection layer is given by

$$d_{AZO} = \frac{\lambda}{4n_{AZO}} \times \left(1 - \frac{\varphi_{AZO/per}}{\pi}\right) \tag{3.5}$$

where, n_{AZO} is the refractive index of the front contact and $\varphi_{AZO/per}$ is a phase shift introduced by the AZO/perovskite interface.

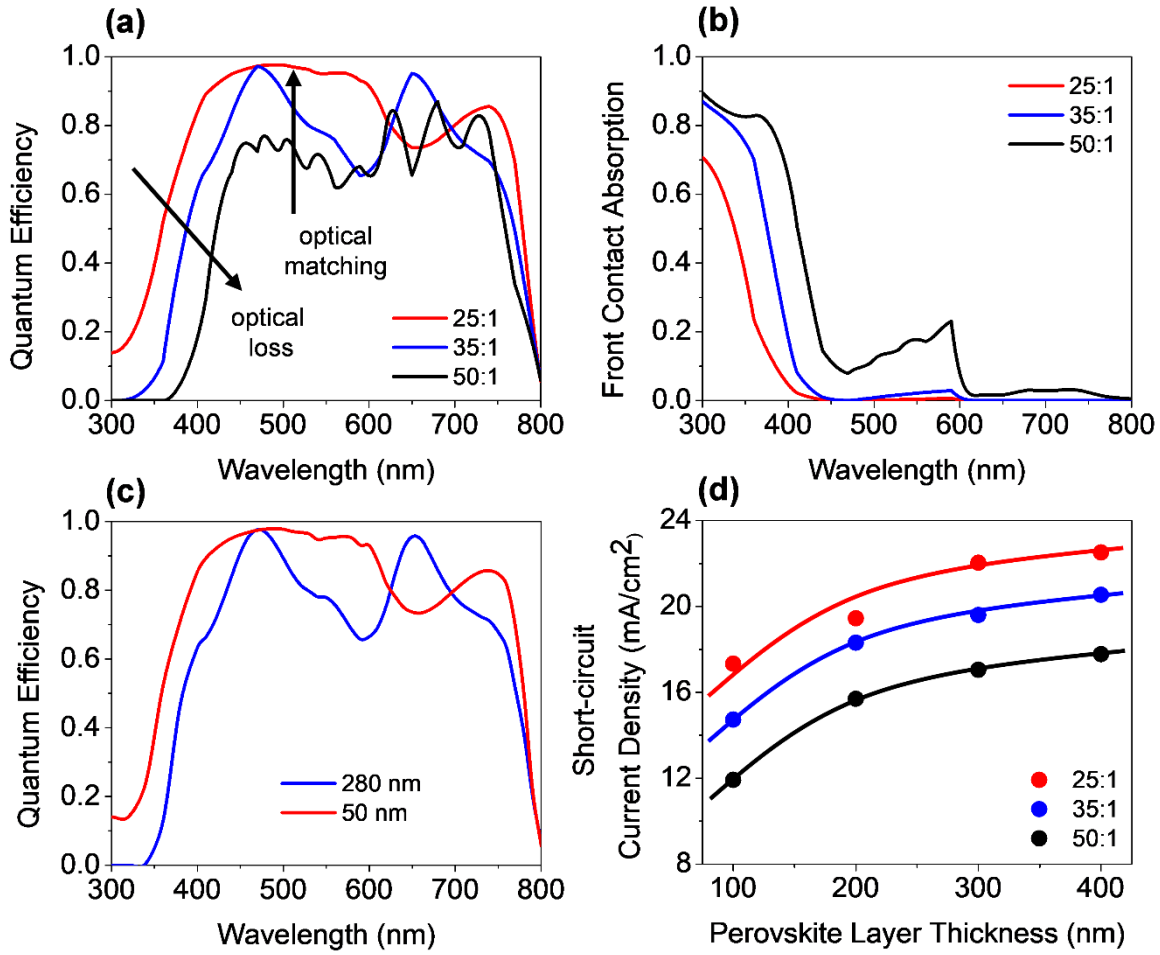

Figure 3.17: (a) Quantum efficiency and (b) front contact absorption of PSC with equal front contact sheet resistance but the different thickness and doping concertation. (c) Quantum efficiency of PSC with equal doping concentration but different thicknesses. (d) Short-circuit current density of PSC with equal front contact sheet resistance but the different thickness and doping concertation as a function of perovskite absorber thickness.

The phase shift is caused by the large extinction coefficient of the perovskite layer. The phase shift is calculated to be approx. $\pi/4$. Without the phase shift, the thickness of the front contact would have to be 65 nm to achieve anti-reflection properties at 500 nm. The phase shift at the AZO/perovskite interface leads to a reduction of the front contact thickness down to 50 nm. Decreasing the doping concentration of the front contact leads to an increased thickness, which causes an increased absorption loss of the front contact. Furthermore, the front contact does not act as an anti-reflection coating anymore. Multiple interferences in the front contact are clearly visible in the QE. A comparison of a solar cell with thin and thick front contact is provided in Figure 3.16(c). The plot shows the power density profile for an incident wavelength of 550 nm and a front contact thickness of 50 nm and 280 nm. The shape of the power density profile is not affected by the different front contact. Only the incoupling of light by the front contact is affected. Moreover, the influence of different front contact thicknesses on the J_{SC} was investigated, which is shown in Figure 3.16(d). The J_{SC} is varied from 17.3 mA/cm^2 to 22.5 mA/cm^2 for perovskite thicknesses from 100 nm to 400 nm, respectively. The J_{SC} is enhanced by 45% for 100 nm thick solar cells and 26% for a solar cell with a thickness of 400 nm. The J_{SC} of the PSC with an anti-reflection coating is comparable to the PSC with a textured front contact.(Mohammad I. Hossain, Hongsingthong, et al., 2019) In this study, Three-dimensional (3D) finite-difference time-domain (FDTD) optical simulations were utilized to investigate the optics and optimize the perovskite solar cells, where detailed information can be found in Chapter 2 (Section 2.3).

3.4 Comparison of Front Contacts

In this Chapter, several metal oxide thin films (e.g., NiO, TiO_2, and ZnO) are investigated as potential charge transport materials (electron and hole transport layers) for planar PSCs. Literature review reveals that such metal oxides are widely used for the fabrication of efficient PSCs. (Möllmann et al., 2019; Paek et al., 2017; Seo et al., 2019; W. Sun et al., 2016; J.-Y. Wang et al., 2009a; Yongzhen Wu et al., 2014; X. Yin et al., 2017; Zardetto et al., 2017) In this study, the influence of different types of front contact on the optics of PSCs is experimentally and theoretically investigated to realize highly efficient PSCs. The aim of this work is not to claim for the fabrication of a best PSC, rather than we wanted to have a reference for the impact of the front contact for solar cell performance, so that we can relate it for our future investigations. Herein, we focused on the following points for realizing next-generation high efficiency solar cells.

1. High quality film preparation (uniform, compact, and smooth)
2. Industrially viable, so that the demonstrated method can be used for large area thin film deposition.
3. Can fulfill the basic requirements of the front contact (e.g., high optical transparency, suitable work function, high lateral conductivity, low parasitic loss, etc)

In this study, we have used Spray Pyrolysis Deposition (SPD), Electron Beam (EB) Deposition, and Atomic Layer Deposition (ALD) for preparing high quality transport materials for PSCs. A fair comparison between different front contacts that realized by several deposition methods on the photovoltaic performance is shown in **Table 3.3**.

Table 3. 3: A comparison of different front contacts on the PSC performance

Parameter	Electron Beam Deposition of NiO		Spray Pyrolysis Deposition of TiO_2		Atomic Layer Deposition of ZnO	
	Experiment	*Simulation*	*Experiment*	*Simulation*	*Experiment*	*Simulation*
J_{SC} (mA/cm^2)	17.2	18.3	21.3	21.4	x	22.2
V_{OC} (V)	1.0	1.01	1.07	1.07	x	1.18
FF (%)	79	81	72	76	x	81
ECE (%)	13.42	14.95	16.55	17.47	x	21.2

3.5 Summary

In this Chapter, a potential use of metal oxide films as charge transport materials for planar perovskite solar cells has been investigated. Several deposition techniques are utilized to prepare high-quality contact materials. The optics and optimization of perovskite solar cells are studied by three-dimensional FDTD optical simulations, where 3D FEM electrical simulations examine electrical effects. Firstly, electron beam physical vapor deposition technique (EBPVD) is used to prepare the high-quality NiO film at a low temperature, which further used as a hole transporting layer for fabricating planar perovskite solar cells. The performance of experimentally realized planar perovskite solar cells is compared with the simulated PSCs, where an excellent agreement is found between experiments and optical simulations. The influence of the NiO film thickness on quantum efficiency (QE) and short-circuit current density (J_{SC}) is discussed. The fabricated champion device exhibited an energy conversion

efficiency of 13.42% with an open-circuit voltage of 1 V; a short-circuit current density of 17.2 mA/cm^{2,} and a fill factor of 78%. It has been found that NiO HTL must be thin to provide high conductivity and transparency so that the absorption loss is minimized. Secondly, the pin-hole free, uniform, and highly compact TiO_2 hole-blocking/electron-transport layer (ETL) is prepared by using spray pyrolysis deposition for the fabrication of high-efficiency perovskite solar cells (PSCs). The concentration of TiO_2 precursor solution has a great effect on the thickness of the ETL. Hence, the TiO_2 concentration iss varied from 0.15 M to 0.40 M for optimizing PSCs. The influence of TiO_2 concentration on the photovoltaic performance was studied. As compared to other TiO_2 concentrations (0.15 M, 0.2 M, 0.25 M, 0.3 M, and 0.4 M), the 0.35 M TiO_2 exhibited a superior photovoltaic performance due to excellent electron injection at the perovskite/TiO_2, which prevents from high leakage currents and recombination of charge carriers. To understand the reproducibility of PSC fabrications, 13 fabricated devices were studied in each group. As anticipated, the 0.35 M TiO_2 demonstrated a better performance in terms of PCE and reproducibility. The best-performance PSC, which has an ETL thickness of ~70 nm, allows realizing a short-circuit current density (J_{SC}) of 21.3 mA/cm^2, open-circuit voltage (V_{OC}) of 1.08 V, fill-factor (FF) of 72%, and power conversion efficiency (PCE) of 16.55%, respectively. Furthermore, three-dimensional Optical and electrical simulations are used to validate the findings in the experiments. It is assumed that the spray-pyrolyzed TiO2 Cl has excellent potential for developing high-efficiency perovskite solar cells.

Finally, AZO and ZnO films were investigated as potential contacts for single-junction perovskite solar cells. AZO and ZnO films were prepared by using ALD at low deposition temperatures. The influence of various doping concentrations on the electrical, optical, and structural properties were investigated by several characterization methods. Films with resistivities down to 5.8×10^{-4} Ω-cm for the thickness of ~50 nm, where an almost 90% optical transmittance was achieved for the

spectral range 400 nm to 1200 nm. It is examined that thin and highly doped metal oxides can be used as efficient perovskite solar cell front contacts. The film acts as an anti-reflection coating, while the optical losses of the front contact are rather low, which allows for reaching a short-circuit current density of up to 22.5 mA/cm^2 from the planar perovskite solar cell having a perovskite absorber thickness of 400 nm.

CHAPTER 4

OPTICS OF PEROVSKITE SOLAR CELL FRONT CONTACTS (TEXTURED)

This chapter presents the optics of perovskite solar cell (PSC) front contacts. A detailed discussion on the light incoupling and the light trapping is provided, which contributes to realize efficient photon management for perovskite solar cells. The textured front contacts can improve the short-circuit current density (J_{SC}) and energy conversion efficiency (ECE) by enhanced light incoupling and/or light trapping. Herein, different deposition methods are used to realize the textured front contacts, which are described in the following sections.

4.1 Self-textured ZnO Films as a Front Contact

The front contact has a crucial role on the optoelectronic properties of PSCs. The front contact is part of the junction of the solar cell, must provide lateral charge transport to the terminals, should allow for an efficient light incoupling, while having low optical losses. So far, investigated PSCs have planar front contacts, which are mainly limited owing to significant reflection losses. The complex requirements of the PSC front contact are described, and the optics of the front contact is investigated in the current study. Metal oxide films were investigated as potential front contacts to study the influence of the front contact on J_{SC} and ECE. The incoupling of light in the solar cell is investigated by 3D FDTD optical simulations and optical measurements of experimentally realized self-textured ZnO films. The ZnO films were prepared by metal-organic chemical vapor deposition (MOCVD) at low temperatures. Furthermore, the influence of free carrier absorption of metal oxide films on the optics of low bandgap and/or tandem solar cells is investigated. Guidelines are provided on how to choose the doping concentration and thickness of the metal oxide films.

4.1.1 Perovskite Solar Cell Structure

Most research on PSCs is still focused on single-junction solar cells. However, the

combination of perovskite and silicon as part of a perovskite/silicon tandem solar cell (TSC) exhibits the largest economic potential, because this combination allows reaching high ECEs, while the manufacturing cost is low.(Bush et al., 2017a; Mohammad I. Hossain et al., 2018a; Jošt et al., 2018; Sahli et al., 2018b; Werner et al., 2018) In this case, the PSC must be integrated on crystalline silicon (c-Si) wafer-based bottom solar cell. Hence, we will focus on device structures in substrate configuration, opposite to solar cells on glass substrates, commonly referred to as solar cells in superstrate configuration. The refractive index of the perovskite material system is comparable to the refractive index of the metal oxide contact layers. Hence, reflections at the metal oxide/perovskite interface are low. The reflection of two materials forming a planar interface increases with increasing refractive index difference between the materials. Hence, the layer stack consisting of the metal oxide layers and the perovskite layer can be treated as one unit with an almost equal refractive index. This simplifies the optical design. Hence, we can focus on the coupling of the incident light in the solar cell. This can be achieved by integrating a pyramidal surface texture on top of the solar cell. Depending on the dimensions of the pyramidal texture, the structure might as well diffract or refract the incident light, so that the optical path length is increased. Consequently, the electrical properties of the solar cells should be comparable to planar perovskite solar cells realized in substrate configuration. It is assumed that the modified optical design does not affect the electrical properties of the solar cells. Hence, it can be expected that the electrical parameter of the solar cell, the open-circuit voltage (V_{OC}), and fill factor (FF), are comparable to planar solar cells in substrate configuration.

Cross-sections of PSCs with smooth and textured front contact are depicted in Figure 4.1(a,b). The photon management in PSCs differs fundamentally from photon management in silicon thin-film and silicon wafer-based solar cells. Silicon exhibits a

distinctly higher refractive index than perovskite so that the interface between the silicon diode and the metal oxide contact layers must be textured to allow for efficient photon management. Nickel oxide (NiO) and zinc oxide (ZnO) layers are used as a hole transporting/electron blocking layer (HTL) and electron transporting/hole blocking layer (ETL), respectively. It is challenging to realize NiO films with high transmission and high conductivity. Hence, a 5 nm NiO layer is combined with a 75 nm thick ITO is used as a contact. Such a double layer of NiO and ITO is used to combine hole transporting/electron blocking with high transmission and low lateral resistivity. It is assumed that the NiO/ITO double layer forms a tunnel junction.

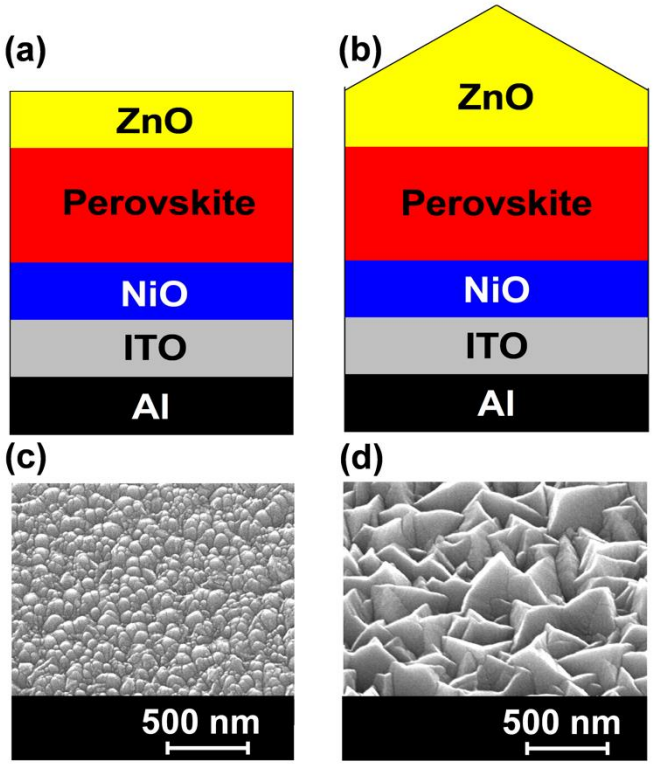

Figure 4.1: Schematic cross-section of a perovskite solar cell with (a) planar and (b) textured zinc oxide front contacts. Corresponding SEM images of (c) smooth and (d) pyramidal textured ZnO films.(Mohammad I. Hossain, Hongsingthong, et al., 2019)

The selected double layer is consistent with layer stacks used by several experimental studies on PSCs in the superstrate configuration.(Forin, Purica, Budianu, & Schiopu, 2012b; J.-Y. Wang et al., 2009b) The formation of a front contact on top of the

perovskite absorber is complex. A variety of materials and material combinations have been investigated. ZnO films have been prepared by spin coating from ZnO nanoparticle solutions, resulting in solar cells with high ECE.(You et al., 2016c) Other authors prepare a C_{60} layer before preparing a ZnO film, or a lithium fluoride (LiF) layer followed by a C_{60} and a zinc oxide layer. The C_{60} and LiF layers are introduced to control the work function and prevent the damage of the underlying perovskite layer. We have investigated the influence of different front contact configurations on the optics of the PSCs. The simulation results are provided in Appendix B (Subsection B.1.1). The C_{60} layer causes absorption losses, and a distinct drop of the quantum efficiency (QE) is observed. The LiF layer has almost no influence on the QE if the LiF layer is placed between the perovskite and the C_{60} layer. The LiF causes only a distinct reflection loss if the LiF is placed between the perovskite and the ZnO layer, and the C_{60} layer is removed (Figure B1.1). However, such a structure has not been proposed as a potential contact configuration. The corresponding simulations are provided in Figure B1.1 of the Appendix. Even though the C_{60} layer leads to a distinct drop in the QE, the C_{60} layer has no influence on the proposed ideas and conclusions. Hence, we focused on the following solar cell with only a ZnO contact layer. An aluminum layer is used as back contact and back reflector. Furthermore, the influence of an encapsulation layer on the solar cell was not considered. Further information on the influence of an encapsulation layer on the optics of the solar cell is provided in Appendix B (subsection B.1.2 and Figure B1.2).

4.1.2 Photon Management

The perovskite device structure in Figure 4.1(b) allows for an enhancement of the ECE by using a different front contact design. On the one hand, the dimensions of the front contact texture must be derived, and on the other hand, it must be possible to fabricate

such structures. In the following, the fabrication of such surface textures by a self-texturing process is investigated. Such self-texturing has been successfully used to increase the J_{SC} and ECE of silicon thin-film solar cells. However, such self-textured contacts have not been investigated as potential front contacts of PSCs. Optical simulations are used to realize the optimal dimensions that are also provided in the following.

4.1.2.1 Experimental Realization of Textured Metal Oxide Contact Layers

Textured ZnO layers doped with aluminum, gallium, or boron can be realized by a variety of deposition methods. ZnO films with pyramidal or inverted pyramidal structure have been realized by chemical vapor deposition (CVD), pulse laser deposition (PLD) or the wet chemical etching of sputtered ZnO films in diluted solutions of hydrochloric or hydrofluoric acids.(Dewan et al., 2015; Dikovska, Atanasov, Vasilev, Dimitrov, & Stoyanchov, 2005; Hongsingthong, Yunaz, Miyajima, & Konagai, 2010; Hwang et al., 2015; Müller, Rech, Springer, & Vanecek, 2004a; Yoo et al., 2008) This study focuses on films prepared by CVD.(Dewan et al., 2015; Hongsingthong et al., 2010; Müller et al., 2004a) The CVD of textured metal oxide films is a standard process used in industry to coat several square meter large glass substrates. As a part of this study, boron-doped ZnO (ZnO:B) film was prepared by a Metal-Organic Chemical vapor deposition (MOCVD) process. Details on the preparation of the zinc oxide films are provided in the experimental section. Figure 4.1(c) exhibits a Scanning Electron Microscope (SEM) image of a smooth boron-doped zinc oxide film. In contrast, Figure 4.1(d) shows a boron-doped film that is covered with quasi-randomly arranged pyramids. Figure 4.1(c) exhibits the SEM of a film prepared by using a D_2O/H_2O ratio of 1, while the D_2O/H_2O ratio is 0 for the film shown in Figure 4.1(d). The size of the pyramids can be controlled by the thickness of the ZnO film. The size of the pyramids increases with increasing thickness of the ZnO film. Each pyramid can be

characterized by a period, p, and a height, h. The opening angle of the pyramid is given by 2×tan(p/2/h). Small pyramids exhibit an opening angle of 135°-140° corresponding to the opening angle of inverted pyramids etched in ZnO single crystals. With increasing film thickness and increasing size of the pyramids, the opening angle decreases.(Boccard et al., 2012) Opening angles down to 40° have been observed for ZnO films with a thickness of up to 7 μm.(Boccard et al., 2012)

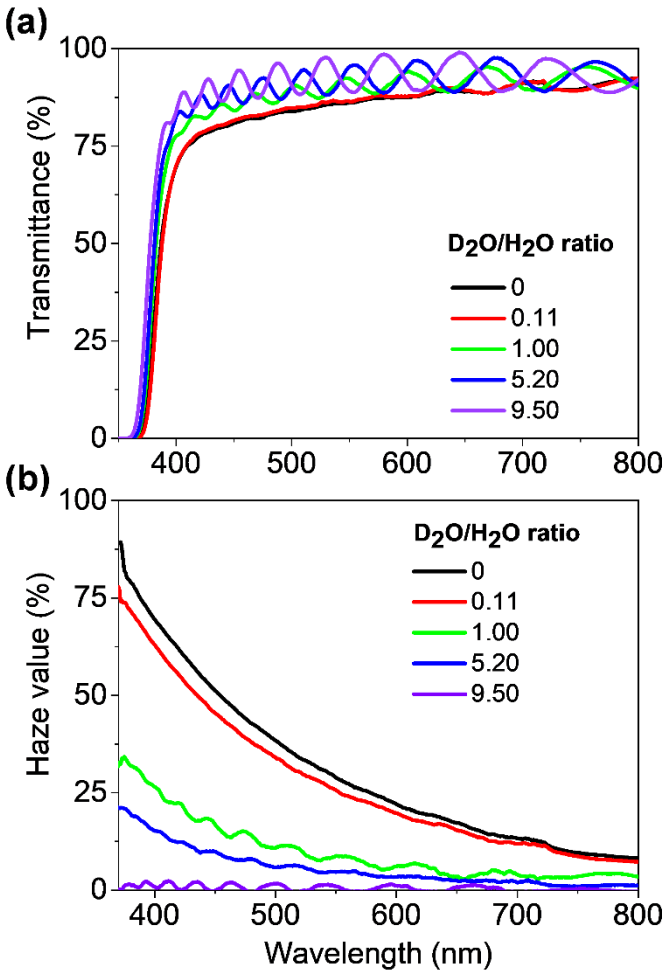

Figure 4.2: (a) Measured total transmission of 1.6 μm thick ZnO film prepared by metal-organic chemical vapor deposition (MOCVD). The roughness of the film was varied by the D_2O/H_2O ratio during the growth process. The roughness increases with decreasing D_2O/H_2O ratio. (b) Haze in transmission. The haze is defined as the diffuse transmission normalized to the total transmission.

The films fabricated as part of this study exhibit a charge carrier concentration of 2×10^{20} cm^{-3} irrespective of the D_2O/H_2O ratio. For D_2O/H_2O ratios of 0 and 0.1, the

electron charge carrier mobility is 15 $cm^2/V/s$, while for higher D_2O/H_2O ratios ranging from 1 to 10, the electron charge carrier mobility is approx. equal to 7.5 $cm^2/V/s$. Fig. 2(a) exhibits the total (specular plus diffuse) transmission of the films. The averaged total transmission for all films is higher than 80% in the spectral range from 400 nm to 800 nm as shown in Figure 4.2(a). The haze in the transmission is shown in Figure 4.2(b). The haze is defined as the diffuse transmission normalized to the total transmission. The haze increases with decreasing D_2O/H_2O ratio and increasing roughness of the ZnO film. With increasing haze more light is diffracted by the texture of the ZnO film. However, the haze does not provide information on the diffraction angle of the diffracted light. Furthermore, it is difficult to directly correlate haze measurements with the QE and J_{SC} of solar cells. Optical simulations allow for a good correlation of the surface texture and the QE.

4.1.2.2 Realizing the Optimal Dimension of the Front Contact

The refractive index of the used ZnO and ITO is depicted in Figure 4.3(a) along with the refractive index of perovskite (methylammonium-lead(n)-iodide, $CH_3NH_3PbI_3$ ($MAPbI_3$)) material used in the investigation. The refractive index of the ZnO and ITO layers is comparable with the refractive index of the perovskite material. The perovskite material system exhibits a high absorption coefficient and, hence, a low absorption or penetration depth. The penetration depth ($t_p=1/\alpha_p(\lambda)$) is the inverse of the absorption coefficient and defined as the thickness at which the incident light intensity drops to 1/e. The dashed lines added to the graph represent the penetration depth for a solar cell with 100 nm and 400 nm thickness, as shown in Figure 4.3(b). The incident light is absorbed up to a wavelength of 610 nm and 770 nm assuming a penetration depth of 200 nm and 800 nm, respectively. The optical data used in this study was adapted from the literature.(Drude, 1900b, 1900a; Löper et al., 2015b; Steinhauser, 2008) We used the finite-difference time-domain (FDTD) simulations to

calculate the 3D optical wave propagation. Details on the method and procedures to calculate power density profiles, the QE, and the J_{SC} are provided in the experimental section.(Dewan et al., 2009; Parsons, Tamang, Jovanov, Wagner, & Knipp, 2017) The optical wave propagation was investigated for pyramids with heights of 200 nm, 400 nm, and 600 nm, while the period is varied from 150 nm to 1200 nm. The pyramids are formed on a continuous layer of ZnO. In the case of an experimentally realized solar cell, the thickness of the continuous layer is determined by the doping concentration, which is linked to the required lateral sheet resistance of the ZnO layer and the growth conditions of the ZnO film.

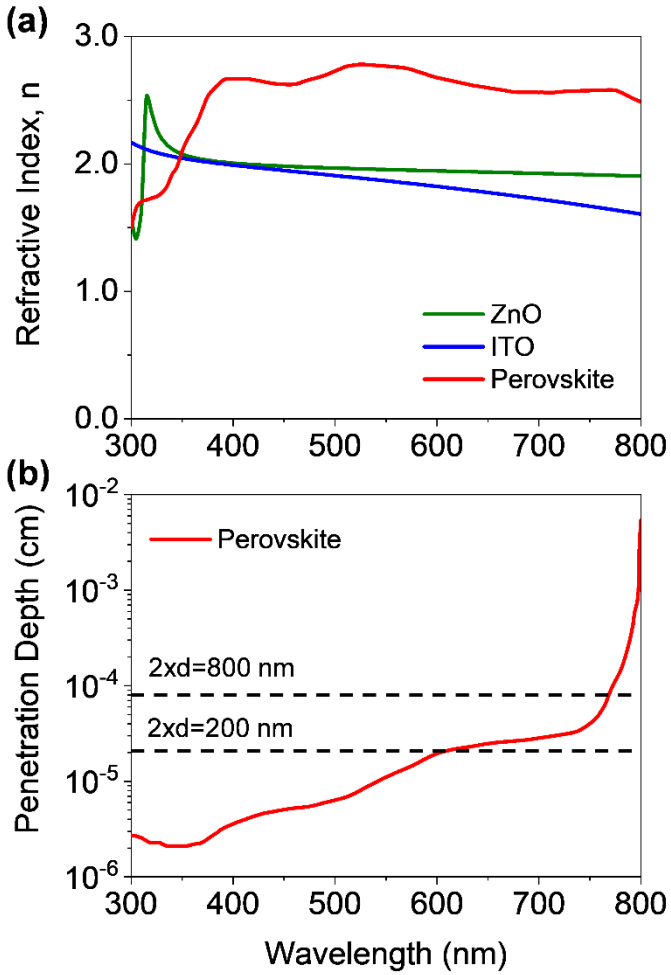

Figure 4.3: (a) Refractive indices of ZnO, ITO, and Perovskite materials. (b) The penetration depth of the Perovskite material.

The influence of the thickness of the continuous layer on the QE and J_{SC} is described

in Appendix B (subsection B.1.3 and Figure B1.3). The absorption losses of the continuous ZnO layer increase with increasing thickness of the film. However, the thickness has no influence on the light incoupling of the solar cell and the light trapping of the solar cell. In the following, it is assumed that the ZnO layer has a thickness of 400 nm, while the period and height of the surface texture are 600 nm and 600 nm. Figure 4.4 exhibits a comparison of QE and total reflection of a pyramidal textured and flat perovskite solar cell with an absorber thickness of 100 nm and 400 nm, respectively. The QE of the planar solar cell is characterized by pronounced interference fringes. The 400 nm thick ZnO front contact is responsible for the formation of interference fringes. As compared to the flat solar cell, the pyramidal textured solar cell shows a higher QE throughout the complete spectral range for the 100 nm and 400 nm thick PSCs. For short wavelengths, the absorption coefficient of the perovskite material is substantial, and the penetration depth is minimal. Hence, the penetration depth is smaller than twice the thickness of the absorber of the solar cell. For a 100 nm thick solar cell, the penetration depth is equal to twice the absorber layer thickness for a wavelength of 580 nm, while for a solar cell with an absorber thickness of 400 nm, the transition point is shifted to 770 nm. The gain of the QEs caused by an improved incoupling of light. Hence, it can be concluded that for short wavelengths, light trapping of the incident, light does not lead to an increased QE. The light might be diffracted by the surface texture, but the diffraction does not lead to increased light absorption. The light is absorbed irrespective of the diffraction of the incident light. For $t_p > 2 \times d$, the situation is different. The penetration depth is larger than two times the thickness of the perovskite absorber, and the gain in the QE is caused by improved incoupling and increased absorption of the incident light due to diffraction.

This is also confirmed by the calculated total reflection of the solar cells in Figure 4.4(c) and 4.4(d). The total reflection is calculated by $R=1-A_{total}$, where A_{total} is the total absorption of the solar cell. The total absorption of the solar cells approaches unity if

the pyramid texture allows for an efficient incoupling and $2\times d>t_p$, which occurs for wavelengths up to 580 nm and 770 nm using 100 nm and 400 nm thick perovskite absorber layers, respectively. For $2\times d<t_p$ the total absorption is distinctly increased, due to the improved incoupling and light trapping, but the total absorption does not approach unity. It should be noted here that the roughness of the perovskite films is not considered in the optical simulations. The roughness of the perovskite film depends on several factors like the deposition method, the temperature during the deposition, and temperatures during potential subsequent deposition steps or annealing procedures.

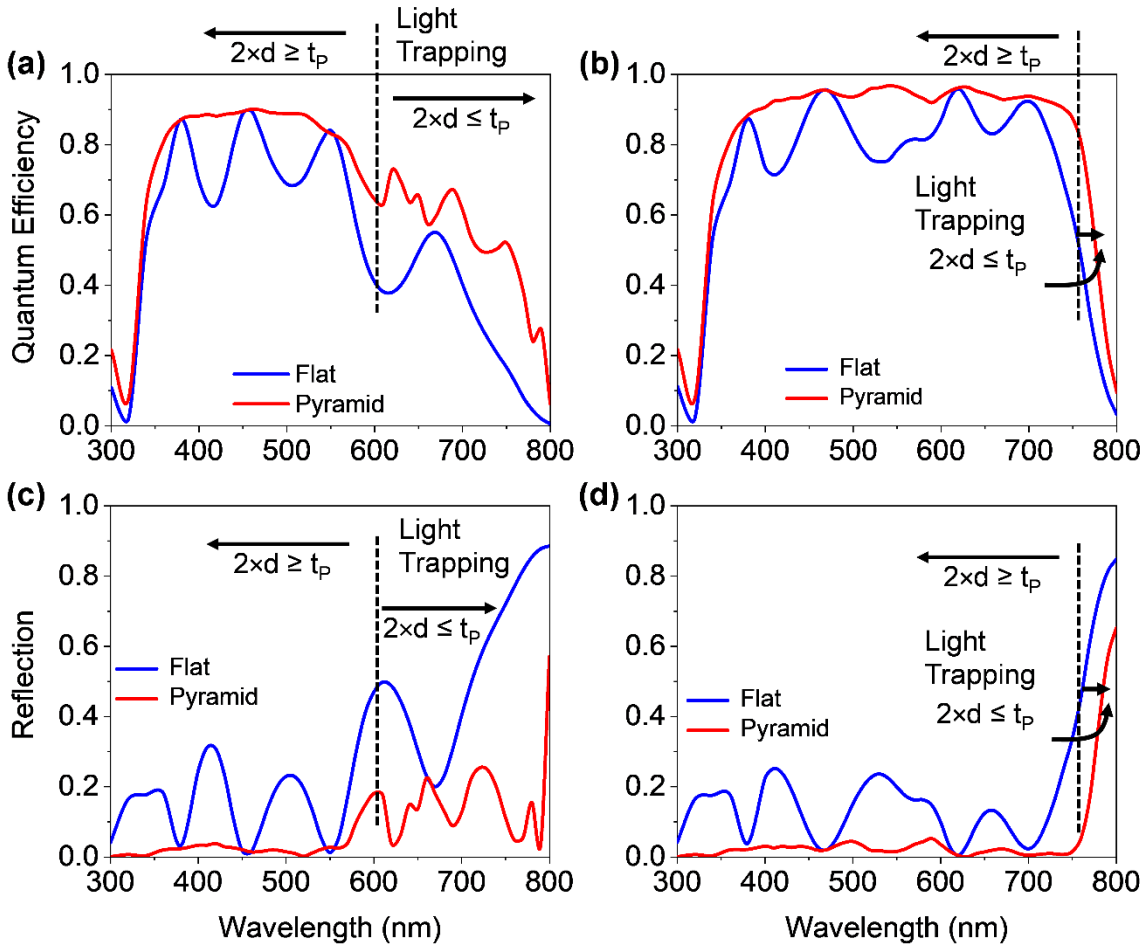

Figure 4.4: Simulated quantum efficiency of flat and pyramidal textured perovskite solar cell with a period and height of 600 nm and 600 nm for a perovskite absorber layer thickness of (a) 100 nm and (b) 400 nm. Reflection of flat and pyramidal textured perovskite solar cell for a perovskite absorber layer thickness of (c) 100 nm and (d) 400 nm. (d and t_p are denoted as the perovskite absorber layer thickness and the penetration depth of perovskite material).

As previously mentioned, the refractive index of the metal oxide contact layers and the perovskite layer is comparable.

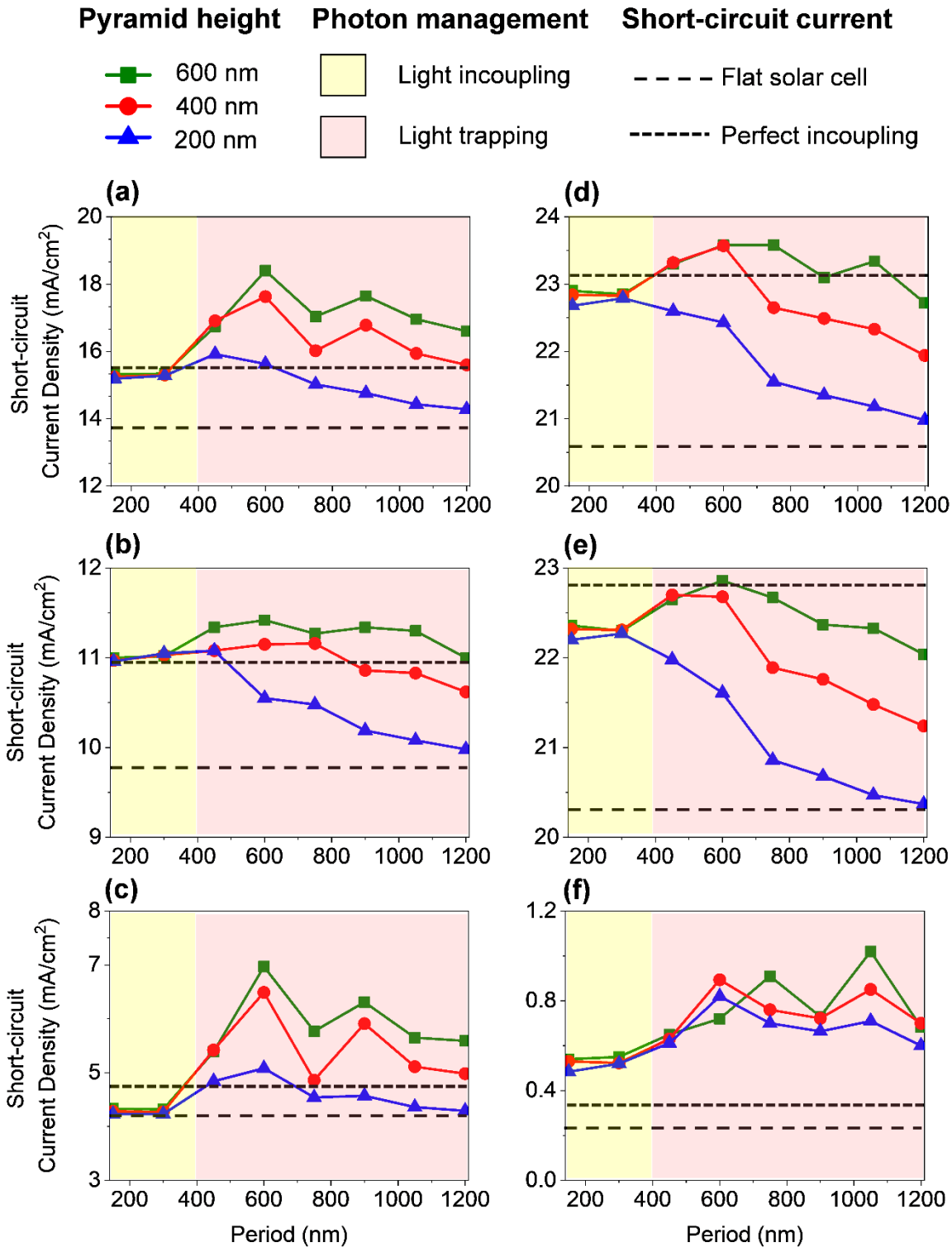

Figure 4.5: Short-circuit current density for perovskite solar cells with absorber thickness of (a,b,c) 100 nm and (d,e,f) 400 nm as a function of the period of the front

pyramidal surface texture. (a,d) Total short circuit current density and (b,e) short circuit current density up to the wavelength where the penetration depth is equal to twice the absorber thickness. (b) For the 100 nm thick perovskite solar cell the short circuit current is calculated from 300 nm to 610 nm, (e) while for the 400 nm thick perovskite solar cell the short circuit current is calculated from 300 nm to 770 nm. (c,f) Short circuit current density for wavelengths where the penetration depth is larger than twice the absorber thickness. (c) For the 100 nm thick perovskite solar cell the short circuit current is calculated from 610 nm to 800 nm, while for the 400 nm thick perovskite solar cell the short circuit current is calculated from 770 nm to 800 nm.

Hence, a rough interface will have only a minimal effect on the optics. It can be expected that the impact of the roughness on the electronic properties is distinctly larger. Only for the planar reference solar cell shown in Figure 4.1(a) the interference fringes will be reduced, while the short circuit current is not affected. In the case of the solar cell structure in Figure 4.1(b), most light propagation is incoherent, so that the QE and the J_{SC} are not affected. In the following, the influence of the dimension of the pyramidal surface texture on J_{SC} is studied. Again, the thickness of the perovskite layer was set to 100 nm and 400 nm. Figure 4.5(a-c) exhibits the J_{SC} for an absorber layer thickness of 100 nm, while the J_{SC} plots for a thickness of 400 nm are shown in Figure 4.5(d-f). Three different pyramid texture heights (200 nm, 400 nm, and 600 nm) are considered for the investigations, while for each height, the period of the pyramid is varied from 150 nm to 1200 nm. Figure 4.5(a,d) exhibits the total J_{SC} of the 100 nm and 400 nm thick solar cells as a function of the period of the surface texture. Short and long dashed lines are added to the graphs. The long-dashed line corresponds to the J_{SC} of a flat solar cell, as shown in Figure 4.1(a). The short-dashed line exhibits the J_{SC} of a flat solar cell, assuming perfect incoupling of the light in the solar cell. Figure 4.5(a,d) shows that the J_{SC} of the textured solar cell is always larger than the J_{SC} of the flat solar cell irrespective of the selected height and period. For small periods of the pyramid texture, $n_{ZnO} \times p_{ZnO} << \lambda$, the pyramidal texture acts like a refractive index gradient, which allows for efficient light incoupling in the solar cell. With increasing

period, the incident light is diffracted, so that a further increase of the J_{SC} is observed. The J_{SC} increases with increasing height of the pyramid. In other words, the opening angle of the pyramid, which is given by $2\times\tan(p/2/h)$, decreases with increasing height of the pyramid. For large opening angles, which are reached for small pyramid heights and larger periods, the incident light is diffracted in small angles. Consequently, the J_{SC} drops below the J_{SC} of a solar cell exhibiting perfect incoupling of light and converges towards the J_{SC} of a flat solar cell. The highest J_{SC} is achieved for a period of the pyramid texture of approximately 500 nm. In the case of the thin perovskite solar cell (100 nm absorber), the J_{SC} is increased from 13.8 to ~18.5 mA/cm^2. The J_{SC} of the thick solar cell (400 nm) is increased from 20.6 to ~23.6 mA/cm^2. This corresponds to a relative J_{SC} gain of 34% (100 nm) and 14.5% (400 nm). The J_{SC} gain is defined as $(I_{SC\_tex}-I_{SC\_flat})/I_{SC\_flat}$, where I_{SC_tex} and I_{SC_flat} are the J_{SC} of the textured and the reference planar (flat) solar cell. For the thin solar cell, a distinct gain of the J_{SC} is achieved due to the increased absorption caused by diffraction, while for the thick solar cell, the absorption is only slightly increased. For this structure, the diffraction of the light has only a small effect on the total J_{SC}. In order to separate the impact of light incoupling from light trapping, the J_{SC} is divided. Figure 4.5(b,e) exhibits the J_{SC} up to the wavelengths where $t_p=2\times d$, which is 580 nm and 770 nm. Up to this wavelength, the gain in the J_{SC} is caused by an improved light incoupling. For longer wavelengths, diffraction has an additional effect on the J_{SC}. The J_{SC} plots for longer wavelengths are shown in Figure 4.5(c, f). For the thin solar cell (Figure 4.5(c)), a large absolute gain of the J_{SC} is observed, while the relative gain of the J_{SC} is small. The absolute J_{SC} is increased by approx. 3 mA/cm^2 for an optimal period. However, the relative gain of the J_{SC} is smaller than 100%. For the thick solar cell, diffraction has only a small effect on the absolute J_{SC}. Hence, the total J_{SC} gain is small, while the relative J_{SC} gain is large. The absolute J_{SC} is increased by approx. 0.8 mA/cm^2 for an optimal period. However, the relative gain of the J_{SC} is approx. 400%.

The influence of the period of the surface texture on the power density map is shown in Figure 4.6. The power density profiles of 100 nm and 400 nm thick perovskite solar cells are shown in Figure 4.6 for an incident wavelength of 700 nm.

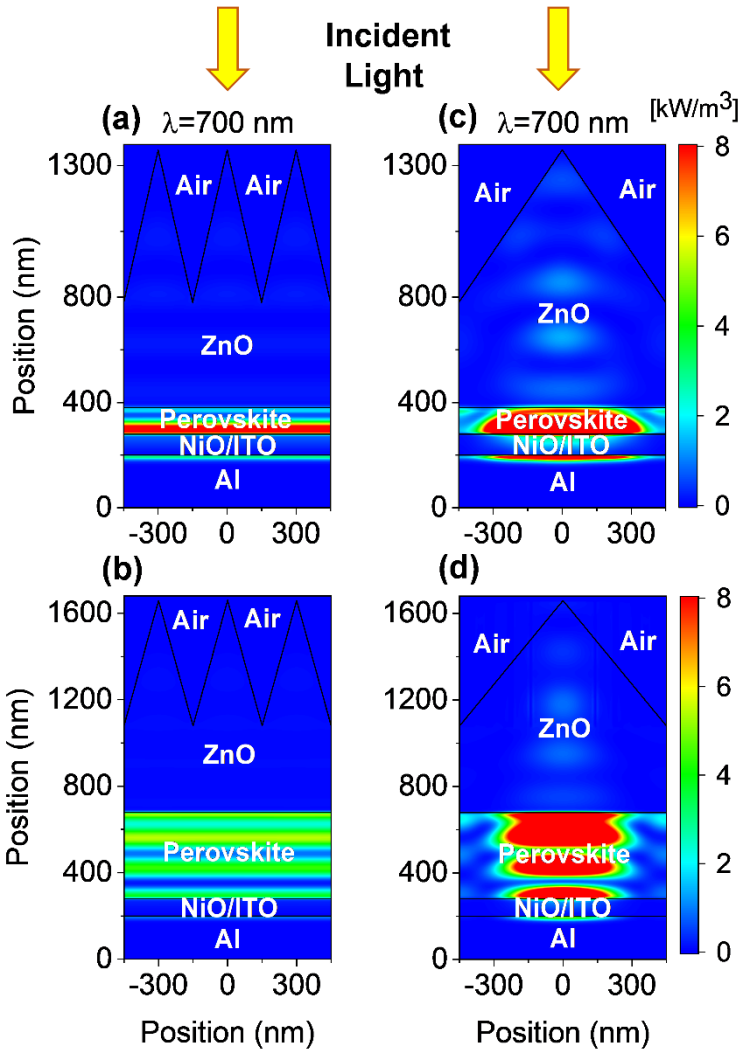

Figure 4.6: Simulated power density profiles of perovskite solar cell with perovskite absorber layer thickness of (a,c) 100 nm and (b,d) 400 nm for a small and large period of (a,c) 300 nm and (b,d) 900 nm and fixed pyramid height of 600 nm, using an incident wavelength of 700 nm.

Surface textures with a period of $n_{ZnO} \times p_{ZnO} << \lambda$, allow for an efficient light incoupling in the solar cells, while for larger periods light trapping is observed. The optical simulations are carried out for periods of 300 nm and 900 nm, while the height is kept

constant at 600 nm. For the case of the 300 nm period, a standing wave is formed in the solar cell, as depicted in Figure 4.6(a) and Figure 4.6(b). The standing wave indicates that the pyramids act as a refractive index grating; however, the light is not diffracted by the pyramids. Whereas, the incident light is diffracted by the pyramid for surface textures with a period of 900 nm.

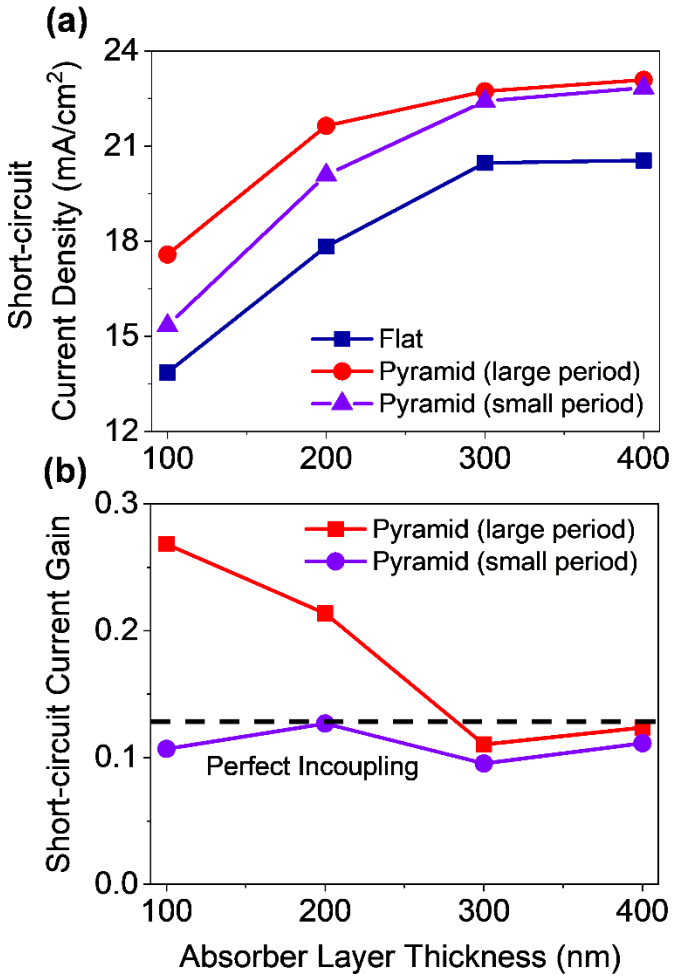

Figure 4.7: (a) A comparison of short-circuit current density among perovskite solar cells with a smooth surface, large period (900 nm), and a small period (300 nm). (b) A comparison of relative short-circuit current density gain between perovskite solar cell with large period (900 nm) and small period (300 nm).

Consequently, a distinctly higher power density is observed for PSCs with large surface texture irrespective of perovskite absorber layer thickness. This is confirmed by the power density profile shown in Figure 4.6(c) and Figure 4.6(d). The J_{SC} as a

function of the solar cell thickness is shown in Figure 4.7(a) for a small (300 nm) and large (900 nm) period. Again, the solar cell on a smooth surface is used as a reference cell here. Furthermore, the J_{SC} gain is plotted in Figure 4.7(b). For thick perovskite absorber layers, both solar cells with small and large surface texture reach equal J_{SC}s. A relative J_{SC} gain of 12.5% is observed. This gain is mainly caused by the improved light incoupling. Very good incoupling is observed for the small and large surface texture. For thin solar cells, the additional diffraction of the incident light leads to an additional gain of the J_{SC}. For the investigated solar cells, a J_{SC} gain of up to 25% is observed. The calculated J_{SC} for the solar cell with the 400 nm thick absorber reaches 90% of the upper theoretical J_{SC} limit of 25.6 mA/cm^2. The almost perfect incoupling can be achieved by using a surface texture, where $n_{ZnO} \times p_{ZnO} << \lambda$. In this case, the height of the pyramid texture must be $h_{ZnO} \geq \lambda/2/n_{ZnO}$. Even for the larger periods, an almost perfect light incoupling can be achieved. The opening angle of the pyramid should be 50° or smaller to achieve an effective light incoupling. ZnO pyramids with such small opening angles can only be fabricated by growing thick ZnO films with large pyramids. Hence good incoupling can experimentally only be achieved by growing large pyramids and thick ZnO films.

4.1.3 Conductivity versus Optical Losses

The absorption loss of the contact layer should be as low as possible, while the conductivity of the contact layers should be as high as possible. However, these two aims contradict each other. By minimizing the lateral resistivity of the contact layers the series resistance is reduced, and the fill factor is maximized. If the doping concentration of the metal oxide layer is low, the series resistance is increased, and the fill factor is lowered so that finally, the ECE is negatively affected. On the other hand, the free carrier absorption of the contacts layer is low if the doping concentration

of the metal oxide film is low. Hence a low doping concentration allows for a high J_{SC}. Most perovskite solar cells are prepared in superstrate configuration on thin but highly doped ITO (Indium tin oxide) front contacts. The transmittance (T), absorbance (A), and reflectance (R) of a typical planar metal oxide layer (zinc oxide) are shown in Figure 4.8. An extended Drude Lorentz model was used to describe the complex refractive index of the metal oxide film.(Drude, 1900b, 1900a) The model used to calculate the optical constants is provided in Appendix B (subsection B.1.4). The spectra can be divided into four regions. a.) the direct band-to-band absorption region for short wavelengths, b.) The transparent region covering the visible and near-infrared part of the optical spectrum and c.) the free carrier absorption region. The free carrier region can be described by the plasma wavelength λ_p and finally, d.) the reflection state.

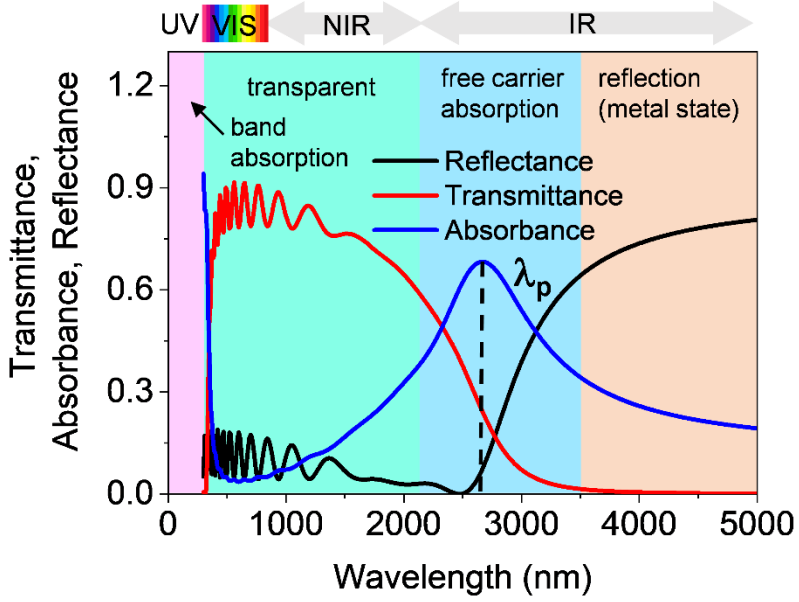

Figure 4.8: The transmittance (T), absorbance (A), and reflectance (R) of a planar zinc oxide film.

The relationship between the doping concentration and the plasma wavelength can be described by

$$\lambda_p = \frac{2\pi \times c}{q}\sqrt{\frac{\varepsilon_0 \varepsilon_\infty m^*}{N_{Opt}}} \quad (4.1)$$

where, c is the speed of light in space, m^* is the effective mass of the electron, ε_0 and ε_∞ are the vacuum and relative permittivity of the metal oxide film, respectively with increasing doping concentration, the plasma wavelength shifts to shorter wavelengths. In the case of a single-junction PSC, a thin and highly doped metal oxide film can be selected. The absorption loss due to free carrier absorption is usually low. For a multi-junction solar cell, like a perovskite/silicon tandem solar cell, the situation is different. The free carrier absorption might have a negative effect on the QE for long wavelengths. The calculated complex refractive indices were compared to experimentally determined optical constants, and a valid agreement was observed. The ZnO layer has a thickness of 400 nm, while the thickness of the ITO layer is only 70 nm. The parameters used for calculating the complex refractive index are provided in Appendix B, in Table B1.

4.1.4 Towards Optimal Front Contacts of Perovskite Solar Cells

The front contacts of PSCs in substrate configuration must fulfill several requirements, as already pointed out in the introduction. Firstly, the front and back contact, together with the perovskite absorber forms the junction of the solar cell. Hence, the work function of the materials must be selected accordingly. Secondly, the front contact must provide high lateral conductivity, so that charges can be transported without significant ohmic losses. Thirdly, light must be efficiently coupled in the solar cells, and fourthly, the absorption loss of the contact layer should be as low as possible. It is difficult for one layer to fulfill all these requirements. Hence, we propose a multi-layer system consisting of three layers. The layers and the function of the individual layers will be described in the following.

I.) High work function and protection layer

The first layer must be directly prepared on the perovskite layer. The work function of the material should be matched to the band structure of the perovskite film to allow for a high V_{OC}. The layer can be thin but should prevent the damage of the underlying perovskite layer due to the subsequent deposition of layers II and III. The layer might be formed by ZnO or other materials. The optical losses of this layer should be low as the layer should be very thin.

II.) Lateral charge transport layer with low optical losses

The layer should provide high lateral conductivity so that charges can be transported to the external terminals or printed front contact grid of the solar cell. At the same time, the optical loss of the layer should be low. For wide bandgap material single-junction solar cells, this can be achieved by thin and highly doped metal oxide films, like the commonly used ITO. For low bandgap materials and multi-junction solar cells, the doping concentration must be lower to prevent absorption losses due to free carrier absorption. Subsequently, metal oxides with high charge carrier mobility like hydrogen doped indium oxide (IOH) or thick metal oxide films could be used.(Barraud et al., 2013a; Takashi Koida, Fujiwara, & Kondo, 2007b; Sai, Matsui, Matsubara, Kondo, & Yoshida, 2014; Tamang, Sai, Jovanov, Matsubara, & Knipp, 2018) It can be expected that the optical loss of the complete front contact layer system is determined by this layer.

III.) Incoupling and/or light trapping layer

The layer allows for efficient coupling of the light in the solar cell. Depending on the needs, the layer might also diffract the light to increase the optical path length. Again, such structures can be realized by using metal oxides. For example, self-texturing ZnO films prepared by MOCVD can be used. In

the case of PSCs, the film does not have to be doped.

If the perovskite is directly deposited on a textured silicon wafer as part of a perovskite/silicon TSC, layer I and II are required, but the layer III is not required anymore.

4.1.5 Experimental Section

4.1.5.1 ZnO Preparation

The ZnO thin films are deposited on Corning 7059 glass substrates using Diethylzinc ($C_4H_{10}Zn$) as a precursor and a mixture of heavy (D_2O) and "light" water (H_2O) as oxidants. Diborane (B_2H_6) (1% H_2 diluted) was used as a dopant gas. The films were grown at substrate temperature and pressure of 160 °C of 3 Torr, respectively. The surface morphology of the ZnO films can be controlled by the D_2O/H_2O ratio. The D_2O/H_2O ratio was varied from 0 to 1. The thickness of the zinc oxide films was kept constant at about 1.6 μm.

4.1.5.2 Optical Simulation Method

Optical wave propagation is investigated by three-dimensional (3D) finite-difference time-domain (FDTD) simulations. The simulations are carried out for an incident wave with an amplitude of 1 V/m and a spectral range from 300 nm to 800 nm. Details are provided in Chapter 2 (Section 2.3).

4.2 Non-resonant ZnO Metasurfaces as a Front Contact

Metasurfaces have gained considerable attention in recent years. So far, most of the work has focused on implementing passive optical components like lenses and polarizers.(Arbabi et al., 2018; H.-T. Chen, Taylor, & Yu, 2016; Genevet, Capasso, Aieta, Khorasaninejad, & Devlin, 2017; Tiguntseva et al., 2017; Y. Zhao, Belkin, & Alù, 2012) However, the optical bandwidth of the implemented structures is limited. Several optoelectronic applications like image sensors, infrared cameras, and SCs require broadband properties, which cannot be provided by most resonant optical metasurfaces. Hence, we focus in this study on non-resonant metasurfaces. By utilizing the pyramid texture on top of the PSC, light incoupling and/or light trapping can be increased, where the pyramid texture is formed by the CVD self-texturing process. The CVD process mostly requires elevated temperatures that may damage the underlying perovskite layer. Hence, as an alternative, we have developed a new process using electrodeposited ZnO metasurfaces. This study aims to develop a non-resonant metasurface with properties equal to pyramidal surface texture, which allows for efficient broadband light incoupling and can be used as a potential light-trapping structure in PSCs. And, the metasurfaces can be prepared at low temperatures. The zinc oxide nanowire-based building blocks of the metasurface can be prepared by a templated electrodeposition through a mask of resist. The phase of the incident light can be controlled by the edge length of the subwavelength large zinc oxide nanowires. An array of zinc oxide nanowires was prepared and characterized in the current study. 3D optical simulations were used to compare solar cells covered with non-resonant metasurfaces with commonly used light trapping structures. Detailed guidelines for the realization of non-resonant metal oxide metasurfaces are provided in the following.

4.2.1 Device Design

The proposed device structures consist of PSCs with integrated non-resonant

metasurfaces. The optics of the device with integrated metasurfaces will be compared to a reference structure using a pyramidal surface texture. Furthermore, the device is compared to a planar reference solar cell. Cross-sections of single-junction devices are shown in Figure 4.9. We focus in this study on device structures in substrate configuration, opposite to solar cells on glass substrates, commonly referred to as solar cells in superstrate configuration.

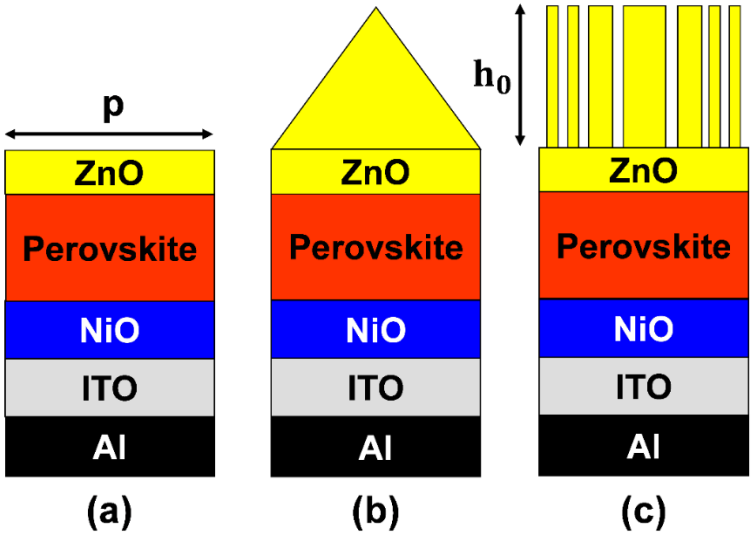

Figure 4.9: The schematic diagrams of (a) planar, (b) front pyramidal textured, and (c) front metasurface structured perovskite solar cells.

The contact layers and the perovskite absorber layer exhibit comparable refractive indices, so that interfaces between the perovskite and the contact layer do not have to be textured. Consequently, the electrical properties of the solar cells should be comparable to planar PSCs. Hence, it can be assumed that the modified optical design does not affect the electrical properties of the solar cells. NiO and ZnO layers were used as hole transporting / electron blocking layer (HTL) and electron transporting / hole blocking layer (ETL). It is difficult to realize NiO films with high transmission and high conductivity, which is why a 5 nm NiO layer was combined with a 75 nm thick ITO HTL with high transmission and low lateral resistivity. It is assumed that the NiO/ITO layer forms a tunnel junction. We used the double layer to be consistent with several

experimental studies on PSCs in the superstrate configuration.(Rakstys et al., 2017; W.-J. Yin, Shi, & Yan, 2014b) An aluminum layer was used as back contact and back reflector. A 400 nm thick metal-doped ZnO transparent conductive oxide was used as an ETL. Furthermore, the layer provides lateral charge transport. A thick but lightly doped ZnO was selected as a front contact and not a thin but highly doped metal oxide layer. By using a thick but lightly doped zinc oxide layer, the parasitic absorption of the front contact can be reduced, which is caused by free carrier absorption for long wavelengths. The free carrier absorption plays a primary role in a single-junction solar cell with narrowband absorbers or TSCs. The ZnO layer can be formed by electrodeposition or low temperature sputtering. The pyramidal surface texture and the nanowire array were added to the top of the continuous ZnO layer, as shown in Figure 4.9(b) and 4.9(c). The planar reference solar cell is shown in Figure 4.9(a). The perovskite active layer thickness varied from 100 nm to 400 nm for the investigation.

4.2.2 Results and Discussion

4.2.2.1 Metasurfaces for Light Trapping

The aim is to realize non-resonant metasurfaces, which imposes a phase change equal to the phase change introduced by pyramidal surface texture. The metasurface consists of ZnO nanowires with a square-shaped base, where the edge length of the ZnO nanowires is distinctly smaller than the incident wavelengths. In general, the phase change imposed on an optical wave by a layer is described by $\phi(x,y)=n(x,y)\times h(x,y)$, where, n(x,y) and h(x,y) are the refractive index and height of the layer as a function of the position x and y. Figure 4.10(a) exhibits the height profile of the pyramid with a square-shaped base, where p and h_0 are the period and height of the tip of the pyramid. The height profile of the pyramid can be represented by

$$h_{ZnO}(x,y) = \begin{cases} h_0 \times \left(1 - \dfrac{|x|}{p/2}\right) & \text{for } -\dfrac{p}{2} \le x \le \dfrac{p}{2} \text{ and } |x| \ge |y| \\ h_0 \times \left(1 - \dfrac{|y|}{p/2}\right) & \text{for } -\dfrac{p}{2} \le y \le \dfrac{p}{2} \text{ and } |y| \ge |x| \end{cases} \quad (4.2)$$

Hence, the phase change of the pyramid can be determined by $\phi_p(x,y,\lambda)=n_{ZnO}(\lambda)\times h_{ZnO}(x,y) + n_{air}\times[h_0-h_{ZnO}(x,y)]$, where, λ is the incident wavelength and $n_{ZnO}(\lambda)$ and n_{air} are the refractive index of the ZnO front contact and the surrounding air. $h_{ZnO}(x,y)$ is the height of the ZnO front contact as a function of the position on the surface. The phase change of the pyramid texture must be equal to the phase change of the metasurface $\phi_M(x,y,\lambda)$.

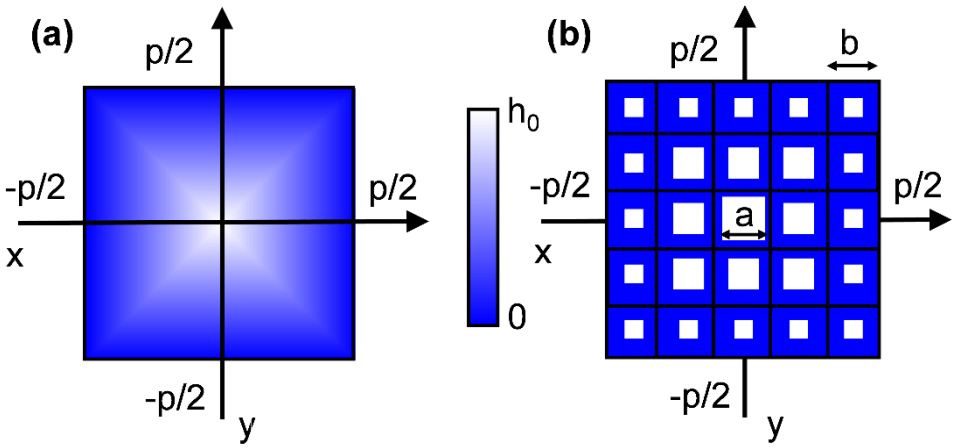

Figure 4.10: Height profile of (a) pyramid surface texture and (b) non-resonant nanowire array.

The phase change of the nanowire array can be described by effective medium theory, so that $\phi_M(x,y,\lambda)=n_{eff}(x,y,\lambda)\times h_0$. The height profile of the nanowire array is shown in Figure 4.10(b). It is assumed that the pyramid and the nanowire arrays are realized by ZnO. The size of the unit cell is p, while h_0 is the height of all nanowires. b and a are the block size and the edge length of the nanowires, which is distinctly smaller than the incident wavelength λ. Hence the following expression of the effective refractive index of the metasurface can be described by

$$n_{eff}(x,y) = \begin{cases} n_{ZnO} - (n_{ZnO} - n_{air}) \times \dfrac{|x|}{p/2} \text{ for } -\dfrac{p}{2} \le x \le \dfrac{p}{2} \text{ and } |x| \ge |y| \\ n_{ZnO} - (n_{ZnO} - n_{air}) \times \dfrac{|y|}{p/2} \text{ for } -\dfrac{p}{2} \le x \le \dfrac{p}{2} \text{ and } |y| \ge |x| \end{cases} \quad (4.3)$$

For the current structure, the effective refractive index can be approximated by a parallel arrangement of optical elements.(Qarony, Hossain, Dewan, et al., 2018) The effective refractive index for the metasurface can be approximated by $n_{eff}(x,y,\lambda)=n_{ZnO}(\lambda)\times f(x,y)+ n_{air}\times[1-f(x,y)]$, where, f(x,y) is the volume ratio of the material. By combing both expressions, the following expression for the volume ratio can be determined: $f(x,y)=h_{ZnO}(x,y)/h_0$. The array of zinc oxide nanowires is based on pillars with a square-shaped base. Hence, the edge length of the pillar can be determined by

$$a(x,y) = b \times \sqrt{\frac{h_{ZnO}^{mean}(x,y)}{h_0}} \quad (4.4)$$

where b is the block size and spacing between pillars, and $h^{mean}(x,y)$ is the mean height of the ZnO profile within a block. The period and height for both structures are considered as 900 nm and 600 nm, respectively. The block size was selected to be $n\times b<<\lambda$, so that the effective medium theory can be applied to describe the phase change of the metasurface. In the current study, the block size was selected to be 90 nm × 90 nm. Hence, the center pillar of the metasurface exhibits the dimensions of 90 nm × 90 nm × 600 nm.

A variety of fabrication methods exist to realize the metasurfaces. We will focus here on templated growth, a method in which a substrate is covered with a patterned mask that acts as a template for the growth of films. Templated growth, in combination with atomic layer deposition (ALD), has been used by several authors to realize optical metasurfaces. We have investigated the combination of templated growth electrodeposition. An array of ZnO nanowire arrays can be prepared by templated electrodeposition of zinc oxide nanowires. Figure 4.11(a) shows the fabrication of a

ZnO nanowire array. An electron beam resist (e.g., PMMA) is patterned on a conductive surface covered with a sputtered gold of sputtered ITO film. The ZnO wires are grown from solution. SEM images of ZnO subwavelength arrays are shown in Figure 4.11(b).

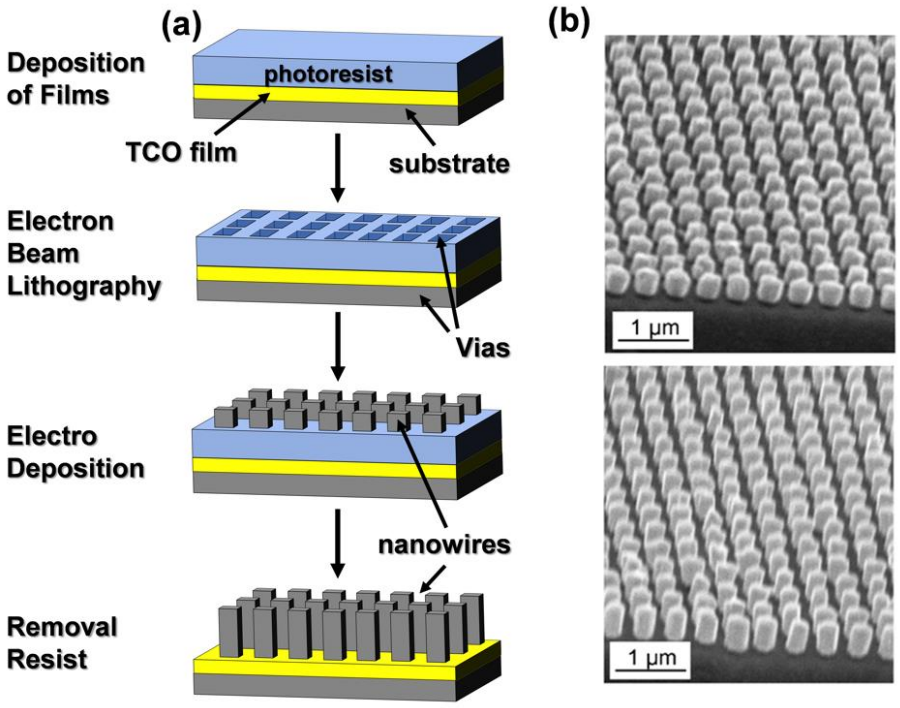

Figure 4.11: (a) Schematic illustration of the fabrication process of zinc oxide nanowires by templated electrodeposition. (b) SEM images of zinc oxide nanowire arrays.(Mohammad I. Hossain et al., 2020)

The height of the nanowires is determined by the thickness of the resist. The fabrication of nanowires with small diameters requires the use of thin e-beam resists, while for long wires, an increased diameter must be accepted. Hence, the dimensions of the ZnO nanowires are determined and limited by the lithographic process. In other words, the height to diameter ratio of the wires is limited by the lithographic process. We have realized periodic nanowires with diameters down to 100 nm and heights of 400-500 nm. The ZnO nanostructures are polycrystalline. Crystalline ZnO tends to grow in a Wurtzite crystal structure. ZnO nanowires grown without a pre-patterned resist coating are characterized by a hexagonal cross-section.(Yumnam & Wagner,

2018) In our study, we opened square-shaped vias in the electron beam resist. The resulting cross-section of the nanowire does not show a clear hexagonal nor a clear square-shaped cross-section, but the cross-section is closer to a hexagonal cross-section. Further details on the electrodeposition of such periodic nanostructures are given in the literature.(Uddin et al., 2017; Yumnam & Wagner, 2018)

To integrate the metasurfaces on PSCs, it will be necessary to use parallel lithography and not a serial lithographic process like electron beam lithography. This requires either a high resolution optical lithographic process or an alternative large-area compatible patterning method. Even without covering a substrate with an electron beam, resist pattern zinc oxide tends to form nanowires by selecting the right deposition conditions. The growth of ZnO nanowires has been demonstrated by a variety of deposition methods including electro deposition.(Jingbiao Cui, 2012; Greene, Yuhas, Law, Zitoun, & Yang, 2006; Z. L. Wang, 2004) By varying the density of the nanowires on the substrate, the refractive index can be controlled as a function of the position on the substrate, and non-resonant metasurfaces can be realized. For example, we have investigated the use of self-assembled monolayers to control the density of nanowires on the substrate. The self-assembled monolayer acts like a resist, and the ZnO nanowires grow only in the regions not covered by the self-assembled monolayers. In the first set of experiments, the coverage of the substrate by a self-assembled monolayer was controlled by the exposure time of the substrate to a solution containing self-assembled molecules. The density of nanowires on the substrate can be controlled from sparse to dense. In the second set of experiments, the self-assembled monolayer was printed on the substrate by microcontact printing to create regions covered by self-assembled molecules. Afterward, ZnO nanowires were grown by electrodeposition. By controlling the coverage of the self-assembled molecules on the substrate, the density of nanowires on the substrate can be

controlled, and the refractive index can be controlled as a function of the position on the substrate. Further information on the use of self-assembled monolayers as a template, and the growth of ZnO nanowire on conductive substrates by electrodeposition is provided in the literature.(Pérez-Tomás, Mingorance, Tanenbaum, & Lira-Cantú, 2018) The underlying ETL layer of the PSC can be prepared by sputtering. The sputtering process can be carried out at low temperatures, and the doping concentration of the ETL can be controlled over a wide range. The ZnO nanowires have only the function to couple the light in the SC. Hence, the nanowires do not have to be doped, and the ZnO nanowires can be grown by electrodeposition.

4.2.2.2 Single-junction Perovskite Solar Cells with Non-resonant Metasurface

The optics of the single-junction PSCs with flat, pyramid texture, and non-resonant metasurfaces metal-oxide front contacts were investigated by 3D FDTD optical simulations. In the first step, the flat and pyramid textured PSCs were compared for different perovskite layer thicknesses. In contrast, the height and period of the pyramid texture were 600 nm and 900 nm, respectively. A comparison of the calculated quantum efficiency (QE) between flat and pyramid textured solar cells is shown in Figure 4.12 for a perovskite absorber thickness of 100 nm. The thickness of the continuous ZnO front contact layer is 400 nm. The QE of the planar solar cell exhibits interference fringes caused by the ZnO layer. Changing the thickness of the ZnO leads to a shift of the interference fringes. However, the J_{SC} is not sensitive to thickness variations. Only for thin ZnO front contacts with typical thicknesses of 50 nm to 80 nm, a distinct change of the J_{SC} is observed. In this case, the front contact acts as an ARC. The interference fringes almost disappear by covering the thick ZnO front contact with pyramid textures. The QE is distinctly increased throughout the whole wavelength spectrum (300 nm - 800 nm) in comparison to the flat solar cell. For short wavelengths ranging from 350 nm to 600 nm, the enhanced QE is observed due to improved light

incoupling. The diffraction of the incident light does not affect the absorption of the solar cell, because the penetration depth is smaller or approximately equal to two times the thickness of the absorber. The penetration depth ($t_p=1/\alpha_p(\lambda)$) is defined as a thickness at which the incident light intensity drops to 1/e. For long wavelengths, the penetration depth is larger than two times the thickness of the absorber layer. For instance, for a wavelength of approximately 600 nm, the penetration depth is equal to two times the thickness of the perovskite layer.

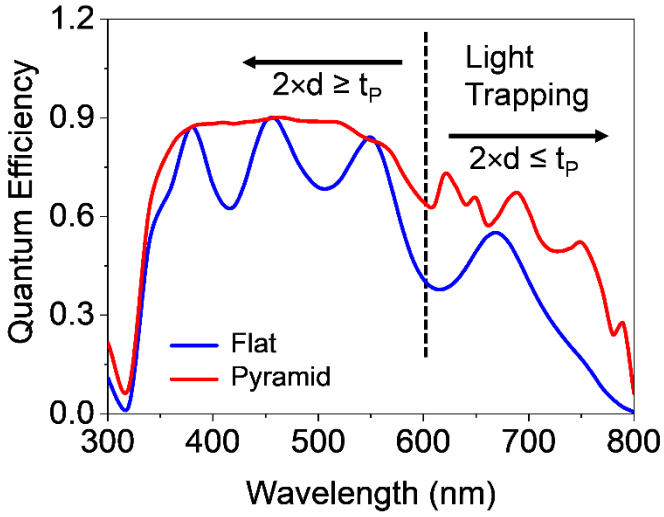

Figure 4.12: Calculated quantum efficiency of flat and pyramidal textured perovskite solar cells. The perovskite absorber layer thickness is 100 nm.

The incident light is diffracted, and a distinct gain of the absorption is obtained. The improved QE leads to an increase of J_{SC} from 13.7 mA/cm^2 to 17.6 mA/cm^2. Furthermore, optical simulations were carried out for different absorber layer thicknesses, periods, and heights of the pyramid texture. The J_{SC} is maximized for an optimal pyramidal surface texture period of 600 nm – 1000 nm. Furthermore, the short-circuit current gain increases with increasing the height of the pyramid. The optimal dimensions of the pyramidal surface texture were used as input parameters in designing the dimensions of the metasurfaces. The height and period of the pyramid were selected to be 600 nm and 900 nm. In the following, the optics of PSCs with

integrated metasurface are compared with pyramidal textured SCs.

The time-averaged power density profiles of PSCs with pyramidal texture and metasurface texture, along with the cross-sections of the devices, are shown in Figures 4.13(a-h). The thickness of the perovskite layer was selected to be 300 nm. Power density maps are shown for monochromatic illumination of 300 nm, 500 nm, and 750 nm.

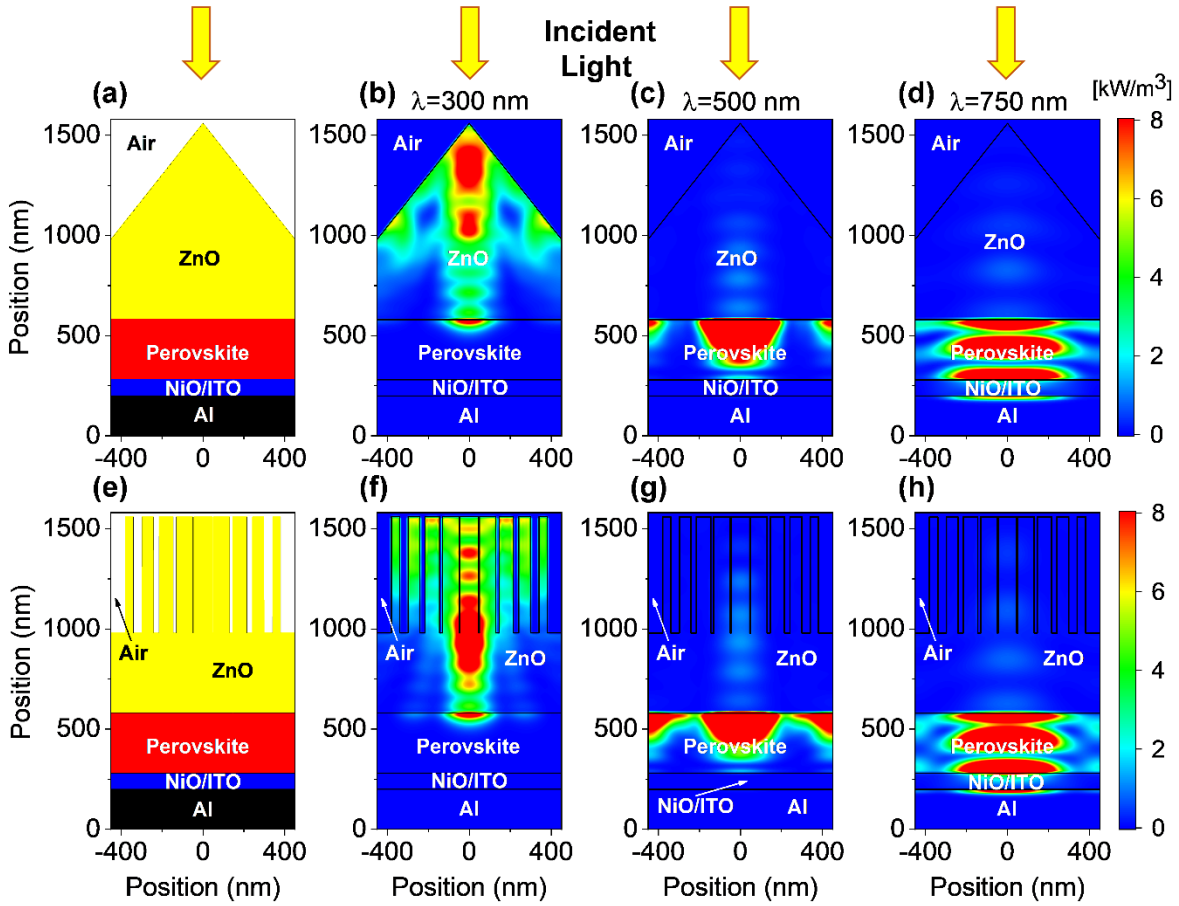

Figure 4.13: (a) Schematic cross-section of perovskite solar cell with pyramid textured front contact and corresponding power loss profiles for an incident wavelength of (b) 300 nm, (c) 500 nm, and (d) 750 nm. (e) Schematic cross-section of perovskite solar cell with metasurface structured front contact and corresponding power loss profiles for an incident wavelength of (f) 300 nm, (g) 500 nm, and (h) 750 nm. The period and height of the structures are 900 nm and 600 nm, respectively.

Both solar cell structures exhibit similar power density maps for all three wavelengths.

For short wavelengths of 300 nm, a significant amount of incident light is absorbed by the ZnO layer, and only a small fraction of light is absorbed by the perovskite layers, as shown in Figures 4.13(b,f). For 300 nm, the photon energy is larger than the bandgap of the ZnO layer with approx. 3.2 eV. For the wavelength of 500 nm, the incident photon is mostly absorbed by the perovskite absorber layer.

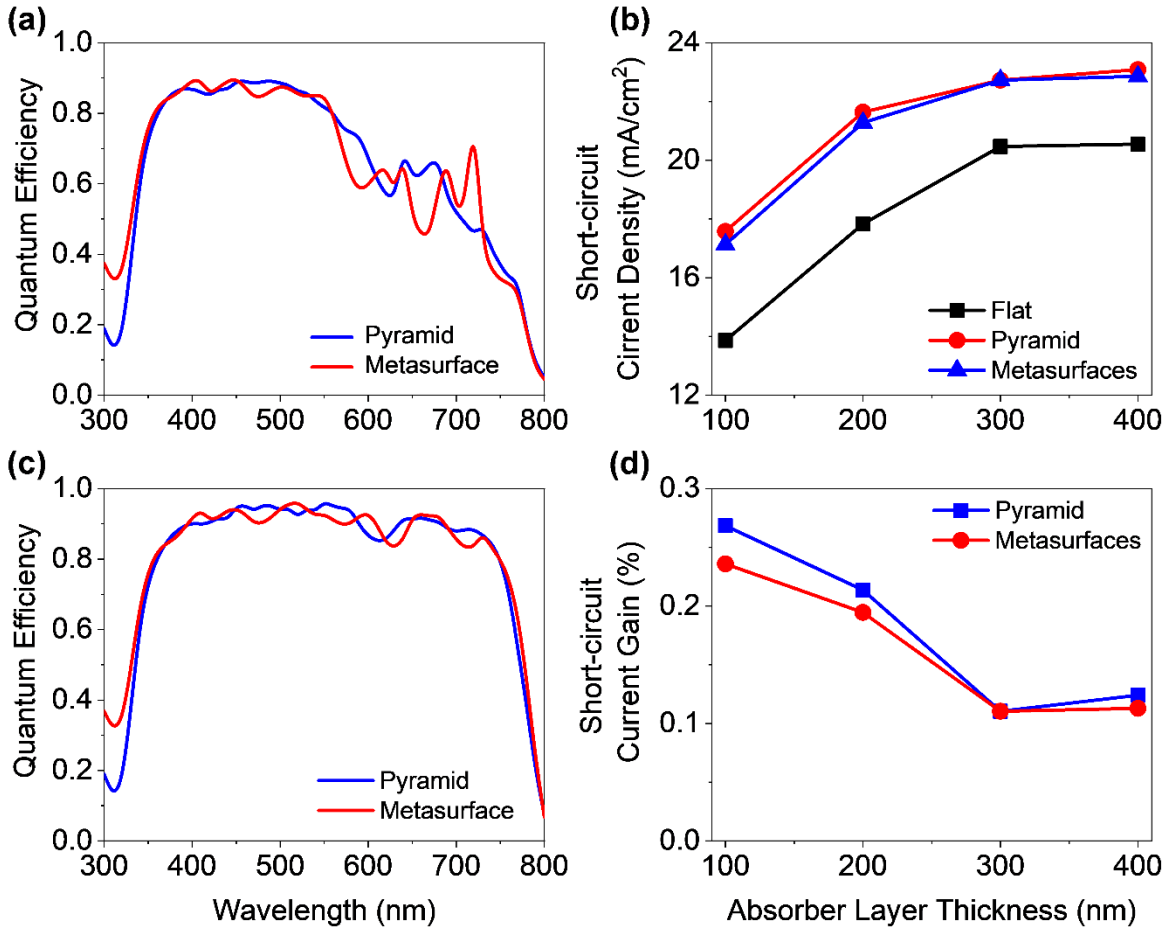

Figure 4.14: (a,b) Quantum efficiency of perovskite solar cell with pyramidal texture and metasurface texture. The perovskite absorber layer has a thickness of (a) 100 nm and (b) 300 nm. (c) Short-circuit current density and (d) short-circuit current gain as a function of the absorber layer thickness.

For 500 nm, the penetration depth of the photon is still smaller than the thickness of the SC so that only a tiny amount of light reaches the back contact, as illustrated in Figures 4.13(c,g). For an incident wavelength of 750 nm, the penetration depth is distinctly increased because the photon energy of the incident light is approaching the

bandgap of the perovskite material ($MAPbI_3$).(Mohammad I. Hossain, Hongsingthong, et al., 2019; Qarony et al., 2015) Hence, the incident light reaches to the back contact, where it is reflected. The incident light is diffracted by the surface textures, resulting in a distinctly higher power density absorbed by the perovskite absorber. This is confirmed by the power density profile shown in Figures 4.13(d,h) and the electric field distribution plots provided in Appendix B (Figure B2.1). A comparison of the simulated QE, J_{SC}, and J_{SC} gain of the perovskite solar cells with pyramidal surface texture and metasurface texture is shown in Figure 4.14. A comparison of the calculated QE for perovskite absorber layer thicknesses of 100 nm and 300 nm is depicted in Figure 4.14(a) and Figure 4.14(b), respectively. The solar cells with pyramidal and metasurface texture exhibit almost equal QEs. Saturation of the J_{SC} is observed for a thickness of 400 nm. A further increase of the absorber thickness leads to minimal gains of the J_{SC}.(Qarony, Hossain, Dewan, et al., 2018) The J_{SC} and J_{SC} gain of the pyramidal and metasurface textured solar cells are shown in Figures 4.14(c) and 4.14(d) for absorber layer thickness ranging from 100 nm to 400 nm. The J_{SC} of PSCs with pyramidal and metasurface texture is distinctly higher than the short circuit current of the flat solar cells irrespective of the thickness of the perovskite layer.

Furthermore, an excellent agreement between the J_{SC} of the pyramidal texture and metasurface textured solar cell is observed. For an absorber thickness of 300 nm, the solar cells reach a J_{SC} of 22.8 mA/cm^2. This corresponds to a J_{SC} gain of 11%. A maximum J_{SC} gain of approx. 25% is obtained for the pyramid and metasurface PSCs for an absorber thickness of 100 nm thick perovskite absorber layer. For thin solar cells, the penetration depth is larger than twice the thickness of the absorber so that the QE and J_{SC} are determined by the diffraction of the incident light. For thicker solar cells, the penetration depth is almost equal to the twice the thickness of the absorber, so that the high QE and J_{SC} is determined by improved light incoupling.

4.2.3 Methods

4.2.3.1 Electrodeposition of Templated Growth Zinc-oxide Nanowires

In the first step, a conductive layer like gold or doped zinc oxide is prepared on the substrate. For example, a doped zinc oxide film can be prepared by sputtering at low temperatures. For templated growth, a non-conductive electron beam resist (e.g., PMMA) was coated on the substrate. Vias with different diameters were opened in the resist layer by standard electron-beam lithography. Subsequently, ZnO was grown electrochemically through the holes. The ZnO nanowires were grown from aqueous $Zn(NO_3)_2$ solution with potassium chloride (KCl) as a supporting electrolyte. A platinum sheet was used as the counter electrode, an Ag/AgCl wire as the reference electrode, and an indium tin oxide (ITO) covered glass slide as the working electrode. The deposition rate of the zinc oxide structures depends on the applied voltage during the electrodeposition, the temperature of the solution, and the concentration of the electrolyte. The zinc oxide nanowires shown in Figure 4.11 were grown at a temperature of 65°C, an applied voltage of - 0.975V, a concentration of 5mM $Zn(NO_3)_2$, and a deposition time of 20 min. Hence the deposition rate is 0.5 nm/s. After the growth of the wires, the resist is stripped by a solvent. Zinc oxide nanowires with diameters down to 100 nm were realized. The preparation process and SEM images of zinc oxide subwavelength arrays are shown in Figure 4.11. The height of the nanowires is determined by the thickness of the resist. The fabrication of nanowires with small diameters requires the use of thin e-beam resists, while for long wires, an increased diameter must be accepted. Hence, we have realized periodic nanowires with diameters down to 100 nm and a height of 400-500 nm.

4.2.3.2 Optical Simulation Method

Optical wave propagation was studied by 3D FDTD simulations. The electromagnetic field distributions and the time-averaged power density distributions are calculated. The optical simulations were carried out using a mesh size of 10 nm. Based on the time-averaged power density distribution, the absorption for each layer of the solar cell is calculated. Details on the calculation of the QE and J_{SC} are given in Chapter 2 (section 2.3).

4.3 Summary

The short-circuit current density and energy conversion efficiency of perovskite solar cells can be increased by utilizing photon management. High short-circuit current density can be achieved by integrating a pyramidal or a metasurface texture on top of a solar cell. In the first part of this study, the optics of single-junction perovskite solar cell front contacts has been studied to improve light incoupling. Metal oxide films were used as front contacts with refractive indices (≅2.2) comparable to the perovskite material system (≅2.5). Hence, the solar cell with contacts can be treated as one unit, and the optics of the solar cell is primarily affected by the optics of the front contact. An optimized front contact of the solar cell consists of a multi-layer of three films with different functions. The first layer with a well-tailored work function is responsible for forming the junction and prevent the damage of the perovskite layer due to subsequent deposition steps. The second layer provides the lateral charge transport to the terminals or a printed metal grid. For wide bandgap material single-junction solar cells, this can be achieved by thin and highly doped metal oxide films. For low bandgap materials and multi-junction solar cells, the doping concentration must be reduced to prevent absorption losses due to free carrier absorption. Subsequently, metal oxides with high charge carrier mobility or thick metal oxide films must be used. The third

layer is responsible for the incoupling and potential diffraction of the incident light. Such function can be implemented by using self-textured zinc oxide films prepared by metal-organic chemical vapor deposition. The surface morphology of the ZnO films can be controlled by the heavy (D_2O) to "light" water (H_2O) ratio during the deposition. Efficient light incoupling is achieved, if the opening angle of the pyramids is smaller than 50°. The size of experimentally realized pyramid textures can be controlled by the growth conditions and the film thickness. Pyramids with small opening angles can be realized by using thick ZnO films and large pyramids. Optical simulations shown that an improved optics of the front contact leads to short-circuit current density gain from 13.8 to ~ 18.5 mA/cm^2 and 20.6 to ~23.6 mA/cm^2 in the case of thin (100 nm absorber) and thick (400 nm absorber) perovskite solar cells, respectively. Hence, the 400 nm thick solar cell reaches 92% of the theoretical short-circuit current density limit of 25.6 mA/cm^2.

In the second part, optics of perovskite solar cells with integrated non-resonant metal oxide metasurfaces has been studied. Non-resonant metasurface nanostructure has been used as a fundamental building block in controlling the phase of the incident light. Such nanostructure non-resonant metasurfaces were realized by preparing periodically arranged zinc oxide nanowire arrays via electrodeposition. The nanowires were prepared by templated growth through a mask of photoresist. Secondly, non-resonant metasurfaces are designed with optical properties comparable to commonly used pyramid textured light trapping structures. Single-junction perovskite solar cells with metasurface and pyramidal surface texture are compared, exhibiting almost identical quantum efficiencies and short-circuit current densities. Compared to the solar cell on the smooth substrate, the single-junction solar cells with metasurface and pyramid textured perovskite solar cells provides a 10-25 % improvement of the short-circuit current density. For perovskite absorber layer thicknesses smaller than 300 nm, a gain of short-circuit current density and energy conversion efficiency of 20-25% is

attained due to the scattering and diffraction of incident light within the solar cell structure. For thicker perovskite absorber layers, the short-circuit current density is increased by 10% due to improved light incoupling. In this study, we have shown an alternative light trapping structure by using non-resonant metal oxide metasurfaces, which will open a new pathway for the implementation of high-efficiency next-generation solar cells.

CHAPTER 5

PEROVSKITE TANDEM SOLAR CELLS: FROM DETAILED BALANCE LIMIT TO PHOTON MANAGEMENT

This chapter discusses the detailed balance theory to achieve photon management in perovskite solar cells (PSCs), which allows realizing enhanced short-circuit current densities (J_{SC}s) and energy conversion efficiencies (ECEs). This chapter aims to optimize the perovskite-based tandem solar cells (TSCs), which can exhibit ECEs exceeding 30%. Furthermore, we describe how optics and nanophotonics can be utilized to optimize not only the J_{SC}s of a solar cell but also all photovoltaic parameters. A detailed optimization process is provided in the following sections.

5.1 From Detailed Balance Theory to Photon Management in Perovskite/Silicon Tandem Solar Cells

High ECEs are essential for the commercialization of solar cells. Hence, most research focuses on the improvement of ECE by utilizing different approaches and novel materials, where multi-junction solar cells are considered as the most promising route to reach high ECE.(Bush et al., 2017b; Leijtens, Bush, Prasanna, & McGehee, 2018; Qarony et al., 2019; Sahli et al., 2018a; Vos, 1980; Werner et al., 2018; D. Zhao et al., 2018) According to the detailed balance limit, the ECE of TSCs can go beyond 40% if optimum bandgap materials are selected for the top and bottom solar cells.(Shockley & Queisser, 1961b; Vos, 1980) The relationship is valid if the bandgap of the bottom diode stays in a range from 0.85 eV to 1.2 eV. Hence, a variety of material combinations can be selected; however, crystalline silicon (c-Si) with a bandgap of 1.15 eV is considered as a well-suited material as the bottom solar cell. A lot of research has been devoted to the development of TSCs using a c-Si bottom solar cell. In this case, the highest ECE can be reached if the bandgap of the top cell is equal to ~1.7 eV.(Shockley & Queisser, 1961b; Vos, 1980) In recent years, the perovskite material system has been investigated as potential material for single-junction PSCs or as material for perovskite/silicon TSCs.(Bush et al., 2017b; Leguy et al., 2015; Sahli

et al., 2018a; Werner et al., 2018; Wolff et al., 2017; W.-J. Yin et al., 2014a) So far, the material exhibits very encouraging results.(Fang et al., 2019; Jeon et al., 2013; M. Liu et al., 2013b; H. Zhang et al., 2017; Zuo et al., 2016, 2019, 2018; Zuo & Ding, 2014) High ECEs have been achieved for single-junction PSCs with open-circuit voltages (V_{OC}s) close to the theoretical limit. Research on perovskite/silicon TSC is still a new research topic. The number of teams working on the realization of record perovskite/silicon TSCs is still small.(Bush et al., 2017b; Sahli et al., 2018a) The realization of perovskite/silicon TSCs with record efficiencies is only possible if the top PSC and the silicon bottom solar cell operate very close to the theoretical limit. To close the gap between theoretical ECE limits and the performance of real solar cells, a thorough investigation of the losses of a solar cell is required. Herein, we study the detailed balance theory and the optics of perovskite/silicon TSCs to obtain the upper limit of ECE. Finally, we propose an optimized device design for a perovskite/silicon TSC to realize ECE over 30% by considering realistic interface morphologies. In the following subsections, more detailed explanations are provided.

5.1.1 Detailed Balance Theory for Tandem Solar Cells

5.1.1.1 Detailed Balance and Charge Transport

The detailed balance limit commonly called the Shockley-Queisser (S-Q) limit, assumes only radiative recombination. However, to provide a more realistic description, additional generation/recombination processes must be considered. To derive the J(V) characteristic of a solar cell the following five processes (already stated in the original work of Shockley and Queisser) must be considered.(Shockley & Queisser, 1961b)

1. Generation of electron-hole pairs by the illumination, G_{Cell}.
2. Radiative recombination, R_R.

3. Non-radiative generation processes or thermal generation, G_0.

4. Non-radiative recombination, R_{NR}.

5. Extraction of electron-hole pairs as current flow, J.

The steady-state J(V) characteristic of the solar cell taking the five process into account can be described by

$$q \times d \times [G_{Cell} + G_0 - R_R(V) - R_{NR}(V)] - J = 0 \quad (5.1)$$

where d is the thickness of the solar cell. The radiative and non-radiative recombination can be described by

$$R_R(V) = R_{R0} \times \exp\left(\frac{qV}{kT_{Cell}}\right) \quad (5.2a)$$

$$R_{NR}(V) = R_{NR0} \times \exp\left(\frac{qV}{kT_{Cell}}\right) \quad (5.2b)$$

where R_{R0} and R_{NR0} are the radiative and non-radiative recombination rates for an applied voltage of zero volts. At full sunlight, the generation G_{Cell} is distinctly larger than the non-radiative generation rate or thermal generation, G_0, so that we will not consider non-radiative generation rate or thermal generation in future calculations. If we further assume that R_{NR} is negligible, we get the following expressing for the open-circuit voltage,

$$V_{OC} = \frac{kT_{Cell}}{q} \times \ln\left(\frac{G_{Cell}}{R_{R0}}\right) \quad (5.3)$$

The expression follows the classical description of the Shockley Queisser limit, which is described in Chapter 2 (subsection 2.4.4). If we consider non-radiative recombination, we receive the following expression for the open-circuit voltage,

$$V_{OC} = \frac{kT_{Cell}}{q} \times \ln\left(\frac{G_{phot}}{R_{R0} + R_{NR}}\right) \quad (5.4)$$

Instead of expressing the V_{OC} in terms of the generation rate, we will describe the V_{OC} in terms of the J_{SC} and the saturation current density, which leads to the following equation,

$$V_{OC} = \frac{kT_{Cell}}{q} \times \ln\left(\frac{J_{SC}}{J_0}\right) = \frac{kT_{Cell}}{q} \times \ln\left(\frac{J_{SC}}{J_O^{rad} + J_O^{non-rad}}\right) \quad (5.5)$$

where the saturation current density is the sum of the radiative recombination saturation current density, J_0^{rad}, and the non-radiative recombination saturation current densities, $J_0^{non\text{-}rad}$, the equation can be rewritten by using the logarithm laws, so that the first term, V_0^{rad}, considers only radiative recombination.

$$V_{OC} = \frac{kT_C}{q} \times \left[\ln\left(\frac{J_{SC}}{J_O^{rad}}\right) + \ln\left(\frac{J_O^{rad}}{J_O^{rad} + J_O^{non-rad}}\right)\right] \quad (5.6)$$

$$= V_{OC}^{rad} + \frac{kT_C}{q} \ln\left(\frac{J_O^{rad}}{J_O^{rad} + J_O^{non-rad}}\right)$$

The first term is equal to the V_{OC} derived in equations 2.38 and 2.45 (Chapter 2). In both cases, only radiative recombination is considered when calculating the V_{OC}. The second term contains all entropic losses that are related to non-radiative recombination and parasitic absorption of photons in the solar cell. The ratio of the radiative recombination saturation current density and the total saturation current density can be expressed as the quantum efficiency (QE) of a pn-junction operating as a light-emitting diode (LED). QE_{LED} is the EQE of the p-n junction operating as an LED.

$$QE_{LED} = \frac{J_O^{rad}}{J_0} = \frac{J_O^{rad}}{J_O^{rad} + J_O^{non-rad}} \quad (5.7)$$

Here, we distinguish the saturation current, J_0^{rad}, that leads to the emission of photons and the saturation current, $J_0^{non\text{-}rad}$, that does not lead to photon emission. The final expression of the open-circuit voltage is given by

$$V_{OC} = V_{OC}^{rad} + \frac{kT_C}{q} \times \ln(QE_{LED}) \tag{5.8}$$

If the non-radiative saturation current density is zero, the external quantum efficiency (EQE) of the LED is equal to one and equation 2.48 is equal the equation 2.38 calculated in the original work of Shockley and Queisser (Chapter 2 (sub-section 2.4.4)). Due to detailed balance, the emission and absorption properties of a solar cell are related. However, the relationship between absorption and emission in a semiconductor is only valid if the quasi-Fermi level splitting is constant over the whole volume of the absorber.(Rau, Paetzold, & Kirchartz, 2014; Wehrspohn, Rau, & Gombert, 2015) The relationship between the QE and absorption of the solar cell with the radiative J_{SC} and non-radiative saturation current density (J_0) is given in equations 5.9 and 5.10.

$$J_{SC} = q\varepsilon_{in} \int_0^{\infty} QE_{cell}(E) \times \phi_{Sun}(E)dE \tag{5.9}$$

$$J_0^{rad} = q\varepsilon_{out} \int_0^{\infty} QE_{cell}(E) \times \phi_{cell}(E)dE \tag{5.10}$$

where ε_{in} and ε_{out} are the etendue describing the incoupling and outcoupling of light. By considering that A(E)+R(E)=1 and $A(E)=QE_{cell}(E)+A_{para}(E)$, where A(E) is the total absorption of the solar cell, R(E) is the total reflection for the solar cell and $A_{para}(E)$ is the parasitic losses an expression for the non-radiative recombination can be derived by

$$J_0^{non-rad} = q\varepsilon_{out} \int_0^{\infty} [A_{Cell}(E) - QE_{cell}(E) - R(E)] \times \phi_{cell}(E)dE \tag{5.11}$$

Equations 5.9 to 5.11 provide some guidelines to maximize the ECE of a real solar cell. By increasing the QE of a solar cell, the J_{SC} and the radiative saturation current density is increased. Furthermore, the QE_{LED} is increased. Hence, the V_{OC} is increased too. Ideally, the QE_{LED} is approaching unity, so that the V_{OC} is converging towards the maximal value. This can be achieved by minimizing the reflection of the solar cell due to improved light incoupling or light trapping or minimizing parasitic losses. Parasitic optical losses or non-radiative losses lead to a drop in the QE_{Cell} and drop of QE_{LED}. Both effects lead to a lowering of the V_{OC}. Hence, such losses should be minimized or avoided. The optics of a solar cell influence all three parameters, J_{SC}, V_{OC}, and FF. By optimizing the optics all three parameters can be increased. On the other hand, non-radiative losses have not only a negative effect on the J_{SC}. The V_{OC} and the FF are negatively affected too.

5.1.1.2 Detailed Balance and Photon Management

The aim of photon management in a solar cell is to increase the QE_{cell} by minimizing reflection and parasitic optical losses. One way to increase QE_{cell} is through light trapping. In this case, the optical path length of light in the solar cell is increased by the design of the solar cell or a specific light-trapping structure, which is integrated into the solar cell. However, the maximal optical path length enhancement is limited to $2n^2$, where n is the refractive index of the absorber material of the solar cell. Hence, the QE of a semiconducting slab is limited to

$$QE_{cell}(E) \cong A_{Cell}(E) = 1 - \exp(-4 \times \alpha(E) \times n^2(E) \times d) \quad (5.12)$$

where $\alpha(E)$ and n(E) are the absorption coefficient and the refractive index, respectively. For short wavelengths, the penetration depth of the photons is typically smaller than twice the thickness of the solar cell. For long wavelengths, the penetration depth might exceed twice the thickness of the solar cell. Hence, light trapping is of

importance for long wavelengths. Equation 5.12 can be developed in a Taylor series. For long wavelength and weak absorbing materials is $1/(4 \times n(E) \times d) >> \alpha(E)$, so that the absorbance for can be approximated by

$$QE_{cell}(E) \cong 4 \times \alpha(E) \times n^2(E) \times d \quad (5.13)$$

The absorption limit derived by Yablonovitch et al. represents a ray optics or geometrical optics limit. The limit is valid for absorber thicknesses much larger than the wavelength of the incident light. The same applies to the dimensions of the light-trapping textures. The size of the surface features must be distinctly more considerable than the incident wavelengths. For thin-film solar cells, these assumptions might not be fulfilled. Yu et al. have shown that higher QEs and J_{SC}s can be achieved by using wave optics .(Yu, Raman, & Fan, 2011; J. Zhu, Yu, Fan, & Cui, 2010) Furthermore, the authors proposed potential solar cells with higher J_{SC}s.(Yu, Raman, & Fan, 2010; Yu et al., 2011; J. Zhu et al., 2010) In general, a variety of optical concepts can be applied to increase the QE of solar cells and/or reduce material consumption in the solar cell fabrication process. The concepts can be divided into three optical domains distinguished by the size of the surface features or surface textures. Features distinctly smaller than the optical wavelength can be used to minimize the reflection at an interface. The optics can be described by effective medium theory. Most of the used structures act as broadband anti-reflection coatings to improve the incoupling of light in the solar cell. If the feature size is comparable to the wavelengths of the incident light, diffraction might be used to increase the optical path lengths of light in the solar cell. This concept is often applied to silicon thin-film solar cells. Silicon, being an indirect semiconductor with a low absorption coefficient close to the bandgap, requires the use of light trapping to reach J_{SC} close to the theoretical limits.

Table 5.1: Optical wave propagation and photon management mechanisms in solar cells.

Feature size	period << wavelength	period ≅ wavelength	period >> wavelength
Physical effect	Formation of a refractive index gradient	Diffraction of light	Refraction of light
Description of optical wave propagation	Effective medium theory	Diffraction theory or numerical simulation	Ray or geometric optics
Potential application	Broadband anti-reflection coating	Light trapping in thin-film solar cell	Light trapping in bulk solar cell

In the case of c-Si wafer-based solar cells, refraction of the incident light is usually used to enhance the optical path length in the solar cell. The textures are usually formed by anisotropic etching of silicon wafers. Table 5.1 describes the optical wave propagation and photon management mechanism in solar cells. In this study, we have investigated the optics of single-junction PSCs and perovskite/silicon TSCs. The absorption coefficients of perovskite and crystalline silicon are shown in Figure 5.1. The perovskite material system is a direct bandgap semiconductor. The material exhibits a high absorption coefficient and a low penetration depth. Furthermore, the diffusion length is larger than the penetration depths. Hence, light trapping is not required to increase the QE and J_{SC} of the solar cell. The emphasis must be on minimizing reflection losses and parasitic losses in the solar cell. The c-Si is an indirect bandgap semiconductor, and the penetration depth close to the bandgap is larger than the thickness of a typical solar cell. Hence, light trapping is applied to increase QE and J_{SC}. Typically, the surface of a crystalline solar cell is characterized by large surface features, which support the refraction of the incident light. Photon Management in silicon solar cells is more complex than photon management in PSCs. In the case of

a silicon solar cell, the incident light must be efficiently coupled in the solar cell, the light in the solar cell must be confined by a light-trapping structure, and lastly, the light trapping structure must be design in a way that parasitic optical losses are kept small.

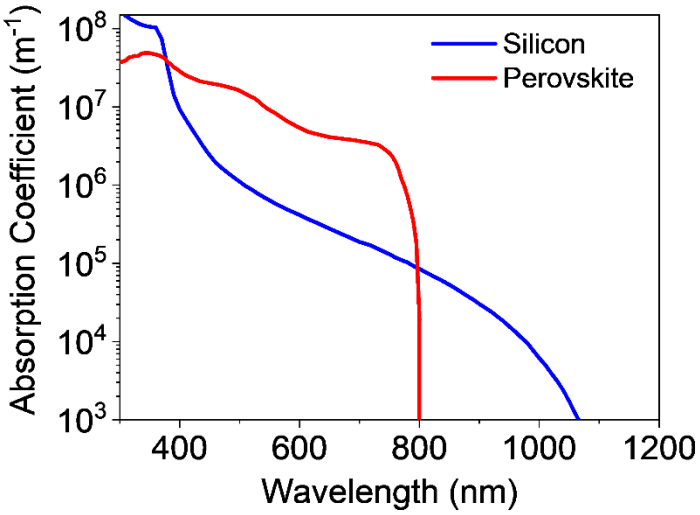

Figure 5.1: Absorption coefficients of crystalline silicon and $MAPbI_3$ perovskite.

In the case of a PSC, the incident light must be efficiently coupled in the solar cell, and optical losses must be minimized. In section 5.1.2, the described guidelines will be used to design solar cells with high J_{SC}s and ECEs. Finite-difference time-domain (FDTD) simulations will be used to simulate the optical wave propagation.

5.1.1.3 Detailed Balance Limit of Tandem Solar Cells

Detailed balance limit calculations are not only restricted to a single-junction solar cell. The calculations can be applied to tandem or multi-junction solar cell. The first detailed balance calculation for TSCs was published by De Vos.(Vos, 1980) A general description of the detailed balance theory for multi-junction solar cells is provided by Green.(M. A. Green, 2003) Here, we discuss the detailed balance limit of TSCs and its implications for perovskite/silicon TSCs. In general, a TSC can be operated as two and four-terminal devices. Plots of the ECE of two and four-terminal TSCs are provided in Figure 5.2a and 5.2b. In the case of a four-terminal device, the incident light is

divided into two diodes, while both diodes are electrically independent. For a variety of combinations of bandgaps, an ECE exceeding 40% can be reached. The electrical output power generated of both diodes is calculated independently and added when calculating the ECE. Only the incident light must be divided amongst the two solar cells. The ECE of a two-terminal device or a serial connected TSC is shown in Figure 5.2a. The ECE is mainly determined by the J_{SC} of the TSC. The total J_{SC} is equal to the J_{SC} of the bottom solar cell if the J_{SC} of the bottom diode is smaller than the J_{SC} of the top diode. The total J_{SC} is determined by the J_{SC} of the top diode if the J_{SC} of the bottom diode is larger than the J_{SC} of the top diode. The J_{SC} of a TSC is matched if the J_{SC} of the top and the bottom diodes is equal or almost equal. The ECE of a TSC is maximized for a combination of top and bottom solar cells with matched bandgaps.

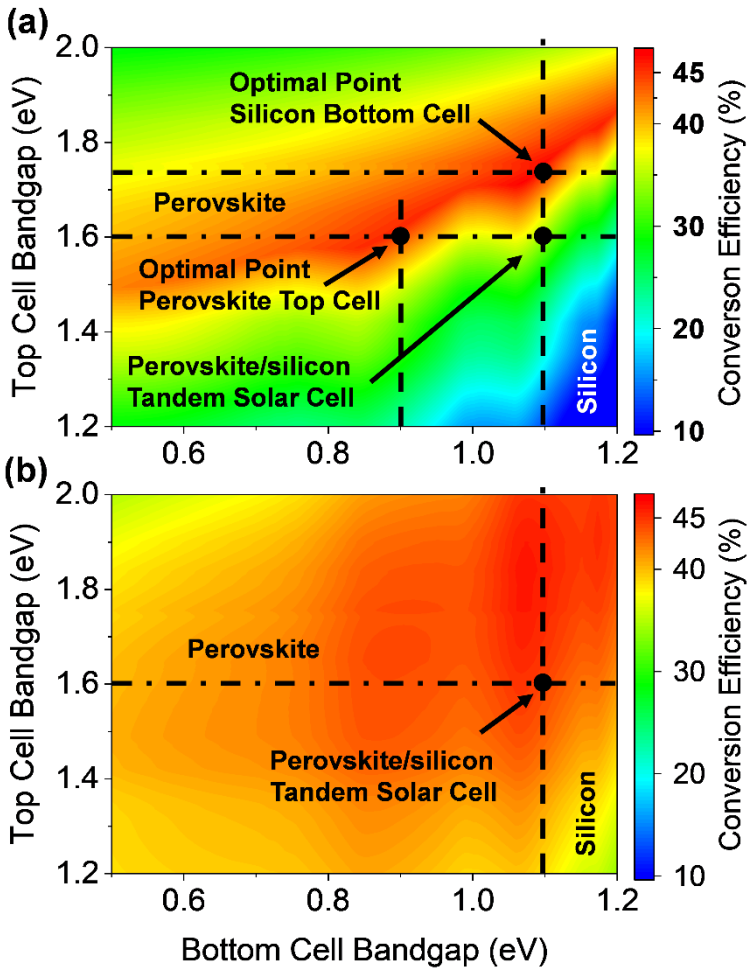

Figure 5.2: Detailed balance conversion efficiency limit for (a) 2-terminal and (b) 4-terminal tandem solar cells.

If the right combination of bandgaps of the top and bottom solar cell is selected, and the J_{SC} of the two terminal TSC is matched, and the two terminal TSCs can reach ECEs equal to the four terminal TSCs. A maximal ECE can be reached if the bandgap of the top cell is equal to $E_{G\_top}=0.5\times E_{G\_bot}+1.15$ eV. Crystalline silicon solar cells represent the dominant commercial solar cell technology. The ECE of a TSC with a c-Si bottom solar cell is maximized if the bandgap of the top diode is approx. 1.725 eV. The combination allows for a maximal ECE of ~43%. In the current study, we use perovskite ($MAPbI_3$) as an absorber with a bandgap of ~1.6 eV. The maximal ECE of a perovskite/silicon TSC is ~33%. If we start with a perovskite top cell and a bandgap of 1.6 eV, the optical bandgap of the bottom solar cell is 0.9 eV, which allows for realizing an upper ECE of ~44%.

5.1.2 Photon Management in Perovskite Solar Cells

Detailed balance calculations presented in the previous section show that ECEs higher than the best single-junction solar cells could be reached by transitioning towards TSCs. The combination of c-Si and the perovskite material system is a perfect match. So far, perovskite/c-Si TSCs in two-terminal configuration and four-terminal configurations have reached ECEs of 25.2% and 26.4%, respectively.(Duong et al., 2017; Sahli et al., 2018a) Recently, the ECE of the perovskite/silicon TSC has reached 28%, as reported by Oxford PV,(Oxford PV-The Perovskite Company, 2020); however, detailed descriptions on how to realize a high ECE have not been revealed yet. The bandgap of the perovskite material system can be controlled over a wide range.(Ju et al., 2018; Noh, Im, Heo, Mandal, & Seok, 2013; L. Wang et al., 2016; Yang, Fiala, Jeangros, & Ballif, 2018) In this study, we will use $CH_3NH_3PbI_3$, the best-studied material out of the group of perovskites. $CH_3NH_3PbI_3$ exhibits a bandgap of

~1.6 eV. The high extinction coefficient and large diffusion length allow for realizing PSCs with high J_{SC}s and ECEs.(Li et al., 2015; Löper et al., 2015a; Rao, Chen, Wang, Kuang, & Su, 2017; van Eerden et al., 2017; Wolff et al., 2017) The optics of the solar cell can be improved by enhanced light incoupling and minimizing optical losses. The largest gains can be achieved by an improved light incoupling.(Qarony, Hossain, Dewan, et al., 2018; Qarony, Hossain, Jovanov, Knipp, & Tsang, 2018) A variety of structures have been investigated that exhibit improved incoupling. Here, we focus on moth-eye textures, which exhibit excellent in- and out-coupling properties.

5.1.2.1 Device Design and Materials

The aim is to realize perovskite/silicon TSCs with a high ECE. In the case of a perovskite/silicon TSC, the top PSC must be fabricated on top of the c-Si bottom solar cell. Therefore, the TSC is a solar cell in a substrate configuration. Hence, we will focus in this study only on solar cells in substrate configuration. In the first step, we investigate single-junction PSCs before moving to a perovskite/silicon TSC. The single-junction PSC consists of a hydrogen doped tin oxide (IOH)/ Nickel oxide (NiO) double layer, a perovskite ($CH_3NH_3PbI_3$) layer, Zinc oxide (ZnO) interlayer, and an aluminum reflector. All charge transport and charge blocking layers used in this study are metal oxides, which can be deposited by physical (PVD) or chemical vapor deposition (CVD). We decided to avoid spin-coated transport and charge blocking layers because the layers must be prepared on textured substrates.(Mohammad I. Hossain, Qarony, Jovanov, Tsang, & Knipp, 2018b) PVD and CVD seem more suited for the deposition of uniform films on textured substrates. Nevertheless, a variety of charge transport and charge blocking layers have been suggested and successfully implemented including well-established materials like Spiro-MeOTAD and TiO_2 or novel materials like graphene oxide or Cu-phthalocyanine.(Jang et al., 2016; Koushik et al., 2017; Z. Liu et al., 2018; Luo et al., 2017; Noh, Jeon, et al., 2013b; Vidyasagar,

Muñoz Flores, & Jiménez Pérez, 2018) Furthermore, it might be necessary to use multiple layers to fulfill all the requirements of the contact layers. The NiO film is used as a hole transport and an electron blocking layer. However, NiO films exhibit a low hole charge carrier mobility, so that the lateral conductivity of the films is too low to realize solar cells with low sheet resistance and high fill factor. Highly doped NiO films exhibit high absorption losses, so that a double layer of IOH/NiO is used. IOH shows a high electron charge carrier mobility, and NiO exhibits a high work function which permits to achieve efficient hole injections and provides good lateral charge transport so that solar cells with low series resistance and high fill factor can be achieved.(Xu et al., 2015b; J. Zhou et al., 2017)

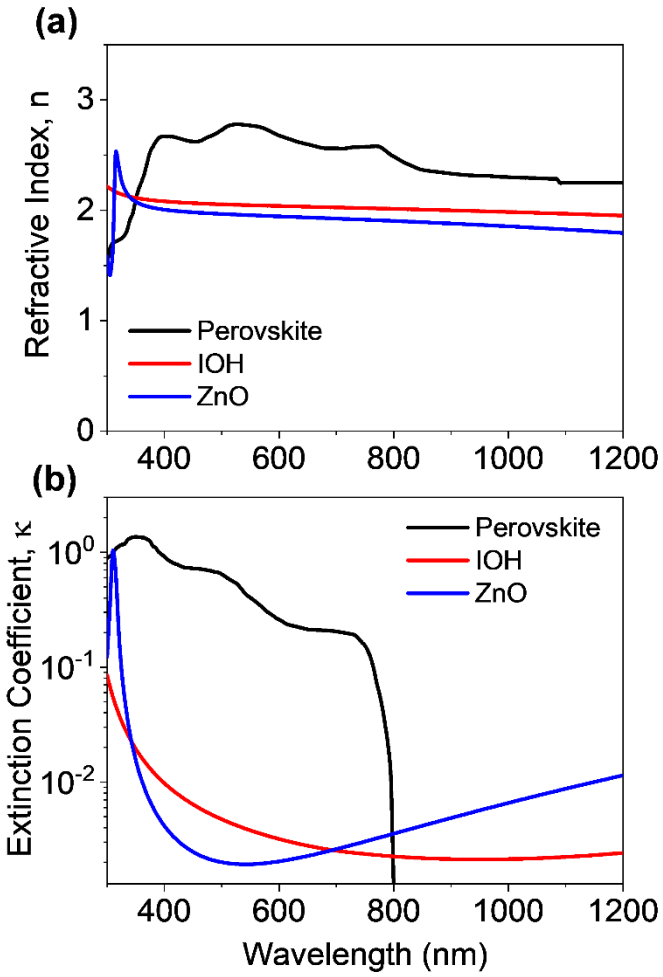

Figure 5.3: (a) Refractive Indices and (b) Extinction coefficients of Perovskite ($CH_3NH_3PbI_3$), IOH, and ZnO materials.

The IOH/NiO double layer forms a tunnel junction. Similar combinations of materials like ITO/NiO were used in literature to experimentally realize PSCs with high ECEs.(W. Chen et al., 2018; Hu et al., 2014) The NiO is only 5 nm thick so that the absorption by the layer is low. Hence, we have not considered the NiO layer in the optical simulations.(Mohammad I. Hossain, Hongsingthong, et al., 2019; Mohammad I. Hossain et al., 2018b) The optical constants used for the simulation were taken from the literature.(Filipič et al., 2015; Mejía Escobar, Pathak, Liu, Snaith, & Jaramillo, 2017; van Eerden et al., 2017) Figure 5.3 illustrates the complex refractive indices and extinction coefficients of IOH, perovskite ($CH_3NH_3PbI_3$), and ZnO. The perovskite material system and the metal oxide contact layers have a comparable refractive index. Hence, the reflection at the perovskite/metal oxide interface is low, and the entire layer stack exhibits a comparable refractive index.(Slawinski, Slawinski, Brown, & Parkin, 2000)

5.1.3 Single-junction Perovskite Solar Cells

In the first step, the investigation started with the implementation of a flat single-junction PSC. Figure 5.4(a) shows the schematic cross-section of a PSC on a smooth or flat substrate. The solar cell consists of a 70 nm front hydrogen doped tin oxide (IOH)/ Nickel oxide (NiO) double layer, a 350 nm perovskite ($CH_3NH_3PbI_3$) material, a 70 nm Zinc oxide (ZnO) layer, and an aluminum (Al) layer as a reflector. The time average power density for the incident wavelength of 400 nm and 750 nm are provided in Figures 5.4(b) and 5.4(c), respectively. Due to the high absorption coefficient of the perovskite material for the short wavelengths (400 nm), most photons are absorbed within a couple of tens of nanometers of the perovskite film. For long wavelengths (750 nm) the absorption coefficient is reduced, and a certain fraction of the incident light

reaches the back reflector, where the light is a reflection so that a standing wave is formed in front of the back reflector. The QE of the PSC is shown in Figure 5.5.

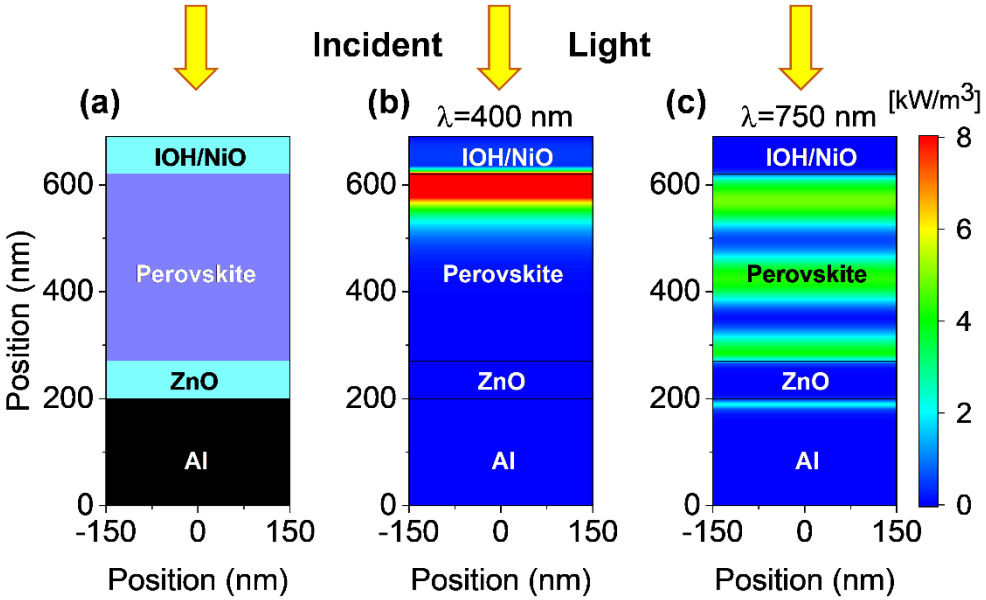

Figure 5.4: (a) Schematic cross-section, and simulated power density under monochromatic illumination of wavelength (b) 400 nm, and (c) 750 nm for the flat perovskite solar cell.

The QE is plotted together with the absorption of the front and back contact and the reflection of the solar cell. The perovskite material system exhibits a bandgap of ~1.6 eV, which results in an upper J_{SC} of 26.9 mA/cm^2. The J_{SC} of the simulated single-junction PSC is 21.4 mA/cm^2. A J_{SC} of 5.5 mA/cm^2 is lost due to absorption and reflection losses. The reflection accounts for an optical loss of 4.4 mA/cm^2, which corresponds to 16% of total J_{SC}, while the absorption losses of the front and back contact account for 4% of the total J_{SC}. The short-circuit current density can be distinctly improved by an improving coupling of the incident light in the solar cell. In the second step, photon management in single-junction PSC is studied using moth-eye surface texture. Moth eye textures have been intensively used to improve the light incoupling in biological or optoelectronic devices and systems.(Chan, Morse, & Gordon, 2018; Kuo, Hsu, Nien, & Yu, 2016; Tan et al., 2017) Moth eye textures act like broadband anti-reflection coatings so that the incoupling of light can be distinctly improved, and the reflection is reduced.(Q. Chen et al., 2009; Woo Leem, Guan, Choi, & Su Yu, 2015) Figure 5.6(a,b) and

Figure 5.6(c,d) show scanning electron microscopy (SEM) and atomic force microscope (AFM) images of moth eye surface textures.(Woo Leem et al., 2015)

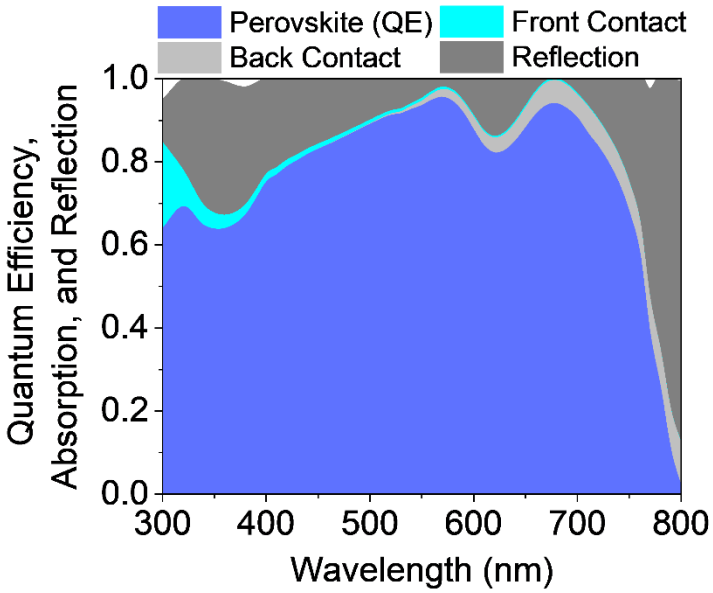

Figure 5.5: Quantum efficiency and absorption of individual layers of a flat perovskite solar cell.

The polymeric moth-eye surface textures were fabricated by casting a Polydimethylsiloxane (PDMS) film on a crystalline silicon master, which was patterned by silicon semiconductor processing. The moth-eye texture is characterized by periodically distributed nipples with a circular base arranged in a hexagonal grid. The surface profile of each nipple of the moth-eye texture exhibits a paraboloid shape. It is shown in our previous studies that paraboloid shaped nipple exhibit almost ideal incoupling properties.(Dewan et al., 2012; Qarony, Hossain, Dewan, et al., 2018) It is assumed that the moth-eye texture used in this study has a diameter of 150 nm and a height of 200 nm.(Woo Leem et al., 2015), as shown in Figure 5.6(e) and Figure 5.6(f). We have integrated the moth-eye texture in a PSC. Figure 5.7(a) shows a cross-section of a textured solar cell. All interfaces of the solar cell structures are moth-eye textured. The power density map for a wavelength of 750 nm is shown in Figure 5.7(b) and the calculated QE is shown in Figure 5.7(e). Furthermore, the QE of a flat or planar solar cell is included in Figure 5.7(e). For short wavelengths, the increased QE is

observed for the moth-eye textured solar cell. For long wavelengths, the planar solar cell exhibits a higher QE.

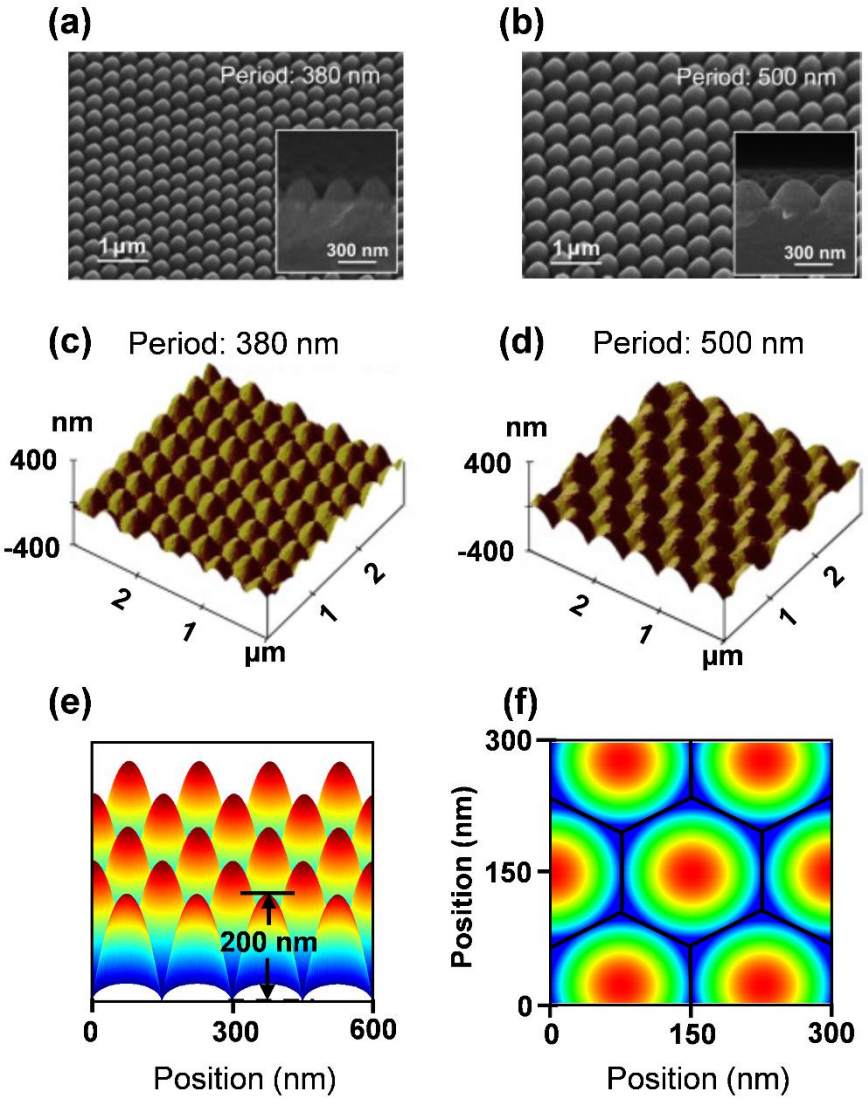

Figure 5.6: (a, b) SEM and (c, d) AFM images of a moth-eye surface texture. Reproduced with permission from Ref.(Woo Leem et al., 2015) Copyright 2019, Elsevier. (e, f) Moth eye surface texture used for the optical simulation of the solar cells.

The drop of the QE is caused by the textured Al back contact. The Al back contact exhibits a high absorption, leading to high non-radiative optical losses for long wavelengths. This is confirmed by the power density map in Figure 5.7(b) for 750 nm.

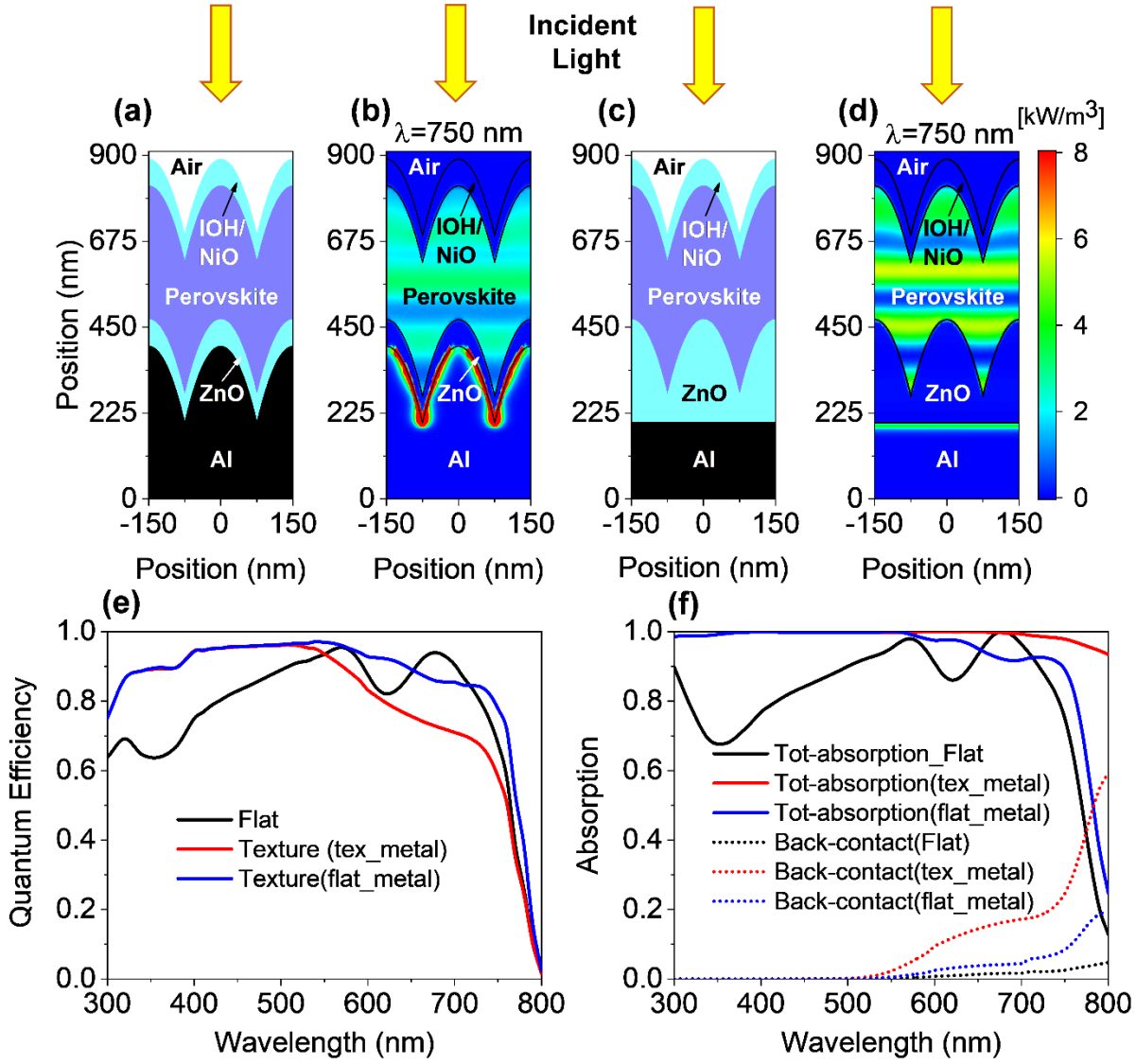

Figure 5.7: (a, c) Schematic cross-sections of a perovskite solar cell with integrated moth-eye textures. (a) An aluminum contact with a moth-eye texture is formed, and all subsequent layers of the solar cell are formed on the textured metal contact. Hence, all layers of the solar cell exhibit a moth-eye texture. (c) A moth-eye textured interlayer is formed on a flat or planar aluminum reflector. All layers are formed on the moth-eye texturized interlayer. Hence, all layers except the aluminum back contact exhibit a moth-eye texture and (b, d) corresponding power density maps for an incident wavelength of 750 nm. Periods and heights of the moth-eye structures are 300 nm and 200 nm, respectively. (e) Comparison of calculated quantum efficiency and optical loss of the metal back contact, and (f) comparison of absorbance for perovskite solar cells with and without integrated moth-eye texture.

The optics of the solar cell can be improved by using a planar Al reflector in combination with a textured interlayer. A schematic cross-section of the solar cell is

shown in Figure 5.7(c) and the corresponding power density map in Figure 5.7(d). The optical loss of the back contact is distinctly reduced. A standing wave is formed in the solar cell. Hence, it can be concluded that the moth-eye texture leads to a good light incoupling, but no diffraction of the incident light is observed. The modified back contact design leads to a distinct gain in the QE shown in Figure 5.7(e) for long wavelengths. The total absorption of the solar cells and the absorption of the back contact is shown in Figure 5.7(f). These two solar cells with moth eye texture exhibit a total absorption close to unity. By minimizing the absorption losses of the contact layers, the QE of the solar cell can be increased. The flat solar cell exhibits a J_{SC} of 21.4 mA/cm^2, while the moth-eye textured solar cells exhibit J_{SC} of 22.6 mA/cm^2 and 23.1 mA/cm^2. The moth-eye textured Al reflector leads to an optical loss of 0.5 mA/cm^2. In the following section, a guideline for realizing perovskite/silicon TSCs with high J_{SC} and ECE is given.

5.1.4 Perovskite/Silicon Tandem Solar Cells

The perovskite and silicon absorbers are used as top and bottom solar cells. c-Si exhibits a bandgap of 1.15 eV so that the solar cell absorbs light up to almost 1200 nm. The upper theoretical limit of the J_{SC} (Shockley Queisser limit) is calculated as 46 mA/cm^2. Experimentally realized single c-Si solar cell exhibit J_{SC} of 41 to 42 mA/cm^2 and ECEs of ~26%.(Yoshikawa et al., 2017a) This means that the maximal J_{SC} of a perovskite/silicon TSC under current matching condition is 23 mA/cm^2.(Mohammad I. Hossain et al., 2018b) Based on the best experimentally realized c-Si solar cells it can be expected that the J_{SC} of the best perovskite/silicon TSCs is in the range from 20 to 21 mA/cm^2.(Green, Hishikawa, et al., 2019; Yoshikawa et al., 2017a) To determine an optical solar cell design, the optical wave propagation must be rigorously simulated. However, the thickness of the TSC is distinctly larger than the wavelength of the

incident light, so that a rigorous simulation is computationally too complex.(Mohammad I. Hossain et al., 2018b) Therefore, a hybrid approach is used to model wave propagation.

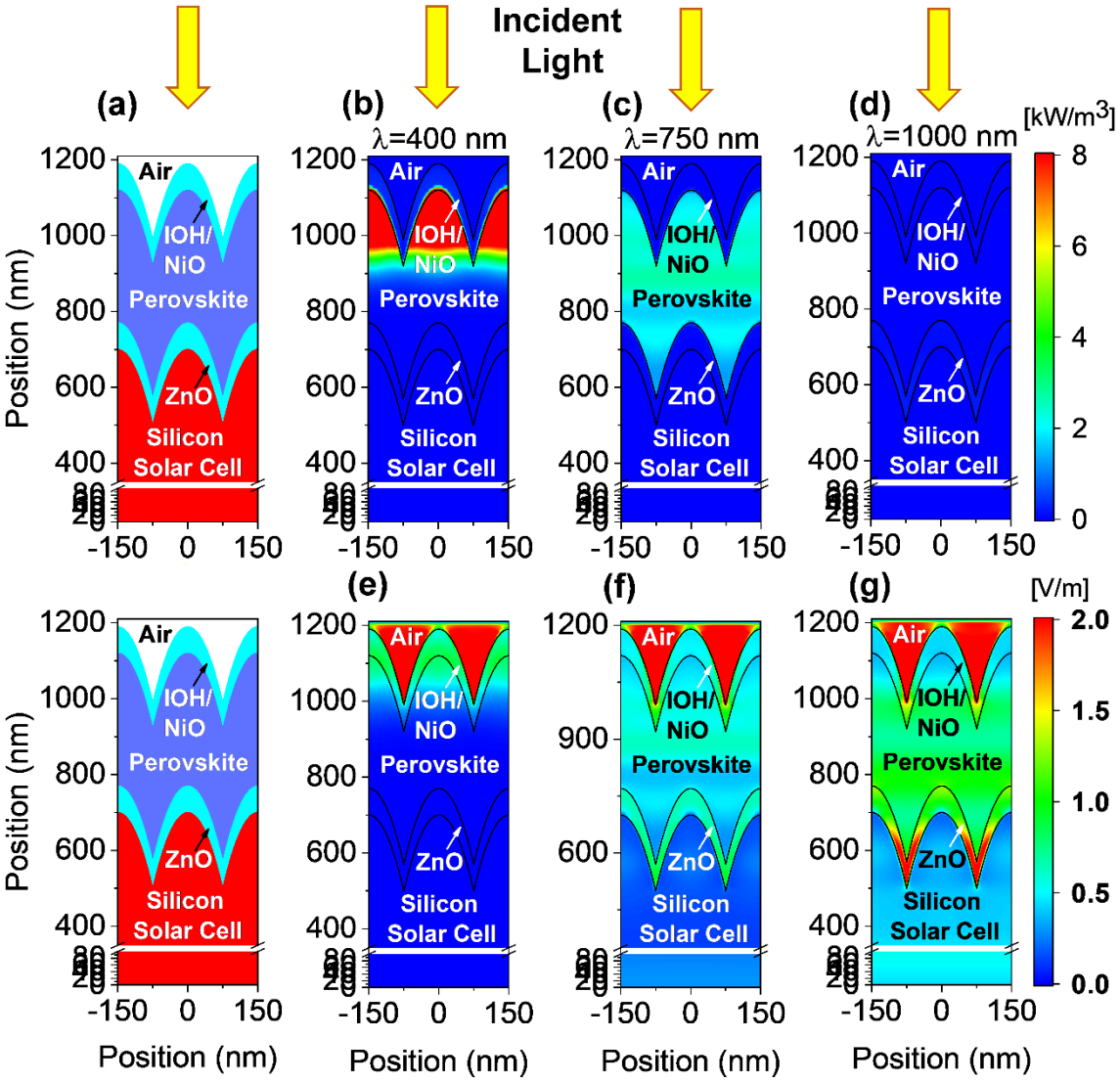

Figure 5.8: (a) Cross-section of moth-eye textured perovskite/silicon tandem solar cell. The corresponding power density map for an incident wavelength of (b) 400 nm, (c) 750 nm, and (d) 1000 nm. The corresponding electric field distribution for an incident wavelength of (e) 400 nm, (f) 750 nm, and (g) 1000 nm.

The top cell consists of a double IOH/NiO front contact, the perovskite material, and a ZnO back contact. The silicon heterojunction bottom solar cell is described by an infinitely thick silicon substrate with a backside texture comparable to the front side

texture of conventional single-junction c-Si solar cells (Mohammad I. Hossain et al., 2018b; Yoshikawa et al., 2017a). To determine the QE of the bottom solar cell, the light transmitted by the top PSC in the bottom solar cell is calculated. Furthermore, it is assumed that light entering the bottom solar cell refracted by the textured backside of the silicon wafer. The QE of the top and bottom solar cell is given by

$$\mathrm{QE_{top}}(\lambda) \approx \mathrm{A_{perovskite}}(\lambda) \quad (5.14)$$

$$\mathrm{QE_{bottom}}(\lambda) \approx \mathrm{QE_{c-Si}}(\lambda) \times \mathrm{T_{perovskite}}(\lambda) \quad (5.15)$$

where $\mathrm{A_{perovskite}}$ and $\mathrm{T_{perovskite}}$ are the absorption and transmission of the perovskite layer. $\mathrm{QE_{c-Si}}$ is the QE is taken from literature for a silicon solar cell with record ECE. The schematic cross-section of a perovskite/silicon TSC with integrated moth-eye texture is depicted in Figure 5.8(a).

The corresponding power density maps and electric field distributions under different wavelengths are shown in Figures 5.8(b-g). For 400 nm, all the incident light is absorbed by the first 100 nm of the perovskite top cell. For a wavelength of 750 nm, most of the light is still absorbed by the top solar cell. Only a small fraction of the incident light enters the bottom cell. For an incident wavelength of 1000 nm almost, all light is transmitted in the bottom diode, where the light is absorbed. The calculated QE for the top, bottom, and total cells under J_{SC} matched condition is illustrated in Figure 5.9. The J_{SC} is matched for a perovskite layer thickness of 350 nm. At approximately 770 nm, both top and bottom exhibit equal QE of roughly 50%. The matched J_{SC} reaches 20.7 mA/cm^2 while the total J_{SC} is 41.4 mA/cm^{2,} which is very close to our predicted reference value taken from record efficiency silicon solar cell. The attained J_{SC} is very close to the upper theoretical limit. To provide a realistic prediction of the ECE of the solar cells, a description of the V_{OC} and the FF is required. The full understanding of the formation of high V_{OC} is needed. It has been proposed that the

high V_{OC} is caused by slow bulk recombination, low density of states in the conduction and valence band or low band tails.(Kirchartz, 2019; Nishiwaki et al., 2018; Y. Zhou & Long, 2017)

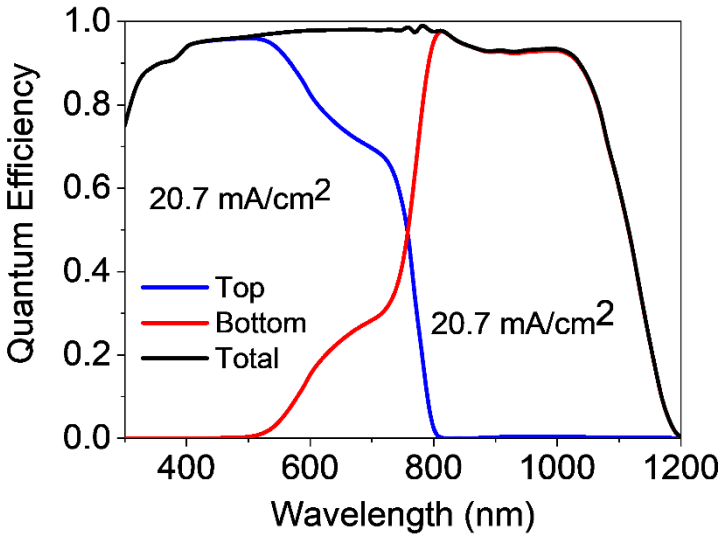

Figure 5.9: The calculated quantum efficiency of the top, bottom, and total perovskite/silicon tandem solar cell under matched short-circuit current conditions.

In this study, we estimate an upper limit of the ECE by combining the optical simulation results with results for experimentally realized solar cells. The best experimentally realized silicon solar cells exhibit a V_{OC} of ~0.74 V and FF of 84.9%, while the best PSCs using a $MAPbI_3$ absorber exhibits 1.182 V V_{OC} and 77% FF.(Green, Hishikawa, et al., 2019; Y. Wang et al., 2018) The maximum ECE can be estimated to ~33%. By using a top PSC with an optimum bandgap of 1.7 eV, a further improved of the V_{OC} and the ECE can be expected. If we assume that the same matching J_{SC} is achieved, the final ECE will increase up to ~35%. We are currently in the process of investigating the optics of perovskite/silicon TSCs with $MAPbI_{1-x}Br_x$ top cell absorbers. By increasing the bandgap of the top diode to 1.7 eV, we like to approach ECEs of 35%.

5.2 Nanophotonic Design of Perovskite/Silicon Tandem Solar Cell

The perovskite material system allows for the realization of perovskite/silicon TSCs with high ECEs at a low cost. To realize such solar cells, the device geometry, device processing, and the contact materials have to be modified in comparison to single-junction PSCs. In this study, a perovskite/silicon TSC will be proposed, which provides ECEs exceeding 30%. The optimization of perovskite/silicon TSCs will be discussed taking realistic device structure into consideration. Strategies will be described to reach high J_{SC}s and high ECEs. High J_{SC}s can be achieved by minimizing reflection losses and optical losses of the contact layers. The realization of perovskite/silicon TSCs with high ECEs requires several modifications of the solar cell design compared to conventionally fabricated single-junction PSCs. Commonly used deposition processes and contact/charge transport materials have to be replaced. Herein, we mainly focus on the optical design of the TSC using nanophotonic approaches to reach high J_{SC}s. A hybrid approach is used to investigate the optics by combining Finite-Difference Time-Domain simulations with experimental measurements. A detailed discussion on the design of the integrated TSC using nanophotonics is provided in the following subsections.

5.2.1 Design of Perovskite/Silicon Tandem Solar Cells

The J_{SC} of record silicon single-junction solar cells ranges from 40 to 42 mA/cm^2. At the same time, the theoretical upper limit is equal to 46 mA/cm^2.(Green, Hishikawa, et al., 2017; Masuko et al., 2014; Shockley & Queisser, 1961a; Yoshikawa et al., 2017b) Hence, the realized solar cells exhibit records very close to the theoretical limit, while losses are deficient, accounting for only 9-13% of the J_{SC}. Losses can be attributed to absorption losses of contact layers and charge transport materials, which do not

contribute to the J_{SC}. Furthermore, the theoretical limits require a charge collection efficiency of 100 %. In the case of a TSC, the J_{SC} has to be matched. In other words, both solar cells have to provide equal J_{SC}. Otherwise, the J_{SC} is limited by matching losses. This leads to an upper theoretical limit for a perovskite/silicon TSC of 23 mA/cm^2. In order to reach an integrated perovskite/silicon TSC with a J_{SC} close to the theoretical limit, several device processing and material aspects have to be considered. Potential design of a perovskite/silicon TSC reaching the required J_{SC} is shown in Figure 5.10.

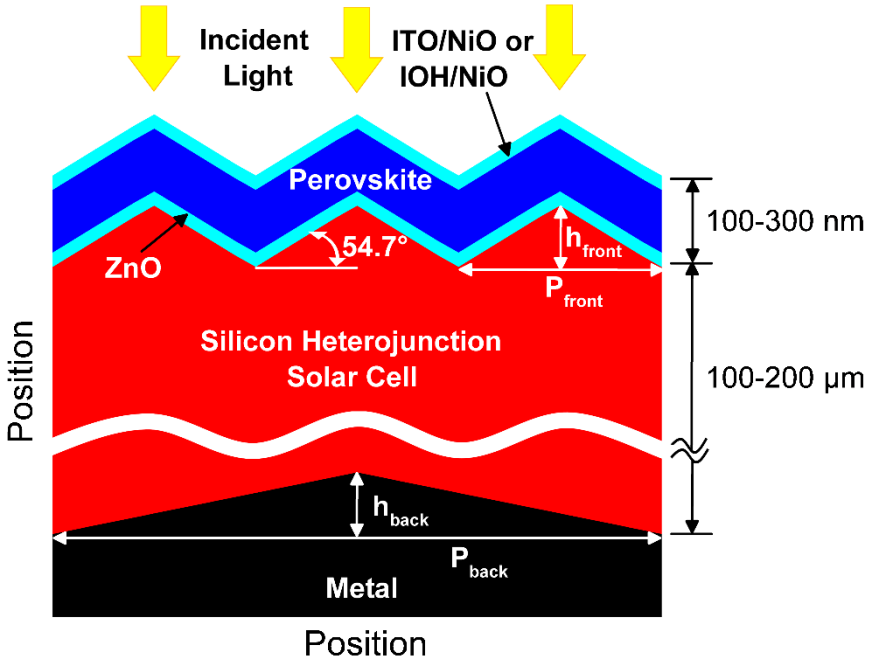

Figure 5.10: Schematic cross-section of the unit cell of an optically optimized perovskite/ silicon tandem solar cell.

A solar cell with very low reflection losses has to be designed. Such low reflection losses can only be reached by texturing the front interface of the solar cell. A planar front contact interface leads to distinct reflection losses and a lowering of the J_{SC}. Hence, the perovskite top cell has to be prepared on a textured silicon solar cell. However, single-junction PSCs are commonly prepared on planar glass substrates coated with a transparent conductive oxide. Most authors use a spin coating to prepare

the complete solar cells or at least the contact/charge transport layers of the solar cell. However, spin coating is not compatible with the fabrication of PSC on a textured silicon solar cell. Hence, some material and fabrication processes have to be replaced. In the following, it is assumed that all layers of the PSC are prepared by physical or chemical vapor deposition (PVD or CVD) techniques. Perovskite films have been prepared by thermal evaporation, allowing for the realization of single-junction solar cells with high ECE.(Fan et al., 2016) Recently, promising results have been presented for perovskite films grown by CVD.(Leyden et al., 2014; Spina et al., 2016) PSCs with high ECEs have been realized using NiO and ZnO as a hole transporting/electron blocking layer (HTL) and an electron transporting/hole blocking layer (ETL).(Xu et al., 2015b; J. Zhou et al., 2017) In both cases, the films have been prepared by the spin coating of nanoparticle films. In this study, it is assumed that the metal oxide films are prepared by sputtering. NiO films exhibit a high work function, while the charge carrier mobility and the conductivity of the films are rather low.(Kwon et al., 2016) Doping the film leads to a distinct increase in the conductivity. However, the increased doping concentration causes a drop in the optical transmission of the film leading to high absorption losses of the NiO film and limiting the J_{SC}. In order to overcome the limitations, the NiO film has been replaced by an ITO/NiO double layer, in which a very thin NiO film allows for efficient hole injection and electron blocking. The much thicker ITO layer is responsible for the lateral conductivity of the screen-printed front contact grid. Both metal oxides are highly doped, which allows for the formation of an efficient tunneling junction. ITO films exhibit typical electron charge carrier mobilities in the range of 10 to 20 cm^2/Vs.(Barraud et al., 2013b; T. Koida, Fujiwara, & Kondo, 2009a) High doping concentrations are required to reach high conductivities of the films. This is not a problem for a single-junction PSC, which exhibits a bandgap of 1.6 eV. However, the situation is different for a TSC, which exhibits high QEs up to almost 1.05 eV (1200 nm). The high doping concentration causes high free carrier absorption,

which limits the QE of the bottom solar cell. The charge carrier mobility of the transparent conductive oxide has to be increased to keep the front contact sheet resistance constant while decreasing the free carrier absorption losses. Hence, the ITO film is replaced by a hydrogen doped indium oxide (IOH) film. IOH exhibits a distinctly higher electron charge carrier mobility.(Barraud et al., 2013b; T. Koida et al., 2009a) Hence, the doping concentration of the IOH film can be reduced while maintaining a constant sheet resistance. Consequently, the free carrier absorption is reduced, and the QE of the bottom cell is increased. The HTL and ETL of the solar cell are formed by sputtering or CVD of zinc oxide films doped by aluminum or boron.(Rech & Wagner, 1999; Steinhauser, 2008) The bottom solar cell consists of a heterojunction silicon solar cell, allowing for high open-circuit voltages (V_{OC}s). In order to allow for the generation of a high J_{SC}, the front interface of the bottom solar cell has to be textured. In this study, it is assumed that the front and back contacts are textured. It is also assumed that the backside of the silicon wafer is covered with a surface texture comparable with conventional single-junction silicon solar cells. The dimensions of the back-contact texture are described by h_{back} and p_{back}. The function of the texture is to refract the light that reaches the back contact. The front side of the silicon wafer is covered with a surface texture with the dimensions of h_{front} and p_{front}. The function of the front contact texture is to minimize reflection losses, while efficiently coupling light in the top and bottom solar cells.

The integration of the PSC on the silicon wafer is getting more difficult with increasing the roughness of the front contact. In this study, a front contact texture is selected that allows for an efficient light incoupling while keeping the roughness of the front contact low. Hence, the dimensions of the front surface texture are distinctly smaller than the texture of the back contact ($h_{front} << h_{back}$ and $p_{front} << p_{back}$). The front and back contact textures are formed by anisotropic etching of a silicon wafer with a {111} crystal

orientation. The anisotropic etching is characterized by the formation of a pyramidal surface texture, which can be described by an etching angle of 54.7° relative to the surface of the silicon wafer. It is considered that the front and back sides of the wafer are covered by such pyramidal textures, so that $h_{front}/(2\times p_{front}) = h_{back}/(2\times p_{back})=\tan(54.7°)=\sqrt{2}$. In this study, the period of the front surface texture is varied from 0 nm to 1000 nm, while keeping the etching angle constant. A period of 0 nm corresponds to a planar surface.

Perovskite/silicon TSCs with high J_{SC}s can be reached by the following three guidelines:

- Firstly, minimizing the reflection losses by improving the light incoupling in the solar cell. An improved incoupling is achieved by texturing the solar cell.
- Secondly, the light has to be efficiently coupled from the top solar cell in the bottom solar cell. The perovskite material exhibits a rather low refractive index of approx. 2, while silicon exhibits a high refractive index of approx. 4, so that an efficient coupling of light in the bottom solar cell is required. An optical matching layer is introduced between the top and bottom solar cell to improve the coupling.
- And thirdly, the optical losses by the contact layers have to be minimized, without negatively affecting the electrical properties of the solar cell.

5.2.2 Optical Material Properties

Several studies on the optical properties of perovskite films have been published.(Löper et al., 2015a; Shirayama et al., 2016a) The published data exhibits a large variety of the extracted absorption coefficient and bandgap. The variations are mainly caused by the high surface roughness of perovskite films compared to other

semiconductor films. Hence, the extracted absorption coefficient is overestimated, and the optical bandgap is underestimated. A very detailed analysis of the influence of the surface roughness on the optical constants has been published by Shirayama et al.(Shirayama et al., 2016a) In our study, we use the optical data published by Löper et al.(Löper et al., 2015a) The adapted complex refractive index of the $CH_3NH_3PbI_3$ perovskite material is provided in Appendix C (Figure C1.1) for the spectral range from 300 nm to 1200 nm. The extinction coefficient is assumed to be zero for optical bandgaps larger than 1.6 eV. The refractive index and extinction coefficient of ITO and IOH are shown in Figure 5.11(a) and Figure 5.11(b), respectively.

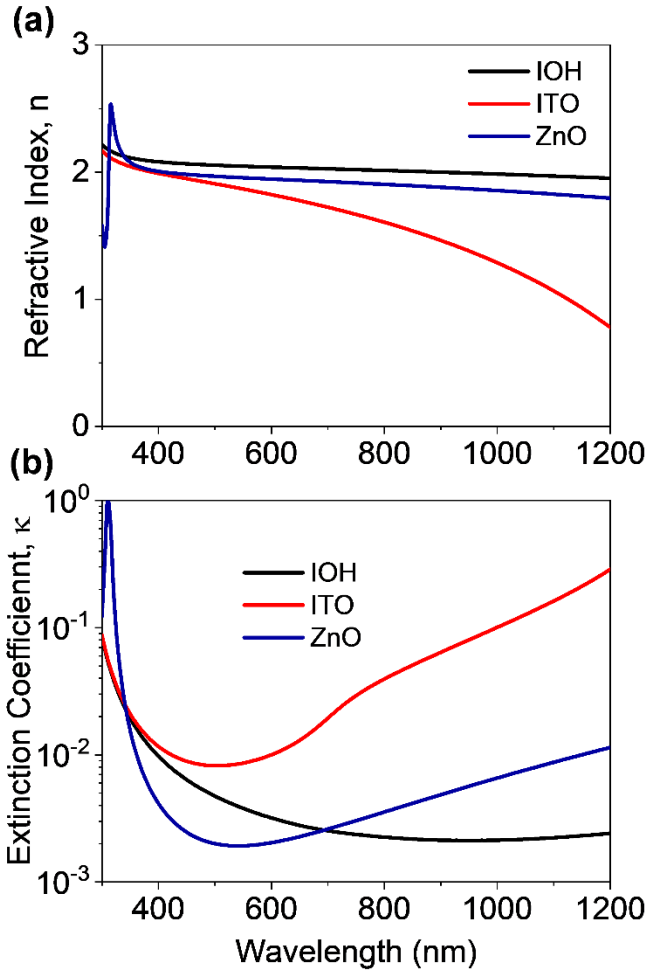

Figure 5.11: (a) Refractive index and (b) extinction coefficient of contact and transparent conductive layers of IOH, ITO, and ZnO.

As mentioned in section 5.2.1, the front transparent conductive oxides have three

functions. The material has to allow for an efficient charge injection in the solar cell while exhibiting a low specific resistivity to minimize the series resistance. At the same time, optical absorption losses by the transparent conductive oxide should be low. A Drude Lorentz model is used to describe the dielectric function of ITO and IOH.(Drude, 1900b, 1900a) The Lorentz term is used to describe the optical properties close to the bandgap of the metal oxide, while a Drude model is used to describe the free carrier absorption. An extended Drude model with a modified expression for the damping frequency is used.(Drude, 1900a) The model considers the drop in the charge carrier mobility as the wavelength is approaching the plasma wavelength.(Drude, 1900a) The dielectric functions are determined by modeling the transmission, absorption, and reflection of experimentally realized ITO and IOH films with equal sheet resistance. The samples are prepared and measured by Koida et.al.(T. Koida et al., 2009a) The IOH film exhibits electron mobility of μ_e=140 cm^2/Vs, which is 5-10 times higher than the electron mobility of ITO. Consequently, the doping concentration of ITO films is 5-10 times lower, which leads to a shift of the plasma wavelength to longer wavelengths. The parameters used to determine the optical constants are provided in Appendix C (Figure C1.2, Figure C1.3, Table C1). In this study, the two materials are compared in terms of the influence of the free carrier absorption on the QE and J_{SC} of the TSC. Furthermore, Figure 5.11 exhibits the optical constants of the ZnO ETL. Again, a Drude Lorentz model is used to model the complex refractive index. The parameters were determined by modeling the transmission, absorption, and reflection of Low-Pressure Chemical Vapor Deposited (LPCVD) films published by Steinhauser.(Steinhauser, 2008) The parameters used to model the ZnO are provided in Appendix C (Figure C1.2, Figure C1.3, Table C1).

5.2.3 Modeling and simulation Method

To determine a realistic description of the solar cells, the optical wave propagation has

to be rigorously simulated. However, the thickness of the TSC is distinctly larger than the wavelength of the incident light, so that a rigorous simulation is very complex and time-consuming. Hence, a hybrid approach is used to model wave propagation. An FDTD approach is used to model the optical wave propagation in the top cell and the coupling of light in the bottom solar cell. The top cell consists of the ITO or IOH front contact, the perovskite material, and a ZnO back contact. The NiO hole transporting layer is not considered by the optical calculations because the layer is very thin. Hence, the absorption by the layer is neglected. The silicon bottom solar cell is described by an infinitely thick silicon substrate with surface texture (h_{front}, p_{front}). In order to determine the QE of the bottom solar cell, the light transmitted by the perovskite top solar cell is calculated. It is assumed that light entering the bottom solar cell is effectively coupled in by the textured front side of the silicon wafer and refracted by the textured backside of the silicon wafer.

The QE of the top and bottom solar cell is calculated by rewriting equations 5.14 and 5.15.

$$\mathrm{QE_{Top}} \approx \mathrm{A_{perovskite}} \tag{5.16}$$

$$\mathrm{QE_{Bot}} \approx \mathrm{QE_{c-Si}} \times \mathrm{T_{Top}} \tag{5.17}$$

where $A_{perovskite}$ is the absorption of the perovskite layer, it is assumed that the collection efficiency of the perovskite layer is 100%.

Light absorbed by the contact and hole/electron transporting layers does not contribute to the QE. The QE of the bottom solar cell is determined by multiplying the transmission of the top cell, $T_{top,}$ with the QE of a single junction solar cell from literature.(Green, Emery, et al., 2017; Yoshikawa et al., 2017b) Based on the QE, the J_{SC} for the top and bottom solar cell was calculated. Details on the calculation of the QE and J_{SC} are given in the literature.(Dewan et al., 2009) In this study, only results

for matched solar cells are presented in this manuscript. The thickness of the top diode is adjusted until the matching of the J_{SC} of the top and bottom solar cell is achieved. All electromagnetic simulations are carried out in three dimensions (3D) for incident light are ranging from 300 nm to 1200 nm. More details about the optical simulation method are provided in Chapter 2 (section 2.3).

5.2.4 Results and Discussions

The schematic cross-section of a perovskite/silicon TSC with a flat front contact is depicted in Figure 5.12(a). The cell consists of a 70 nm ITO/NiO transparent front contact followed by a perovskite layer with a thickness of 225 nm, and a 70 nm thick ZnO as a transport layer.

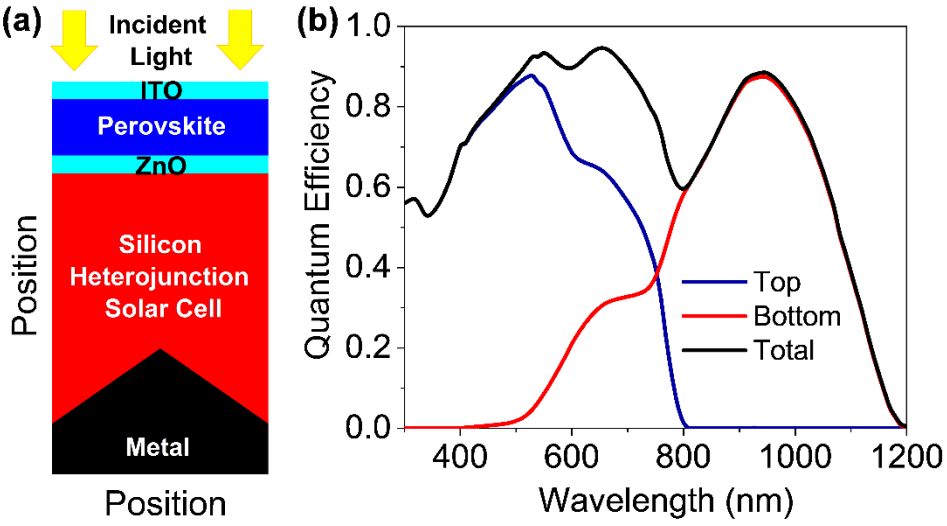

Figure 5.12: (a) The schematic cross-section of perovskite/silicon tandem solar cell with a flat front contact. (b) Corresponding external quantum efficiency for the top, bottom, and tandem solar cells. The NiO film is assumed to be very thin relative to the thickness of the ITO layers so that the layer is not considered by the optical calculations.

The NiO film is assumed to be very thin relative to the thickness of the ITO layers so that the layer is not considered by the optical calculations. The calculated QE under current matched conditions is given in Figure 5.12(b). The QE of the top and bottom

solar cell was calculated according to Equations (1) and (2). The solar cell exhibits a J_{SC} of 17.2 mA/cm^2. The J_{SC} represents the highest current for a perovskite/silicon TSC with a flat front contact without anti-reflection coating. The results are in very good agreement with the recently published experimental results by Bush et.al.(Bush et al., 2017b) However, the low J_{SC} of the TSC prevents the realization of a solar cell with ECEs exceeding single-junction silicon solar cells with record ECE.

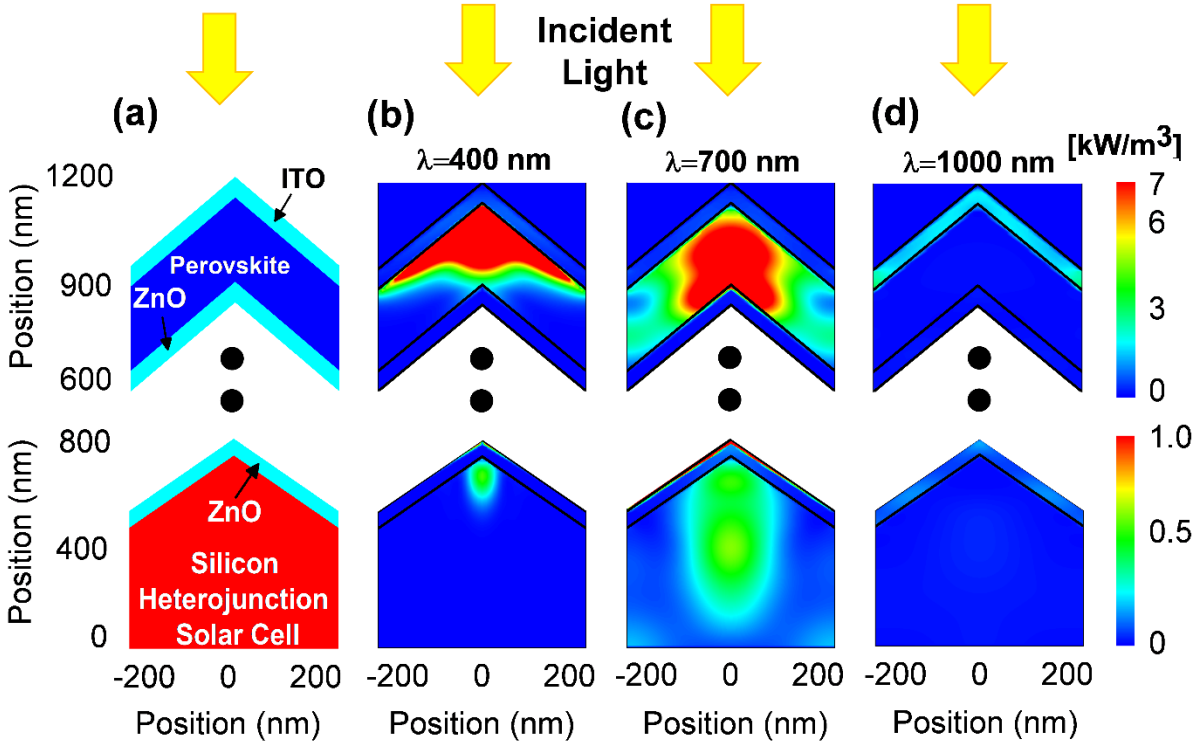

Figure 5.13: (a) The schematic cross-section of perovskite/silicon tandem solar cell with a pyramid textured front contact. (b) Simulated power loss map of perovskite/silicon tandem solar for monochromatic illumination of 400 nm, (c) 700 nm, and (d) and 1000 nm. The NiO films are assumed to be very thin so that the layer is not considered by the optical calculations.

Therefore, an efficient light incoupling concept is needed to reduce reflection losses. In the next step, the silicon wafer was textured before adding the top PSC. By texturing the top solar cell, the incoupling of the light is improved and the QE and J_{SC} are enhanced. The dimensions of the surface texture are described by a pyramidal texture. The dimension of the pyramids is determined by h_{front} and p_{front}. The texture is formed

by anisotropic etching of a silicon wafer with a {111} crystal orientation. The pyramidal surface texture is described by a constant $h_{front}/(2\times p_{front})$ ratio of $\sqrt{2}$ correspondings to an etching angle of 54.7° relative to the surface of the silicon wafer. The time average power loss map of a TSC with a period of 450 nm is shown in Figure 5.13 under monochromatic illumination with wavelengths of 400 nm, 700 nm, and 1000 nm. The top and bottom diodes in Figure 5.13 are visualized separately because of the distinctly different absorption coefficient of the top PSC and the silicon bottom cells. Due to the high absorption coefficient of perovskite for short wavelengths, all photons are absorbed by the top diode (Figure 5.13(b)). For a wavelength of 700 nm, most of the incident light is still absorbed by the top diode, but a smaller fraction of light is already absorbed by the bottom diode. For a wavelength of 1000 nm, no light is absorbed by the perovskite layer as shown in Figure 5.13(c). The light penetrates deep into the silicon bottom solar cell. A distinct fraction of the light is absorbed by the ITO front contact because of the high free carrier absorption. The light absorbed by the ITO does not contribute to the J_{SC}.

In the next step, the influence of the period of the surface texture on the QE and J_{SC} is studied. For each period, the J_{SC} of the top and bottom solar cells were matched by adjusting the thickness of the top solar cell. Figure 5.15(a) shows the relationship between the perovskite layer thickness of the top cell and the period of the front texture for matched J_{SC} conditions. The period is varied from 100 nm to 1000 nm leading to an increased perovskite layer thickness from 225 nm to 370 nm. The influence of the period of the surface texture on the QE of the top and the bottom diode is shown in Figures 5.14(a) and 5.14(b). Texturing the front surface leads to an improved incoupling of light in the solar cell. Therefore, the QE of the top cell is increased for short wavelengths (300 nm - 500 nm). Furthermore, more light is coupled to the bottom solar cell. Consequently, the J_{SC} of the top and bottom solar cells is increased. In order

to match the J_{SC} of the bottom solar cell by the top solar cell, the thickness of the top cell has to be increased. The increased thickness of the top cell lowers the transmission of the top cell and the QE of the bottom solar in the spectral range between 500 nm and 800 nm. The small absorption of the top solar cell for wavelengths larger than 900 nm is caused by small inaccuracies in fitting the optical constants of perovskite by the FDTD simulation tool. However, the absorption of wavelengths >900 nm has no influence on the J_{SC}. The J_{SC} is only calculated for photon energies larger than the bandgap. Hence, the absorption of wavelengths >780 nm represents parasitic optical losses.

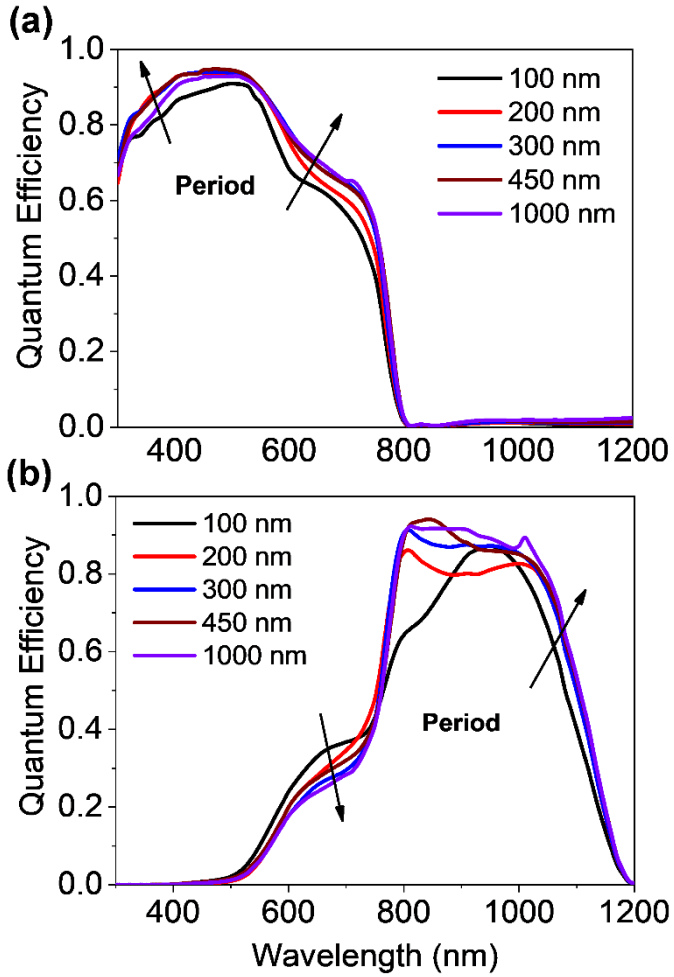

Figure 5.14: Influence of the period of the surface texture on the matched short-circuit current of the (a) top and (b) bottom solar cells.

The thickness of the top solar cell is increased until the J_{SC} of the top, and bottom solar

cells are matched. A maximum matched J_{SC} of 20 mA/cm^2 is achieved for periods of the surface texture of 450 nm or larger. In this case, the thickness of the top cell is equal to 285 nm. The matched J_{SC} as a function of the period of the surface texture is shown in Figure 5.15(b). For periods of the surface texture larger than 450 nm, the matched J_{SC} remains almost unchanged.

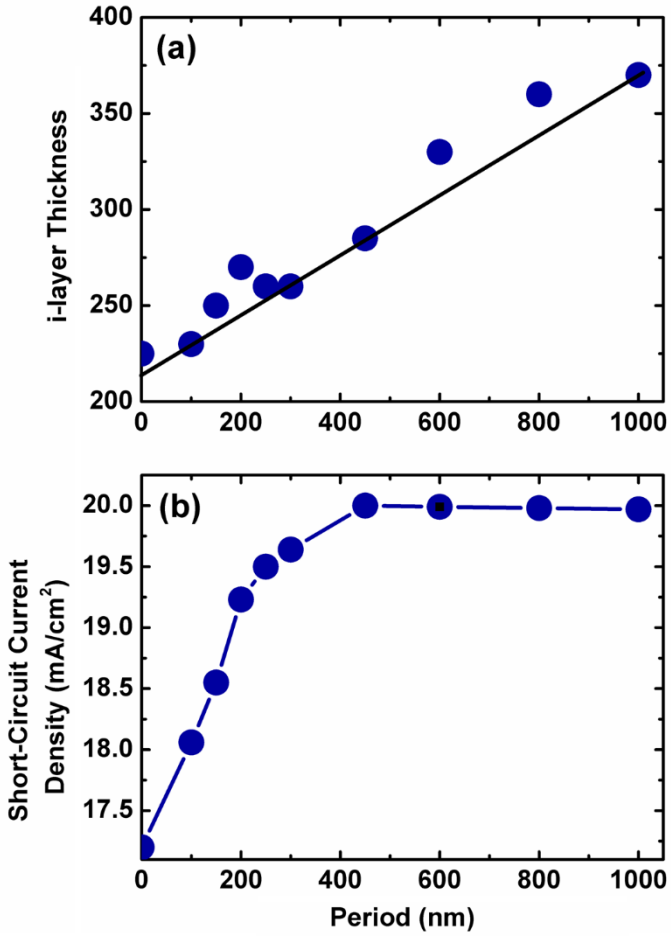

Figure 5.15: (a) Relationship between the period of surface texture and perovskite layer thickness of the top solar cell of a perovskite/silicon tandem solar cell under short-circuit current matching conditions. (b) Short-circuit current density as a function of the period of the surface texture.

It should be mentioned that the etching angle of the substrate relative to the surface of the silicon wafer remains constant at 54.7°so that an increased period results in an increased height of the surface texture. The root means square roughness of the

substrate is directly proportional to the height of the pyramids. Hence, it can be concluded that for a constant etching angle, the period is directly proportional to the root mean square roughness of the substrate. With increasing roughness, the integration of the top cell on the textured substrate is getting more complex. Furthermore, the diffraction of the incident light decreases with an increasing surface period. For larger periods, the light is only refracted by the surface of the solar cell. This leads to a drop in the J_{SC} of the top solar cell. To compensate for the drop of the $J_{SC,}$ the thickness of the top solar cell has to be increased from 285 nm to 370 nm for a surface period of 1000 nm. So, an optimum period of the surface texture and perovskite layer thickness of 450 nm and 285 nm is obtained. In the following, the optical incoupling of the light in the bottom diode is investigated. The perovskite and metal oxide contact layers exhibit refractive indices of approximately 2, while silicon exhibits a refractive index of 4. Hence, a distinct reflection at the interface can be expected. However, the used structure shows the very good coupling of the light from the top to the bottom diode. In order to illustrate the good incoupling of the light, the refractive index is plotted as a function of the height of the solar cell. The effective medium approach is used to calculate the effective refractive index as a function of the height, where n_{per} and n_{si} are the refractive index of perovskite and silicon ($n_{per}\approx n_{ZnO}\approx n_{ITO}\approx n_{IOH}\approx 2$, $n_{si}\approx 4$). The effective medium approach is applicable if the surface texture is distinctly smaller than the incident wavelength. This assumption might not be fulfilled. However, the approach provides a reasonable approximation. For a pyramidal surface texture, a parabolic change of the refractive index is calculated. If the pyramids would be replaced by cones with a parabolic surface profile, a linear change of the refractive index as a function of the height would be observed. A cone-like surface texture allows for an almost perfect incoupling of the light in the solar cell. The pyramidal structure is very close in terms of the incoupling. If the PSC would be

prepared on a flat silicon bottom cell, an abrupt change of the refractive index would be observed, which leads to maximum reflection losses, as shown in Figure 5.12.

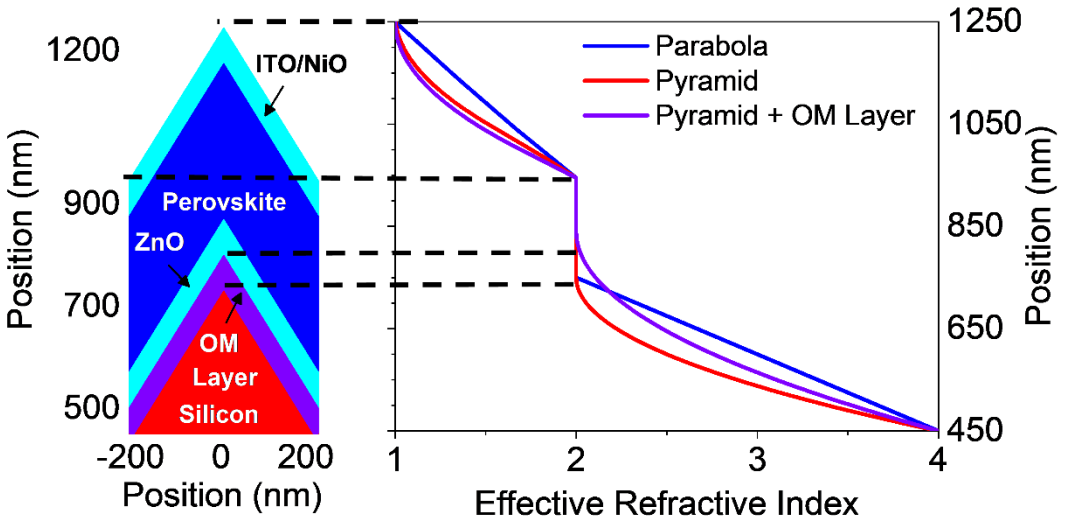

Figure 5.16: Cross-section of the textured perovskite/silicon tandem solar cell with an effective refractive index as a function of the height of the solar cell.

The incoupling of light in the flat bottom cell could be improved by introducing an optical matching (OM) layer with a refractive index of $n_{OM}=(n_{ZnO}\times n_{si})^{0.5}\approx 3.5$, a low extinction coefficient and the thickness of the OM-layer to be equal to an odd multiple of the quarter wavelength of the light that should be coupled in the bottom diode. In the case of a textured perovskite/silicon TSC, the situation is different. Both interfaces of the textured solar cell (air/perovskite and perovskite/silicon) in Figure 5.16 can be approximated by a parabolic refractive index gradient, allowing for an excellent incoupling in the top and bottom solar cells. In the case of the red curve (Figure 5.16), it is assumed that the refractive index of the OM-layer is 2, while in the case of the purple curve, the refractive index is set to 3.5. It can be seen that the OM-layer has only a small effect on the effective refractive index. This is confirmed by FDTD simulations of the solar cell structure with and without an OM-layer. Introducing an OM-layer does not lead to an increased total QE and J_{SC}. Hence, no additional optical matching layer is required. Two reasons are responsible for the good incoupling of the light in the bottom diode. Firstly, the top cell is prepared on a textured surface.

Secondly, the refractive index of the contact/charge-transporting layers of the top cell is almost equal to the refractive index of the perovskite layer.

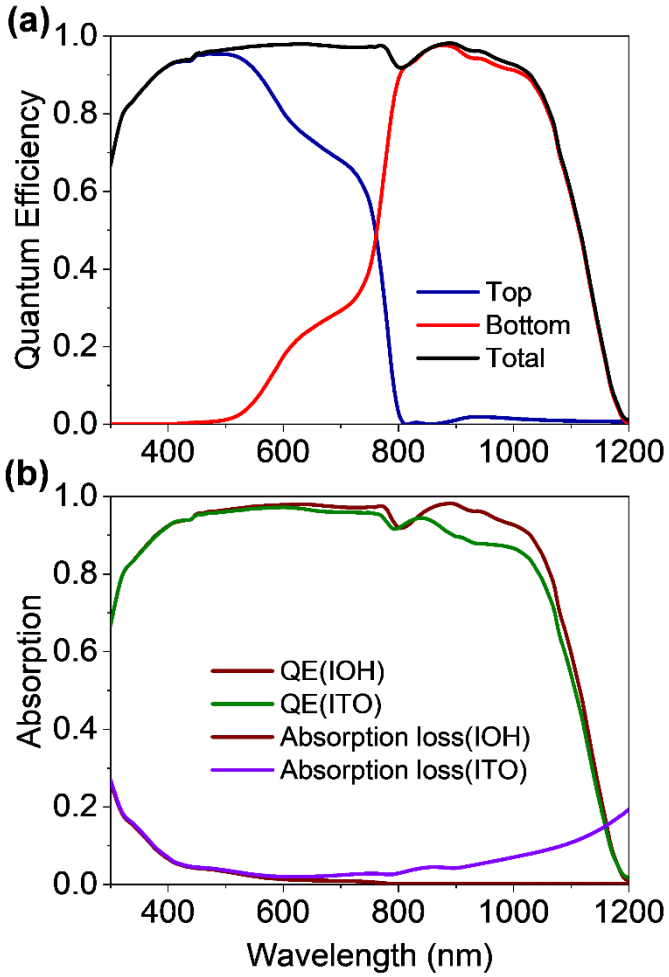

Figure 5.17: (a) Calculated quantum efficiency of top, bottom and, total perovskite/silicon tandem solar cell using a hydrogen doped indium oxide front contact (b) Calculated quantum efficiency and absorption of front contact of perovskite/silicon tandem solar cell with hydrogen doped indium oxide and indium tin oxide front contacts.

In the third step of the optimization process, the parasitic absorption of the solar cells is minimized by replacing the indium tin oxide front contact with hydrogen doped indium oxide. ITO films exhibit rather a low electron charge carrier mobilities (10 - 25 cm^2/Vs), so that high doping concentrations are required to realize front contacts with high conductivity. The high doping concentration causes high free carrier absorption, which limits the QE of the silicon bottom solar cell.(Barraud et al., 2013b; T. Koida et

al., 2009a) In the following calculations, the sheet resistance of the front contact was assumed to be 35 Ω. The sheet resistance is consistent with data published in the literature for highly efficient silicon heterojunction solar cells.(Barraud et al., 2013b; T. Koida et al., 2009a) The charge carrier mobility of the transparent conductive oxide has to be increased to keep the front contact sheet resistance constant while decreasing the free carrier absorption losses. Hence, the ITO film is replaced by a hydrogen doped indium oxide (IOH) film. Hydrogen doped indium oxide exhibits a distinctly higher electron charge carrier mobility.(Barraud et al., 2013b) Sputtered hydrogen doped indium layers exhibit 5 to10 times higher electron mobility (μ_e=66 cm^2/Vs) than ITO layers. Subsequently, the doping concentration of IOH films is 5-10 lower, which leads to a shift of the plasma wavelength to longer wavelengths. Hence the absorption loss of the front contact for long wavelengths is distinctly reduced and the QE of the bottom solar cell is increased for wavelengths larger than 800 nm. Later, the thickness of the top cell is slightly increased to reach a matched J_{SC} of 20.61 mA/cm^2. Figure 5.17(a) shows the calculated QE under matched current conditions. Replacing the ITO by the IOH leads to a gain of the J_{SC} of 0.61 mA/cm^2 due to the lower optical losses of IOH front contact, which is seen in Figure 5.17(b). The theoretical limit of the J_{SC} for an ideal TSC is 23 mA/cm^2. The experimentally measured bottom solar cell has imposed an upper limit of the J_{SC} of 21.4 mA/cm^2 on the studied solar cell. Hence, the achieved J_{SC} is very close to this limit. Later, the study has been extended for the larger structures, where optical simulation results are included in Appendix C (Figure C1.4). The study revealed the influence of different growth mechanisms on the fabrication of perovskite/silicon TSCs. A detailed discussion is provided in the literature.(Wayesh Qarony; Mohammad Ismail Hossain; Vladislav Jovanov; Alberto Salleo; Dietmar Knipp; Yuen Hong Tsang;, 2019) A potential ECE of the perovskite/silicon TSC can be estimated by combining the calculated J_{SC} with V_{OC}s and FFs measured for single-junction perovskite and silicon solar cells. The best

experimentally realized perovskite single-junction solar cells exhibit V_{OC} and FF of 1.182 V and 77%. In comparison, the best silicon solar cells exhibit V_{OC} and FF of 0.74 V and 84.9%.(Green, Hishikawa, et al., 2019; Y. Wang et al., 2018) By considering a reduction of the V_{OC} of the bottom solar cell due to the reduced J_{SC} an ECE of 32.5% can be estimated for a perovskite/silicon TSC. In order to reach higher ECE, the V_{OC} of the PSC has to be further increased.

5.3 Optically Rough but Electrically Flat Tandem Solar Cells

5.3.1 Perovskite/Silicon Tandem Solar Cells

This is the prolonged version of the study, as described in Chapter 4 (Section 4.1), where only single-junction PSCs were investigated. In this study, we focus on the implementation of perovskite/silicon TSCs, where optimized single-junction PSC is used as a potential top cell for realizing perovskite/silicon TSC. It is found that the textured PSCs lead to a distinct improvement of J_{SC}s and ECEs, which are done by either PVD or CVD techniques. However, the textured perovskite surface may affect the microstructure, and electronic structure of perovskite material, which reduces the electronic performances (V_{OC}, FF), resulting in, the ECE of a solar cell is negatively influenced. Hence, it is assumed that the planar perovskite layer may overcome such problems. At this stage, it remains unclear which structure is better, herein, we present an alternative device structure for the fabrication of perovskite/silicon TSCs that we named optically rough but electrically flat (OREF) design. By considering OREF design, advantages from textured solar cells can be achieved while maintaining the flat absorber layer. In the proposed structure, interfaces between perovskite and contacts are assumed to be flat, and the air/front contact interface is being textured, which improves both optical and electrical performances in the solar cell. The aim of this study is not to claim that the OFER design is better than all textured TSC. The study proposes an alternative device design for realizing efficient perovskite/silicon TSCs. In this study, two different metal oxides are utilized as front contacts and compared in terms of their QE and J_{SC}. In the case of a single-junction PSC, a thin and highly doped metal oxide film can be selected. The absorption loss due to free carrier absorption is usually low. For a perovskite/silicon TSC, the situation is different. The free carrier absorption might have a negative effect on the QE for long wavelengths. Figure 5.18

exhibits the optical simulation of the OFER perovskite/silicon TSC. Details on the calculation of the QE are provided in Ref.(Mohammad I. Hossain et al., 2018a)

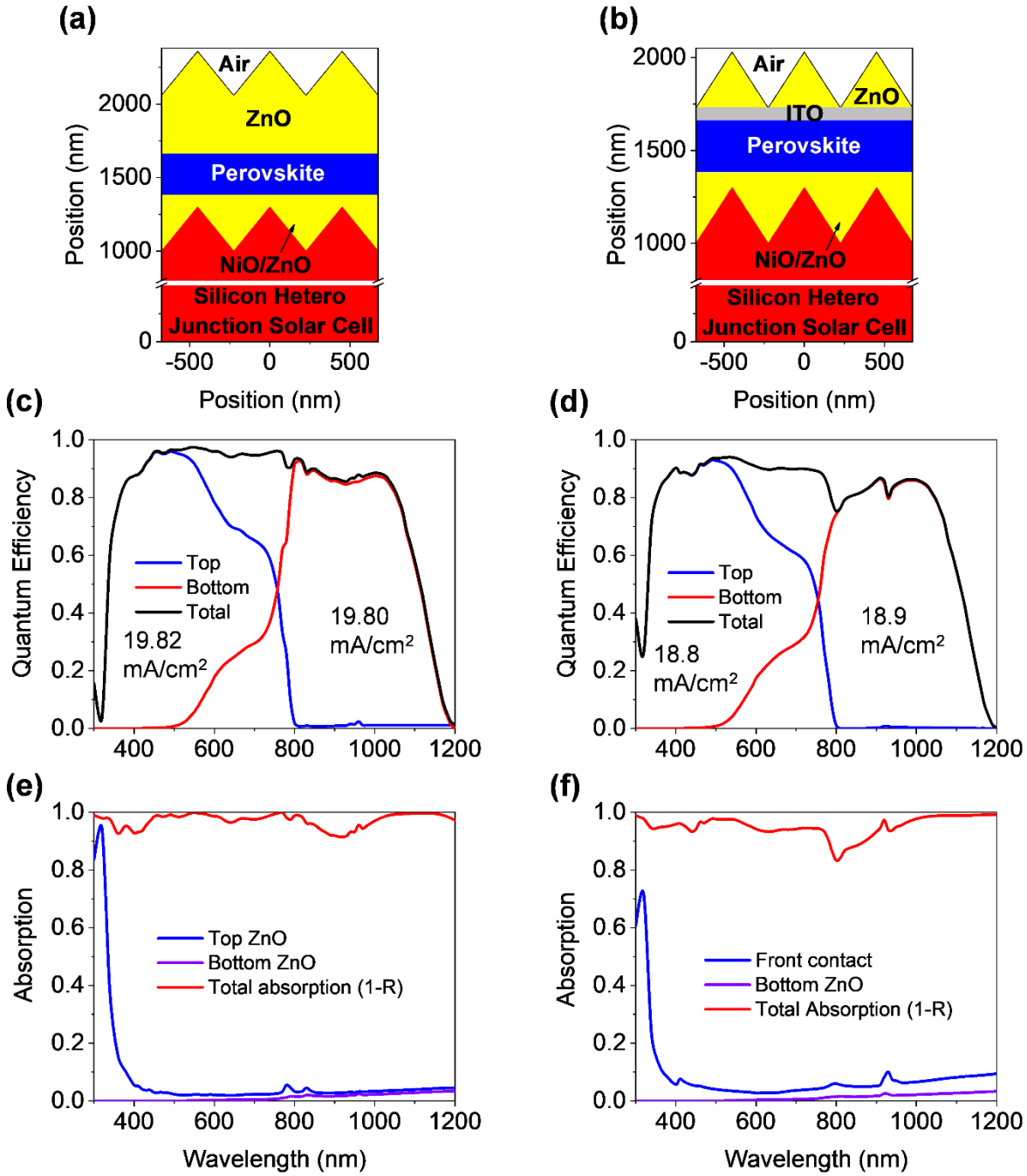

Figure 5.18: The schematic sketch of electrically flat and optically rough perovskite/silicon tandem solar cells with (a) a continuous ZnO front contact and (b) continuous ITO front contact. The corresponding quantum efficiency of the top and bottom cell and the total quantum efficiency are shown in (c,d). The corresponding total absorption (1-R) and the absorption of front and back contacts are also shown in (e,f).

A TSC with a continuous ZnO front contact layer is compared to a TSC with a continuous ITO layer with equal conductivity. An extended Drude Lorentz model was used to describe the complex refractive index of ZnO and ITO. The model used to calculate the optical constants is provided in Appendix B (Section B.1.4). The calculated complex refractive indices were compared to experimentally determined optical constants, and a good agreement was observed. The ZnO layer has a thickness of 400 nm, while the thickness of the ITO layer is only 70 nm. The parameters used for calculating the complex refractive index are provided in Appendix B (Table B1). The TSC, as depicted in Figures 5.18(a, b, c), exhibits almost equal performance with the previously investigated all textured perovskite/silicon TSC described in Section 5.2. Here, we have compared the ZnO font contact with an ITO layer with equal conductivity. Due to the higher doping concentration of the ITO layer, distinctly higher absorption of the front ITO layer is observed, as shown in Figure 5.18(f). The optical loss increases from 1.65 mA/cm^2 to 2.5 mA/cm^2, while the total J_{SC} drops to approximately 19 mA/cm^2. It can be concluded that high doping concentrations and thin metal oxide front contacts can be used for solar cells using materials with large bandgaps, while for low bandgap solar cells or multijunction solar cells the doping concentration should be reduced and the thickness of the front contact should be increased to limit the optical losses of the front contact. It is believed that the OFER device design can be applied to other TSCs. In the next section, all perovskite TSC is discussed by utilizing the OFER device structure.

5.3.2 Perovskite/Perovskite Tandem Solar Cells

Perovskite/perovskite TSCs covered with a flat front contact, a pyramidal front contact, and a metasurface front contact are shown in Figures 5.19. The dimensions of the front contact of the TSC are identical with the dimensions used for the investigated

single-junction PSC, as described in Chapter 4 (Section 4.2).

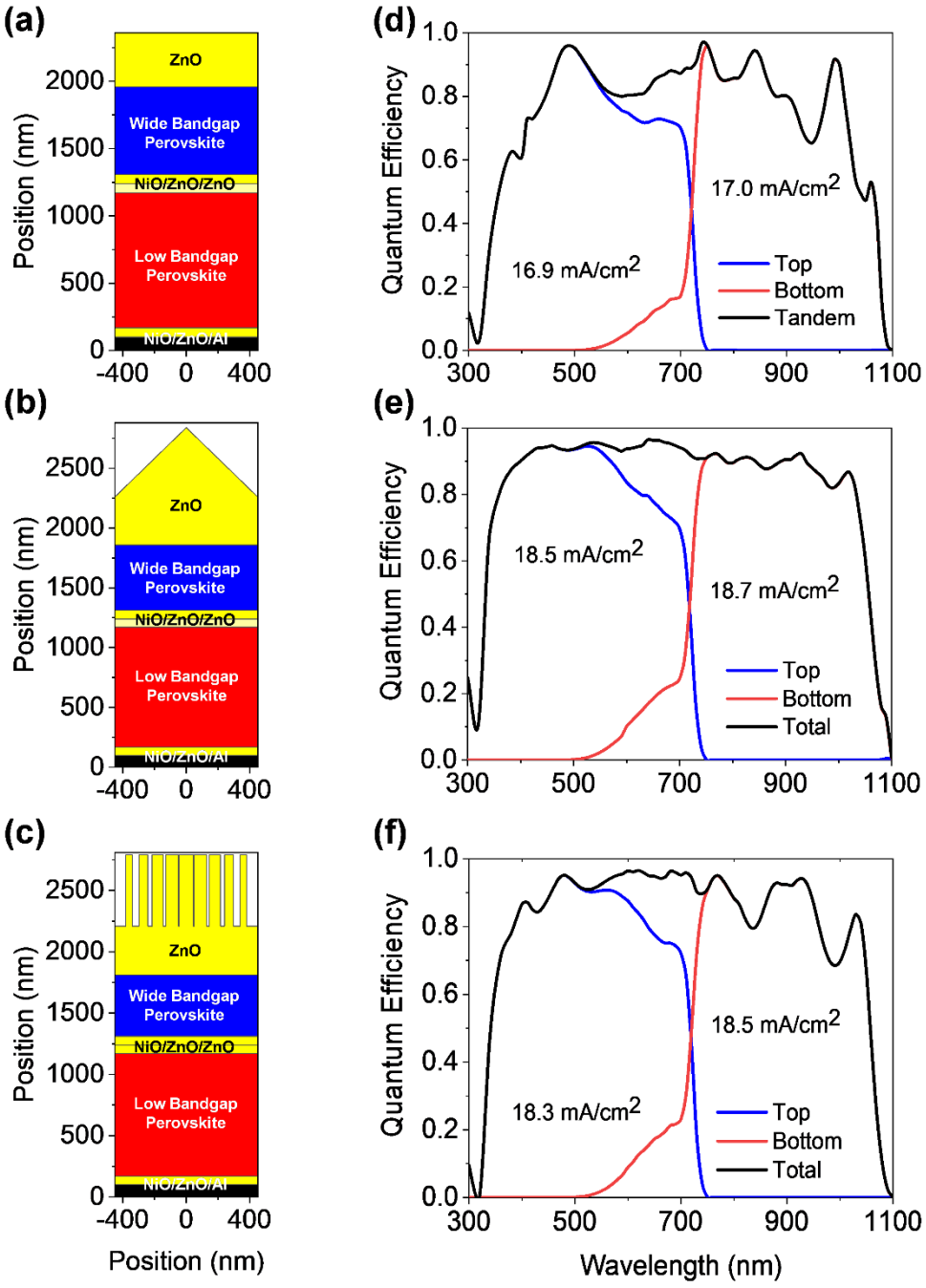

Figure 5.19: Schematic sketches of perovskite/perovskite tandem solar cells with (a) the flat, (b) the pyramid texture, and (b) the integrated metasurfaces front contacts. (d,e,f) Corresponding simulated quantum efficiencies and short-circuit current densities.

The thickness of the front ZnO layer was kept constant to 400 nm, and the height and

period of the pyramid and the nanowires used to form the metasurface were also kept constant at 600 nm and 900 nm, respectively. Figures 5.19(a), 5.19(b), and 5.19(c) display the schematic cross-sections of perovskite/perovskite TSCs with flat, pyramid texture, and integrated metasurfaces, where a wide bandgap (E_g~1.78 eV) perovskite (MAPbBrI) and small bandgap (E_g~1.16 eV) perovskite (MAPbSnI) were used as top cell and bottom cell, respectively. The thickness of the bottom perovskite absorber was 1000 nm for all three solar cells, while the top cell has absorber thicknesses of 650 nm, 500 nm, and 500 nm for flat, pyramid texture, and metasurface structured perovskite/perovskite tandem solar cells. The corresponding simulated QEs are shown in Figures 5.19(d), 5.19(e), and 5.19(f). Visible light is absorbed by the top perovskite absorber, while near-infrared light is absorbed by the bottom diode. All three tandem solar cells in Figure 5.19 are current matched. The J_{SC}s of perovskite/perovskite TSCs with flat, pyramid texture, and integrated metasurfaces are 16.9 mA/cm^2, 18.5 mA/cm^2, and 18.3 mA/cm^2, respectively. The TSC with pyramid and metasurface front contact reveal almost equal J_{SC}s. As compared to the flat tandem solar cell, solar cells with pyramid texture and optical metasurfaces provide an increased J_{SC}s of approx. 10%. Hence, the results for the TSCs are consistent with the results for the single-junction PSCs. The integration of a pyramid texture or a non-resonant metasurface allows for an improved light incoupling and an increased J_{SC}. By combining the calculated J_{SC} with an experimentally realized electrical parameter of PSCs, an ECEs for both perovskite/perovskite TSCs can be estimated to beyond 30%.(D. Chen et al., 2018; Yumnam & Wagner, 2018)

To conclude, several perovskite materials current have been investigated for single or multi-junction solar cells, which exhibit a comparable refractive index. Hence, the approach can be applied to a variety of perovskite materials without making significant adjustments to the dimensions.

5.3.3 Summary

In the first section of this chapter, we study the detailed balance theory (Shockley Queisser model) to realize a fundamental understanding of energy conversion efficiency losses and limits of single-junction and tandem solar cells. However, only recent work on more generalized detailed balance limits shows that the Shockley Queisser model must be extended to take charge transport, e.g., non-radiative, into account. Furthermore, optical limits, e.g., imposed by the Yablonovitch limit, must be considered. It is shown that the optics of a solar cell has not only an influence on the short-circuit current density but all solar cell parameters. The influence of photon management on the solar cell parameters of a perovskite single-junction solar cell and a perovskite/silicon solar cell is discussed in greater details. The photon management of a perovskite single-junction solar cell can be predominately improved by an improved light incoupling and a reduction of optical losses in the solar cell. The photon management of silicon solar cells is more complicated. In addition to improving light incoupling and minimizing optical losses to the light must be trapped in a solar cell. We have proposed a potential design for the perovskite/silicon tandem solar cells using a moth-eye surface texture, which allows for an improving light incoupling. The proposed perovskite/silicon tandem solar cell exhibits an energy conversion efficiency of over 32%, and a matched short-circuit current density of 20.7 mA/cm^2.

Secondly, the study aims at providing guidelines for the realization of perovskite/silicon solar cells with high energy conversion efficiency. Perovskite/silicon tandem solar cells have been designed with short-circuit current densities exceeding 20 mA/cm^2 while taking realistic device structures into consideration. A realistic set of input parameters was selected, which involves the material properties and geometry of the tandem solar cell. The high short-circuit current density allows for the realization of perovskite/silicon tandem solar cells with conversion efficiencies exceeding 30%. To allow for a realistic

description of the optical wave propagation, a hybrid approach was used, which combines Finite-Difference Time-Domain simulations with experimentally measured data of the bottom solar cell. The perovskite/silicon tandem solar cell has to be textured to minimize reflection losses. Hence the perovskite top cell has to be prepared on top of the textured silicon bottom cell. This requires the use of materials and deposition techniques compatible with the fabrication on a textured substrate. In this study, ITO/NiO and IOH/NiO hole and ZnO electron transporting layers were used, which can be prepared by sputtering. Optimal dimensions of the surface texture were derived, assuming that the top solar cell is prepared on an anisotropic etched silicon solar cell. For a period of the surface texture of approximately 500 nm or larger the short-circuit current density is maximized. Furthermore, the textured silicon solar cell allows for an almost perfect incoupling of the longer wavelengths light in the bottom cell. In the next step, the contact layers were optimized by minimizing the free carrier absorption losses. The ITO/NiO front contact was replaced by an IOH/NiO layer, which exhibits 3-5 times higher electron mobility. The higher charge carrier mobility allows for using a lower doping concentration while keeping the sheet resistance of the contact layer constant. The use of hydrogen doped indium oxide allows for the gain of the short-circuit current density of 0.6 mA/cm^2, resulting in a total short-circuit current density of 20.6 mA/cm^2.

Finally, in addition to the all textured perovskite/silicon solar cells, we proposed an alternative device design, we named the optically rough but electrical flat design, for the perovskite-based tandem solar cells. In the proposed TSC design, interfaces between perovskite absorber and contacts are assumed to be flat and front contact is covered with a textured surface. Hence, both optical and electrical performances are improved in the case of tandem solar cells. The optical simulation results of OFER TSC provided a comparable short-circuit current densities and estimated ECEs with

all-textured TSCs. Therefore, we believe that the proposed device structure is an alternative solution for the implementation of high-efficiency TSCs.

CHAPTER 6

MULTISPECTRAL COLOR IMAGE SENSORS WITH PEROVSKITE ALLOYS

This chapter discusses how multi-bandgap perovskite material systems can be used to implement efficient color image sensors, which have no color aliasing or color Moiré error. Here, we focus on the vertically stacked color sensor design, which has an enormous advantage than conventional filter-based optical color imaging. In the first step, we focus on the three-channel vertically stacked color image sensor using tunable bandgap mixed-halide perovskites. Then, the mixed-halide perovskites have been used to realize six-channel vertically stacked multispectral image sensors. Herein, devices are compared based on their quantum efficiencies (QEs) and spectral responsivities (SRs); hence, we aim to maximize the QEs and SRs of investigated sensors. Detailed explanations of perovskite optical color sensors are provided in the following sections.

6.1 Three-channel Perovskite Color Image Sensor

Image sensing technology has a great impact on our daily life by providing visual information, contributing to improvements in healthcare, safety, and security, and it is an essential part of our personal communication and entertainment. Most electronic imaging technology is based on the use of CMOS (Complementary Metal-oxide Semiconductor) electronics in combination with arrays of silicon photodetectors. Throughout the last two decades, the pixel size of image sensors has been reduced, and the resolution has been increased, while the cost has been reduced.(El Gamal & Eltoukhy, 2005; Theuwissen, 2008) However, the basic color detection scheme remains unchanged. Color image sensors usually consist of an array of photodiodes, which are covered by a side-by-side arrangement of optical filters to detect the colors red, green, and blue.(Bayer, 1976; Lukac & Plataniotis, 2005a) Hence, a color pixel consists of three sensor elements to detect the colors red, green, and blue. Most real devices use a Bayer filter arrangement, which consists of a 1x red, 2x green, and 1x blue filters.(Bayer, 1976) However, for simplicity, we will use the most fundamental

implementation in this manuscript. The efficiency of the detection process is characterized by the normalized optical efficiency (NOE), which can be used to characterize grayscale and color image sensors. The NOE is defined as the ratio of optical power absorbed by the photodetector to power incidence on the total pixel area.(Marinelli & Palange, 2011) Amongst others, the NOE is limited by geometrical factors like the area fill factor (AFF), which is the ratio of the actual detector size to the overall size of the color pixel. For simplicity, we assume AFF to be 100%. In the case of a grayscale camera without optical filters and an AFF of 100%, the NOE is equal to the quantum efficiency ($QE_{BW}(\lambda)$) of the individual diodes.

$$NOE_{BW}(\lambda) \cong QE_{BW}(\lambda). \tag{6.1}$$

However, in the case of a color camera using optical filters, the NOE is given by

$$NOE_{CFA}(\lambda) \cong \frac{1}{A_{CP}} \times \left(A_R \times T_R(\lambda) + A_G \times T_G(\lambda) + A_B \times T_B(\lambda)\right) \times QE_{BW}(\lambda) \tag{6.2}$$

where T_R, T_G and T_B are the transmissions of the color filters. We assume the peak transmission of the filters to be 100% for the three color channels. A_R, A_G, and A_B are the areas of the red, green, blue color detector and A_{CP} is the area of the total color pixel. In the case of a color filter array, A_R, A_G, and A_B are equal to $1/3 \times A_{CP}$, so that the NOE is given by

$$NOE_{CFA}(\lambda) \cong \frac{1}{3} \times QE_{BW}(\lambda). \tag{6.3}$$

Hence, the NOE exhibits an upper limit of 33%, because 2/3 of total incident photons are not used as part of the detection process.(Gunturk et al., 2005a) For instance, when red light is incident on a color pixel, only the red channel detects a signal, but the red detector covers only 1/3 of the pixel area.

This, consequently, limits the image contrast and the low-level light sensitivity of the

sensors. Hence, the NOE is limited by the side-by-side arrangement of the color filter, resulting in the reduction of the dynamic range by 20×log(N)≈ 10 dB and increase the signal to noise ratio (SNR). The NOE can be increased by a vertically stacked color sensor. The detection principle is based on the wavelength-dependent absorption of photons penetrating a semiconductor. The effect can be used to realize color sensors if the photogenerated charges are collected at different depths of the device. Our sensor consists of three vertically stacked semiconductor diodes. Blue light is absorbed by the top diode, while the green and red light are absorbed by the middle and bottom diodes, respectively. The vertically stacked color sensor does not require the use of color filters, allowing to capture images without sampling artifacts like color aliasing or color Moiré. The NOE of the stacked color sensor (SCS) can be calculated by

$$NOE_{SCS}(\lambda) \cong \frac{1}{A_{CP}} \times \left(A_R \times QE_R(\lambda) + A_G \times QE_G(\lambda) + A_B \times QE_B(\lambda)\right) \quad (6.4)$$

Because the area of each sensor channel is equal to the total area of the color pixel, A_R=A_G=A_B=A_{CP} and equation 4 can be simplified to

$$NOE_{SCS}(\lambda) \cong QE_R(\lambda) + QE_G(\lambda) + QE_B(\lambda). \quad (6.5)$$

The idea of using vertically stacked color sensing technology has been proposed and implemented several years ago by a variety of research teams.(Herzog, Knipp, Stiebig, & Koenig, 1998; Hubel et al., 2004; Jansen-van Vuuren, Armin, Pandey, Burn, & Meredith, 2016; Lyon & Hubel, 2002; Merrill, 1999; Theil et al., 2000; Topic, Stiebig, Knipp, & Smole, 1999). Some years later, the first commercial product based on stacked color sensors was offered by Foveon.(Hubel et al., 2004) Hence, the sensor concept is commonly referred to as the Foveon sensor. Almost all work on stacked vertically color sensors is based on silicon technology. However, the use of an indirect bandgap and low bandgap material like silicon leads to poor color separation. Due to the indirect bandgap, a considerable overlap of the spectral responsivities (SRs) of the color

channels and a high color error is observed.(Hubel, 2005a)

In this study, mixed-halide perovskite materials are studied for the realization of SCSs. Perovskites have recently gained substantial attention due to their outstanding optical and electronic properties. Unlike silicon, mixed-halide perovskites exhibit a direct bandgap, and the bandgap can be tuned over a wide spectral range by changing the composition of the halide components in the mixed-halide perovskites. Hence, the bandgaps can be matched very well to the SRs of the human vision system. Additionally, the higher absorption coefficient and electron/hole diffusion length allow for developing sensors with high QE and high NOE. Herein, perovskite alloys are used to study the three-channel vertically stacked color sensors, where the perovskite material systems exhibit an excellent optical bandgap tunability with direct bandgap semiconductor properties. The electronic structure and bandgap can be nicely tuned only by changing the composition of the halide components in the mixed-halide perovskites. The study primarily focuses on achieving very high QE and SR of such vertically stacked perovskite color sensor by introducing textured interfaces in the devices. Finally, a colorimetric characterization method is utilized to determine the color error and compare with conventional color imagers.

6.1.1 Optical Properties of Bandgap Tunable Mixed Halide Perovskite

The aim of digital cameras is to mimic or replicate the human vision system. Hence, the human vision system represents the reference system for the evaluation or benchmarking of different color sensors or imaging technologies. The International Commission on Illumination (CIE) works on colorimetry and defined a standard for the specification of color stimuli.(CIE: Publication No. 15.2, 1986) A particular color stimulus in the visible wavelength region is represented by tristimulus values XYZ in the CIE

system. The XYZ values were experimentally determined by using human observers.(Fernandez-Maloigne & Trémeau, 2013) This experiment resulted in the definition of color matching functions (CMFs) and the standards that are used by industry. The CMFs are provided in section 6.1.3(B). We used the CMF to derive the design of the color sensor. The CMF exhibits maxima of the sensitivities at 2.75 eV, 2.2 eV and 2.05 eV, and cut-off energies at 2.5 eV, 2.1 eV and 1.8 eV. We selected absorbers with bandgaps equal to the cut-off energies of 2.5 eV (blue), 2.1 eV (green), and 1.8 eV(red). The absorber with a bandgap of 2.5 eV is used for the top diode, a material with a bandgap of 2.1 eV is used for the middle diode and 1.8 eV for the bottom diode, respectively.

The perovskite material system is usually composed of three elements, an organic/inorganic cation (Cs^+, $MA^+(CH_3NH_3^+)$, and FA^+ $(NH_2CH_3NH_2^+)$, a divalent cation (Pb^+ or Sn^+), and a monovalent halide anion (I^-, Cl^-, or Br^-).(Stranks & Snaith, 2015b) The electronic structure of the perovskite material systems can be tuned over an extensive range. In this study, the bandgap must be tuned from 2.5 eV to 1.8 eV, which can only be achieved by replacing the monovalent halide anions (I^-, Cl^-, or Br^-). The resulting materials are $MAPbCl_3$, $MAPbBr_3$, and $MAPbI_3$, with bandgaps of 3.1 eV, 2.3 eV, and 1.6 eV.(Fujiwara, Kato, Tamakoshi, Miyadera, & Chikamatsu, 2018; Kumawat et al., 2015; Leguy et al., 2016; Noh, Im, et al., 2013; J.-S. Park et al., 2015; Shirayama et al., 2016b)

To implement the required bandgaps, mixed-halide perovskites will have to be used. A $MAPb(I_{1-x}Br_x)_3$ mixture will be used for the middle and bottom diode while a $MAPb(Br_{1-x}Cl_x)_3$ mixture is used for the top diode. In a first step, the composition of the material was determined by using the bowing parameters which is given for the mixed-halide perovskites of $MAPbI_{1-x}Br_x$ and $MAPbBr_{1-x}Cl_x$ by the following analytically expression: $E_g(x) = 1.61 + 0.34x + 0.33x^2$ eV and $E_g(x) = 2.28 + 0.48x + 0.3x^2$ eV, respectively. To tailor the absorber materials to the required bandgaps, the top diode is based on

$MAPb(Br_{1-x}Cl_x)_3$, with a concentration of x=37%. The absorbers of the middle and bottom diodes are based on $MAPb(I_{1-x}Br_x)_3$, with a concentration of x=80% and 40%. The optical-constant spectra of the desired alloy compositions were calculated by applying the energy shift model. Halogen composition-dependent optical bandgaps of mixed-halide organic-inorganic perovskite materials are provided in Appendix D (Figure D1.1). The optical constants of single-phase materials (i.e., $MAPbI_3$,(Shirayama et al., 2016b) $MAPbBr_3$,(J.-S. Park et al., 2015) and $MAPbCl_3$ (Leguy et al., 2016)) where used as input parameters. The optical function of an arbitrary composition is synthesized from a pair of known optical functions. In this case, the optical spectra of the end compositions are blue (or red)-shifted so that the bandgap energies match with that of the target composition.(Minoura et al., 2015; Snyder, Woollam, Alterovitz, & Johs, 1990a) In the calculation of a $MAPb(I_{1-x}Br_x)_3$ alloy, for example, the optical spectrum of $MAPbI_3$ is shifted toward higher energy, while that of $MAPbBr_3$ is red-shifted, and these two spectra are synthesized with appropriate weighting factors. The extinction coefficient of the perovskite alloys of $MAPb(Br_{0.63}Cl_{0.37})_3$, $(MAPbI_{0.2}Br_{0.8})_3$ and $MAPb(I_{0.6}Br_{0.4})_3$ calculated by the energy shift model are shown in **Figure 6.1.**

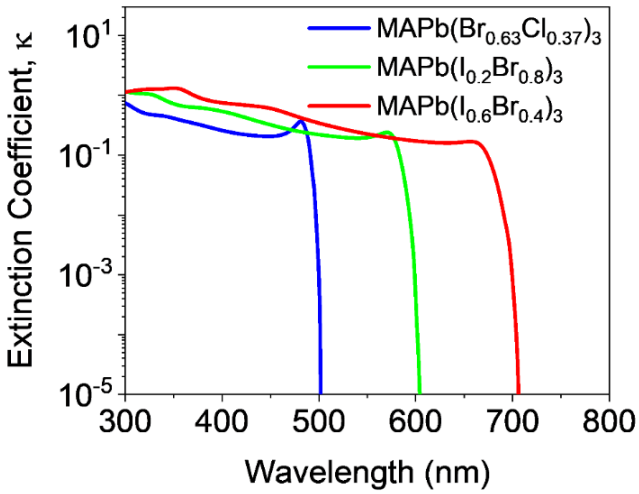

Figure 6.1: Extinction coefficient of calculated mixed-halide perovskites of $MAPb(Br_{0.63}Cl_{0.37})_3$, $(MAPbI_{0.2}Br_{0.8})_3$, and $MAPb(I_{0.6}Br_{0.4})_3$ with an optical bandgap of 2.5 eV, 2.1 eV, and 1.8 eV, respectively. MAPbBr0.63Cl0.37, MAPbI0.2Br0.8, and MAPbI0.6Br0.4 with an optical bandgap of 2.5 eV, 2.1 eV, and 1.8 eV, respectively.

6.1.2 Device Design and Methods for Optical Wave Propagation Calculation

The schematic cross-sections of vertically stacked perovskite color sensors with planar and textured interfaces are shown in Figure 6.2(a) and Figure 6.2(c), respectively. The flat device structure in Figure 6.2(a) consists of a 75 nm doped ZnO used as a hole blocking / electron transporting layer (ETL), followed by a $MAPb(Br_{1-x}Cl_x)_3$ absorber with a bandgap of 2.5 eV. The absorber detects blue light in the top diode. $MAPb(I_{1-x}Br_x)_3$ absorbers with bandgaps of 2.1 and 1.8 eV are used to form the middle (green) and bottom (red) absorber layers, while an 80 nm double layer of NiO / ZnO is used as electron blocking layer / hole transporting layer (HTL). A very thin (5 nm) layer of NiO facilitates the efficient transport of holes and blocking of the electrons. However, the use of a thick ZnO layer (75 nm) allows for a high lateral electrical conductivity of each contact, resulting in a low series resistance and low absorption loss of the contact layers. Such contact layers have been commonly utilized for the realization of efficient perovskite solar cells (PSCs).(Forin, Purica, Budianu, & Schiopu, 2012a; J.-Y. Wang et al., 2009a; You et al., 2016a) The textured substrate is formed by placing a textured zinc oxide (ZnO) layer on top of the metal back reflector before depositing all other layers. A textured zinc oxide layer can be formed by direct deposition of films using metal-organic chemical vapor deposition (MOCVD), pulsed laser deposition, or sputtering followed by wet etching.(Hongsingthong et al., 2010; Mohammad I. Hossain, Hongsingthong, et al., 2019; Müller, Rech, Springer, & Vanecek, 2004b; Tsoutsouva, Panagopoulos, Papadimitriou, Fasaki, & Kompitsas, 2011) Additionally, an UV blocking layer of $MAPbCl_3$ with a bandgap of 3.1 eV is placed on top of the color sensor to suppress the incident light below 400 nm because the human vision system is not sensitive to wavelengths smaller than 400 nm. The planar and textured color sensors consist of an equal layer stack. Only the layer stack of the textured color sensor is formed on a textured substrate, and a UV blocking layer is placed on top of the detector.

The optics of the designed sensor devices were studied with the aid of three-dimensional (3D) finite-difference time-domain (FDTD) simulations,(Taflove, Hagness, & Piket-May, 2005) where the optical properties of materials and geometry of the device structures used as input parameters for the calculations. The optical wave propagations within the device structures were modeled for incident wavelengths in the range of 300 nm to 800 nm. At first, the electromagnetic field distribution was calculated within sensor devices from the optical wave propagations. Then the QEs and SRs of the sensors were calculated from the electromagnetic fields. It is assumed that the photon absorbed by the perovskite absorbers contribute to the QE and SR, whereas photons absorbed by the contact and transport layers do not contribute to the QE. Furthermore, the upper limit of the collection efficiency is assumed to be 100%, since the thicknesses of all the perovskite absorbers are smaller than the diffusion lengths of the materials.

6.1.3 Results and Discussions

A. Perovskite color sensors

In the first part, vertically stacked perovskite color sensors with flat interfaces are investigated, as shown in Figure 6.2(a). Mixed-halide perovskites with bandgaps of 2.5, 2.1, and 1.8 eV were used as absorber layers of the top, middle, and bottom diode, respectively. The bandgaps of the absorbers were selected to be equal to the cut-off energies of 2.5 eV (blue), 2.1 eV (green), and 1.8 eV (red) of the CMFs. The thicknesses of the perovskite absorbers were selected to be larger than the penetration depth at the band edge with 500, 700, and 1000 nm. The calculated QE for the three color channels is depicted in Figure 6.2(b). Furthermore, the SR of the sensor calculated by $SR(\lambda)=q\times\lambda\times QE(\lambda)/(h\times c)$, which is also provided in Appendix D (Figure D1.2), where q is the elementary electron charge, λ is the wavelength, $QE(\lambda)$ is the quantum efficiency, h is Planck's constant, and c is the speed of light. The sensor exhibits maxima of the spectral response at 480, 568, and 670 nm with Full Width Half Maxima (FWHM) at 111

nm, 92 nm, and 93 nm, respectively. The CIE standard color-matching functions exhibit maxima of the spectral response at 450, 550, and 650 nm with FWHM ranging from 60 nm to 100 nm.

A comparison of the sensor characteristics with other vertically stacked sensor exhibits a distinct better agreement with the color-matching function than other structures in literature.(Ganesh, Shivanna, Friend, & Narayan, 2019; Gautam, Bag, & Narayan, 2011; Herzog et al., 1998; Hubel, 2005a; Hubel et al., 2004; Jansen-van Vuuren et al., 2016; Knipp et al., 2006; Lyon & Hubel, 2002; Merrill, 1999; Theil et al., 2000; Yakunin, Shynkarenko, Dirin, Cherniukh, & Kovalenko, 2017) Stacked silicon sensors suffer from the large overall of the spectral responsivities due to the indirect bandgap of crystalline silicon. The idea of using stacked perovskite sensors has been proposed by Yakunin et al. using a mechanically stacked sensor consisting of individual $MAPbI_3$, $MAPbBr_3$, and $MAPbCl_3$ detectors.(Yakunin et al., 2017) However, the spectral characteristics were not matched to the human vision system. Hence, the stacked perovskite color sensor exhibits a color error distinctly higher than the color errors of sensors using side-by-side filter arrangement. Almost all other stacked color sensors exhibit color errors lower than the color error of the stacked sensor presented by Yakunin et al. but still higher than sensors using optical filters. In the case of most other color sensors, the color separation and the color error are limited by the considerable overlap of the SRs.(El Gamal & Eltoukhy, 2005; Hubel, 2005a; Knipp et al., 2006) The sensor described in **Figure 6.2(a)** exhibits a color error smaller than all previously published stacked color sensors and comparable to the sensor using a side-by-side filter arrangement. Further details on the colorimetric characterization of the sensor are provided in the upcoming sections of the manuscript.

Prior to providing a basic introduction to the color science and the colorimetric characterization of the SCS, further improvements of the sensor structure will be discussed. The improvements will lead to a reduction of the color error and an

enhancement of the QE and NOE. The color sensor is sensitive in the spectral range from 350 nm to 400 nm, while the human receptors are not sensitive in this spectral region. The sensitivities between 350 nm and 400 nm lead to an increased color error of the sensor.

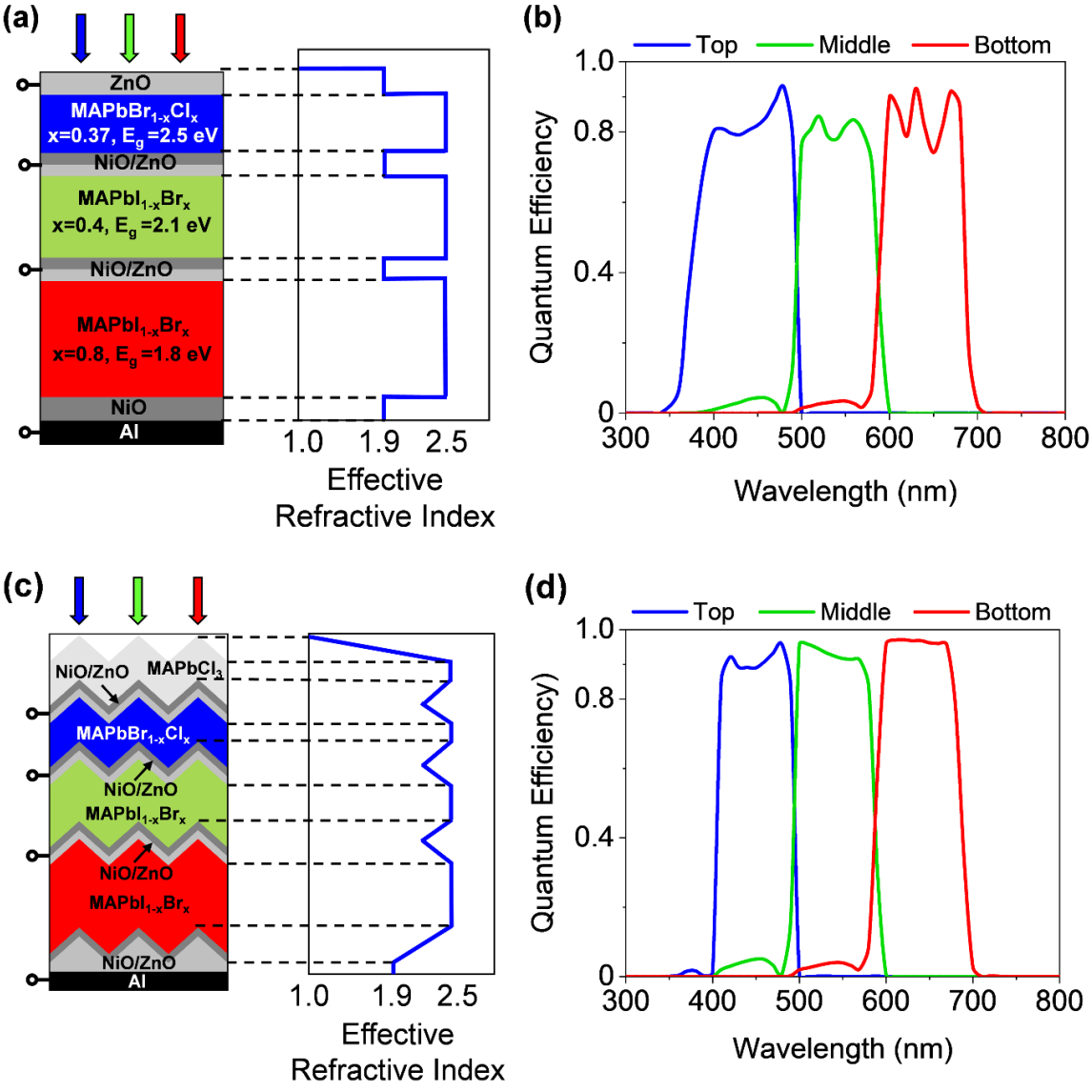

Figure 6.2: Schematic cross-section and corresponding effective refractive index of (a) flat and (c) textured vertically stacked perovskite color sensor. The simulated corresponding quantum efficiency of (b) flat and (d) textured vertically stacked perovskite color sensor.

The short wavelengths sensitivity can be reduced by placing a UV blocking layer on the sensor layer stack. The cut-off wavelength and cut-off energy of the UV blocking layer

should be 400 nm and 3.1 eV, which matched exactly with the bandgap of $MAPbCl_3$. In the following, a $MAPbCl_3$ layer is placed on top of the color sensor with a thickness of 500 nm, which is larger than the penetration depth for a wavelength of 400 nm. Hence, the $MAPbCl_3$ layer acts as a low pass filter in terms of the incident photon energies and as a high pass filter in terms of the incident wavelengths. A plot of the QE for a stacked planar sensor with a UV blocking layer is included in Appendix D (Figure D1.3).

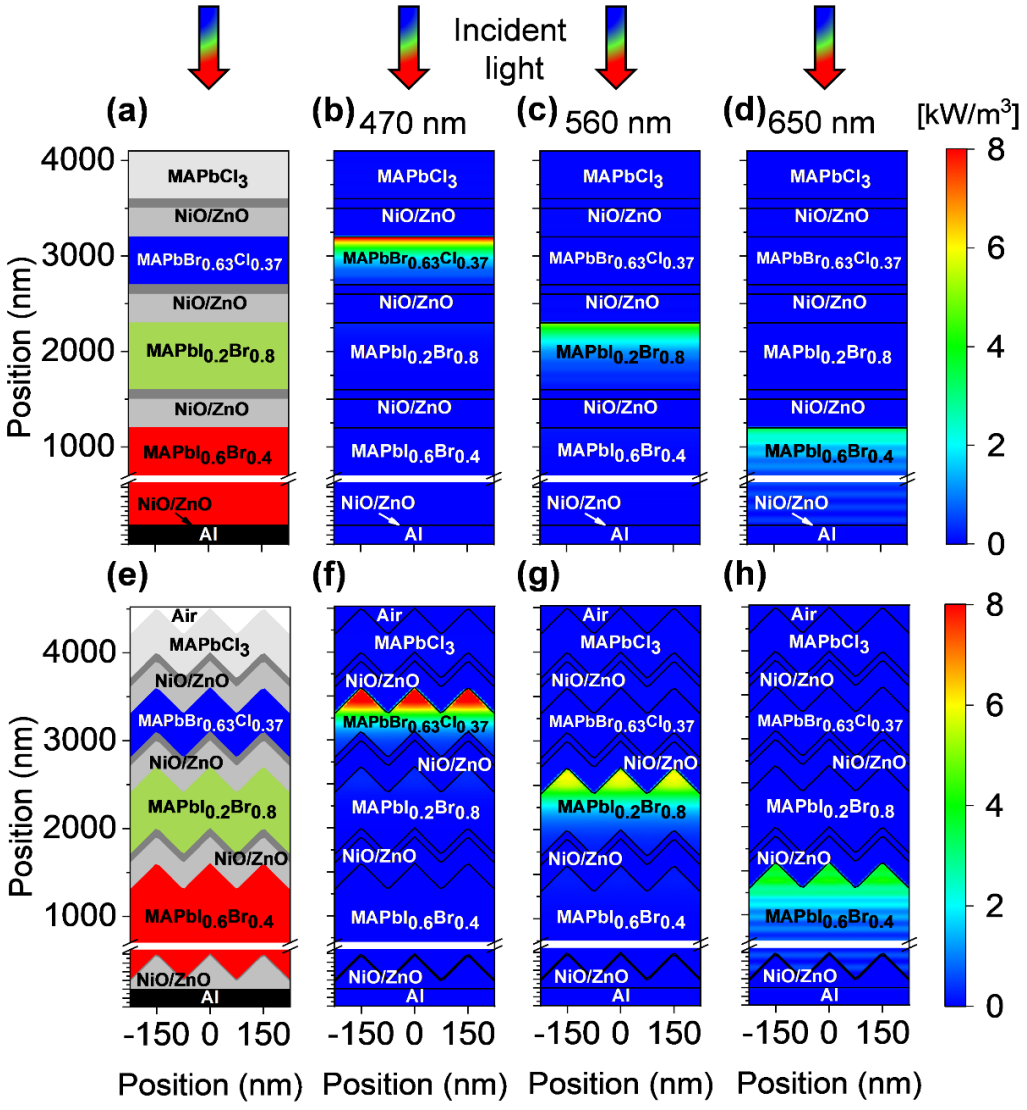

Figure 6.3: Schematics of (a) flat and (e) textured vertically stacked perovskite color sensor. Power density plots of (b-d) flat and (f-h) textured vertically stacked perovskite color sensor with an incident wavelength of (b, f) 470, (c, g) 560, and (d, h) 650 nm.

The top, middle, and bottom diode exhibit bandgaps of 2.5 eV, 2.1 eV, 1.8 eV. Hence,

photons with photon energies larger than 3.1 eV are not absorbed, and no infrared blocking filter is required. On the other hand, silicon exhibits a bandgap of 1.14 eV, and photons with energies from 1.8 eV to 1.14 eV must be blocked from entering the silicon-based sensors. All three diodes exhibit maxima of the QE and the NOE exceeding 80%. This is distinctly higher than the theoretical upper limit of sensors using a side-by-side arrangement of optical filters. But the QEs of the stacked perovskite color sensors do not approach 100% because of reflection losses. The reflection losses are caused by refractive index differences between the perovskite layers and the metal oxide contact layers. This is schematically illustrated in **Figure 6.2(a)**. The differences are small, but the small differences add up and result in total reflection losses of up to 20%. Furthermore, the QEs of the three sensor channels exhibit interference fringes due to Fabry Perot resonances.

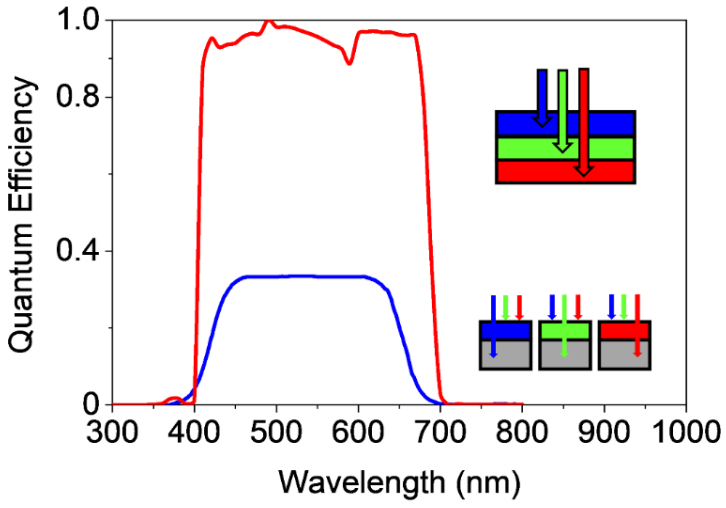

Figure 6.4: Comparison of total quantum efficiencies between a conventional color sensor with a side-by-side arrangement of optical color filters (blue) and vertically stacked perovskite color sensor (red) with maximum quantum efficiency approaching unity.

The number of interference fringes increases from the top to the middle and the bottom diode. A comparison of the stacked perovskite thin-film color sensor with stacked silicon thin-film sensors shows that the effect of interference fringes is much more pronounced

for stacked silicon thin film color sensors. Nevertheless, small changes in the thickness of the individual layers due to variations as part of a manufacturing process have a distinct effect on the QE and SR. The reproducibility of the sensors can be distinctly improved, and the formation of interference fringes can be reduced by reducing the reflection at the interfaces between the perovskite layers and the metal oxide layers. Hence, we introduced an interface texture. The function of the texture is to form a refractive index gradient, as shown in **Figure 6.2(c)**. The function is not to diffract the incident light. The period and height of the pyramid were selected by 150 nm and 300 nm. The QE of the sensor with textured interfaces and a UV blocking layer is shown in **Figure 6.2(d)**. The sensor device exhibits QEs, with absolute values exceeding 90%. Furthermore, the formation of interference fringes is distinctly reduced. The effect of the surface texture on the power density distribution of a sensor with planar and textured interfaces is shown in **Figure 6.3**. An improved light incoupling but no diffraction of the incident light is observed. The peak wavelength of the spectral responsivity and the FWHM is not affected by introducing textured interfaces. The calculated QE of the three channels is used as input to calculate the NOE, which is shown in **Figure 6.4**. Furthermore, the theoretical upper limit of the NOE of a color sensor using a side-by-side arrangement is shown in **Figure 6.4**. The NOE of a conventional color sensor with a side-by-side arrangement of the optical color sensor is limited to 33%.

B. Color Science of Perovskite Color Sensor

In this part of the manuscript, the vertically stacked perovskite color sensor with QE and NOE exceeding 90% is colorimetrically characterized. The color error is compared with the color error of conventional color sensor with optical color filters as well as the only commercialized vertically stacked Foveon color sensor using crystalline silicon.(Hubel, 2005a; Hubel et al., 2004; Lyon & Hubel, 2002; Merrill, 1999) The aim of a camera system is to produce an accurate color of objects in a scene. Such color reproduction is

achieved when the imaging sensor is able to provide the same results as the human eye. This is achieved if the CMFs can be represented by a linear combination of the sensitivities of the three sensor channels. In this case, the transformation from camera RGB to XYZ can be defined as

$$x = \boldsymbol{M} f \tag{6.6}$$

where *x* is a 3×1 vector containing the XYZ values for a pixel with RGB values in a 3×1 vector denoted by *f*. **M** is the 3×3 matrix that transforms the values on RGB to values in XYZ. This transformation matrix is obtained by using the camera sensor sensitivities. The condition for having a linear relationship between sensor sensitivities and the color matching function is known as Luther condition.

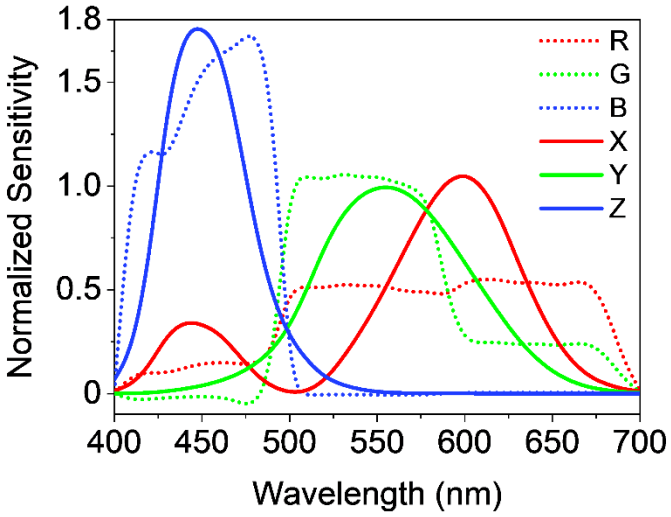

Figure 6.5: Standard CIE color-matching functions and calculated color matching function (CMF) of the investigated perovskite vertically stacked color sensor. A linear color transformation was used.

Due to limitations of filters, sensors, and the issues related to signal to noise ratio, the Luther condition is usually not valid in trichromatic color cameras.(Hong, Luo, & Rhodes, 2001) For the conversion of camera RGB values into XYZ, empirical data-driven methods are often used. The data-based correction method uses a set of samples with known XYZ values. The same samples are acquired in RGB through camera, and the

transformation matrix for RGB to XYZ conversion is estimated. There are many methods for the determination of the transformation matrix **M**. Although many researchers worked on complex models, the International Color Consortium prefers simple linear transforms to enable quick color reproduction across various display and print devices. A comparison of the CMFs with the transformed RGB signals of the sensor signals for the vertically stacked perovskite sensor is shown in **Figure 6.5**. A simple linear transformation was used. A good agreement between the absorption bands of the sensor channels and the CMFs is achieved. The deviation of the transformed sensor signals from the CMFs is caused by the optical properties of the perovskites. The perovskites are direct bandgap materials, and the extinction coefficient is only slightly wavelength-dependent, as shown in **Figure 6.1**. The resulting sensor signals exhibit a box-like characteristic if the thickness of the perovskite absorber is larger than the penetration depth. The colorimetric characterization was performed using a linear method, allowing us to conduct comparative analysis among several color sensors.

We computed the color reproduction of these color sensors in terms of color difference metric known as CIEDE2000.(CIE, 2001) The process for computation of XYZ from the camera RGB through the transformation matrix **M** and the computation of error is described in the literature.(Khan, 2018) As shown in **Table 6.1**, the conventional color sensor with optical color filters exhibits a color error of 4.4, whereas a stacked silicon detector exhibits a color error of 5.6. Both sensors are based on crystalline silicon. The indirect bandgap of crystalline silicon limits the color separation of the individual channels and a large overlap of the spectral responsivities is observed. Hence, the stacked silicon color sensor exhibits a color error, which is higher than conventional sensors using optical filters. The vertically stacked color sensor based on mixed-halide perovskites exhibits a color error as low as 3.6. The color error of the vertically stacked perovskite three-color sensor is comparable or even better than the typical conventional color sensors with CFA as well as the Foveon sensor. Furthermore, the NOE of the

simulated stacked perovskite color sensor exceeds 90%, which is almost three times higher than the color sensor with CFA.

Table 6.1: Comparison of the vertically stacked perovskite color sensor with conventional color sensors using optical color filters and the vertically stacked Foveon color sensor. The sensors are compared in terms of the used materials, color errors, and NOEs.

Sensor	Sensor with Color Filter Array (CFA)	Foveon Sensor (Stacked silicon diodes)	Stacked perovskites diodes
Arrangement of sensor channels	side-by-side	vertical	vertical
Materials	crystalline silicon sensor plus polymer filters	crystalline silicon (Foveon sensor)	$MAPb(Br_{1-x}Cl_x)_3$ $MAPb(I_{1-x}Br_x)_3$
Color error	4.4	5.6	3.6
Normalized optical efficiency	max. 33%	High	approaching unity
Reference	(El Gamal & Eltoukhy, 2005)	(Hubel, 2005a)	**this study**

The color separation approach described in this manuscript is not limited to sensors with three color channels. The sensor concept can be extended to vertically stacked multispectral color sensors with high NOEs. For example, the number of sensor channels can be extended to 4 or 6 channels. Multispectral sensors can be applied for applications, which cannot be addressed by commonly used three color sensors. The spectral information is valuable for applications like disease detection in plants,

determination of quality of fruits and vegetables, inspection of electrical instruments, accurate reproduction of color and tint in textile industry, and many more.

6.2 Multispectral Image Color Sensor with Perovskite Alloys

Electromagnetic waves are carriers of energy and information, which propagate in time and space. An ideal electromagnetic sensor array would measure the light intensity and the wavelength of the electromagnetic wave as a function of time and position. The human vision system and digital cameras allow for detecting the light intensity of visible light as a function of time and position. The spectral information is measured in the form of “colors”, which represent an integral over a spectral range. Figure 6.6 is a schematic representation of three different arrangements of measuring color spectral information. The spectrometers are commonly used to measure the spectral characteristics of electromagnetic waves. However, spectrometers do not provide spatial information. Hence, a spectrometer can be seen as a single-pixel camera with high spectral resolution. Then, the color imager or color image sensor, as shown in Figure 6.6(a), is a detection process of discriminating color spectral information of incident EM wave as a function of different wavelengths and penetration depths of photons, where the photon generated charge carriers are collected at different depth of the device. The conventional color imager contains an image sensor with a two-dimensional array of a pixel, where the sensor is coated with color filter array (CFA) for the transmission of three different colors of blue, green, and red.(Lukac & Plataniotis, 2005a) A raw image captured by color imager can be considered as three different color images of RGB, which is recombined as a single colorful image with the aid of the demosaicing algorithm.(Gunturk, Glotzbach, Altunbasak, Schafer, & Mersereau, 2005b; Hubel et al., 2004) The vertically stacked color imager described here is free of CFA. On the other hand, multispectral cameras provide spectral and spatial information as a function of time. Multispectral cameras capture images for many spectral channels so that the spectral information of the image can be reconstructed. Moreover, the multispectral sensor is not limited to three colors only. Nevertheless, the realization of such cameras

is technically complex and expensive in comparison to classical digital cameras that mimic the human vision system. However, multispectral cameras allow for new applications in health, security, quality inspections of products and sorting, PCB inspection, counterfeit detection, communication systems, etc. For instance, multispectral image sensors have recently been used in label-free optical imaging, including fluorescence lifetime imaging for the characterizations and diagnosis of biological tissues, and potential applications of real-time assessment of tumor margins in surgical oncology.(Alfonso-Garcia et al., 2018; Boppart et al., 2017; Esperón-Moldes et al., 2019; Y. Sun et al., 2018; Unger et al., 2020)

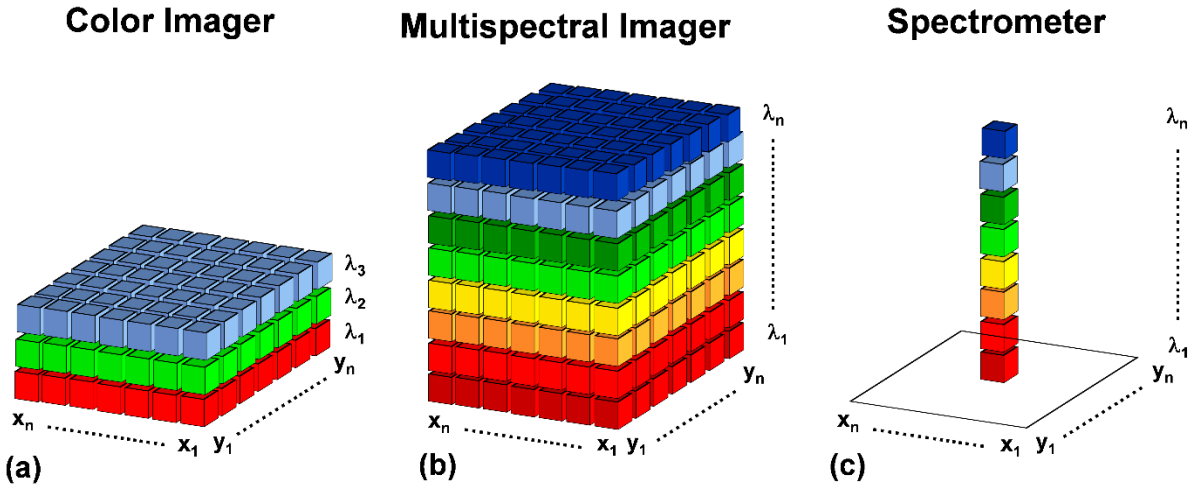

Figure 6.6: Schematic cross-sections of (a) color image sensor with vertically stacked three-color sensor array consisting of semiconductor diodes with three different bandgaps, (b) multispectral image sensor array, and (c) spectrometer.

However, the existing multispectral image sensor applied to those applications uses color filter array. The filters create color aliasing or color artifacts in the images. Hence, further computational image processing is required to perform correcting and recombining them together. In this section, mixed-halide perovskites are used to realize six-channel vertically stacked multispectral image sensor, where we aim to maximize QEs and SRs of sensors so that greater detection and efficiency can be achieved. Perovskites based three-channel color imagers can be comparable to conventional color sensors with CFA, while the six-channel perovskite sensors can be demonstrated

for capable of enabling to reconstruct incident spectra with outperforming all other such characterized sensors in terms of high QE, SR, as well as low color error.

6.2.1 Optical Material Properties

Mixed-halide perovskites are a class of semiconductor materials that can exhibit bandgap tunability by changing the composition of the halide elements. Moreover, the excellent optoelectronic material properties, including direct bandgap of perovskites, allow exhibiting very good color separation in the six-channel image sensors as well. As described in Section 6.1.1, experimentally realized optical properties of single halide perovskites (e.g., $MAPbI_3$, $MAPbCl_3$, and $MAPbBr_3$) are used to calculate the optical constants of the mixed-halide perovskites with required bandgaps using the energy shift model.(Snyder, Woollam, Alterovitz, & Johs, 1990b) By changing the halide compositions, the required bandgaps are determined, where the composition-dependent perovskite bandgaps are shown in Figure 6.7.

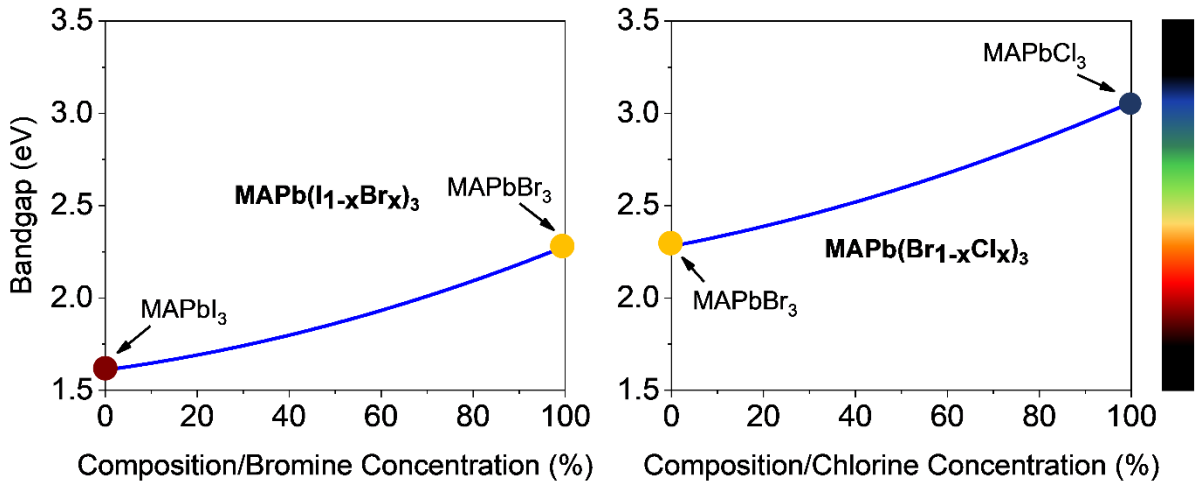

Figure 6.7: Halide Composition-dependent optical bandgap of mixed-halide perovskite materials.

Six different bandgaps (2.75, 2.5, 2.25, 2.08, 1.92, and 1.8 eV) are determined from the energy shift model, where a detailed description of material bandgaps and halide

composition values are illustrated in Appendix D (Table D1.2). In every case, the thicknesses of the individual absorbers are larger than their penetration depths. The optical constants are matched with the provided color matching functions of CIE standard observer.(Cohen, Wyszecki, & Stiles, 1968) Complex refractive indices and dielectric constants of the calculated mixed-halide perovskite materials with such bandgaps are shown in Figure 6.8.

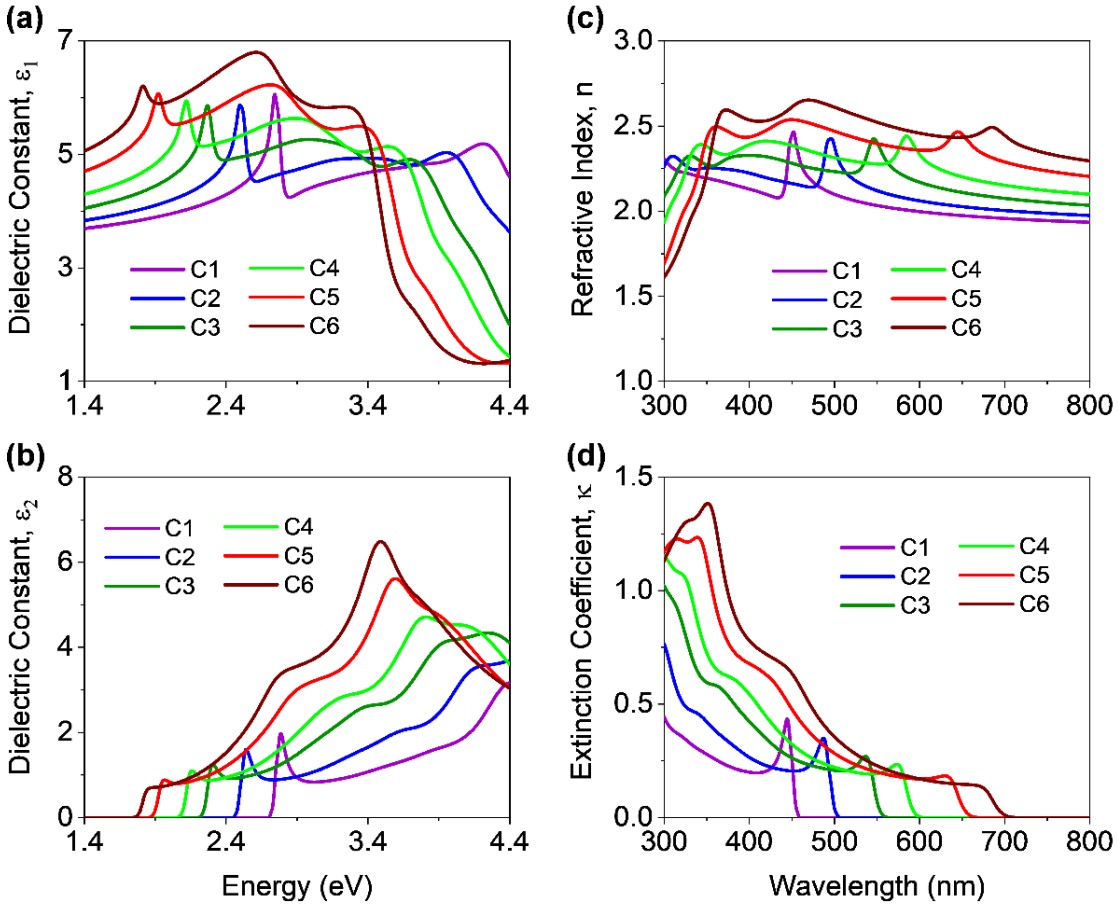

Figure 6.8: (a) Real and (b) imaginary parts of the complex dielectric constant; (c) refractive index and (d) extinction coefficient of calculated mixed-halide perovskites of C1($MAPbCl_{0.68}Br_{0.32}$), C2($MAPbCl_{0.37}Br_{0.63}$), C3($MAPbBr_{0.96}I_{0.04}$), C4($MAPbBr_{0.79}I_{0.21}$), C5($MAPbBr_{0.5}I_{0.5}$), and C6($MAPbBr_{0.38}I_{0.62}$) with an optical bandgap of 2.75, 2.5, 2.25, 2.08, 1.92, and 1.8 eV, respectively.

6.2.2 Device Design and Methods

The schematic cross-sections of three-channel and six-channel vertically stacked perovskite color sensors are shown in Figure 6.9(a) and Figure 6.9(b), respectively. The ZnO and ZnO/NiO contacts have thicknesses of 100 nm and 400 nm, respectively. In a three-channel sensor, top, middle, and bottom absorber have a thickness of 500 nm, 700 nm, and 1000 nm, respectively. In contrast, in the six-channel sensor, channel-1, channel-2, channel-3, channel-4, channel-5, and channel-6 has a thickness of 500 nm, 600 nm, 800 nm, 1200 nm, 1800 nm, and 2200 nm, respectively.

As described in Section 6.1.2, 3D FDTD methods are used to investigate the optics of the designed sensor devices, where the optical properties of materials and geometry of the device structures used as input parameters for the calculations.

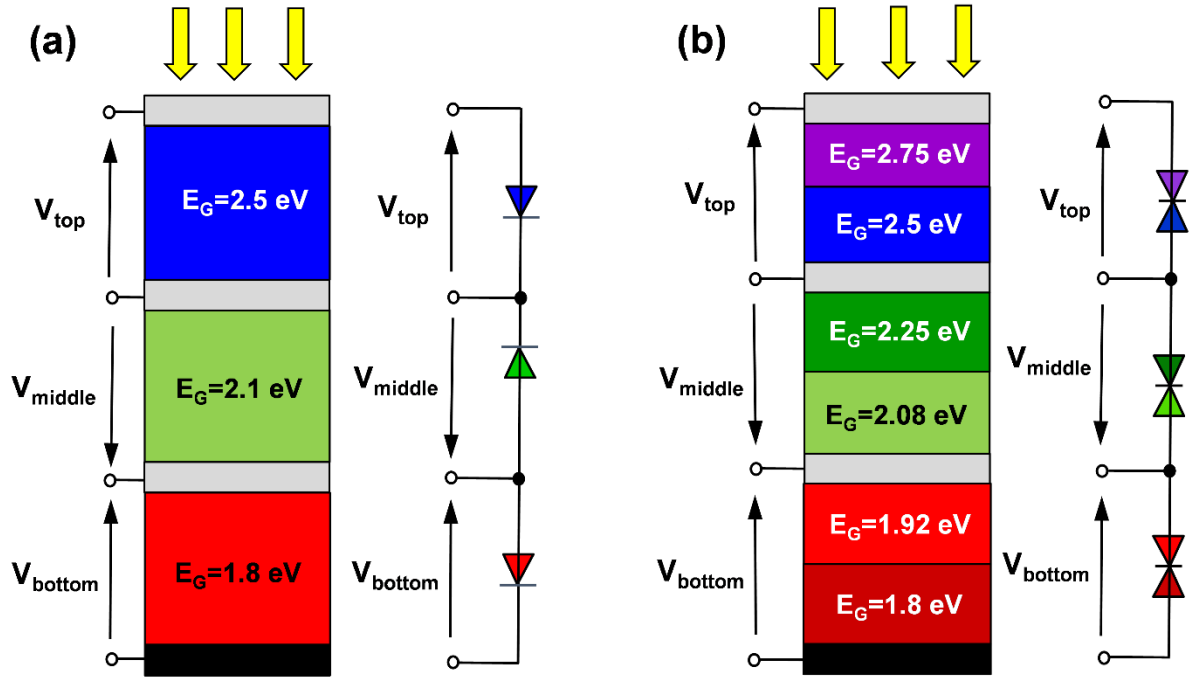

Figure 6.9: Schematic cross-section of (a) three-channel and (b) six-channel color image sensors with mixed-halide perovskites.

Additionally, an UV blocking layer of $MAPbCl_3$ with a bandgap of 3.1 eV is used in the textured device to suppress the incident lights below 400 nm, since they are not

sensitive to the human vision system. Light propagations through both sensors are illustrated schematically in Figure 6.10.

6.2.3 Results and Discussions

In the current study, perovskites-based image sensors are studied for high QEs and SRs, where interfaces of all the layers are pyramidically textured. In the first step, three-channel color imagers are investigated for a maximum QE and SR. The device structure is provided in Figure 6.9(a) and in Appendix D (Figure D2.1).

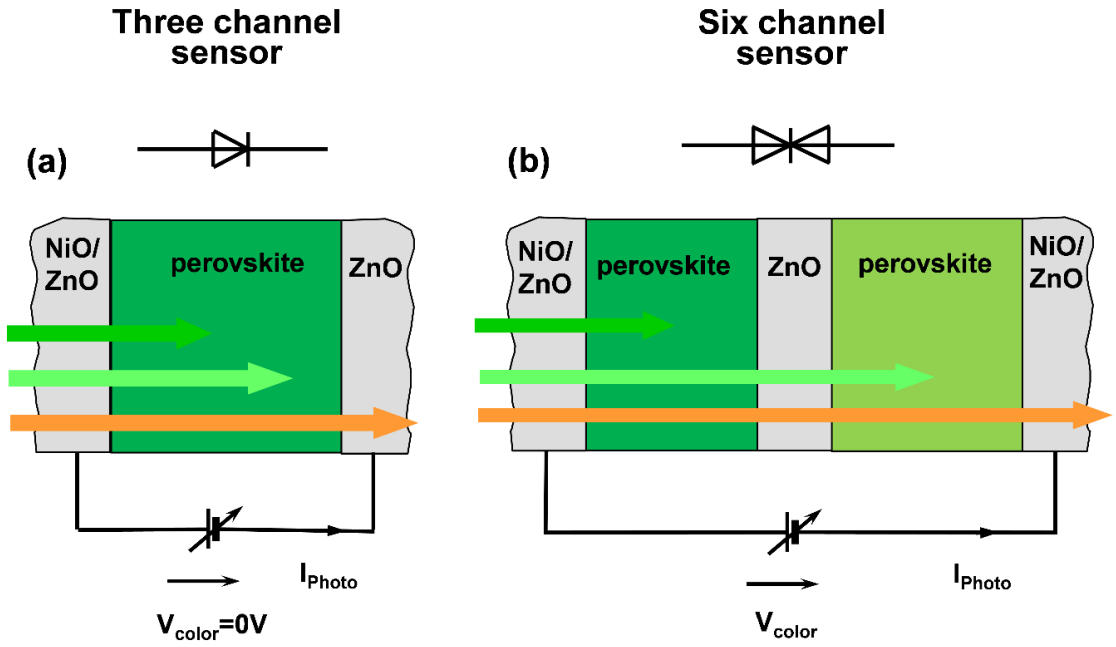

Figure 6.10: Schematics of optical wave propagation through (a) the three-channel and (b) the six-channel sensors with perovskites alloys.

The thicknesses of each perovskite absorbers are selected to be larger than the penetration depths of the absorbers. In this case, the thicknesses of the top, middle, and bottom perovskite absorbers are optimized to be 500 nm, 700 nm, and 1000 nm, respectively. The simulated quantum efficiency is depicted in Figure 6.11(a). Furthermore, the QE of a three-channel perovskite sensor coated on flat surfaces are

also provided in Appendix D (Figure D2.1(b)) as a reference. Textured interfaces lead to the reduction of surface reflection and enhancement of the optical path length in the sensor devices. Consequently, compared to the flat image sensor, the QEs of the textured device are distinctly increased in all three channels (C1, C2, and C3).

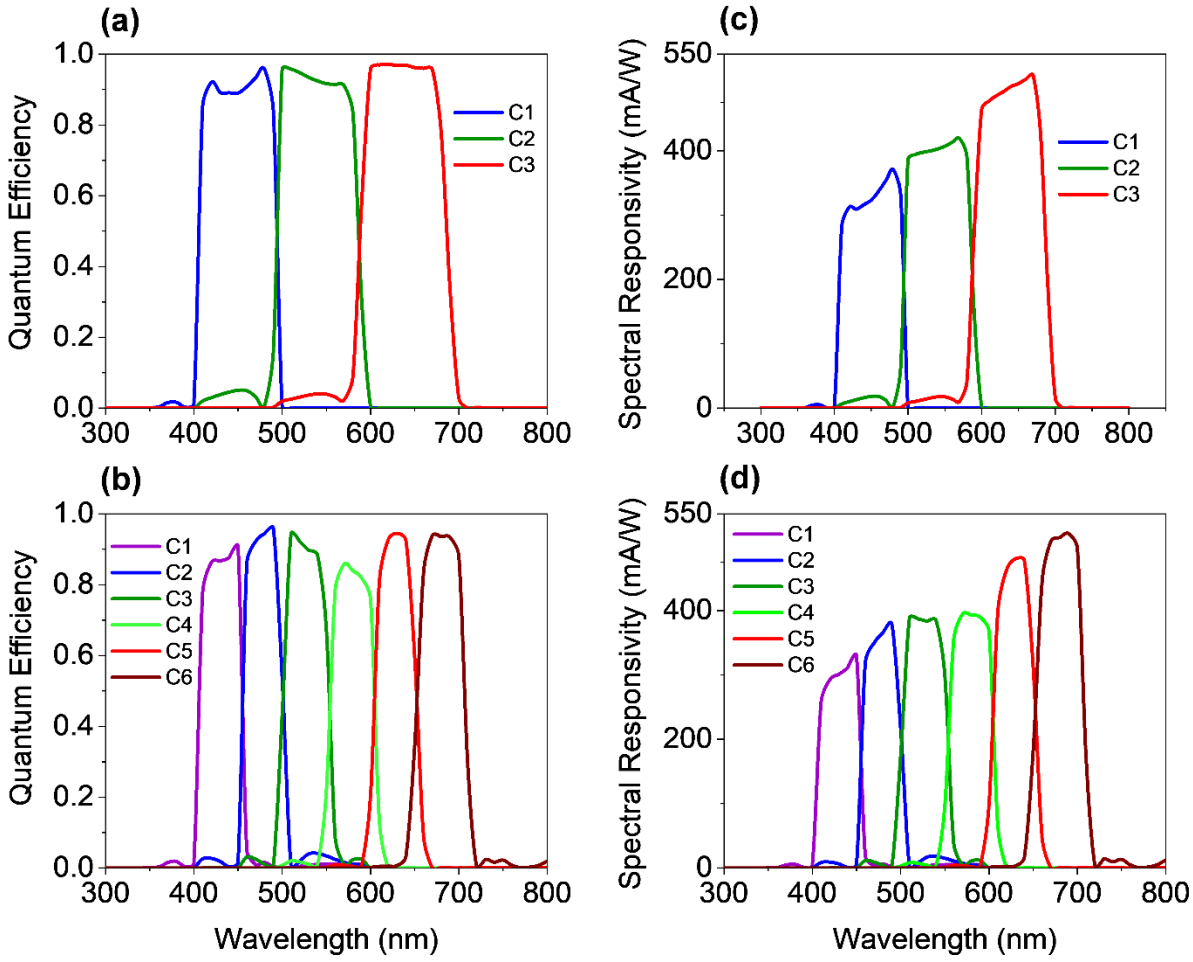

Figure 6.11: Simulated quantum efficiency of (a) three-channel and (b) six-channel perovskite color sensors. (c,d) The corresponding spectral responsivity of sensors.

Furthermore, the interference fringes exhibited in the flat sensor due to Fabry Perot resonances are not pronounced anymore by introducing textured surfaces. Quantitatively, the QEs are approaching to almost unity or 100%. Such a high QE obtained in the three-channel color imager could lead to the high contrast of imaging as well as a very high level of light sensitivity. In the next, the SR is determined using $SR(\lambda)=q\times\lambda\times QE(\lambda)/(h\times c)$, where λ is the wavelength, q is the elementary electron charge,

h is Planck's constant, and c is the speed of light. Ideally, the spectral response and corresponding full width at half maximum (FWHM) of a color sensor are matched with a CIE standard color-matching functions. The matching function is provided in Figure 6.5, which exhibits the maxima of the spectral response at 450, 550, and 650 nm with FWHM ranging from 60 nm to 100 nm. As shown in Figure 6.11(c), the FWHM of the spectral responsivity for the three-cannel sensor device ranges between 87 nm and 97 nm with maxima at 480, 568, and 670 nm, which is in very good agreement of CIE spectral response. This leads to the reduction of the color error as well, which will be explained in greater detail in the following.

In the following, the results of multispectral image sensors are discussed. Multispectral image sensors capture image data within specific wavelength ranges across the electromagnetic spectrum. Such an image sensor can measure light in a small number of spectrum band based on the design of the sensor. Hence, the multispectral image sensor allows us to obtain additional information beyond three fundamental RGB colors that human eyes usually cannot detect. In this study, a six-channel multispectral image sensor (SMIS) is designed and investigated, where six different perovskite semiconductor diodes are vertically stacked. The device structure of the SMIS is shown in Figure 6.9(b). Furthermore, the detailed layer sequence, function of each layer, materials used in the layers and their associated bandgaps, and thickness of the layers of the SMIS is included in Appendix D (Table D2.1). Again, the thicknesses of the perovskite absorber layers for the SMIS device are considered to be larger than the penetration depths of the materials, so that the photon absorption can be maximized. The optics of the multispectral image sensor is also simulated by FDTD and evaluated based on the QE and SR. The QE and corresponding SR of the SMIS is depicted in Figure 6.11(b) and Figure 6.11(d), respectively. As shown, SMIS exhibits three more colors than a three-channel color image sensor, allowing it to obtain more information of a captured image. Hence, unlike the three-channel perovskite image sensor, the

SMIS device exhibits QEs for six distinct colors of the incident wavelengths, including purple color captured by channel 1 (C1) at 450 nm of wavelength to the deep red color located at 700 nm of wavelength captured by channel 6 (C6). A maximum QE of >95% is exhibited by the channels C2, C3, C5, and C6, whereas about ~85% QE is absorbed in the channels C1 and C4. Such a high photodetection efficiency of sensor could offer rigorous scanning results, allowing to utilize them in wide applications. Then the peaks and FWHM of the SR of the multispectral image sensor are comparable to the CIE matching function, allowing to achieve very low color error.

6.3 Summary

Vertically stacked perovskite color sensors were proposed and investigated. The sensor allows for sensing colors without using optical filters. Furthermore, the sensors are color aliasing and color Moiré error-free. The color-matching functions were used as guidelines to select the appropriate perovskite mixed-halide and device structure. The optical constants of the mixed-halide perovskites were obtained by optical measurements in combination with an energy shift model. The vertically stacked color sensor structure consisted of three perovskite diodes with bandgaps of 2.5 eV, 2.1 eV, and 1.8 eV. The optical wave propagation within the sensor structure was described by finite-difference time-domain (FDTD) simulations. The calculated quantum efficiency exceeds 90% and is almost 3 times higher than the theoretical upper limit of conventional sensors using color filter arrays. The stacked perovskite color exhibits color error comparable with sensors using optical filters, which has not been achieved by previous stacked color sensors. The sensor concept is not limited to three-channel sensors. The concepts can be expanded to multispectral or multichannel sensors, which open the door to a variety of new applications.

Next, a three-channel optical imager and a six-channel multispectral image sensor have been designed, the optics has been simulated by FDTD, and the characteristics

performance of the devices has been evaluated by color science. Perovskite-based three-channel image sensor exhibits very high photodetection ability with spectral responsivity very much comparable to CIE standard matching function. Consequently, the investigated color error of the three-channel sensor is comparable to sensors using optical filters. Then the investigated multispectral optical color sensors enable color aliasing free color detection with imaging arrays by stacking perovskite thin-film sensors on top of each other. The sensor elements can be vertically integrated on a readout electronic, enabling high area fill factors. The six-channel sensor enables the reconstruction of incident spectra. Moreover, the six-channel multispectral image sensor investigated here outperforms all other characterized sensor devices. Furthermore, these sensors are much more efficient, affordable, and easier to integrate into a vision system, allowing to implement them in new wide applications, including life science or medical science, aerospace, agriculture, autonomous vehicles.

CHAPTER 7

SUMMARY AND FUTURE WORKS

This Chapter summarizes the entire works demonstrated in the thesis. The summary of this is alienated into three parts: 1) Optics of perovskite solar cell front contacts, 2) Realization of highly efficient perovskite-based tandem solar cells, and 3) Efficient multispectral color image sensors with perovskite alloys. A short discussion on some ongoing and future works related to this thesis is additionally presented, which are 1) Visibly transparent solar cells build from optical antennas, and 2) Spectral splitting: a novel approach for realizing efficient all-perovskite tandem solar cells.

7.1 Summary

7.1.1 Optics of Perovskite Solar Cells Front Contacts

Charge transport/contact layers, especially, the front contact, has a substantial influence on the optics and photovoltaic performance of perovskite solar cells. Metal oxide contacts have attracted considerable attention to the perovskite solar cell research community due to their excellent optoelectronic properties. Hence, in this part, different metal oxides contact materials for perovskite solar cells are investigated for realizing high short-circuit current densities and energy conversion efficiencies. Investigated metal oxide films are prepared by several deposition methods. Herein, NiO films are prepared by the electron beam physical vapor deposition technique (EBPVD), TiO_2 films are prepared by spray pyrolysis deposition (SPD), ZnO films are realized by atomic layer deposition (ALD) and metal-organic chemical vapor deposition (MOCVD). MOCVD methods are also used to grow a pyramid-shaped ZnO film through the self-texturing process. Furthermore, non-resonant optical metasurfaces are realized by preparing periodically arranged ZnO nanowire arrays via electrodeposition. The nanowires were prepared by templated growth through a mask of photoresist. In this study, planar perovskite single-junction solar cells with metal oxide front contacts are fabricated experimentally, where the optics and optimization

of solar cells are studied by three-dimensional finite-difference time-domain (FDTD) optical simulations. The electrical effects of solar cells are exploited by 3D finite element method (FEM) simulations. Adapted numerical methods exhibit excellent agreement with the findings from the experiments. Investigations allow realizing high short-circuit current densities and energy conversion efficiencies while quantum efficiencies approach unity. This is happened due to the great optoelectronic properties of metal oxides and perovskite material systems. Metal oxide films as front contacts are used in the experiment have a comparable refractive index (2.2~2.5) with the perovskite material system. Hence, the solar cell with contacts can be treated as one unit, which reduces the front contact reflections significantly. Thus, the optics of the solar cell is primarily affected by the optics of the front contact. The front contact requirements for realizing high-efficiency perovskite solar cells are extensively discussed. The influence of free carrier absorption on photovoltaic performance is discussed. Photon management is studied by improving light incouping and light-trapping in the solar cell, which is done by the utilization of self-textured ZnO and ZnO optical metasurfaces. Finally, it is found that the efficient front contact, which is thin, lightly doped, and texture, has the potential to reach high short-circuit current density and energy conversion efficiency.

7.1.2 Realization of Highly Efficient Perovskite-based Tandem Solar Cells

Perovskite material systems allow for realizing perovskite-based tandem solar cells with high short-circuit current densities and energy conversion efficiencies. However, it is necessary to realize the optimum device design and the upper limit of the energy conversion efficiency of the tandem solar cell. In the case of perovskite/silicon tandem solar cell, the perovskite top cell has to be prepared on top of the textured silicon bottom cell, which requires the use of materials and deposition techniques compatible

with the fabrication on a textured substrate. Furthermore, the optics of perovskite solar cell differs from the silicon solar cells due to their difference in refractive indices. Hence, we have studied from the detailed balance theory (Shockley Queisser model) to the photon management perovskite/silicon tandem solar cells in greater details, which give a fundamental understanding of energy conversion efficiency losses and limits of single-junction and tandem solar cells. It has been found that the optics of a solar cell has not only an influence on the short-circuit current density but all solar cell parameters. In this part, the influence of photon management on the solar cell parameters of a perovskite single-junction solar cell and a perovskite/silicon solar cell is discussed broadly. The photon management of a perovskite single-junction solar cell can be predominately improved by an improved light incoupling and a reduction of optical losses in the solar cell, where the photon management of silicon solar cells is more complex that usually requires light trapping. The photon management in perovskite/silicon tandem solar cells is examined by the utilization of moth-eye and pyramid surface textures. We have proposed a nanophotonic design of the perovskite/silicon tandem solar cell by considering realistic device geometry and experimental processability. The proposed design perovskite/silicon tandem solar cell exhibits an energy conversion efficiency beyond 30% with a short-circuit current density exceeding 20 mA/cm^2 under matching condition. To allow for a realistic description of the optical wave propagation, a hybrid approach was used, which combines finite-difference time-domain simulations with experimentally measured data of the bottom solar cell. In addition to that, we have investigated perovskite/perovskite tandem solar cells for realizing high energy conversion efficiency by taking advantage of the multi-bandgap property of the perovskite material system. We have considered almost perfect perovskite absorbers for the tandem solar cell, which can be fabricated at a low cost. Detailed guidelines for the realization of perovskite/silicon and perovskite/perovskite tandem solar cells with high energy

conversion efficiencies have been provided in the thesis.

7.1.3 Efficient Multispectral Color Image Sensors with Perovskite Alloys

The potential use of mixed-halide perovskite materials has been used to realize vertically stacked three-channel and six-channel color image sensors. The vertically stacked design can exhibit the sensor performance almost three times higher than the traditional color sensors with optical filters. The optical materials properties have been selected by analyzing the color matching functions provided by the CIE standard observer. The optical constants of the mixed-halide perovskite materials used in the investigations are calculated using an energy shift model. , the optics has been simulated by FDTD, and the characteristics performance of the devices has been evaluated by color science. In the first step, the vertically stacked color sensor structure consisted of three perovskite diodes allows achieving higher quantum efficiency and spectral responsivity. The quantum efficiency and spectral responsivity is much higher than the Foveon color sensor technology and almost three times higher than the conventional color sensor with CFA. Furthermore, the spectral responsivity of such a device exhibits the maxima of peaks at 480, 560, and 670 nm with FWHM ranging 87 nm to 97 nm, agreeing nicely with the CIE standard color-matching functions. Hence, the color error calculated by colorimetric characterization in this study exhibits as low as 3.7, which is comparable or even smaller than the color error shown by the conventional color sensors using optical color filters (~4.4-5) as well as the Foveon vertically stacked color sensors (~5). Next, mixed-halide perovskites are utilized to realize six-channel multispectral image sensor, which has a very high photodetection ability with spectral responsivity very much comparable to CIE standard matching function. Then the investigated multispectral optical color sensors enable color aliasing free color detection with imaging arrays by stacking perovskite thin-film sensors on top of each other. The

sensor elements can be vertically integrated on a readout electronic, enabling high area fill factors. The six-channel sensor enables the reconstruction of incident spectra. Moreover, the six-channel multispectral image sensor investigated here outperforms all other characterized sensor devices. Furthermore, these sensors are much more efficient, affordable, and easier to integrate into a vision system, allowing them to implement them in new wide applications, including life science or medical science, aerospace, agriculture, autonomous vehicles.

7.2 Future Works

7.2.1 Visibly Transparent Solar Cells Build from Optical Antennas

7.2.1.1 Background

Currently, fossil energy sources are replaced by efficient and cost-effective renewable energy sources. Photovoltaics can make a major contribution to the transformation of the energy sector. Beside classical roof-top installations and solar farms, alternative solar cell concepts have gained significant interest, like building-integrated photovoltaics (BIPV). Building-integrated photovoltaics is often based on transparent solar cells integrated into windows or skylights roofs to realize energy sustainable buildings. Or transparent solar cells are part of co-energy harvesting systems or agri-photovoltaics, which allows for electrical energy generation while growing fruits or vegetables at the same time. Transparent or semitransparent solar cells are solar cells that combine the benefits of visible light transparency and electrical energy generation. The most transparent solar cell is based on crystalline silicon solar cells. The transmission is achieved by partially patterning the solar cell or partially opening windows in a solar module. However, such solutions are non-spectrally selective solar cells. In other words, the absorption and transmission of the solar cell are independent of the

wavelength. Detailed balance or Shockley Queisser limit calculations can be used to determine the upper energy conversion efficiency (ECE) limit of non-spectrally and spectrally selective solar cells as a function of the average visible transmission.

7.2.1.2 Novelty and Aim of the Project

The ECE of transparent solar cells can be distinctly increased by using a spectrally selective solar cell that absorbs ultraviolet and near-infrared light, while visible light is not or only partially absorbed by the solar cell. The ECE of non-spectrally solar cells with an average visible transmission of 100% is zero. In comparison, the energy conversion efficiency of a spectrally selective solar cell can be up to 21% for 100% visible light transmission. Spectrally selective solar cells with an average visible transmission of 100% can reach up to 2/3 of the ECE of conventional solar cells. We propose a design of a spectrally selective solar cell that exceeds the Shockley Queisser limit of a non-spectrally selective solar cell. The approach is based on the use of optical antennas or metasurfaces. Up to our knowledge for the first time, a spectrally selective solar cell is proposed, which uses optical antennas. All spectrally selective solar cells described in the literature are based on organic molecules or carbon-based material system. In this study, we use standard inorganic solar energy materials.

7.2.1.3 Design and Analysis

Transparent solar cells can be divided into non-spectrally and spectrally selective solar cells. A comparison between the conventional solar cell and the visibly transparent solar cell is shown schematically in Figure 7.1. We propose a design of a spectrally selective solar cell that exceeds the Shockley Queisser limit of a non-spectrally selective solar cell. This has not be demonstrated before. In other words, we want to design a solar cell with efficiency in the red area. Figure 7.3 shows the ECE of solar cells against different average visible transmissions (AVTs).

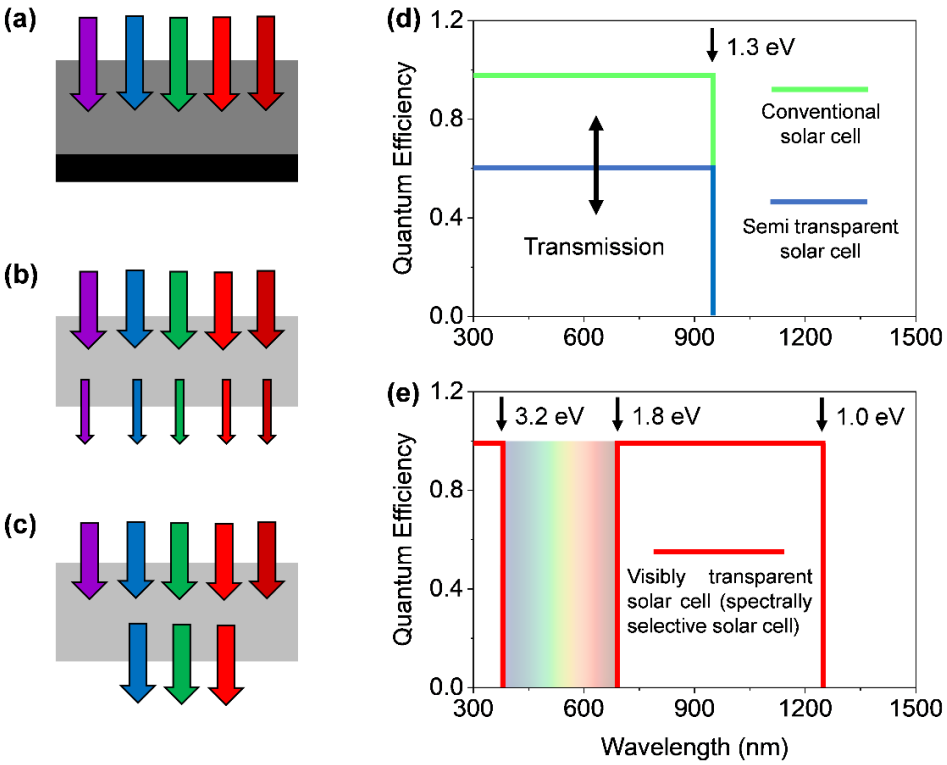

Figure 7.1: (a) Conventional solar cell, (b) Semitransparent solar cell, (c) Visibly transparent solar cell (spectrally selective solar cell), (d) Quantum efficiency of conventional solar cell and semitransparent solar cell, (e) Quantum efficiency of the visibly transparent solar cell (spectrally selective solar cell).

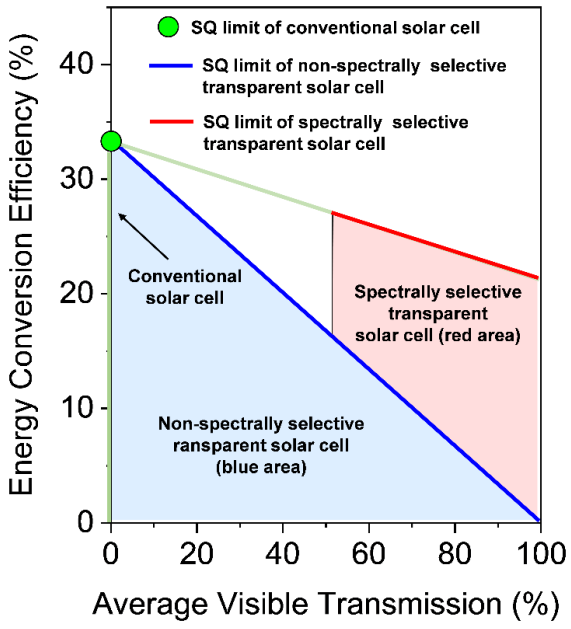

Figure 7.2: Energy conversion efficiencies of solar cells for different average visible transmissions.

7.2.2 Nano Concentrator Solar Cells build from Optical Antenna

7.2.2.1 Background and Objective

Over the past few years, there has been renewed interest in perovskite materials for fabricating solar cells because of their great optoelectronic properties, such as ease of fabrication, low deposition temperature, tunable bandgap, and large diffusion length. It is believed that the perovskite/perovskite tandem solar cell has the potential to cross the SQ limit of single-junction solar cells. Typically, a wide bandgap perovskite absorber and a narrow bandgap perovskite absorber are employed as top and bottom cells in the all perovskite TSC structure, so that high energy photons are absorbed by only the top cell before transmitting low energy photons to the bottom cell. Hence, selecting proper materials with complementary bandgaps is essential.

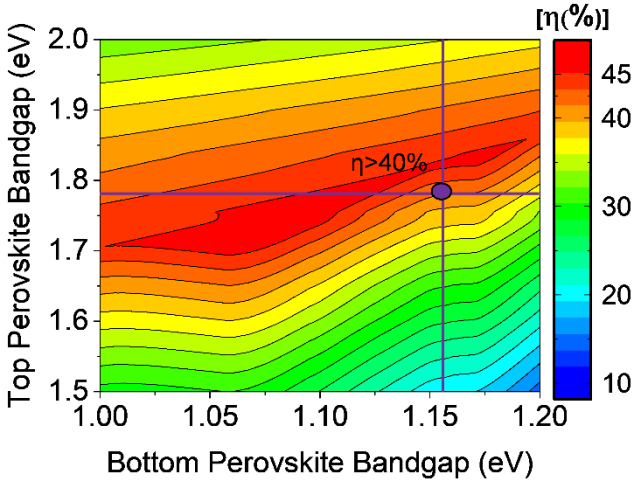

Figure 7.3: Detailed balance limit (SQ limit) of a two-terminal perovskite/perovskite tandem solar cells.

According to the detailed-balance theory, the ECE of TSC may go beyond 45% if the optimum material bandgaps (~1.1 eV and ~1.73 eV) are selected, as shown in Figure 7.13. By realizing the perovskite/perovskite tandem solar cell, some distinctive advantages can be achieved, such as low-temperature processes for all the sub-cells, low fabrication costs, and compatible for flexible and lightweight applications.

In this study, we systematically investigate the optical and electrical properties of the solar cell for realizing a perovskite/perovskite tandem solar cell with an energy conversion efficiency beyond 30%, where perovskite materials with suitable bandgaps are designated in the device structure. The optics and electrical properties of solar cells are meticulously investigated by three-dimensional (3D) electromagnetic simulations.

7.2.2.2 Design and Materials

In general, the design of perovskite/perovskite TSC is challenging due to the integration of distinctive materials, where material bandgaps have to be energetically matched so that optical losses are minimized, and ECE is maximized. Furthermore, the current from the top cell to the bottom cell has to be matched under the short-circuit condition. By texturing the solar cell interfaces, matched J_{SC} can be improved; however, it negatively affects the electrical properties (V_{OC} and FF) of the solar cell. Hence, a potential device design demands flat interfaces between contacts and perovskite absorber. Furthermore, the front contact of the perovskite/perovskite TSC should provide a suitable work function, high lateral conductivity, and low absorption losses for realizing high ECE. The indium-doped tin oxide (ITO) is commonly used as a front contact. Nonetheless, it does allow free carrier absorptions in the longer wavelengths that hinder maximizing the ECE. In this study, initially, planar perovskite/perovskite tandem solar cells are investigated. Next, a novel approach has been realized for efficient perovskite/perovskite tandem solar cells by maintaining planar technology. A schematic cross-section of the investigated planar perovskite/perovskite tandem solar cell is depicted in Figure 7.4(a), where a similar solar cell structure is adapted for both subcells. The front contact/electron transporting layer (ETL) consists of a 70 nm double ITO/NiO followed by a perovskite absorber layer.

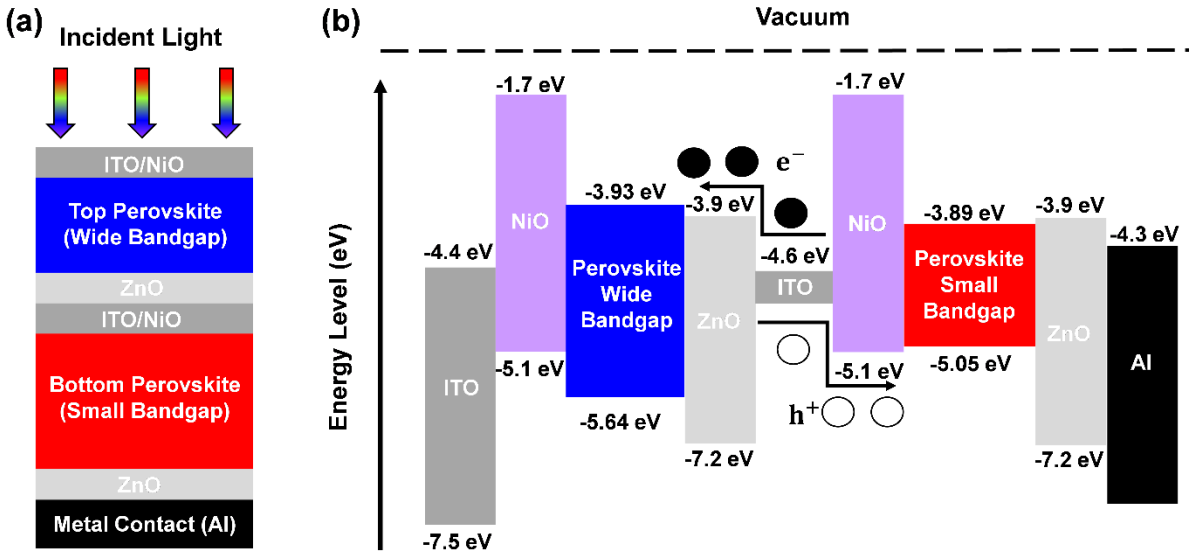

Figure 7.4: (a) Schematic representation and (b) corresponding energy levels of the investigated perovskite/perovskite tandem solar cell.

The NiO allocates achieving high FF by providing high work function and efficient hole transporting / electron blocking, where ITO enables a high lateral conductivity. A 70 nm ZnO is occupied as a hole transporting layer (HTL). It is assumed that the ZnO/ITO/NiO combined layer forms a tunneling junction for supporting efficient charge carrier transportation. A 100 nm thick aluminum (Al) is used as a back reflector. Energy levels of the investigated perovskite/perovskite tandem solar cell are shown in Figure 7.4(b), where the NiO is placed between perovskites and ZnO layer. In this study, top perovskite and bottom perovskite absorber have bandgaps of 1.78 eV and 1.16 eV, respectively; hence, it is assumed that the proposed all perovskite tandem solar cell can exhibit an energy conversion efficiency over 30%. The theoretical limit of the investigated perovskite/perovskite tandem solar cell is estimated to beyond 40%, as shown in Figure 7.3. Here, materials used for the realization of perovskite/perovskite TSCs are energetically and optically matched, which allow improving photon absorption with efficient charge carrier transportation and light incoupling. Perovskites and contact materials have a comparable refractive index that aids in reducing the optical losses by acting as a single block. However, the planar solar cell structure is

limited due to higher optical losses caused by an unwanted high reflection. Therefore, we propose a novel approach for designing all perovskite tandem solar cells, where optical antennas based on nanowires are considered. The schematic of the device design is shown in Figure 7.5. Up to our knowledge, this is the first time that the nanowire-based perovskite/perovskite tandem solar cell is investigated.

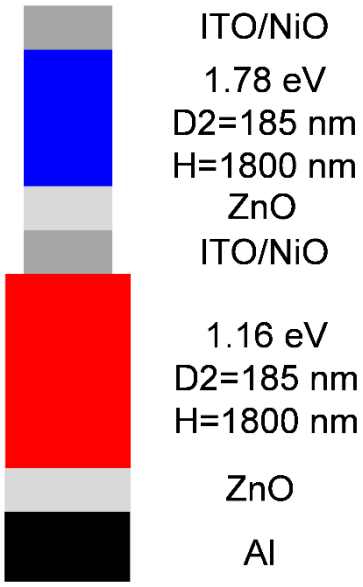

Figure 7.5: (a) Schematic representation of the nanowire-based perovskite/perovskite tandem solar cell. Top and bottom absorber nanowires have diameters of 185 nm and 1800, respectively. The height of both nanowires is 1800 nm.

APPENDIX A

A.1 Electron Beam Physical Vapor Deposition of NiO Films

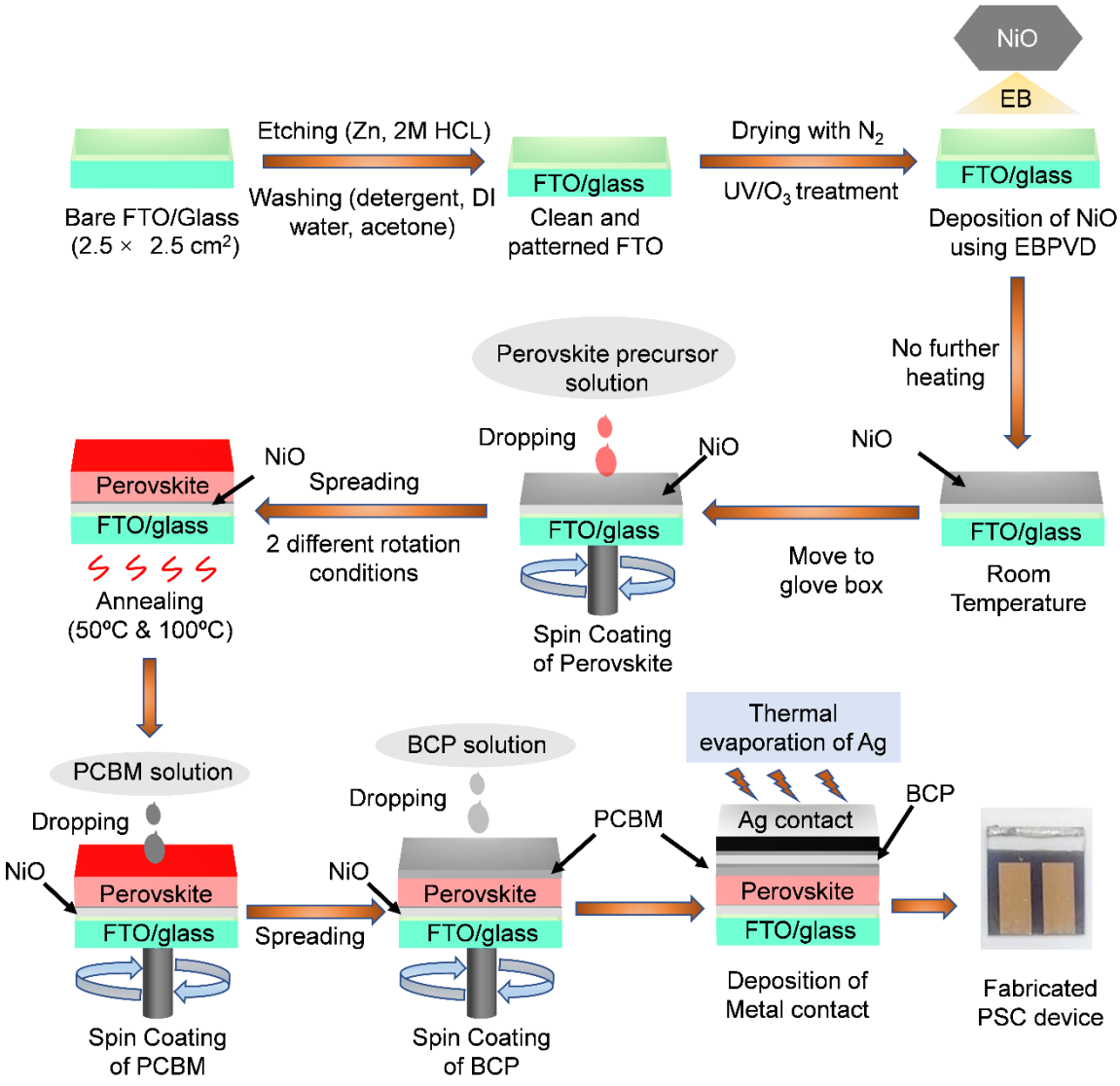

Figure A1.1: Schematic illustration of the perovskite solar cell fabrication.

Table A1.1: Photovoltaic parameter of perovskite solar cell with different NiO thicknesses.

NiO Thickness (nm)	Jsc (mA/cm^2)	VOC (V)	FF	ECE (%)
25	17.90	0.95	0.72	12.24
50	17.10	0.99	0.79	13.37
75	13.78	0.95	0.72	9.42
100	12.07	0.92	0.66	7.32

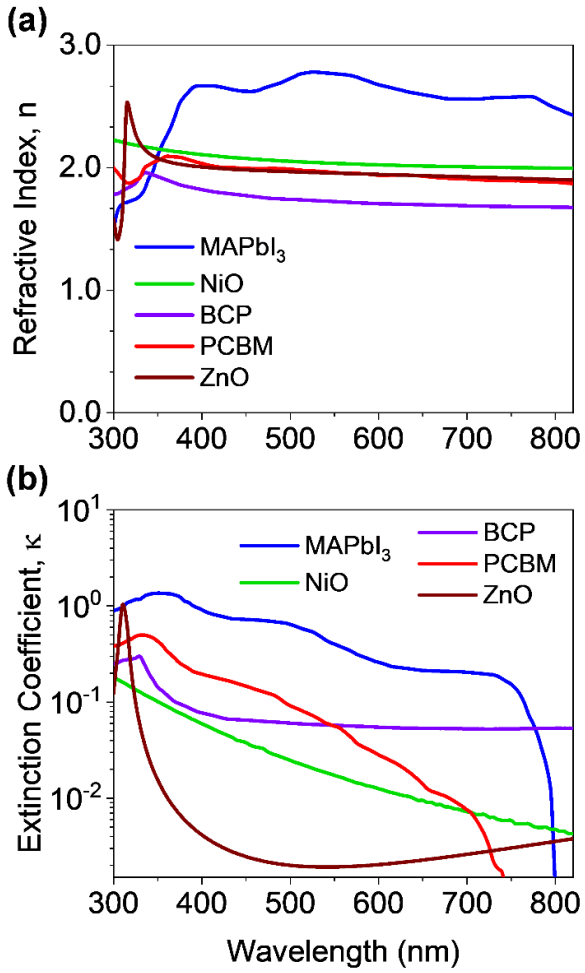

Figure A1.2: (a) Refractive index and (b) extinction coefficient of $MAPbI_3$ perovskite, ZnO, NiO, BCP, and PCBM.

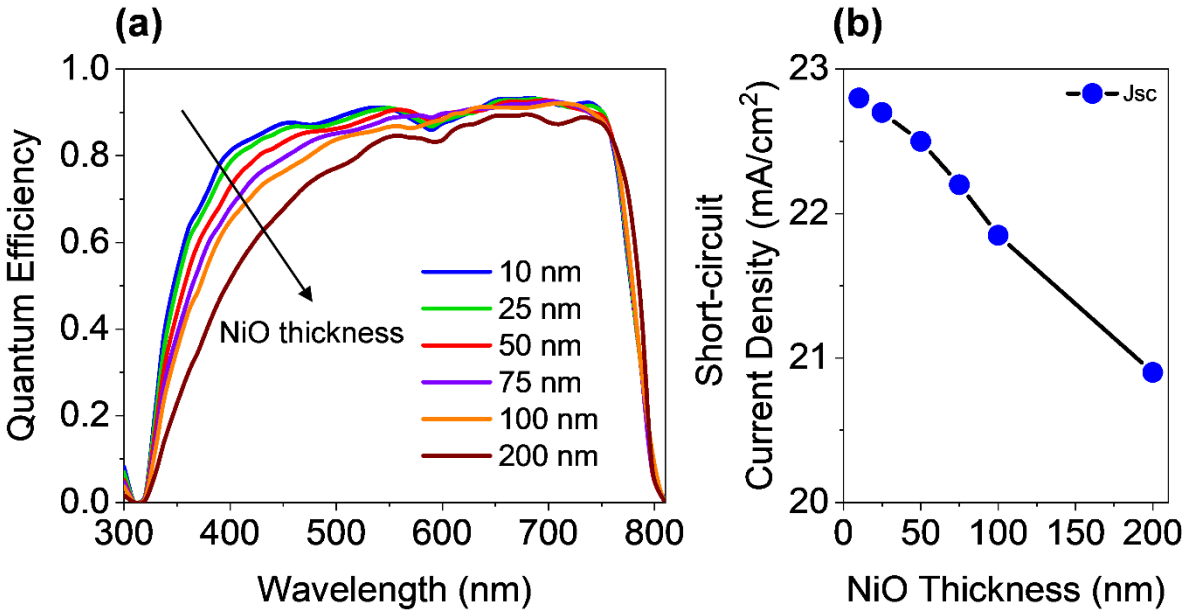

Figure A1.3: Influence of the NiO film thickness on (a) quantum efficiency and (b) short-circuit current density of pyramid textured perovskite solar cells.

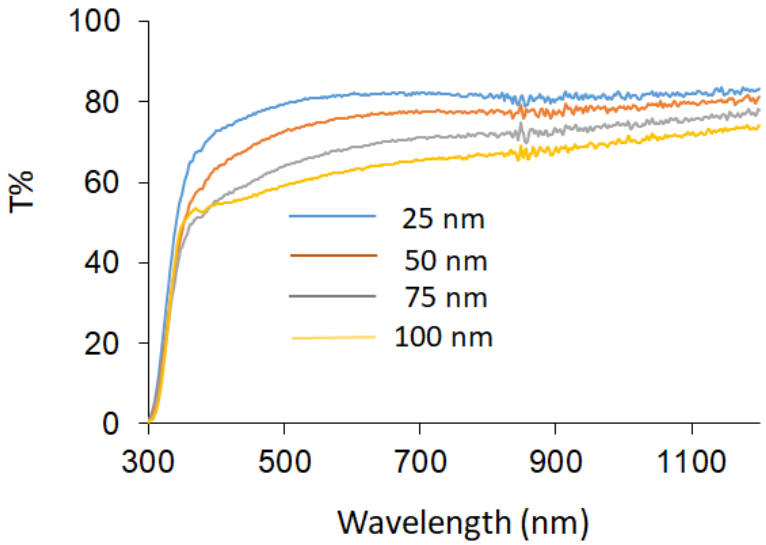

Fig. A1: Thickness dependent optical transmittance of NiO film on FTO substrates.

A.2 Spray Pyrolysis Deposition of TiO_2 Films

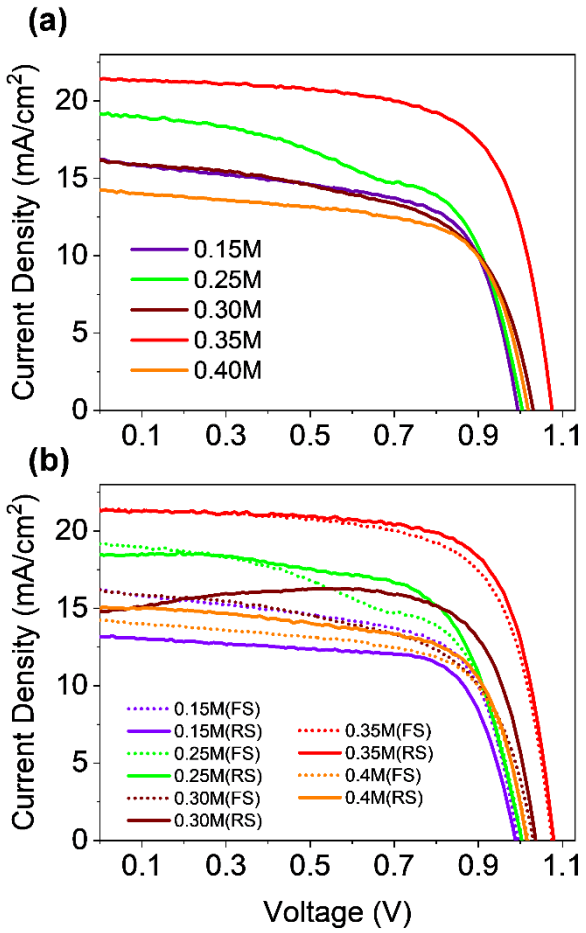

Figure A2.1: Current-voltage (J-V) curves of (a) the forward scan (from -0.1 V to 1.2 V), and (b) both forward scan (from -0.1 V to 1.2 V) and reverse scan (from 1.2 V to -0.1 V) for the fabricated planar PSCs with different TiO_2 precursor solution concentration (from 0.15 m to 0.40 M).

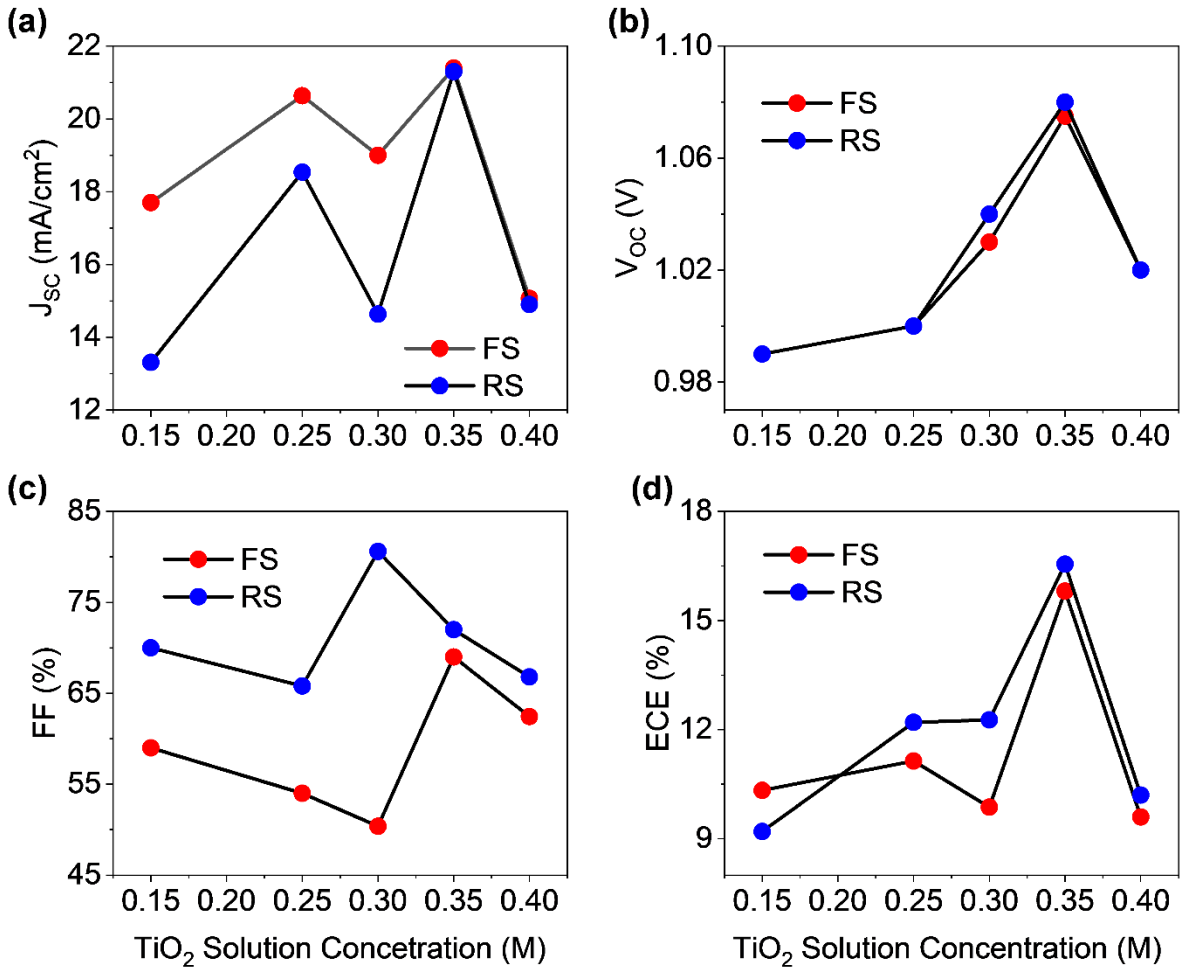

Figure A2.2: TiO_2 precursor solution concentration dependent (a) J_{SC}, (b) V_{OC}, (c) FF, and (d) ECE with a scan from 1.2 V to 0.1 V and a scan rate of 0.05 V/s.

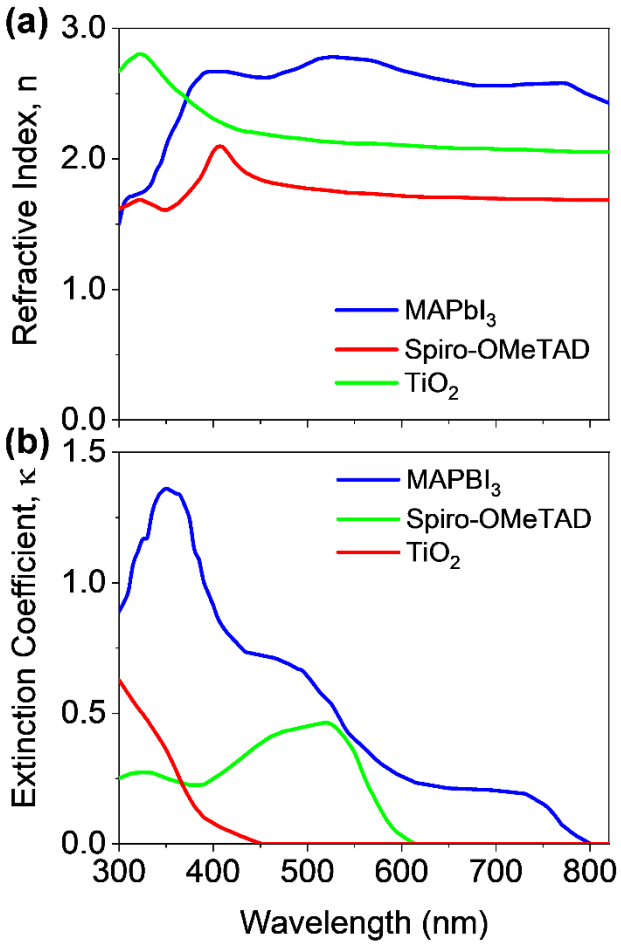

Figure A2.3: (a) Refractive index and (b) extinction coefficient of $MAPbI_3$ perovskite, Spiro-OMeTAD, and TiO_2.

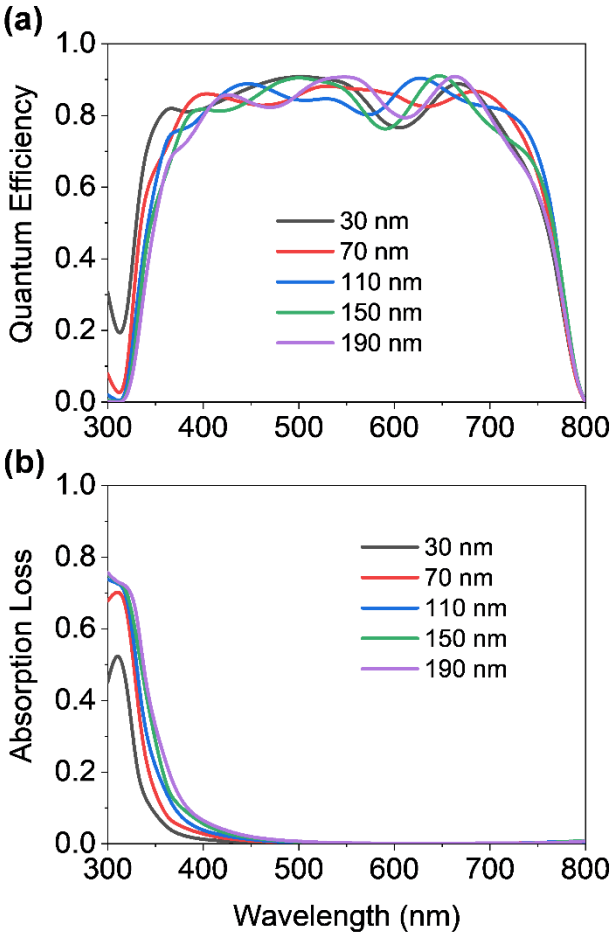

Figure A2.4: (a) The influence of TiO2 ETL thickness on QE and J_{SC}. (b) The corresponding parasitic loss in the ETL layer.

A.3 Atomic Layer Deposition of ZnO Films

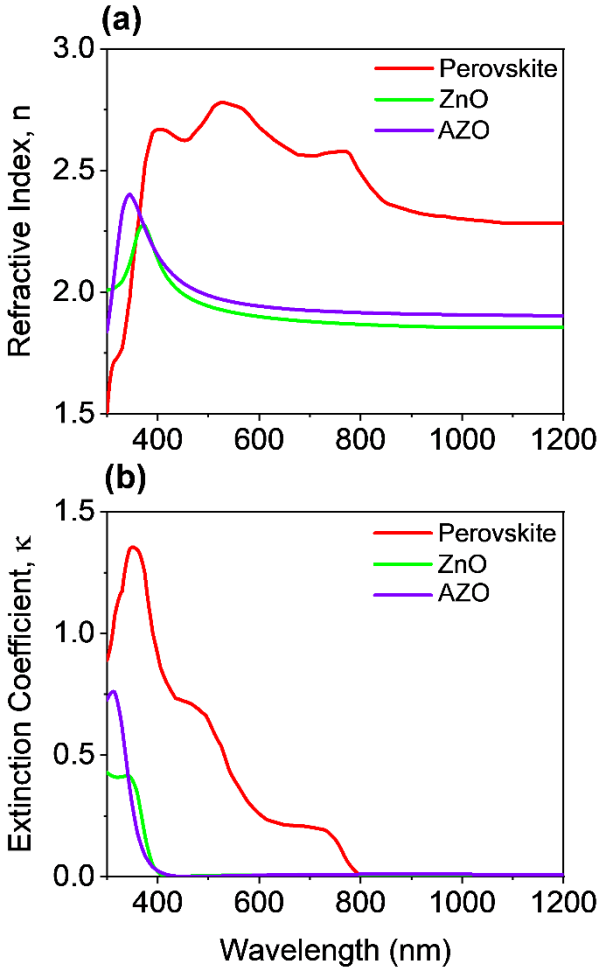

Figure A3.1: (a) Refractive index and (b) extinction coefficient of perovskite ($MAPbI_3$), ZnO, and AZO for the realization of perovskite solar cells.

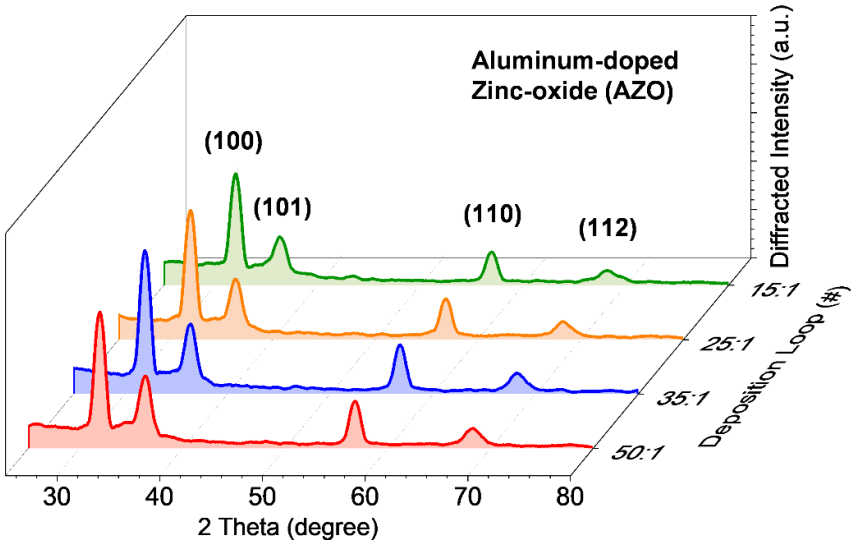

Figure A3.2: X-ray diffraction patterns of AZO films with various deposition cycles, grown on Si substrates.

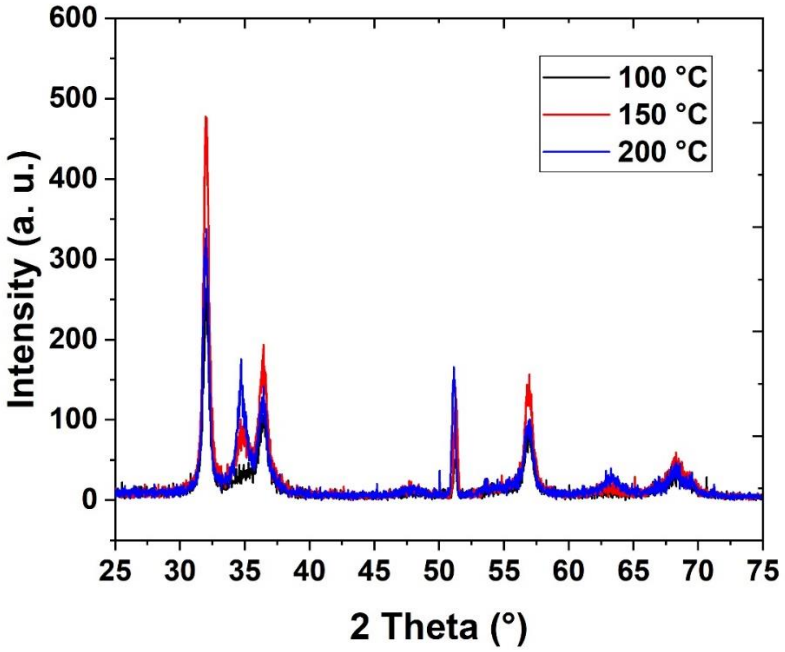

Figure A3.3: X-ray diffraction patterns of AZO films with various deposition temperatures, grown on Si substrates. The deposition cycle ratio is 25:1.

APPENDIX B

B.1 Self-textured ZnO Films as a Front Contact

B.1.1 Influence of different front contact configurations on the optics of the solar cells

Figure B1.1 exhibits the influence of different front contact configurations (ZnO, ZnO+C_{60}, ZnO+LiF, and ZnO+C_{60}+LiF) on the QE and reflection of single-junction PSCs. The perovskite solar cell has a perovskite layer thickness of 100 nm 400 nm.

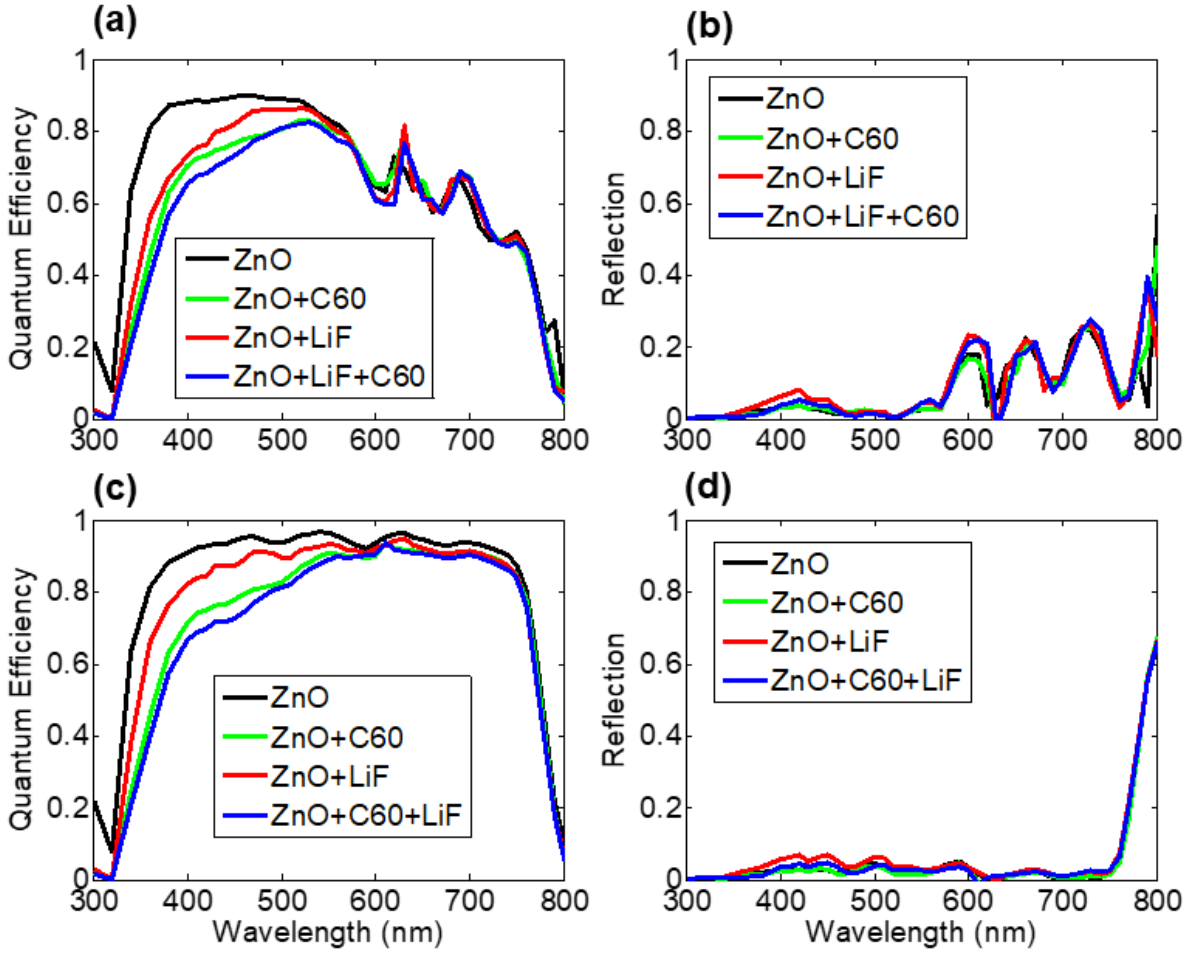

Figure B1.1: Simulated quantum efficiency and reflection of perovskite solar cells using different front contact combinations for (a,b) 100 nm absorber and (c,d) 400 nm absorber. The pyramid has a period of 600 nm and a height of 600 nm.

A solar cell with only a ZnO front contact exhibits a high QE and a high J_{SC}. Some authors add a C_{60} and LiF layer to improve the electrical properties of the solar cell. If a C_{60} layer is inserted between the ZnO and perovskite layers, the QE is distinctly decreased. The QE is reduced due to the optical loss of the C_{60} layer. If the C_{60} layer is replaced by a LiF layer, the QE is reduced too, because of an increased reflection of the solar cell. However, the LiF layer has almost no influence on the QE if the LiF layer is placed between the perovskite and the C_{60} layer.

B.1.2 Effect of an encapsulation layer on the optics of the solar cell

The encapsulation of a solar cell in substrate configuration will lead to a lowering of the J_{SC}. But this is the case for all solar cells in substrate configuration, including all c-Si solar cells. Figure A4.2 exhibits the influence of an encapsulation layer with a refractive index of 1.5 on the optics of the solar cell. For small periods of the surface texture, the effect is rather small, and a small drop in the QE and J_{SC} is observed. For larger periods and thin solar cells, the effect is more pronounced. A drop of the QE is observed for longer wavelengths. To account for this, the period size must be reduced.

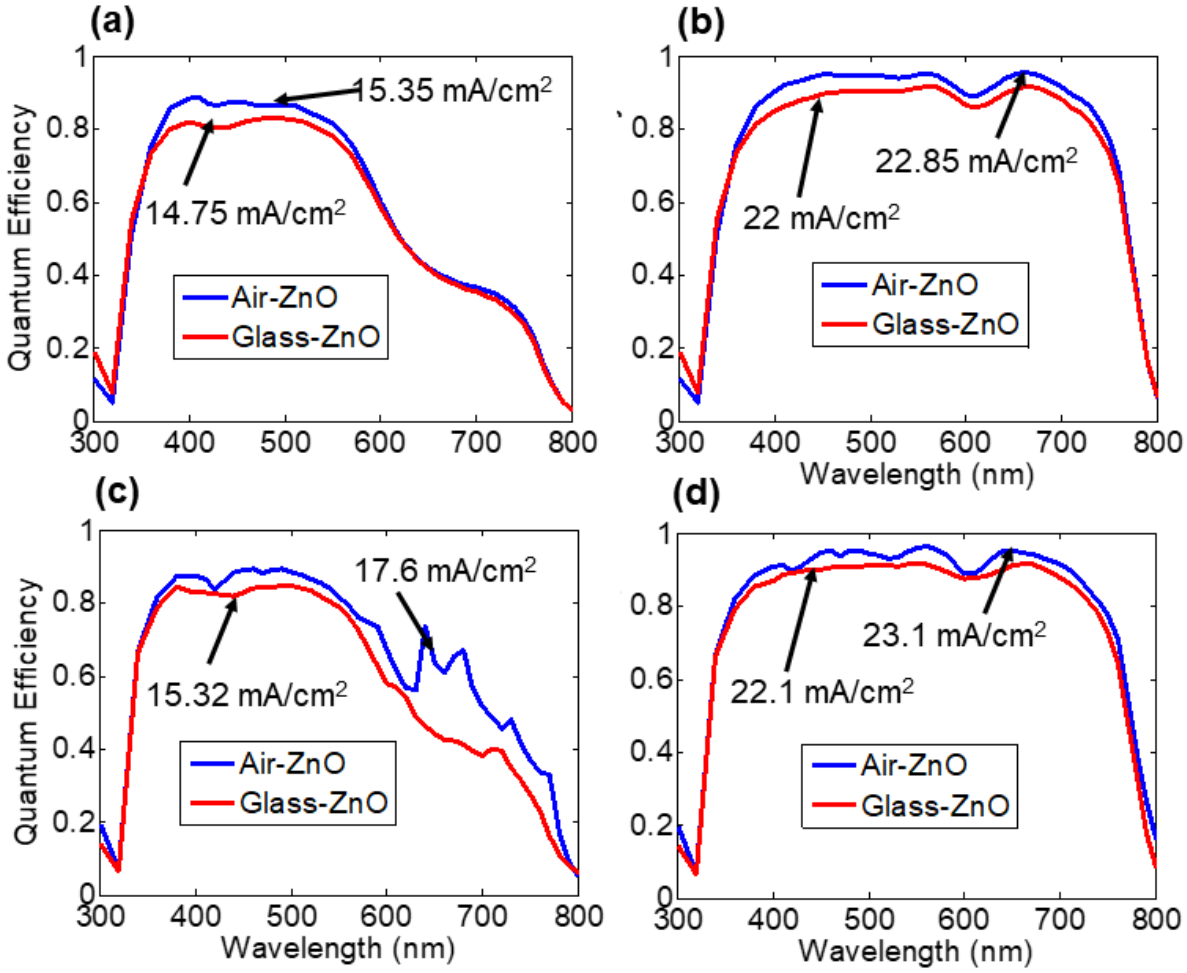

Figure B1.2: A comparison of simulated quantum efficiency between Air-ZnO interface and Glass-ZnO interface perovskite solar cells for a period of (a,b) 300 nm, (c,d) 900 nm. The perovskite absorbing layer has a thickness of (a,c) 100 nm, (b,d) 400 nm. The height of the pyramid texture is kept constant to 600 nm for both period cases. The corresponding short circuit current density is represented in the graphs.

B.1.3 Influence of the ZnO front contact layer thickness on the optics of the solar cell

The thickness and doping concentration of the ZnO front contact layer is determined by the required lateral electrical sheet resistance and the optical losses of the layer. Furthermore, the self-texturing of the film and the size of the pyramids on the surface of the ZnO film is linked to the total thickness of the ZnO film. The height of the pyramid increases, and the opening angle of the pyramid decreases with increasing total film

thickness. The influence of the thickness of the ZnO front contact on the QE and J_{SC} is shown in Figure B1.3. The thickness of the ZnO is varied from 400 nm to 2000 nm, while the thickness of the perovskite layer is kept constant at 400 nm. With increasing ZnO film thickness, an increased absorption in the ZnO layer is observed, which reduces the QE of the solar cell. However, the thickness has no influence on the light incoupling of the solar cell and the light trapping of the solar cell.

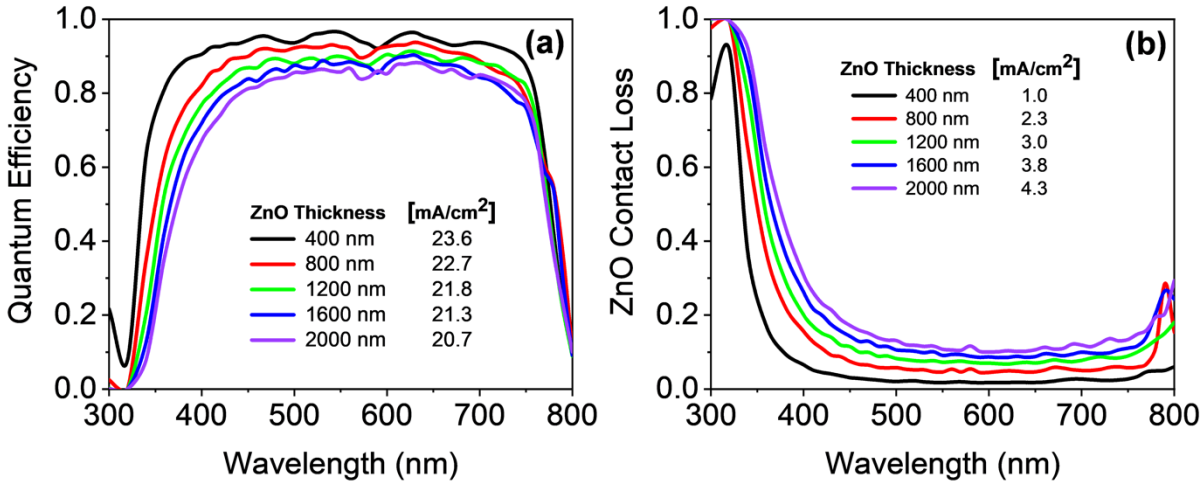

Figure B1.3: A comparison of simulated (a) quantum efficiency and (b) ZnO front contact loss for the textured perovskite solar cell, while the pyramid only covers the front contact and front contact layer thickness is varied from 400 nm to 2000 nm. The perovskite absorbing layer has a thickness of 400 nm. The pyramid has a period of 600 nm and a height of 600 nm.

B.1.4 Extended Drude Lorentz Dielectric Model

The complex refractive index of the metal oxide films is required as an input parameter for the optical simulation.(Mohammad I. Hossain, Qarony, Jovanov, Tsang, & Knipp, 2018c)

$$n + ik = \sqrt{\varepsilon(\omega)} \tag{B1}$$

The dielectric function is determined by using a Drude Lorentz model. The dielectric function is given by

$$\varepsilon(\omega)=\varepsilon_L(\omega)+\varepsilon_D(\omega) \tag{B2}$$

where $\varepsilon_D(\omega)$ and $\varepsilon_L(\omega)$ are the Lorentz and Drude contributions to the dielectric function. The Lorentz dielectric function is given by

$$\varepsilon_L(\omega)=\frac{\Omega_N^2}{\Omega_0^2-\omega^2-i\Omega_\Gamma\omega} \tag{B3}$$

where Ω_N, Ω_0 and Ω_Γ are the plasma frequency, resonant frequency, and damping frequency. The Drude dielectric function is given by

$$\varepsilon_D(\omega)=\varepsilon_\infty-\frac{\omega_N^2}{\omega^2+i\Gamma\omega} \tag{B4}$$

The Drude dielectric function is given by where ε_∞ , ω_N and Γ are the high-frequency dielectric function, the unscreened plasma frequency, and the damping frequency. Equation B1 to B4 were used to describe the complex refractive index of the zinc oxide film.[B1] To describe the ITO film, the Drude model was extended by the following expression for the frequency dependent damping frequency,

$$\Gamma(\omega)=\Gamma_L-\frac{\Gamma_L-\Gamma_H}{\pi}\times\left[\arctan\left(\frac{\omega-\omega_{cross}}{\omega_{width}}\right)+\frac{\pi}{2}\right] \tag{B5}$$

where Γ_{min} and Γ_{max} are the minimal and maximal of the damping frequency, while ω_{cross} and ω_{width} are the crossover frequency, and the width of the transition region.[B2-B4] The extended Drude model accounts for the frequency-dependent mobility, where the conductive for $\omega\rightarrow0$ corresponds to the DC conductivity. The measured reflectance, transmittance, and absorbance in Figure B1.4 were fitted by using equation B1 to B5.

The parameters used to fit the experimental data are summarized in Table B1.1. Based on the extracted plasma frequency the doping concentration was determined by

$$N_{opt} = \frac{\omega_N^2 \varepsilon_0 m_e}{q^2} \tag{B6}$$

where ε_0, m_e, and q are the vacuum permittivity, the mass of an electron and elementary charge. Furthermore, the DC conductivity (σ_{DC}) and resistivity (ρ_{DC}) of the metal oxide films can be determined by

$$\sigma_{DC} = \frac{1}{\rho_{DC}} = \frac{\varepsilon_0 \omega_N^2}{\Gamma} \tag{B7}$$

Based on the optical determined electrical parameters of the films the charge carrier mobility can be calculated by

$$\mu_{opt} \approx \frac{\sigma_{DC}}{q N_{opt}} = \frac{q}{\Gamma m_e} \tag{B8}$$

Table B1.1: Summary of Drude, extended Drude, and Lorentz dielectric model. Extracted doping concentration and charge carrier mobility and experimental data from literature.(T. Koida, Fujiwara, & Kondo, 2009b; Steinhauser, 2008)

	Material	
Extracted parameters	**ITO**	**ZnO**
N_{opt}:= Doping concentration [1/cm^3]	10×10^{20}	22×10^{19}
μ_{opt}:= Carrier mobility [cm^2/V/s]	22.5	35
ρ_{opt}:= Electrical Resistivity [Ωcm]	2.3×10^{-4}	1.3×10^{-3}

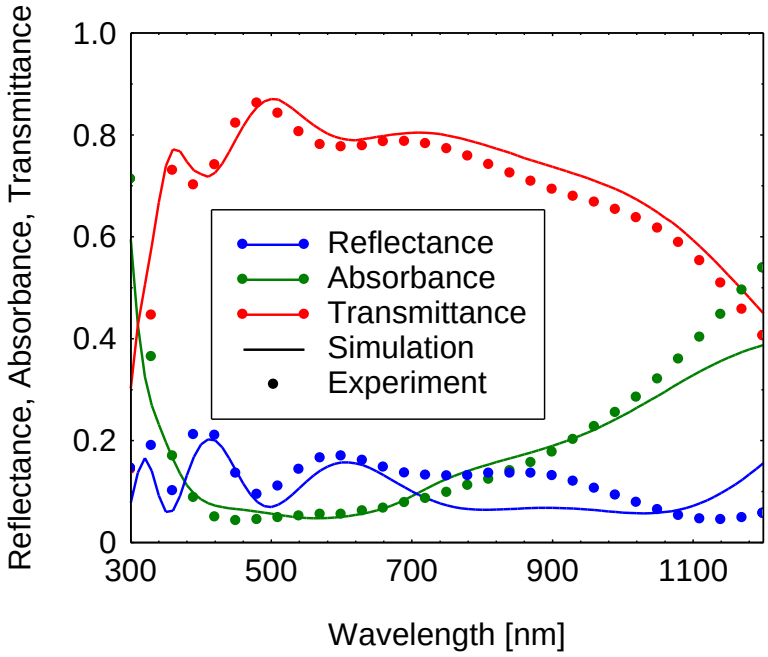

Figure B1.4: Measured and simulated reflectance, transmittance, and the absorbance of an ITO film with a thickness of 240 nm prepared on a glass substrate. A Lorentz and an extended Drude Model were used to describe the complex refractive index of the ITO film. Parameters used for the calculation of the reflectance, transmittance, and absorbance are given in Table B1. The measured data is adapted from Ref.(T. Koida et al., 2009b; Steinhauser, 2008)

Figure B1.4 exhibits measurements of the reflectance, transmittance and absorbance of a 240 nm thick ITO layer. The data is adapted from Ref. B5. The reflectance, transmittance and absorbance are simulated by using the above described Drude Lorentz model to provide the complex refractive index of the ITO layer. The parameters required to model the complex refractive index of the ITO layer are provided in Table B1. A good agreement between the measured reflectance, transmittance and absorbance is observed. The high absorbance of the ITO film for long wavelengths is caused by the high free carrier absorption.

B.2 Non-resonant ZnO Metasurfaces as a Front Contact

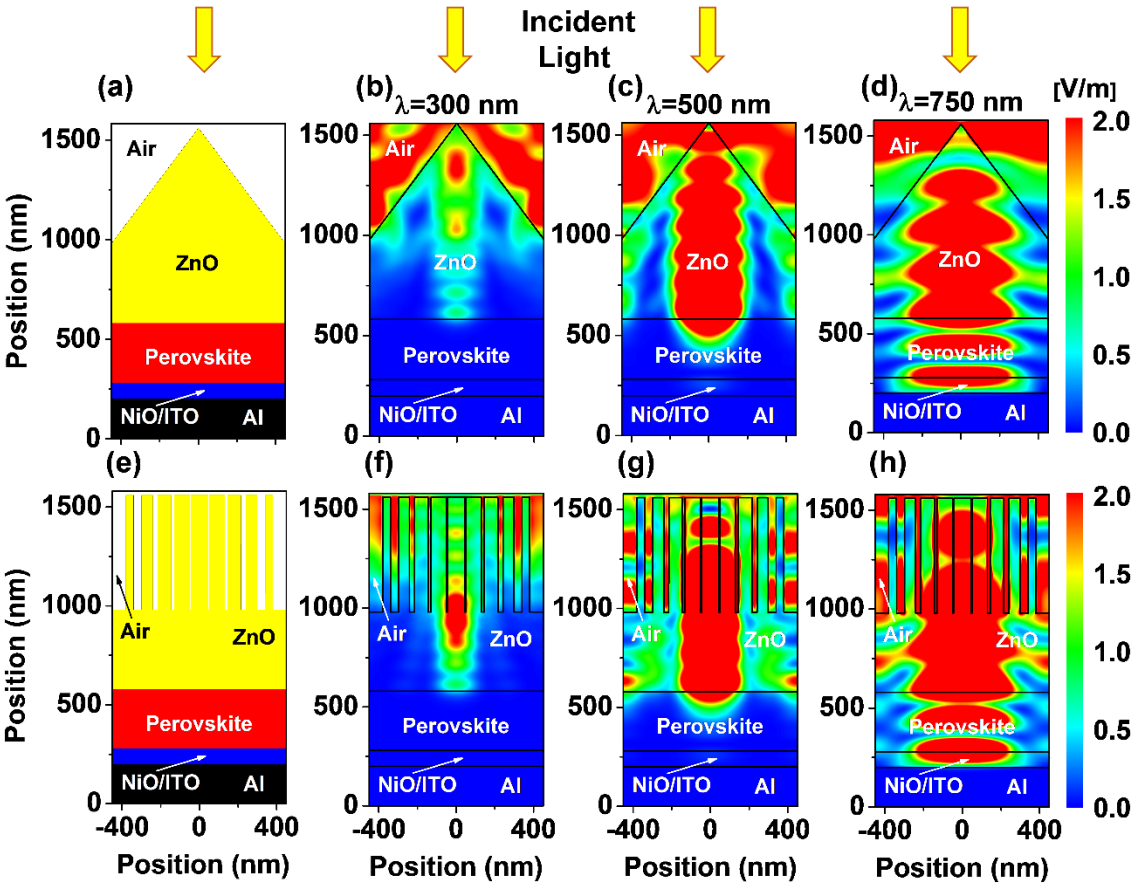

Figure B2.1: (a) Schematic cross-section of perovskite solar cell with pyramid textured front contact and corresponding electric field distribution for an incident wavelength of (b) 300 nm, (c) 500 nm, and (d) 750 nm. (e) Schematic cross-section of perovskite solar cell with metasurfaces structured front contact and corresponding electric field distribution for an incident wavelength of (f) 300 nm, (g) 500 nm, and (h) 750 nm. The period and height of the structures are 900 nm and 580 nm, respectively.

APPENDIX C

C.1 Nanophotonic Design of Perovskite/Silicon Tandem Solar Cells

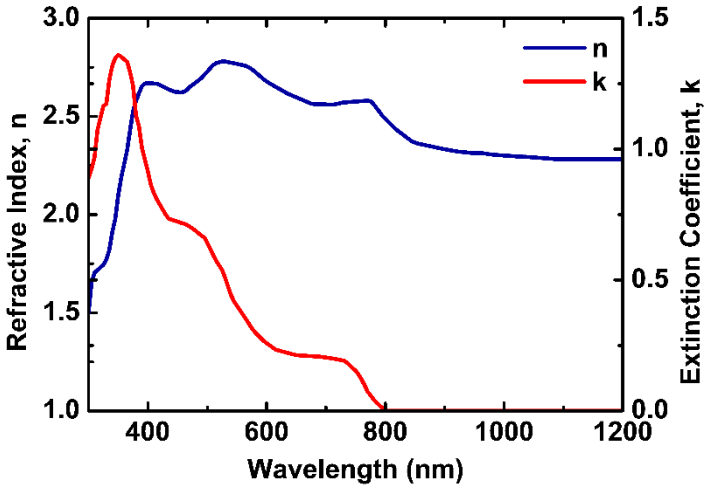

Figure C1.1: Refractive index (n) and extinction coefficient (k) of $CH_3NH_3PbI_3$ perovskite adapted from Löper et.al.(Löper et al., 2015a)

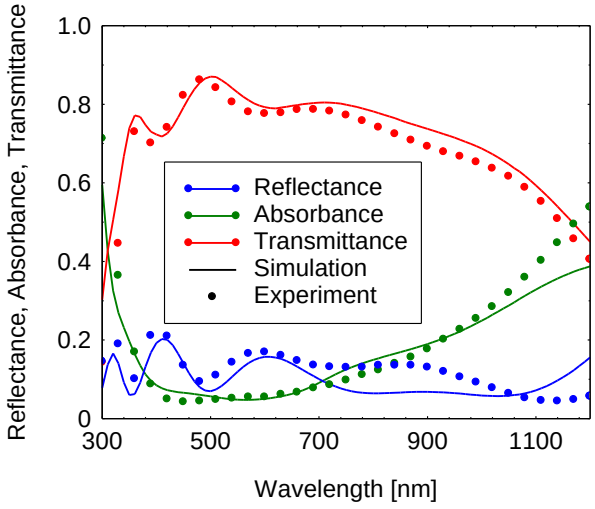

Figure C1.2: Measured and simulated reflectance, transmittance, and absorbance of an ITO film with a thickness of 240 nm prepared on a glass substrate. A Lorentz and an extended Drude model was used to describe the complex refractive index of the ITO film. Parameters used for the calculation of the reflectance, transmittance, and absorbance are given in Table C1. The measured data is adapted from Ref.(Takashi Koida, Fujiwara, & Kondo, 2007a)

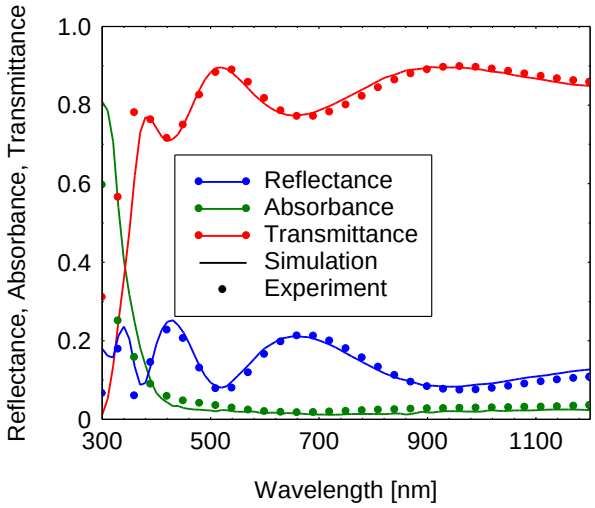

Figure C1.3: Measured and simulated reflectance, transmittance, and absorbance of an IOH film with a thickness of 240 nm prepared on a glass substrate. A Lorentz and an extended Drude model was used to describe the complex refractive index of the IOH film. Parameters used for the calculation of the reflectance, transmittance, and absorbance are given in Table C1. The measured data is adapted from Ref.(Takashi Koida et al., 2007a)

The complex refractive index of metal oxide films is required as the input parameter for the optical simulation.

$$n + ik = \sqrt{\varepsilon(\omega)} \tag{C1}$$

The dielectric function is determined by using a Drude Lorentz model. The dielectric function is given by

$$\varepsilon(\omega) = \varepsilon_L(\omega) + \varepsilon_D(\omega) \tag{C2}$$

where $\varepsilon_D(\omega)$ and $\varepsilon_L(\omega)$ are the Lorentz and Drude contributions to the dielectric function. The Lorentz dielectric function is given by

$$\varepsilon_L(\omega) = \frac{\Omega_N^2}{\Omega_0^2 - \omega^2 - i\Omega_\Gamma\omega} \tag{C3}$$

where Ω_N, Ω_0 and Ω_Γ are the plasma frequency, resonant frequency and damping

frequency. The Drude dielectric function is given by

$$\varepsilon_D(\omega) = \varepsilon_\infty - \frac{\omega_N^2}{\omega^2 + i\Gamma\omega} \quad \text{(C4)}$$

The Drude dielectric function is given by where ε_∞ , ω_N and Γ are the high frequency dielectric function, the unscreened plasma frequency and the damping frequency. Equation C1 to C4 were used to describe the complex refractive index of the zinc oxide film.[C](Steinhauser, 2008) To describe the ITO and IOH film the Drude model was extended by the following expression for the frequency dependent damping frequency,

$$\Gamma(\omega) = \Gamma_L - \frac{\Gamma_L - \Gamma_H}{\pi} \times \left[\arctan\left(\frac{\omega - \omega_{cross}}{\omega_{width}}\right) + \frac{\pi}{2}\right] \quad \text{(C5)}$$

where Γ_{min} and Γ_{max} are the minimal and maximal of the damping frequency, while ω_{cross} and ω_{width} are the crossover frequency and the width of the transition region.[C4–C6] The extended Drude model accounts for the frequency dependent mobility, where the conductive for $\omega \rightarrow 0$ corresponds to the DC conductivity. The measured reflectance, transmittance, and absorbance in Figure C1.2 and Figure C1.3 was fitted by using equation C1 to C5. The parameters used to fit the experimental data are summarized in Table C1.1.

Based on the extracted plasma frequency the doping concentration was determined by

$$N_{opt} = \frac{\omega_N^2 \varepsilon_0 m_e}{q^2} \quad \text{(C6)}$$

where ε_0, m_e, and q are the vacuum permittivity, mass of an electron and elementary charge. Furthermore, the DC conductivity (σ_{DC}) and resistivity (ρ_{DC}) of the metal oxide films can be determined by

$$\sigma_{DC} = \frac{1}{\rho_{DC}} = \frac{\varepsilon_0 \omega_N^2}{\Gamma} \quad \text{(C7)}$$

Based on the optical determined electrical parameters of the films the charge carrier mobility can be calculated by

$$\mu_{opt} \approx \frac{\sigma_{DC}}{qN_{opt}} = \frac{q}{\Gamma m_e} \quad \text{(C8)}$$

Table C1.1: Summary of Drude, extended Drude and Lorentz dielectric model. Extracted doping concentration and charge carrier mobility and experimental data from literature.(T. Koida et al., 2009b; Steinhauser, 2008)

	Material		
Extracted parameters	**ITO**	**IOH**	**ZnO**
N_{opt}:= Doping concentration [1/cm^3]	10×10^{20}	3.9×10^{20}	2.5×10^{19}
μ_{opt}:= Carrier mobility [cm^2/V/s]	22.5	66	35
ρ_{opt}:= Electrical Resistivity [Ωcm]	2.3×10^{-4}	2.4×10^{-4}	7×10^{-3}

(Courtesy: Dr. Asman Tamang, Jacobs University Bremen, Germany)

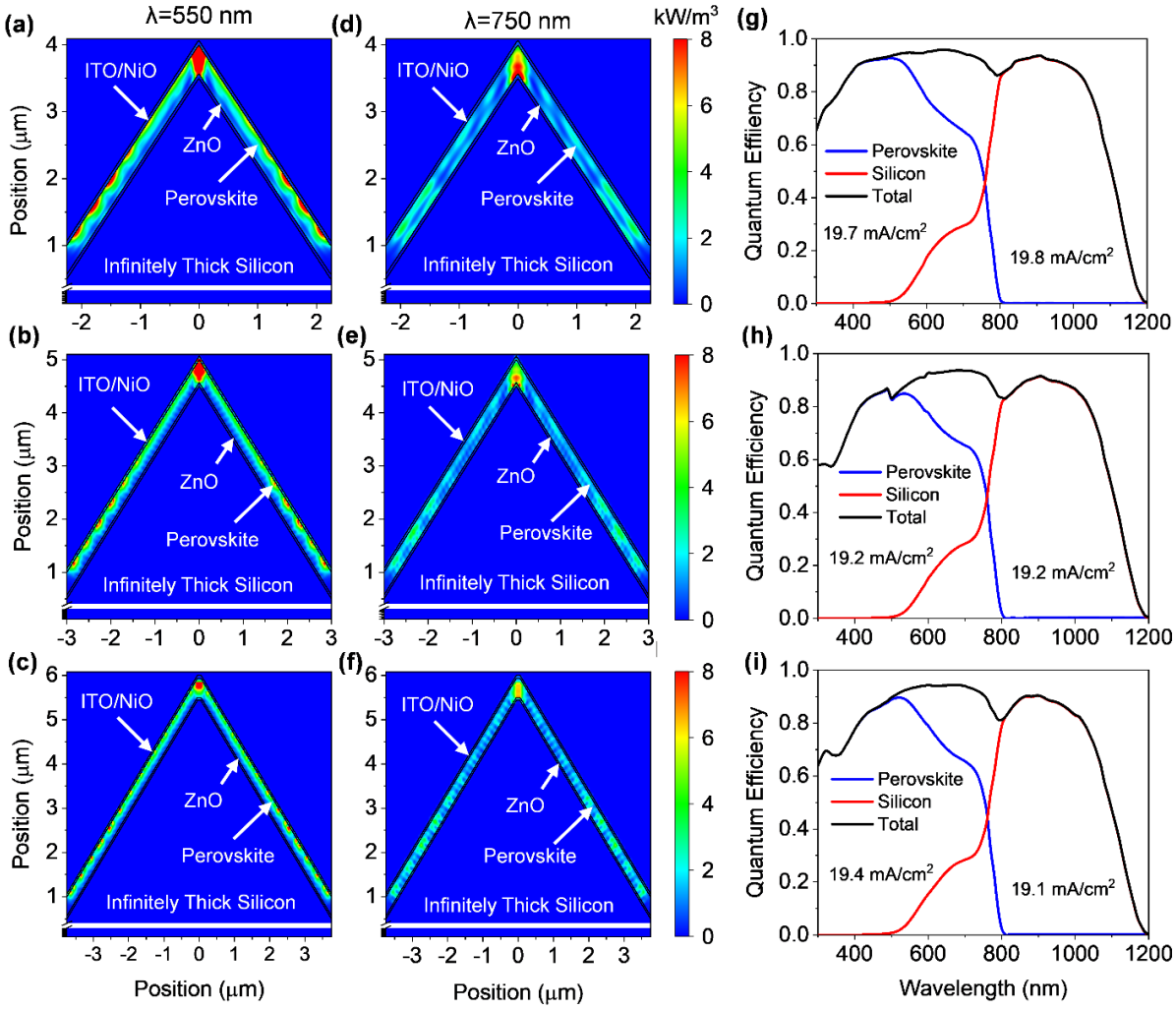

Figure C1.4: Power density distribution of perovskite top solar cells of perovskite/silicon tandem solar cell for film growth in the direction of the substrate normal for an incident wavelength of (a-c) 550 nm and (d-f) 750 nm. Different pyramid texture periods of (a,d) 4500 nm, (b,e) 6000 nm, and (c,f) 7500 nm are used for the investigation, where period to height ratio is kept constant.

APPENDIX D

D.1 Three-Channel Vertically Stacked Perovskite Color Sensor

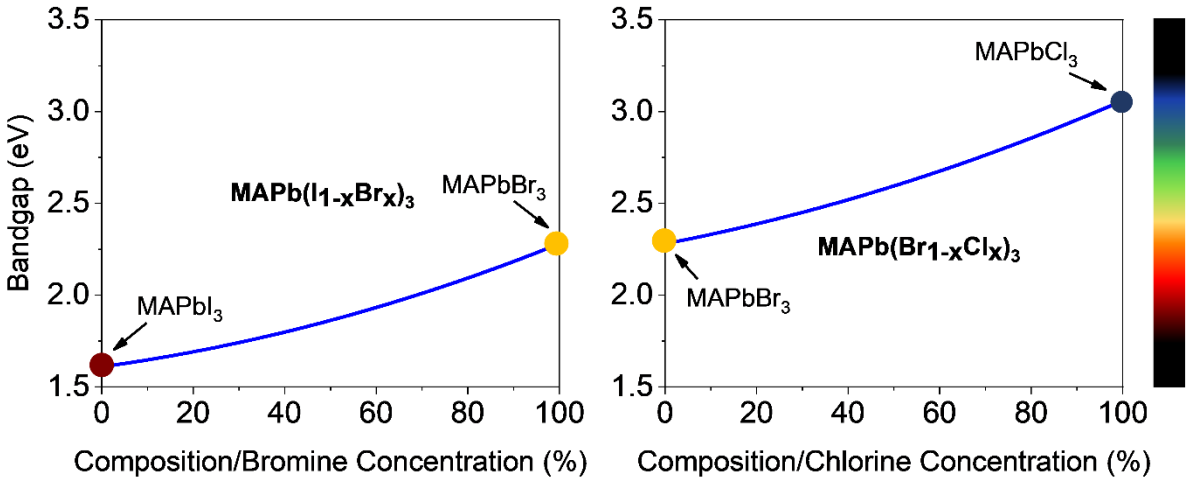

Figure D1.1: Bandgap of perovskites alloys as a function of the composition.

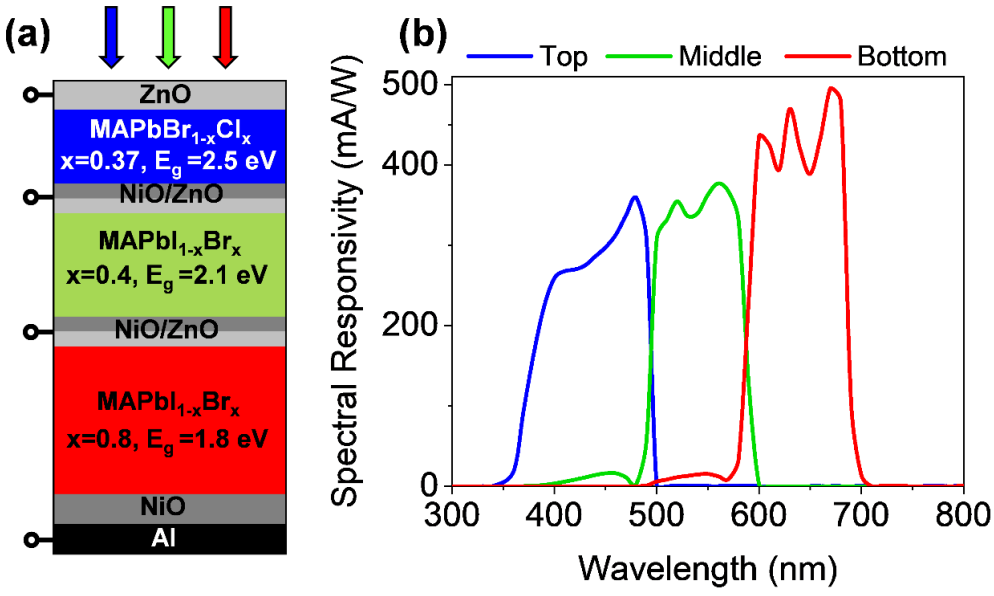

Figure D1.2: (a) Schematic cross-section (b) The simulated spectral responsivity of vertically stacked of a vertically stacked color sensor using perovskite alloys.

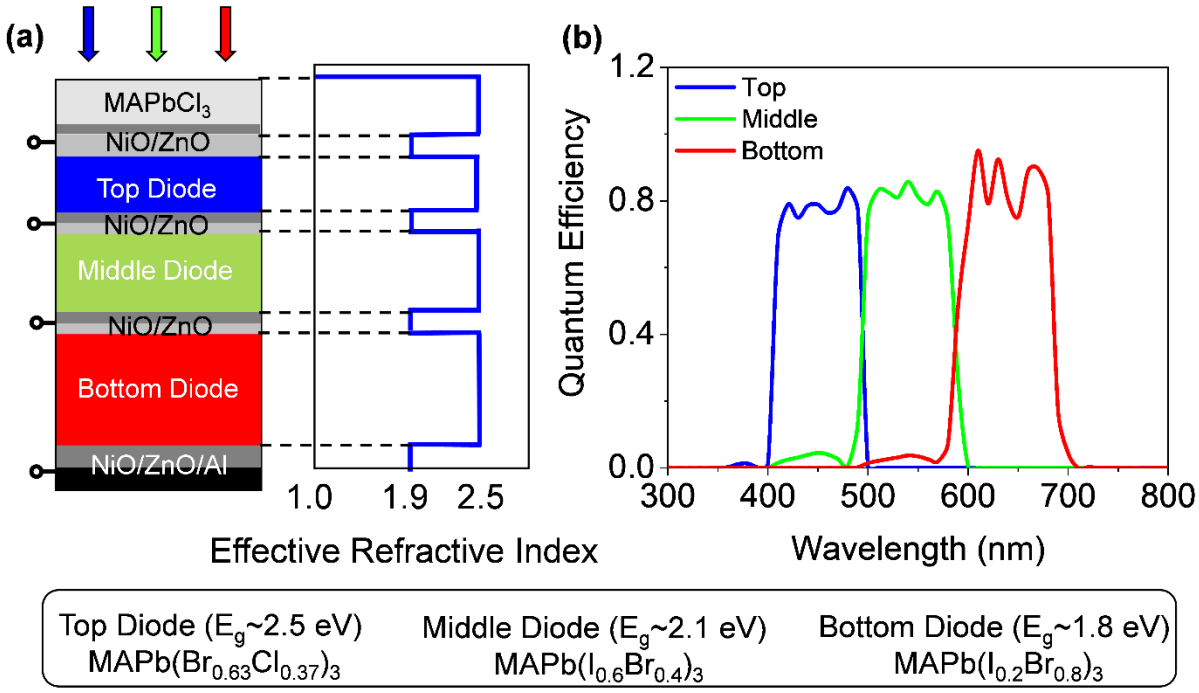

Figure D1.3: (a) Schematic cross-section and corresponding effective refractive index of flat vertically stacked perovskite color sensor with a UV blocking layer. (b) The simulated corresponding quantum efficiency of the flat vertically stacked perovskite color sensor.

D.2 Multispectral Imaging with Perovskite Alloys

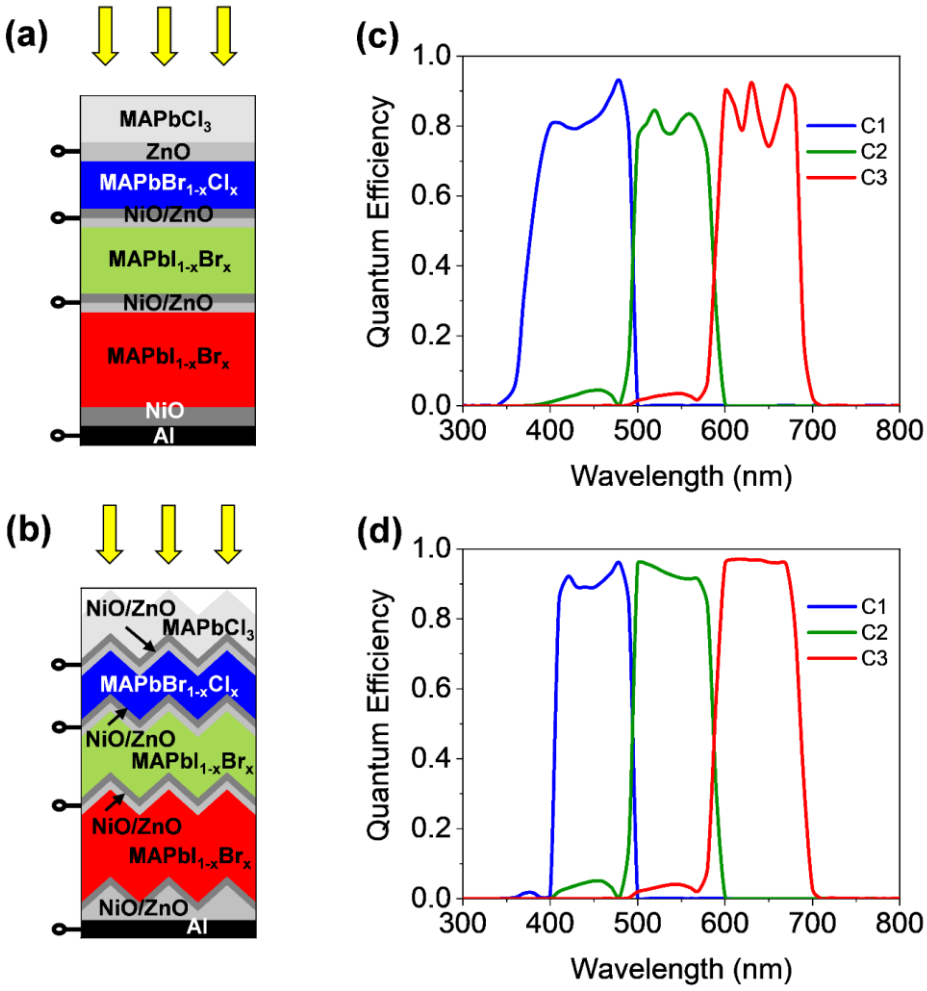

Figure D2.1: Schematic cross-section of (a) a flat and (b) textured vertically stacked color sensor using perovskite alloys. (c,d) Corresponding calculated quantum efficiencies.

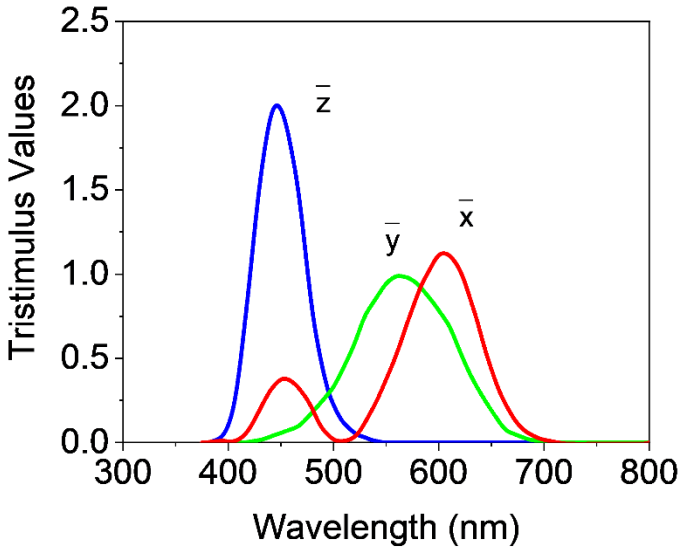

Figure D2.2: Standard color matching function for human vision by CIE.

Table D2.1: Material properties and device descriptions of the six-channel multispectral image sensor.

Layer	Function	Material	Cut-off wavelength	Bandgap	Composition	Thickness
1	UV blocking	MAPbCl3		3.1 eV		
2	Contact 1	NiO/ZnO				400 nm
3	absorber 1 / Channel 1	$MAPbCl_xBr_{1-x}$	450 nm	2.75 eV	x=0.68	larger than penetration depth
4		ZnO				100 nm
5	absorber 2 / Channel 2	$MAPbCl_xBr_{1-x}$	500 nm	2.5 eV	x=0.37	larger than penetration depth
6	Contact 2	NiO/ZnO				400 nm
7	absorber 3 / Channel 3	$MAPbBr_xI_{1-x}$	550 nm	2.25 eV	x=0.96	larger than penetration depth
8		ZnO				100 nm
9	absorber 4 / Channel 4	$MAPbBr_xI_{1-x}$	600 nm	2.08 eV	x=0.79	larger than penetration depth
10	Contact 3	NiO/ZnO				400 nm
11	absorber 5 / Channel 5	$MAPbBr_xI_{1-x}$	650 nm	1.92 eV	x=0.50	larger than penetration depth
12		ZnO				100 nm
13	absorber 6 / Channel 6	$MAPbBr_xI_{1-x}$	700 nm	1.8 eV	x=0.38	larger than penetration depth
14	Contact 4	NiO/Al				

REFERENCES

Abzieher, T., Moghadamzadeh, S., Schackmar, F., Eggers, H., Sutterlüti, F., Farooq, A., … Paetzold, U. W. (2019). Electron-Beam-Evaporated Nickel Oxide Hole Transport Layers for Perovskite-Based Photovoltaics. *Advanced Energy Materials*, *9*(12), 1802995. https://doi.org/10.1002/aenm.201802995

Alfonso-Garcia, A., Shklover, J., Sherlock, B. E., Panitch, A., Griffiths, L. G., & Marcu, L. (2018). Fiber-based fluorescence lifetime imaging of recellularization processes on vascular tissue constructs. *Journal of Biophotonics*, *11*(9), e201700391. https://doi.org/10.1002/jbio.201700391

Alharbi, F. H., & Kais, S. (2015). Theoretical limits of photovoltaics efficiency and possible improvements by intuitive approaches learned from photosynthesis and quantum coherence. *Renewable and Sustainable Energy Reviews*, *43*, 1073–1089. https://doi.org/10.1016/j.rser.2014.11.101

An, Q., Fassl, P., Hofstetter, Y. J., Becker-Koch, D., Bausch, A., Hopkinson, P. E., & Vaynzof, Y. (2017). High performance planar perovskite solar cells by ZnO electron transport layer engineering. *Nano Energy*, *39*, 400–408. https://doi.org/10.1016/j.nanoen.2017.07.013

Arbabi, E., Arbabi, A., Kamali, S. M., Horie, Y., Faraji-Dana, M., & Faraon, A. (2018). MEMS-tunable dielectric metasurface lens. *Nature Communications*, *9*(1), 812. https://doi.org/10.1038/s41467-018-03155-6

Aydin, E., Troughton, J., De Bastiani, M., Ugur, E., Sajjad, M., Alzahrani, A., … De Wolf, S. (2018). Room-Temperature-Sputtered Nanocrystalline Nickel Oxide as Hole Transport Layer for p–i–n Perovskite Solar Cells. *ACS Applied Energy Materials*, *1*(11), 6227–6233. https://doi.org/10.1021/acsaem.8b01263

Barraud, L., Holman, Z. C., Badel, N., Reiss, P., Descoeudres, A., Battaglia, C., … Ballif, C. (2013a). Hydrogen-doped indium oxide/indium tin oxide bilayers for high-efficiency silicon heterojunction solar cells. *Solar Energy Materials and Solar Cells*, *115*, 151–156. https://doi.org/10.1016/j.solmat.2013.03.024

Barraud, L., Holman, Z. C., Badel, N., Reiss, P., Descoeudres, A., Battaglia, C., … Ballif, C. (2013b). Hydrogen-doped indium oxide/indium tin oxide bilayers for high-efficiency silicon heterojunction solar cells. *Solar Energy Materials and Solar Cells*, *115*, 151–156. https://doi.org/10.1016/j.solmat.2013.03.024

Bayer, B. E. (1976). Color Imaging Array. *US Patent*.

Boccard, M., Cuony, P., Battaglia, C., Hänni, S., Nicolay, S., Ding, L., … Ballif, C. (2012). Nanometer- and micrometer-scale texturing for high-efficiency micromorph thin-film silicon solar cells. *IEEE Journal of Photovoltaics*, *2*(2), 83–87. https://doi.org/10.1109/JPHOTOV.2011.2179414

Boppart, S. A., Brown, J. Q., Farah, C. S., Kho, E., Marcu, L., Saunders, C. M., & Sterenborg, H. J. C. M. (2017). Label-free optical imaging technologies for rapid translation and use during intraoperative surgical and tumor margin assessment. *Journal of Biomedical Optics*, *23*(02), 1. https://doi.org/10.1117/1.JBO.23.2.021104

Burschka, J., Kessler, F., Nazeeruddin, M. K., & Grätzel, M. (2013). Co(III) Complexes as p-Dopants in Solid-State Dye-Sensitized Solar Cells. *Chemistry of Materials*, *25*(15), 2986–2990. https://doi.org/10.1021/cm400796u

Burschka, J., Pellet, N., Moon, S. J., Humphry-Baker, R., Gao, P., Nazeeruddin, M. K., & Grätzel, M. (2013). Sequential deposition as a route to high-performance perovskite-sensitized solar cells. *Nature*, *499*(7458), 316–319. https://doi.org/10.1038/nature12340

Bush, K. A., Palmstrom, A. F., Yu, Z. J., Boccard, M., Cheacharoen, R., Mailoa, J. P., … McGehee, M. D. (2017a). 23.6%-efficient monolithic perovskite/silicon tandem solar cells with improved stability. *Nature Energy*, *2*(4), 17009. https://doi.org/10.1038/nenergy.2017.9

Bush, K. A., Palmstrom, A. F., Yu, Z. J., Boccard, M., Cheacharoen, R., Mailoa, J. P., … McGehee, M. D. (2017b). 23.6%-efficient monolithic perovskite/silicon tandem

solar cells with improved stability. *Nature Energy*, *2*(4), 17009. https://doi.org/10.1038/nenergy.2017.9

Castelli, I. E., García-Lastra, J. M., Thygesen, K. S., & Jacobsen, K. W. (2014). Bandgap calculations and trends of organometal halide perovskites. *APL Materials*, *2*(8), 081514. https://doi.org/10.1063/1.4893495

Chan, L. W., Morse, D. E., & Gordon, M. J. (2018). Moth eye-inspired anti-reflective surfaces for improved IR optical systems & visible LEDs fabricated with colloidal lithography and etching. *Bioinspiration & Biomimetics*, *13*(4), 041001. https://doi.org/10.1088/1748-3190/aab738

Chandezon, J., Maystre, D., & Raoult, G. (1980). A new theoretical method for diffraction gratings and its numerical application. *Journal of Optics*. https://doi.org/10.1088/0150-536X/11/4/005

Chen, D., Manley, P., Tockhorn, P., Eisenhauer, D., Köppel, G., Hammerschmidt, M., … Jäger, K. (2018). Nanophotonic Light Management for Perovskite-Silicon Tandem Solar Cells. *Journal of Photonics for Energy*, *8*(2), 022601.

Chen, H.-L., Lu, Y.-M., & Hwang, W.-S. (2006). Thickness dependence of electrical and optical properties of sputtered Nickel oxide films. *Thin Solid Films*, *514*(1–2), 361–365. https://doi.org/10.1016/j.tsf.2006.04.041

Chen, H.-T., Taylor, A. J., & Yu, N. (2016). A review of metasurfaces: physics and applications. *Reports on Progress in Physics*, *79*(7), 076401. https://doi.org/10.1088/0034-4885/79/7/076401

Chen, Q., Hubbard, G., Shields, P. A., Liu, C., Allsopp, D. W. E., Wang, W. N., & Abbott, S. (2009). Broadband moth-eye antireflection coatings fabricated by low-cost nanoimprinting. *Applied Physics Letters*, *94*(26), 263118. https://doi.org/10.1063/1.3171930

Chen, W., Wu, Y., Tu, B., Liu, F., Djurišić, A. B., & He, Z. (2018). Inverted planar organic-inorganic hybrid perovskite solar cells with NiO x hole-transport layers as

light-in window. *Applied Surface Science*, *451*, 325–332. https://doi.org/10.1016/j.apsusc.2018.04.230

Chung, H., Sun, X., Mohite, A. D., Singh, R., Kumar, L., Alam, M. A., & Bermel, P. (2017). Modeling and designing multilayer 2D perovskite / silicon bifacial tandem photovoltaics for high efficiencies and long-term stability. *Optics Express*, *25*(8), A311. https://doi.org/10.1364/OE.25.00A311

CIE: Publication No. 15.2. (1986). *Colorimetry* (2nd ed.). Austria, Central Bureau of the CIE.

CIE. (2001). *Improvement to industrial colour-difference evaluation*. Vienna: Central Bureau of the CIE.

Cohen, J., Wyszecki, G., & Stiles, W. S. (1968). Color Science: Concepts and Methods, Quantitative Data and Formulas. *The American Journal of Psychology*, *81*(1), 128. https://doi.org/10.2307/1420820

Conings, B., Baeten, L., De Dobbelaere, C., D'Haen, J., Manca, J., & Boyen, H.-G. (2014). Perovskite-Based Hybrid Solar Cells Exceeding 10% Efficiency with High Reproducibility Using a Thin Film Sandwich Approach. *Advanced Materials*, *26*(13), 2041–2046. https://doi.org/10.1002/adma.201304803

Cui, Jin, Meng, F., Zhang, H., Cao, K., Yuan, H., Cheng, Y., … Wang, M. (2014). CH 3 NH 3 PbI 3 -Based Planar Solar Cells with Magnetron-Sputtered Nickel Oxide. *ACS Applied Materials & Interfaces*, *6*(24), 22862–22870. https://doi.org/10.1021/am507108u

Cui, Jingbiao. (2012). Zinc oxide nanowires. *Materials Characterization*, *64*, 43–52. https://doi.org/10.1016/j.matchar.2011.11.017

Curzon, F. L., & Ahlborn, B. (1975). Efficiency of a Carnot engine at maximum power output. *American Journal of Physics*, *43*(1), 22–24. https://doi.org/10.1119/1.10023

Da, Y., Xuan, Y., & Li, Q. (2018). Quantifying energy losses in planar perovskite solar

cells. *Solar Energy Materials and Solar Cells*, *174*, 206–213. https://doi.org/10.1016/j.solmat.2017.09.002

De Vos, A., Landsberg, P. T., Baruch, P., & Parrott, J. E. (1993). Entropy fluxes, endoreversibility, and solar energy conversion. *Journal of Applied Physics*, *74*(6), 3631–3637. https://doi.org/10.1063/1.354503

Dewan, R. (2011). *Thesis-Optics in Thin-Film Silicon Solar Cells with Periodic Surface Texture*. Jacobs University Bremen, Germany.

Dewan, R., Fischer, S., Benno Meyer-Rochow, V., Özdemir, Y., Hamraz, S., & Knipp, D. (2012). Studying nanostructured nipple arrays of moth eye facets helps to design better thin film solar cells. *Bioinspiration and Biomimetics*, *7*(1), 016003. https://doi.org/10.1088/1748-3182/7/1/016003

Dewan, R., Marinkovic, M., Noriega, R., Phadke, S., Salleo, A., & Knipp, D. (2009). Light trapping in thin-film silicon solar cells with submicron surface texture. *Optics Express*, *17*(25), 23058. https://doi.org/10.1364/OE.17.023058

Dewan, R., Shrestha, S., Jovanov, V., Hüpkes, J., Bittkau, K., & Knipp, D. (2015). Random versus periodic: Determining light trapping of randomly textured thin film solar cells by the superposition of periodic surface textures. *Solar Energy Materials and Solar Cells*, *143*, 183–189. https://doi.org/10.1016/j.solmat.2015.06.014

Dexter, D. L. (1958). Optical properties of solids. *Il Nuovo Cimento Series 10*, *7*(2 Supplement), 245–286. https://doi.org/10.1007/BF02751482

Dikovska, A. O., Atanasov, P. A., Vasilev, C., Dimitrov, I. G., & Stoyanchov, T. R. (2005). Thin ZnO films produced by pulsed laser deposition. In *Journal of Optoelectronics and Advanced Materials* (Vol. 7, pp. 1329–1334).

Drude, P. (1900a). Zur Elektronentheorie der Metalle; II. Teil. Galvanomagnetische und thermomagnetische Effecte. *Annalen Der Physik*, *308*(11), 369–402. https://doi.org/10.1002/andp.19003081102

Drude, P. (1900b). Zur Elektronentheorie der Metalle. *Annalen Der Physik*, *306*(3), 566–613. https://doi.org/10.1002/andp.19003060312

Dualeh, A., Moehl, T., Tétreault, N., Teuscher, J., Gao, P., Nazeeruddin, M. K., & Grätzel, M. (2014). Impedance Spectroscopic Analysis of Lead Iodide Perovskite-Sensitized Solid-State Solar Cells. *ACS Nano*, *8*(1), 362–373. https://doi.org/10.1021/nn404323g

Duong, T., Wu, Y., Shen, H., Peng, J., Fu, X., Jacobs, D., … Catchpole, K. (2017). Rubidium Multication Perovskite with Optimized Bandgap for Perovskite-Silicon Tandem with over 26% Efficiency. *Advanced Energy Materials*, *7*(14), 1700228. https://doi.org/10.1002/aenm.201700228

El Gamal, A., & Eltoukhy, H. (2005). CMOS image sensors. *IEEE Circuits and Devices Magazine*, *21*(3), 6–20. https://doi.org/10.1109/MCD.2005.1438751

Esperón-Moldes, U. S., Pardo-Seco, J., Montalván-Suárez, M., Fachal, L., Ginarte, M., Rodríguez-Pazos, L., … Vega, A. (2019). Biogeographical origin and timing of the founder ichthyosis TGM1 c.1187G > A mutation in an isolated Ecuadorian population. *Scientific Reports*, *9*(1), 7175. https://doi.org/10.1038/s41598-019-43133-6

Fan, P., Gu, D., Liang, G.-X., Luo, J.-T., Chen, J.-L., Zheng, Z.-H., … Zhang, W. (2016). High-performance perovskite CH3NH3PbI3 thin films for solar cells prepared by single-source physical vapour deposition. *Scientific Reports*, *6*(July), 29910. https://doi.org/10.1038/srep29910

Fang, Z., Liu, L., Zhang, Z., Yang, S., Liu, F., Liu, M., & Ding, L. (2019). CsPbI2.25Br0.75 solar cells with 15.9% efficiency. *Science Bulletin*, *64*(8), 507–510. https://doi.org/10.1016/j.scib.2019.04.013

Fernandez-Maloigne, C., & Trémeau, A. (2013). Color Appearance Models. In *Digital Color* (pp. 65–92). Hoboken, NJ USA: John Wiley & Sons, Inc. https://doi.org/10.1002/9781118562680.ch3

Filipič, M., Löper, P., Niesen, B., Wolf, S. De, Krč, J., Ballif, C., & Topič, M. (2015). CH3NH3PbI3 perovskite / silicon tandem solar cells: characterization based optical simulations. *Optics Express*, *23*(7), A263–A278. https://doi.org/10.1364/OE.23.00A263

Forin, C. C., Purica, M., Budianu, E., & Schiopu, P. (2012a). p-NiO/ITO transparent heterojunction - Preparation and characterization. In *CAS 2012 (International Semiconductor Conference)* (Vol. 1, pp. 131–134). IEEE. https://doi.org/10.1109/SMICND.2012.6400676

Forin, C. C., Purica, M., Budianu, E., & Schiopu, P. (2012b). p-NiO/ITO transparent heterojunction — Preparation and characterization. In *CAS 2012 (International Semiconductor Conference)* (pp. 131–134). IEEE. https://doi.org/10.1109/SMICND.2012.6400676

Fujiwara, H., Kato, M., Tamakoshi, M., Miyadera, T., & Chikamatsu, M. (2018). Optical Characteristics and Operational Principles of Hybrid Perovskite Solar Cells. *Physica Status Solidi (A)*, *215*(12), 1700730. https://doi.org/10.1002/pssa.201700730

Ganesh, N., Shivanna, R., Friend, R. H., & Narayan, K. S. (2019). Wavelength-Dependent Charge Carrier Dynamics for Single Pixel Color Sensing Using Graded Perovskite Structures. *Nano Letters*, *19*(9), 6577–6584. https://doi.org/10.1021/acs.nanolett.9b02839

Gautam, V., Bag, M., & Narayan, K. S. (2011). Single-Pixel, Single-Layer Polymer Device as a Tricolor Sensor with Signals Mimicking Natural Photoreceptors. *Journal of the American Chemical Society*, *133*(44), 17942–17949. https://doi.org/10.1021/ja207853e

Genevet, P., Capasso, F., Aieta, F., Khorasaninejad, M., & Devlin, R. (2017). Recent advances in planar optics: from plasmonic to dielectric metasurfaces. *Optica*, *4*(1), 139. https://doi.org/10.1364/OPTICA.4.000139

Geng, Y., Guo, L., Xu, S.-S., Sun, Q.-Q., Ding, S.-J., Lu, H.-L., & Zhang, D. W. (2011). Influence of Al Doping on the Properties of ZnO Thin Films Grown by Atomic Layer Deposition. *The Journal of Physical Chemistry C*, *115*(25), 12317–12321. https://doi.org/10.1021/jp2023567

Green, M. A., Dunlop, E. D., Levi, D. H., Hohl-Ebinger, J., Yoshita, M., & Ho-Baillie, A. W. Y. (2019). Solar cell efficiency tables (version 54). *Progress in Photovoltaics: Research and Applications*, *27*(7), 565–575. https://doi.org/10.1002/pip.3171

Green, M. A., Emery, K., Hishikawa, Y., Warta, W., & Dunlop, E. D. (2016). Solar cell efficiency tables (version 47). *Progress in Photovoltaics: Research and Applications*, *24*(1), 3–11. https://doi.org/10.1002/pip.2728

Green, M. A., Emery, K., Hishikawa, Y., Warta, W., Dunlop, E. D., Levi, D. H., & Ho-Baillie, A. W. Y. (2017). Solar cell efficiency tables (version 49). *Progress in Photovoltaics: Research and Applications*, *25*(1), 3–13. https://doi.org/10.1002/pip.2855

Green, M. A., Hishikawa, Y., Dunlop, E. D., Levi, D. H., Hohl-Ebinger, J., & Ho-Baillie, A. W. Y. (2018). Solar cell efficiency tables (version 52). *Progress in Photovoltaics: Research and Applications*, *26*(7), 427–436. https://doi.org/10.1002/pip.3040

Green, M. A., Hishikawa, Y., Dunlop, E. D., Levi, D. H., Hohl-Ebinger, J., Yoshita, M., & Ho-Baillie, A. W. Y. (2019). Solar cell efficiency tables (Version 53). *Progress in Photovoltaics: Research and Applications*, *27*(1), 3–12. https://doi.org/10.1002/pip.3102

Green, M. A., Hishikawa, Y., Warta, W., Dunlop, E. D., Levi, D. H., Hohl-Ebinger, J., & Ho-Baillie, A. W. H. (2017). Solar cell efficiency tables (version 50). *Progress in Photovoltaics: Research and Applications*, *25*(7), 668–676. https://doi.org/10.1002/pip.2909

Green, M. A., Ho-Baillie, A., & Snaith, H. J. (2014). The emergence of perovskite solar cells. *Nature Photonics*, *8*(7), 506–514. https://doi.org/10.1038/nphoton.2014.134

Green, M. A., Jiang, Y., Soufiani, A. M., & Ho-Baillie, A. (2015). Optical Properties of Photovoltaic Organic–Inorganic Lead Halide Perovskites. *The Journal of Physical Chemistry Letters*, *6*(23), 4774–4785. https://doi.org/10.1021/acs.jpclett.5b01865

Greene, L. E., Yuhas, B. D., Law, M., Zitoun, D., & Yang, P. (2006). Solution-Grown Zinc Oxide Nanowires. *Inorganic Chemistry*, *45*(19), 7535–7543. https://doi.org/10.1021/ic0601900

Gunturk, B. K., Glotzbach, J., Altunbasak, Y., Schafer, R. W., & Mersereau, R. M. (2005a). Demosaicking: color filter array interpolation. *IEEE Signal Processing Magazine*, *22*(1), 44–54. https://doi.org/10.1109/MSP.2005.1407714

Gunturk, B. K., Glotzbach, J., Altunbasak, Y., Schafer, R. W., & Mersereau, R. M. (2005b). Demosaicking: color filter array interpolation. *IEEE Signal Processing Magazine*, *22*(1), 44–54. https://doi.org/10.1109/MSP.2005.1407714

Guziewicz, E., Kowalik, I. A., Godlewski, M., Kopalko, K., Osinniy, V., Wójcik, A., … Guziewicz, M. (2008). Extremely low temperature growth of ZnO by atomic layer deposition. *Journal of Applied Physics*, *103*(3), 033515. https://doi.org/10.1063/1.2836819

Hao, F., Stoumpos, C. C., Cao, D. H., Chang, R. P. H., & Kanatzidis, M. G. (2014). Lead-free solid-state organic–inorganic halide perovskite solar cells. *Nature Photonics*, *8*(6), 489–494. https://doi.org/10.1038/nphoton.2014.82

Hecht, E. (2010). Hecht's Response. *The Physics Teacher*, *48*(1), 5–6. https://doi.org/10.1119/1.3274347

Hegedus, S. S., & Luque, A. (2005). Status, Trends, Challenges and the Bright Future of Solar Electricity from Photovoltaics. In *Handbook of Photovoltaic Science and Engineering* (Vol. 1, pp. 1–43). Chichester, UK: John Wiley & Sons, Ltd. https://doi.org/10.1002/0470014008.ch1

Heo, J. H., Im, S. H., Noh, J. H., Mandal, T. N., Lim, C.-S., Chang, J. A., … Seok, S. Il. (2013). Efficient inorganic–organic hybrid heterojunction solar cells containing

perovskite compound and polymeric hole conductors. *Nature Photonics*, *7*(6), 486–491. https://doi.org/10.1038/nphoton.2013.80

Herzog, P. G., Knipp, D., Stiebig, H., & Koenig, F. (1998). Characterization of novel three- and six-channel color moire free sensors. In G. B. Beretta & R. Eschbach (Eds.), *Color Imaging: Device-Independent Color, Color Hardcopy, and Graphic Arts IV* (pp. 48–59). https://doi.org/10.1117/12.334603

Hong, G., Luo, M. R., & Rhodes, P. A. (2001). A study of digital camera colorimetric characterization based on polynomial modeling. *Color Research & Application*, *26*(1), 76–84. https://doi.org/10.1002/1520-6378(200102)26:1<76::AID-COL8>3.0.CO;2-3

Hongsingthong, A., Yunaz, I. A., Miyajima, S., & Konagai, M. (2010). ZnO films prepared by two-step MOCVD process for use as front TCO in silicon-based thin film solar cells. In *2010 35th IEEE Photovoltaic Specialists Conference* (pp. 001508–001511). IEEE. https://doi.org/10.1109/PVSC.2010.5615836

Hossain, Mohammad I., Hongsingthong, A., Qarony, W., Sichanugrist, P., Konagai, M., Salleo, A., … Tsang, Y. H. (2019). Optics of Perovskite Solar Cell Front Contacts. *ACS Applied Materials & Interfaces*, *11*(16), 14693–14701. research-article. https://doi.org/10.1021/acsami.8b16586

Hossain, Mohammad I., Qarony, W., Jovanov, V., Tsang, Y. H., & Knipp, D. (2018a). Nanophotonic design of perovskite/silicon tandem solar cells. *Journal of Materials Chemistry A*, *6*(8), 3625–3633. https://doi.org/10.1039/C8TA00628H

Hossain, Mohammad I., Qarony, W., Jovanov, V., Tsang, Y. H., & Knipp, D. (2018b). Nanophotonic design of perovskite/silicon tandem solar cells. *Journal of Materials Chemistry A*, *6*(8), 3625–3633. https://doi.org/10.1039/c8ta00628h

Hossain, Mohammad I., Qarony, W., Jovanov, V., Tsang, Y. H., & Knipp, D. (2018c). Nanophotonic design of perovskite/silicon tandem solar cells. *Journal of Materials Chemistry A*, *6*(8), 3625–3633. https://doi.org/10.1039/c8ta00628h

Hossain, Mohammad I., Qarony, W., Ma, S., Zeng, L., Knipp, D., & Tsang, Y. H. (2019). Perovskite/Silicon Tandem Solar Cells: From Detailed Balance Limit Calculations to Photon Management. *Nano-Micro Letters*, *11*(1), 58. https://doi.org/10.1007/s40820-019-0287-8

Hossain, Mohammad I., Yumnam, N., Qarony, W., Salleo, A., Wagner, V., Knipp, D., & Tsang, Y. H. (2020). Non-resonant metal-oxide metasurfaces for efficient perovskite solar cells. *Solar Energy*, *198*(August 2019), 570–577. https://doi.org/10.1016/j.solener.2020.01.082

Hossain, Mohammad Ismail, Hasan, A. K. M., Qarony, W., Shahiduzzaman, M., Islam, M. A., Ishikawa, Y., … Tsang, Y. H. (2020). Electrical and Optical Properties of Nickel-Oxide Films for Efficient Perovskite Solar Cells. *Small Methods*, *2000454*, 2000454. https://doi.org/10.1002/smtd.202000454

Hu, L., Peng, J., Wang, W., Xia, Z., Yuan, J., Lu, J., … Tang, J. (2014). Sequential Deposition of CH 3 NH 3 PbI 3 on Planar NiO Film for Efficient Planar Perovskite Solar Cells. *ACS Photonics*, *1*(7), 547–553. https://doi.org/10.1021/ph5000067

Hubel, P. M. (2005a). Foveon technology and the changing landscape of digital cameras. In *Final Program and Proceedings - IS and T/SID Color Imaging Conference*.

Hubel, P. M. (2005b). Foveon Technology and the Changing Landscape of Digital Cameras. In *Color and Imaging Conference, 13th Color and Imaging Conference Final Program and Proceedings*.

Hubel, P. M., Liu, J., & Guttosch, R. J. (2004). Spatial frequency response of color image sensors: Bayer color filters and Foveon X3. In M. M. Blouke, N. Sampat, & R. J. Motta (Eds.), *Sensors and Camera Systems for Scientific, Industrial, and Digital Photography Applications V* (p. 402). https://doi.org/10.1117/12.561568

Hwang, K.-H., Nam, S.-H., Jung, W. S., Lee, Y. M., Yang, H.-S., & Boo, J.-H. (2015). Wet Chemical Etching of Al-doped ZnO Film Deposited by RF Magnetron

Sputtering Method on Textured Glass Substrate for Energy Application. *Bulletin of the Korean Chemical Society*, *36*(3), 850–854. https://doi.org/10.1002/bkcs.10159

Inan, U. S., & Marshall, R. A. (2011). *Numerical electromagnetics: The FDTD method*. *Numerical Electromagnetics: The FDTD Method*. https://doi.org/10.1017/CBO9780511921353

Iqbal, J., Jilani, A., Ziaul Hassan, P. M., Rafique, S., Jafer, R., & Alghamdi, A. A. (2016). ALD grown nanostructured ZnO thin films: Effect of substrate temperature on thickness and energy band gap. *Journal of King Saud University - Science*, *28*(4), 347–354. https://doi.org/10.1016/j.jksus.2016.03.001

Jang, S., Yoon, J., Ha, K., Kim, M., Kim, D. H., Kim, S. M., … Choi, M. (2016). Facile fabrication of three-dimensional TiO 2 structures for highly efficient perovskite solar cells. *Nano Energy*, *22*, 499–506. https://doi.org/10.1016/j.nanoen.2016.02.050

Jansen-van Vuuren, R. D., Armin, A., Pandey, A. K., Burn, P. L., & Meredith, P. (2016). Organic Photodiodes: The Future of Full Color Detection and Image Sensing. *Advanced Materials*, *28*(24), 4766–4802. https://doi.org/10.1002/adma.201505405

Jassim, S. A.-J., Zumaila, A. A. R. A., & Al Waly, G. A. A. (2013). Influence of substrate temperature on the structural, optical and electrical properties of CdS thin films deposited by thermal evaporation. *Results in Physics*, *3*, 173–178. https://doi.org/10.1016/j.rinp.2013.08.003

Jeon, N. J., Lee, J., Noh, J. H., Nazeeruddin, M. K., Grätzel, M., & Seok, S. Il. (2013). Efficient inorganic-organic hybrid perovskite solar cells based on pyrene arylamine derivatives as hole-transporting materials. *Journal of the American Chemical Society*, *135*(51), 19087–19090. https://doi.org/10.1021/ja410659k

Jiang, Y., Green, M. A., Sheng, R., & Ho-Baillie, A. (2015). Room temperature optical

properties of organic–inorganic lead halide perovskites. *Solar Energy Materials and Solar Cells*, *137*, 253–257. https://doi.org/10.1016/j.solmat.2015.02.017

Jlassi, M., Sta, I., Hajji, M., & Ezzaouia, H. (2014). Optical and electrical properties of nickel oxide thin films synthesized by sol–gel spin coating. *Materials Science in Semiconductor Processing*, *21*, 7–13. https://doi.org/10.1016/j.mssp.2014.01.018

Jošt, M., Köhnen, E., Morales-Vilches, A. B., Lipovšek, B., Jäger, K., Macco, B., … Albrecht, S. (2018). Textured interfaces in monolithic perovskite/silicon tandem solar cells: advanced light management for improved efficiency and energy yield. *Energy & Environmental Science*, *11*(12), 3511–3523. https://doi.org/10.1039/C8EE02469C

Ju, D., Dang, Y., Zhu, Z., Liu, H., Chueh, C.-C., Li, X., … Tao, X. (2018). Tunable Band Gap and Long Carrier Recombination Lifetime of Stable Mixed CH 3 NH 3 Pb x Sn 1– x Br 3 Single Crystals. *Chemistry of Materials*, *30*(5), 1556–1565. https://doi.org/10.1021/acs.chemmater.7b04565

Juarez-Perez, E. J., Wußler, M., Fabregat-Santiago, F., Lakus-Wollny, K., Mankel, E., Mayer, T., … Mora-Sero, I. (2014). Role of the Selective Contacts in the Performance of Lead Halide Perovskite Solar Cells. *The Journal of Physical Chemistry Letters*, *5*(4), 680–685. https://doi.org/10.1021/jz500059v

Keun Kim, S., Seong Hwang, C., Ko Park, S.-H., & Jin Yun, S. (2005). Comparison between ZnO films grown by atomic layer deposition using H2O or O3 as oxidant. *Thin Solid Films*, *478*(1–2), 103–108. https://doi.org/10.1016/j.tsf.2004.10.015

Khan, H. A. (2018). Color characterization methods for a multispectral camera. *Electronic Imaging*, *2018*(16), 221-1-221–228. https://doi.org/10.2352/ISSN.2470-1173.2018.16.COLOR-221

Khosrow-Pour, D.B.A., M. (Ed.). (2009). *Encyclopedia of Information Science and Technology, Second Edition*. *Encyclopedia of Information Science and Technology, Second Edition*. IGI Global. https://doi.org/10.4018/978-1-60566-

026-4

Kim, H.-S., Lee, C.-R., Im, J.-H., Lee, K.-B., Moehl, T., Marchioro, A., … Park, N.-G. (2012). Lead Iodide Perovskite Sensitized All-Solid-State Submicron Thin Film Mesoscopic Solar Cell with Efficiency Exceeding 9%. *Scientific Reports*, *2*(1), 591. https://doi.org/10.1038/srep00591

Kim, Y. C., Yang, T.-Y., Jeon, N. J., Im, J., Jang, S., Shin, T. J., … Seo, J. (2017). Engineering interface structures between lead halide perovskite and copper phthalocyanine for efficient and stable perovskite solar cells. *Energy Environ. Sci.*, *10*(10), 2109–2116. https://doi.org/10.1039/C7EE01931A

Kirchartz, T. (2019). High Open-Circuit Voltages in Lead-Halide Perovskite Solar Cells – Experiment , Theory and Open Questions. *Arxiv*. https://doi.org/10.1098/rsta.2018.0286

Knipp, D., Street, R. A., Stiebig, H., Krause, M., Jeng-Ping Lu, Ready, S., & Ho, J. (2006). Vertically integrated amorphous silicon color sensor arrays. *IEEE Transactions on Electron Devices*, *53*(7), 1551–1558. https://doi.org/10.1109/TED.2006.875822

Koida, T., Fujiwara, H., & Kondo, M. (2009a). High-mobility hydrogen-doped In2O3In2O3 transparent conductive oxide for a-Si:H/c-Si heterojunction solar cells. *Solar Energy Materials and Solar Cells*, *93*(6–7), 851–854. https://doi.org/10.1016/j.solmat.2008.09.047

Koida, T., Fujiwara, H., & Kondo, M. (2009b). High-mobility hydrogen-doped In2O3In2O3 transparent conductive oxide for a-Si:H/c-Si heterojunction solar cells. *Solar Energy Materials and Solar Cells*, *93*(6–7), 851–854. https://doi.org/10.1016/j.solmat.2008.09.047

Koida, Takashi, Fujiwara, H., & Kondo, M. (2007a). Hydrogen-doped In 2 O 3 as High-mobility Transparent Conductive Oxide. *Japanese Journal of Applied Physics*, *46*(No. 28), L685–L687. https://doi.org/10.1143/JJAP.46.L685

Koida, Takashi, Fujiwara, H., & Kondo, M. (2007b). Hydrogen-doped In2O3 as High-mobility Transparent Conductive Oxide. *Japanese Journal of Applied Physics*, *46*(No. 28), L685–L687. https://doi.org/10.1143/JJAP.46.L685

Kojima, A., Teshima, K., Shirai, Y., & Miyasaka, T. (2009). Organometal Halide Perovskites as Visible-Light Sensitizers for Photovoltaic Cells. *Journal of the American Chemical Society*, *131*(17), 6050–6051. https://doi.org/10.1021/ja809598r

Kosyachenko, L. A. (2015). *Solar Cells - New Approaches and Reviews*. (L. A. Kosyachenko, Ed.), *Solar Cells - New Approaches and Reviews*. InTech. https://doi.org/10.5772/58490

Koushik, D., Verhees, W. J. H., Kuang, Y., Veenstra, S., Zhang, D., Verheijen, M. A., … Schropp, R. E. I. (2017). High-efficiency humidity-stable planar perovskite solar cells based on atomic layer architecture. *Energy & Environmental Science*, *10*(1), 91–100. https://doi.org/10.1039/C6EE02687G

Kumawat, N. K., Dey, A., Kumar, A., Gopinathan, S. P., Narasimhan, K. L., & Kabra, D. (2015). Band Gap Tuning of CH 3 NH 3 Pb(Br 1– x Cl x) 3 Hybrid Perovskite for Blue Electroluminescence. *ACS Applied Materials & Interfaces*, *7*(24), 13119–13124. https://doi.org/10.1021/acsami.5b02159

Kuo, W.-K., Hsu, J.-J., Nien, C.-K., & Yu, H. H. (2016). Moth-Eye-Inspired Biophotonic Surfaces with Antireflective and Hydrophobic Characteristics. *ACS Applied Materials & Interfaces*, *8*(46), 32021–32030. https://doi.org/10.1021/acsami.6b10960

Kwon, U., Kim, B.-G., Nguyen, D. C., Park, J.-H., Ha, N. Y., Kim, S.-J., … Park, H. J. (2016). Solution-Processible Crystalline NiO Nanoparticles for High-Performance Planar Perovskite Photovoltaic Cells. *Scientific Reports*, *6*(1), 30759. https://doi.org/10.1038/srep30759

Landsberg, P. T., & Tonge, G. (1980). Thermodynamic energy conversion efficiencies.

Journal of Applied Physics, *51*(7), R1–R20. https://doi.org/10.1063/1.328187

Landsberg, Peter T., & Markvart, T. (1998). THE CARNOT FACTOR IN SOLAR-CELL THEORY. *Solid-State Electronics*, *42*(4), 657–659. https://doi.org/10.1016/S0038-1101(97)00253-0

Lee, J.-W., Seol, D.-J., Cho, A.-N., & Park, N.-G. (2014). High-Efficiency Perovskite Solar Cells Based on the Black Polymorph of HC(NH 2) 2 PbI 3. *Advanced Materials*, *26*(29), 4991–4998. https://doi.org/10.1002/adma.201401137

Leguy, A. M. A., Azarhoosh, P., Alonso, M. I., Campoy-Quiles, M., Weber, O. J., Yao, J., … Barnes, P. R. F. (2016). Experimental and theoretical optical properties of methylammonium lead halide perovskites. *Nanoscale*, *8*(12), 6317–6327. https://doi.org/10.1039/C5NR05435D

Leguy, A. M. A., Hu, Y., Campoy-Quiles, M., Alonso, M. I., Weber, O. J., Azarhoosh, P., … Barnes, P. R. F. (2015). Reversible Hydration of CH3NH3PbI3 in Films, Single Crystals, and Solar Cells. *Chemistry of Materials*, *27*(9), 3397–3407. https://doi.org/10.1021/acs.chemmater.5b00660

Leijtens, T., Bush, K. A., Prasanna, R., & McGehee, M. D. (2018). Opportunities and challenges for tandem solar cells using metal halide perovskite semiconductors. *Nature Energy*, *3*(10), 828–838. https://doi.org/10.1038/s41560-018-0190-4

Leyden, M. R., Ono, L. K., Raga, S. R., Kato, Y., Wang, S., & Qi, Y. (2014). High performance perovskite solar cells by hybrid chemical vapor deposition. *J. Mater. Chem. A*, *2*(44), 18742–18745. https://doi.org/10.1039/C4TA04385E

Li, Y., Yan, W., Li, Y., Wang, S., Wang, W., Bian, Z., … Gong, Q. (2015). Direct Observation of Long Electron-Hole Diffusion Distance in CH3NH3PbI3 Perovskite Thin Film. *Scientific Reports*, *5*(1), 14485. https://doi.org/10.1038/srep14485

Lim, J., & Lee, C. (2007). Effects of substrate temperature on the microstructure and photoluminescence properties of ZnO thin films prepared by atomic layer deposition. *Thin Solid Films*, *515*(7–8), 3335–3338.

https://doi.org/10.1016/j.tsf.2006.09.007

Limpert, S., Bremner, S., & Linke, H. (2015). Reversible electron–hole separation in a hot carrier solar cell. *New Journal of Physics*, *17*(9), 095004. https://doi.org/10.1088/1367-2630/17/9/095004

Liu, M., Johnston, M. B., & Snaith, H. J. (2013a). Efficient planar heterojunction perovskite solar cells by vapour deposition. *Nature*, *501*(7467), 395–398. https://doi.org/10.1038/nature12509

Liu, M., Johnston, M. B., & Snaith, H. J. (2013b). Efficient planar heterojunction perovskite solar cells by vapour deposition. *Nature*, *501*(7467), 395–398. https://doi.org/10.1038/nature12509

Liu, Z., Sun, B., Liu, X., Han, J., Ye, H., Shi, T., … Liao, G. (2018). Efficient Carbon-Based CsPbBr3 Inorganic Perovskite Solar Cells by Using Cu-Phthalocyanine as Hole Transport Material. *Nano-Micro Letters*, *10*(2), 34. https://doi.org/10.1007/s40820-018-0187-3

Loeper, P., Stuckelberger, M., Niesen, B., Werner, J., Filipic, M., Moon, S.-J., … Ballif, C. (2015). Complex Refractive Index Spectra of CH3NH3PbI3 Perovskite Thin Films Determined by Spectroscopic Ellipsometry and Spectrophotometry. *Journal of Physical Chemistry Letters*, *6*(1), 66–71. https://doi.org/10.1021/jz502471h

Löper, P., Stuckelberger, M., Niesen, B., Werner, J., Filipič, M., Moon, S.-J., … Ballif, C. (2015a). Complex Refractive Index Spectra of CH 3 NH 3 PbI 3 Perovskite Thin Films Determined by Spectroscopic Ellipsometry and Spectrophotometry. *The Journal of Physical Chemistry Letters*, *6*(1), 66–71. https://doi.org/10.1021/jz502471h

Löper, P., Stuckelberger, M., Niesen, B., Werner, J., Filipič, M., Moon, S.-J., … Ballif, C. (2015b). Complex Refractive Index Spectra of CH3NH3PbI3 Perovskite Thin Films Determined by Spectroscopic Ellipsometry and Spectrophotometry. *The Journal of Physical Chemistry Letters*, *6*(1), 66–71.

https://doi.org/10.1021/jz502471h

Lopez-Delgado, R., Higuera-Valenzuela, H. J., Zazueta-Raynaud, A., Ramos, A., Pelayo, J. E., Berman, D., … Ayon, A. (2016). Enhancing the power conversion efficiency of solar cells employing down-shifting silicon quantum dots. *Journal of Physics: Conference Series*, *773*, 012087. https://doi.org/10.1088/1742-6596/773/1/012087

Lopez-Delgado, R., Zhou, Y., Zazueta-Raynaud, A., Zhao, H., Pelayo, J. E., Vomiero, A., … Ayon, A. (2017). Enhanced conversion efficiency in Si solar cells employing photoluminescent down-shifting CdSe/CdS core/shell quantum dots. *Scientific Reports*, *7*(1), 14104. https://doi.org/10.1038/s41598-017-14269-0

Lopez-Delgado, Rosendo, Higuera-Valenzuela, H. J., Zazueta-Raynaud, A., Ramos-Carrazco, A., Pelayo, J. E., Berman-Mendoza, D., … Ayon, A. (2018). Solar cell efficiency improvement employing down-shifting silicon quantum dots. *Microsystem Technologies*, *24*(1), 495–502. https://doi.org/10.1007/s00542-017-3405-x

Lukac, R., & Plataniotis, K. N. (2005a). Color filter arrays: design and performance analysis. *IEEE Transactions on Consumer Electronics*, *51*(4), 1260–1267. https://doi.org/10.1109/TCE.2005.1561853

Lukac, R., & Plataniotis, K. N. (2005b). Color filter arrays: Design and performance analysis. *IEEE Transactions on Consumer Electronics*. https://doi.org/10.1109/TCE.2005.1561853

Luo, H., Lin, X., Hou, X., Pan, L., Huang, S., & Chen, X. (2017). Efficient and Air-Stable Planar Perovskite Solar Cells Formed on Graphene-Oxide-Modified PEDOT:PSS Hole Transport Layer. *Nano-Micro Letters*, *9*(4), 39. https://doi.org/10.1007/s40820-017-0140-x

Luque, A., & Hegedus, S. (2010a). *Handbook of Photovoltaic Science and Engineering*. (A. Luque & S. Hegedus, Eds.), *Handbook of Photovoltaic Science and*

Engineering. Chichester, UK: John Wiley & Sons, Ltd. https://doi.org/10.1002/9780470974704

Luque, A., & Hegedus, S. (2010b). *Handbook of Photovoltaic Science and Engineering*. (A. Luque & S. Hegedus, Eds.), *Handbook of Photovoltaic Science and Engineering*. Chichester, UK: John Wiley & Sons, Ltd. https://doi.org/10.1002/9780470974704

Lyon, R. F., & Hubel, P. M. (2002). Eyeing the camera: Into the next century. In *Final Program and Proceedings - IS and T/SID Color Imaging Conference* (pp. 349–355).

M. A. Green. (2003). *Third generation photovoltaics: advanced solar energy conversion*. *Springer, Berlin Heidelberg*.

Marinelli, R., & Palange, E. (2011). OPTICAL PERFORMANCES OF LENSLESS SUB-2MICRON PIXEL FOR APPLICATION IN IMAGE SENSORS. *Progress In Electromagnetics Research B*, *31*, 1–14. https://doi.org/10.2528/PIERB11032306

Markvart, T., & Landsberg, P. T. (2002). Thermodynamics and reciprocity of solar energy conversion. *Physica E: Low-Dimensional Systems and Nanostructures*, *14*(1–2), 71–77. https://doi.org/10.1016/S1386-9477(02)00352-1

Masuko, K., Shigematsu, M., Hashiguchi, T., Fujishima, D., Kai, M., Yoshimura, N., … Okamoto, S. (2014). Achievement of more than 25% conversion efficiency with crystalline silicon heterojunction solar cell. *IEEE Journal of Photovoltaics*, *4*(6), 1433–1435. https://doi.org/10.1109/JPHOTOV.2014.2352151

Meier, J., Spitznagel, J., Kroll, U., Bucher, C., Faÿ, S., Moriarty, T., & Shah, A. (2004). Potential of amorphous and microcrystalline silicon solar cells. *Thin Solid Films*, *451–452*, 518–524. https://doi.org/10.1016/j.tsf.2003.11.014

Meillaud, F., Shah, A., Droz, C., Vallat-Sauvain, E., & Miazza, C. (2006). Efficiency limits for single-junction and tandem solar cells. *Solar Energy Materials and Solar Cells*, *90*(18–19), 2952–2959. https://doi.org/10.1016/j.solmat.2006.06.002

Mejía Escobar, M. A., Pathak, S., Liu, J., Snaith, H. J., & Jaramillo, F. (2017). ZrO 2 /TiO 2 Electron Collection Layer for Efficient Meso-Superstructured Hybrid Perovskite Solar Cells. *ACS Applied Materials & Interfaces*, *9*(3), 2342–2349. https://doi.org/10.1021/acsami.6b12509

Merrill, R. (1999). Color separation in an active pixel cell imaging array using a triple-well structure. *US Patent 5,965,875*. Retrieved from http://www.google.com/patents?hl=en&lr=&vid=USPAT5965875&id=CxcZAAAAEBAJ&oi=fnd&dq=Color+separation+in+an+active+pixel+cell+imaging+array+using+a+triple-well+structure&printsec=abstract

Minoura, S., Maekawa, T., Kodera, K., Nakane, A., Niki, S., & Fujiwara, H. (2015). Optical constants of Cu(In, Ga)Se 2 for arbitrary Cu and Ga compositions. *Journal of Applied Physics*, *117*(19), 195703. https://doi.org/10.1063/1.4921300

Moehl, T., Im, J. H., Lee, Y. H., Domanski, K., Giordano, F., Zakeeruddin, S. M., … Grätzel, M. (2014). Strong Photocurrent Amplification in Perovskite Solar Cells with a Porous TiO 2 Blocking Layer under Reverse Bias. *The Journal of Physical Chemistry Letters*, *5*(21), 3931–3936. https://doi.org/10.1021/jz502039k

Mohammad, A., Shukla, D., Ilhom, S., Willis, B., Johs, B., Okyay, A. K., & Biyikli, N. (2019). Real-time in situ ellipsometric monitoring of aluminum nitride film growth via hollow-cathode plasma-assisted atomic layer deposition. *Journal of Vacuum Science & Technology A*, *37*(2), 020927. https://doi.org/10.1116/1.5085341

Mohammad Ismail Hossain. (2013). *Enhancement of Light-trapping in Single and Multi-junction Thin Film Silicon Solar Cells on Periodic Textured Substrate Mohammad Ismail Hossain Enhancement of Light-trapping in Single and Multi-junctions Thin Film Silicon Solar Cells on Periodic Textured*. Jacobs University Bremen, Germany. https://doi.org/10.13140/RG.2.2.29273.67686

Moharam, M. G., Pommet, D. A., Grann, E. B., & Gaylord, T. K. (1995). Stable implementation of the rigorous coupled-wave analysis for surface-relief gratings:

enhanced transmittance matrix approach. *Journal of the Optical Society of America A: Optics, Image Science, and Vision*. https://doi.org/10.1364/JOSAA.12.001077

Möllmann, A., Gedamu, D., Vivo, P., Frohnhoven, R., Stadler, D., Fischer, T., … Mathur, S. (2019). Highly Compact TiO 2 Films by Spray Pyrolysis and Application in Perovskite Solar Cells. *Advanced Engineering Materials*, *21*(4), 1801196. https://doi.org/10.1002/adem.201801196

Müller, J., Rech, B., Springer, J., & Vanecek, M. (2004a). TCO and light trapping in silicon thin film solar cells. *Solar Energy*, *77*(6), 917–930. https://doi.org/10.1016/j.solener.2004.03.015

Müller, J., Rech, B., Springer, J., & Vanecek, M. (2004b). TCO and light trapping in silicon thin film solar cells. *Solar Energy*, *77*(6), 917–930. https://doi.org/10.1016/j.solener.2004.03.015

Nishiwaki, M., Nagaya, K., Kato, M., Fujimoto, S., Tampo, H., Miyadera, T., … Fujiwara, H. (2018). Tail state formation in solar cell materials: First principles analyses of zincblende, chalcopyrite, kesterite, and hybrid perovskite crystals. *Physical Review Materials*, *2*(8), 085404. https://doi.org/10.1103/PhysRevMaterials.2.085404

Noh, J. H., Im, S. H., Heo, J. H., Mandal, T. N., & Seok, S. Il. (2013). Chemical Management for Colorful, Efficient, and Stable Inorganic–Organic Hybrid Nanostructured Solar Cells. *Nano Letters*, *13*(4), 1764–1769. https://doi.org/10.1021/nl400349b

Noh, J. H., Jeon, N. J., Choi, Y. C., Nazeeruddin, M. K., Grätzel, M., & Seok, S. Il. (2013a). Nanostructured TiO2/CH3NH3PbI3 heterojunction solar cells employing spiro-OMeTAD/Co-complex as hole-transporting material. *Journal of Materials Chemistry A*. https://doi.org/10.1039/c3ta12681a

Noh, J. H., Jeon, N. J., Choi, Y. C., Nazeeruddin, M. K., Grätzel, M., & Seok, S. Il.

(2013b). Nanostructured TiO2/CH3NH3PbI3 heterojunction solar cells employing spiro-OMeTAD/Co-complex as hole-transporting material. *Journal of Materials Chemistry A*, *1*(38), 11842. https://doi.org/10.1039/c3ta12681a

Oxford PV-The Perovskite Company. (2020). Oxford PV perovskite solar cell achieves 28% efficiency. Retrieved April 11, 2020, from https://www.oxfordpv.com/news/oxford-pv-perovskite-solar-cell-achieves-28-efficiency

Paek, S., Qin, P., Lee, Y., Cho, K. T., Gao, P., Grancini, G., … Nazeeruddin, M. K. (2017). Dopant-Free Hole-Transporting Materials for Stable and Efficient Perovskite Solar Cells. *Advanced Materials*, *29*(35), 1606555. https://doi.org/10.1002/adma.201606555

Palanchoke, U., Boutami, S., & Gidon, S. (2017). Spectral sorting of visible light using dielectric gratings. *Optics Express*, *25*(26), 33389. https://doi.org/10.1364/OE.25.033389

Park, J.-S., Choi, S., Yan, Y., Yang, Y., Luther, J. M., Wei, S.-H., … Zhu, K. (2015). Electronic Structure and Optical Properties of α-CH 3 NH 3 PbBr 3 Perovskite Single Crystal. *The Journal of Physical Chemistry Letters*, *6*(21), 4304–4308. https://doi.org/10.1021/acs.jpclett.5b01699

Park, N.-G. (2015a). Perovskite solar cells: an emerging photovoltaic technology. *Materials Today*, *18*(2), 65–72. https://doi.org/10.1016/j.mattod.2014.07.007

Park, N.-G. (2015b). Perovskite solar cells: an emerging photovoltaic technology. *Materials Today*, *18*(2), 65–72. https://doi.org/10.1016/j.mattod.2014.07.007

Parsons, R., Tamang, A., Jovanov, V., Wagner, V., & Knipp, D. (2017). Comparison of Light Trapping in Silicon Nanowire and Surface Textured Thin-Film Solar Cells. *Applied Sciences*, *7*(4), 427. https://doi.org/10.3390/app7040427

Paulose, R., Mohan, R., & Parihar, V. (2017). Nanostructured nickel oxide and its electrochemical behaviour—A brief review. *Nano-Structures & Nano-Objects*, *11*,

102–111. https://doi.org/10.1016/j.nanoso.2017.07.003

Pérez-Tomás, A., Mingorance, A., Tanenbaum, D., & Lira-Cantú, M. (2018). Metal Oxides in Photovoltaics: All-Oxide, Ferroic, and Perovskite Solar Cells. In *The Future of Semiconductor Oxides in Next-Generation Solar Cells* (pp. 267–356). Elsevier. https://doi.org/10.1016/B978-0-12-811165-9.00008-9

Pi, X., Li, Q., Li, D., & Yang, D. (2011). Spin-coating silicon-quantum-dot ink to improve solar cell efficiency. *Solar Energy Materials and Solar Cells*, *95*(10), 2941–2945. https://doi.org/10.1016/j.solmat.2011.06.010

Piegari, A., & Flory, F. (2013). *Optical thin films and coatings: From materials to applications*. *Optical Thin Films and Coatings: From Materials to Applications*. https://doi.org/10.1533/9780857097316

Planck, M. (1901). Ueber das Gesetz der Energieverteilung im Normalspectrum. *Annalen Der Physik*, *309*(3), 553–563. https://doi.org/10.1002/andp.19013090310

Popovic, Z. P. B. D., & Neff, H. P. (2000). *Introductory Electromagnetics*. *Prentice Hall*. https://doi.org/10.1108/IJOPM-12-2015-0775

Qarony, W. (2019). *OPTICS IN PEROVSKITES AND LOW- MOBILITY MATERIALS BASED SOLAR CELLS AND COLOR VISION IN OPTICS IN PEROVSKITES AND LOW- MOBILITY MATERIALS BASED SOLAR CELLS*. The Hong Kong Polytechnic University, Hong Kong.

Qarony, W., Hossain, M. I., Dewan, R., Fischer, S., Meyer-Rochow, V. B., Salleo, A., … Tsang, Y. H. (2018). Approaching Perfect Light Incoupling in Perovskite and Silicon Thin Film Solar Cells by Moth Eye Surface Textures. *Advanced Theory and Simulations*, *1*(8), 1800030. https://doi.org/10.1002/adts.201800030

Qarony, W., Hossain, M. I., Hossain, M. K., Uddin, M. J., Haque, A., Saad, A. R., & Tsang, Y. H. (2017). Efficient amorphous silicon solar cells: characterization, optimization, and optical loss analysis. *Results in Physics*, *7*, 4287–4293.

https://doi.org/10.1016/j.rinp.2017.09.030

Qarony, W., Hossain, M. I., Jovanov, V., Knipp, D., & Tsang, Y. H. (2018). Maximizing the short circuit current of organic solar cells by partial decoupling of electrical and optical properties. *Applied Nanoscience*, *8*(3), 339–346. https://doi.org/10.1007/s13204-018-0713-0

Qarony, W., Hossain, M. I., Salleo, A., Knipp, D., & Tsang, Y. H. (2019). Rough versus planar interfaces: How to maximize the short circuit current of perovskite single and tandem solar cells. *Materials Today Energy*, *11*, 106–113. https://doi.org/10.1016/j.mtener.2018.10.001

Qarony, W., Jui, Y. A., Das, G. M., Mohsin, T., Hossain, M. I., & Islam, S. N. (2015). Optical Analysis in CH3NH3PbI3 and CH3NH3PbI2Cl Based Thin-Film Perovskite Solar Cell. *American Journal of Energy Research*, *3*(2), 19–24. https://doi.org/10.12691/ajer-3-2-1

Rakstys, K., Paek, S., Gao, P., Gratia, P., Marszalek, T., Grancini, G., … Nazeeruddin, M. K. (2017). Molecular engineering of face-on oriented dopant-free hole transporting material for perovskite solar cells with 19% PCE. *Journal of Materials Chemistry A*, *5*(17), 7811–7815. https://doi.org/10.1039/C7TA01718A

Rao, H.-S., Chen, B.-X., Wang, X.-D., Kuang, D.-B., & Su, C.-Y. (2017). A micron-scale laminar MAPbBr 3 single crystal for an efficient and stable perovskite solar cell. *Chem. Commun.*, *53*(37), 5163–5166. https://doi.org/10.1039/C7CC02447A

Rau, U., Paetzold, U. W., & Kirchartz, T. (2014). Thermodynamics of light management in photovoltaic devices. *Physical Review B*, *90*(3), 035211. https://doi.org/10.1103/PhysRevB.90.035211

Rawat, R., Lamba, R., & Kaushik, S. C. (2017). Thermodynamic study of solar photovoltaic energy conversion: An overview. *Renewable and Sustainable Energy Reviews*, *71*, 630–638. https://doi.org/10.1016/j.rser.2016.12.089

Rech, B., & Wagner, H. (1999). Potential of amorphous silicon for solar cells. *Applied*

Physics A: Materials Science & Processing, *69*(2), 155–167. https://doi.org/10.1007/s003390050986

Reference Solar Spectral Irradiance: ASTM G-173. (n.d.). Retrieved March 19, 2018, from http://rredc.nrel.gov/solar/spectra/am1.5/astmg173/astmg173.html

Rühle, S. (2017). The detailed balance limit of perovskite/silicon and perovskite/CdTe tandem solar cells. *Physica Status Solidi (A)*, *214*(5), 1600955. https://doi.org/10.1002/pssa.201600955

Ryu, Y. R., Zhu, S., Budai, J. D., Chandrasekhar, H. R., Miceli, P. F., & White, H. W. (2000). Optical and structural properties of ZnO films deposited on GaAs by pulsed laser deposition. *Journal of Applied Physics*, *88*(1), 201–204. https://doi.org/10.1063/1.373643

Sadiku, M. N. O. (2015). *Numerical Techniques in Electromagnetics with MATLAB®*. *Numerical Techniques in Electromagnetics with MATLAB®*. CRC Press. https://doi.org/10.1201/9781315222622

Sahli, F., Werner, J., Kamino, B. A., Bräuninger, M., Monnard, R., Paviet-Salomon, B., … Ballif, C. (2018a). Fully textured monolithic perovskite/silicon tandem solar cells with 25.2% power conversion efficiency. *Nature Materials*, *17*(9), 820–826. https://doi.org/10.1038/s41563-018-0115-4

Sahli, F., Werner, J., Kamino, B. A., Bräuninger, M., Monnard, R., Paviet-Salomon, B., … Ballif, C. (2018b). Fully textured monolithic perovskite/silicon tandem solar cells with 25.2% power conversion efficiency. *Nature Materials*, *17*(9), 820–826. https://doi.org/10.1038/s41563-018-0115-4

Sai, H., Matsui, T., Matsubara, K., Kondo, M., & Yoshida, I. (2014). 11.0%-Efficient Thin-Film Microcrystalline Silicon Solar Cells With Honeycomb Textured Substrates. *IEEE Journal of Photovoltaics*, *4*(6), 1349–1353. https://doi.org/10.1109/JPHOTOV.2014.2355037

Saleh, B. E. A., & Teich, M. C. (2007). Fundamentals of Photonics , 2nd Edition. *Wiley*.

Sap, J. A., Isabella, O., Jäger, K., & Zeman, M. (2011). Extraction of optical properties of flat and surface-textured transparent conductive oxide films in a broad wavelength range. *Thin Solid Films*, *520*(3), 1096–1101. https://doi.org/10.1016/j.tsf.2011.08.023

Seo, S., Jeong, S., Park, H., Shin, H., & Park, N. G. (2019). Atomic layer deposition for efficient and stable perovskite solar cells. *Chemical Communications*, *55*(17), 2403–2416. https://doi.org/10.1039/c8cc09578g

Seo, S., Park, I. J., Kim, M., Lee, S., Bae, C., Jung, H. S., … Shin, H. (2016). An ultra-thin, un-doped NiO hole transporting layer of highly efficient (16.4%) organic–inorganic hybrid perovskite solar cells. *Nanoscale*, *8*(22), 11403–11412. https://doi.org/10.1039/C6NR01601D

Shah, A., Meier, J., Vallat-Sauvain, E., Droz, C., Kroll, U., Wyrsch, N., … Graf, U. (2002). Microcrystalline silicon and 'micromorph' tandem solar cells. *Thin Solid Films*, *403–404*, 179–187. https://doi.org/10.1016/S0040-6090(01)01658-3

Shi, D., Adinolfi, V., Comin, R., Yuan, M., Alarousu, E., Buin, A., … Bakr, O. M. (2015). Low trap-state density and long carrier diffusion in organolead trihalide perovskite single crystals. *Science*, *347*(6221), 519–522. https://doi.org/10.1126/science.aaa2725

Shirayama, M., Kadowaki, H., Miyadera, T., Sugita, T., Tamakoshi, M., Kato, M., … Fujiwara, H. (2016a). Optical Transitions in Hybrid Perovskite Solar Cells: Ellipsometry, Density Functional Theory, and Quantum Efficiency Analyses for CH2NH3PbI3. *Physical Review Applied*, *5*(1), 014012. https://doi.org/10.1103/PhysRevApplied.5.014012

Shirayama, M., Kadowaki, H., Miyadera, T., Sugita, T., Tamakoshi, M., Kato, M., … Fujiwara, H. (2016b). Optical Transitions in Hybrid Perovskite Solar Cells: Ellipsometry, Density Functional Theory, and Quantum Efficiency Analyses for CH3NH3PbI3. *Physical Review Applied*, *5*(1), 014012.

https://doi.org/10.1103/PhysRevApplied.5.014012

Shockley, W., & Queisser, H. J. (1961a). Detailed balance limit of efficiency of p-n junction solar cells. *Journal of Applied Physics*, *32*(3), 510–519. https://doi.org/10.1063/1.1736034

Shockley, W., & Queisser, H. J. (1961b). Detailed Balance Limit of Efficiency of p-n Junction Solar Cells. *Journal of Applied Physics*, *32*(3), 510–519. https://doi.org/10.1063/1.1736034

Singh, J., Quli, F., Wolfe, D. E., & Schriempf, J. (1999). An Overview: Electron Beam-Physical Vapor Deposition Technology-Present and Future Applications. *Surface Engineering: Science and Technology I*. https://doi.org/10.1016/j.jpowsour.2014.06.128

Slawinski, M. A., Slawinski, R. A., Brown, R. J., & Parkin, J. M. (2000). A generalized form of Snell's law in anisotropic media. *GEOPHYSICS*, *65*(2), 632–637. https://doi.org/10.1190/1.1444759

Snyder, P. G., Woollam, J. A., Alterovitz, S. A., & Johs, B. (1990a). Modeling Al x Ga 1− x As optical constants as functions of composition. *Journal of Applied Physics*, *68*(11), 5925–5926. https://doi.org/10.1063/1.346921

Snyder, P. G., Woollam, J. A., Alterovitz, S. A., & Johs, B. (1990b). Modeling AlxGa1-xAs optical constants as functions of composition. *Journal of Applied Physics*. https://doi.org/10.1063/1.346921

Spina, M., Bonvin, E., Sienkiewicz, A., Náfrádi, B., Forró, L., & Horváth, E. (2016). Controlled growth of CH3NH3PbI3 nanowires in arrays of open nanofluidic channels. *Scientific Reports*, *6*(1), 19834. https://doi.org/10.1038/srep19834

Staelin, D. H. (2011). *Electromagnetics and Applications*. *Department of Electrical Engineering and Computer Science Massachusetts Institute of Technology Cambridge, MA*.

Steen, W. . (2000). Principles of Optics M. Born and E. Wolf, 7th (expanded) edition,

Cambridge University Press, Cambridge, 1999, 952pp. 37.50/US $59.95, ISBN 0-521-64222-1. *Optics & Laser Technology*, *32*(5), 385. https://doi.org/10.1016/S0030-3992(00)00061-X

Steinhauser, J. (2008). *Low Pressure Chemical Vapor Deposited Zinc Oxide for Silicon Thin Film Solar Cells- Optical and Electrical Properties*. *Ph.D. Thesis, Institute of Microtechnology, University of Neuchâtel*.

Stranks, S. D., & Snaith, H. J. (2015a). Metal-halide perovskites for photovoltaic and light-emitting devices. *Nature Nanotechnology*, *10*(5), 391–402. https://doi.org/10.1038/nnano.2015.90

Stranks, S. D., & Snaith, H. J. (2015b). Metal-halide perovskites for photovoltaic and light-emitting devices. *Nature Nanotechnology*, *10*(5), 391–402. https://doi.org/10.1038/nnano.2015.90

Sun, W., Li, Y., Ye, S., Rao, H., Yan, W., Peng, H., … Huang, C. (2016). High-performance inverted planar heterojunction perovskite solar cells based on a solution-processed CuO x hole transport layer. *Nanoscale*, *8*(20), 10806–10813. https://doi.org/10.1039/C6NR01927G

Sun, Y., You, S., Tu, H., Spillman, D. R., Chaney, E. J., Marjanovic, M., … Boppart, S. A. (2018). Intraoperative visualization of the tumor microenvironment and quantification of extracellular vesicles by label-free nonlinear imaging. *Science Advances*, *4*(12), eaau5603. https://doi.org/10.1126/sciadv.aau5603

Sze, S. M., & Ng, K. K. (1995). *Physics of Semiconductor Devices Physics of Semiconductor Devices*. *WILEY- INTERSCIENCE A JOHN WILEY & SONS, INC., PUBLICATION*. https://doi.org/10.1007/978-3-319-03002-9

Taflove, A., Hagness, S. C., & Piket-May, M. (2005). Computational Electromagnetics: The Finite-Difference Time-Domain Method. In *The Electrical Engineering Handbook* (pp. 629–670). Elsevier. https://doi.org/10.1016/B978-012170960-0/50046-3

Tamang, A., Sai, H., Jovanov, V., Matsubara, K., & Knipp, D. (2018). Silicon Thin-Film Solar Cells Approaching the Geometric Light-Trapping Limit: Surface Texture Inspired by Self-Assembly Processes. *ACS Photonics*, *5*(7), 2799–2806. https://doi.org/10.1021/acsphotonics.7b01397

Tan, G., Lee, J.-H., Lan, Y.-H., Wei, M.-K., Peng, L.-H., Cheng, I.-C., & Wu, S.-T. (2017). Broadband antireflection film with moth-eye-like structure for flexible display applications. *Optica*, *4*(7), 678. https://doi.org/10.1364/OPTICA.4.000678

Theil, J. A., Cao, M., Kooi, G., Ray, G. W., Greene, W., Lin, J., … Yoon, U. (2000). Hydrogenated Amorphous Silicon Photodiode Technology for Advanced CMOS Active Pixel Sensor Imagers. *MRS Proceedings*, *609*, A14.3. https://doi.org/10.1557/PROC-609-A14.3

Theuwissen, A. J. P. (2008). CMOS image sensors: State-of-the-art. *Solid-State Electronics*, *52*(9), 1401–1406. https://doi.org/10.1016/j.sse.2008.04.012

Tiguntseva, E., Chebykin, A., Ishteev, A., Haroldson, R., Balachandran, B., Ushakova, E., … Zakhidov, A. (2017). Resonant silicon nanoparticles for enhancement of light absorption and photoluminescence from hybrid perovskite films and metasurfaces. *Nanoscale*, *9*(34), 12486–12493. https://doi.org/10.1039/C7NR01631J

Topic, M., Stiebig, H., Knipp, D., & Smole, F. (1999). Optimization of a-Si:H-based three-terminal three-color detectors. *IEEE Transactions on Electron Devices*, *46*(9), 1839–1845. https://doi.org/10.1109/16.784182

Tsoutsouva, M. G., Panagopoulos, C. N., Papadimitriou, D., Fasaki, I., & Kompitsas, M. (2011). ZnO thin films prepared by pulsed laser deposition. *Materials Science and Engineering: B*, *176*(6), 480–483. https://doi.org/10.1016/j.mseb.2010.03.059

Uddin, M. J., Hossain, M. K., Qarony, W., Hossain, M. I., Mia, M. N. H., & Hossen, S. (2017). Time and pressure dependent deformation of microcontact printed

channels fabricated using self-assembled monolayers of alkanethiol on gold. *Journal of Science: Advanced Materials and Devices*, *2*(3), 385–391. https://doi.org/10.1016/j.jsamd.2017.07.008

Unger, J., Hebisch, C., Phipps, J. E., Lagarto, J. L., Kim, H., Darrow, M. A., … Marcu, L. (2020). Real-time diagnosis and visualization of tumor margins in excised breast specimens using fluorescence lifetime imaging and machine learning. *Biomedical Optics Express*, *11*(3), 1216. https://doi.org/10.1364/BOE.381358

van Eerden, M., Jaysankar, M., Hadipour, A., Merckx, T., Schermer, J. J., Aernouts, T., … Paetzold, U. W. (2017). Optical Analysis of Planar Multicrystalline Perovskite Solar Cells. *Advanced Optical Materials*, *5*(18), 1700151. https://doi.org/10.1002/adom.201700151

Vidyasagar, C. C., Muñoz Flores, B. M., & Jiménez Pérez, V. M. (2018). Recent Advances in Synthesis and Properties of Hybrid Halide Perovskites for Photovoltaics. *Nano-Micro Letters*, *10*(4), 68. https://doi.org/10.1007/s40820-018-0221-5

VIII. A dynamical theory of the electromagnetic field. (1865). *Philosophical Transactions of the Royal Society of London*, *155*, 459–512. https://doi.org/10.1098/rstl.1865.0008

Vos, A. De. (1980). Detailed balance limit of the efficiency of tandem solar cells. *Journal of Physics D: Applied Physics*, *13*(5), 839–846. https://doi.org/10.1088/0022-3727/13/5/018

Wakamiya, A., Endo, M., Sasamori, T., Tokitoh, N., Ogomi, Y., Hayase, S., & Murata, Y. (2014). Reproducible Fabrication of Efficient Perovskite-based Solar Cells: X-ray Crystallographic Studies on the Formation of CH 3 NH 3 PbI 3 Layers. *Chemistry Letters*, *43*(5), 711–713. https://doi.org/10.1246/cl.140074

Wang, J.-Y., Lee, C.-Y., Chen, Y.-T., Chen, C.-T., Chen, Y.-L., Lin, C.-F., & Chen, Y.-F. (2009a). Double side electroluminescence from p-NiO/n-ZnO nanowire

heterojunctions. *Applied Physics Letters*, *95*(13), 131117. https://doi.org/10.1063/1.3232244

Wang, J.-Y., Lee, C.-Y., Chen, Y.-T., Chen, C.-T., Chen, Y.-L., Lin, C.-F., & Chen, Y.-F. (2009b). Double side electroluminescence from p-NiO/n-ZnO nanowire heterojunctions. *Applied Physics Letters*, *95*(13), 131117. https://doi.org/10.1063/1.3232244

Wang, L., Yuan, G. D., Duan, R. F., Huang, F., Wei, T. B., Liu, Z. Q., … Li, J. M. (2016). Tunable bandgap in hybrid perovskite CH3NH3Pb(Br3−yXy) single crystals and photodetector applications. *AIP Advances*, *6*(4), 045115. https://doi.org/10.1063/1.4948312

Wang, Y., Liang, Y., Zhang, Y., Yang, W., Sun, L., & Xu, D. (2018). Pushing the Envelope: Achieving an Open-Circuit Voltage of 1.18 V for Unalloyed MAPbI 3 Perovskite Solar Cells of a Planar Architecture. *Advanced Functional Materials*, *28*(30), 1801237. https://doi.org/10.1002/adfm.201801237

Wang, Z. L. (2004). Zinc oxide nanostructures: growth, properties and applications. *Journal of Physics: Condensed Matter*, *16*(25), R829–R858. https://doi.org/10.1088/0953-8984/16/25/R01

Wayesh Qarony; Mohammad Ismail Hossain; Vladislav Jovanov; Alberto Salleo; Dietmar Knipp; Yuen Hong Tsang; (2019). Influence of perovskite interface morphology on the photon management in perovskite / silicon tandem solar cells. *ACS Applied Materials & Interfaces*.

Wehrspohn, R. B., Rau, U., & Gombert, A. (2015). *Photon Management in Solar Cells*. (R. B. Wehrspohn, U. Rau, & A. Gombert, Eds.), *Photon Management in Solar Cells*. Weinheim, Germany: Wiley-VCH Verlag GmbH & Co. KGaA. https://doi.org/10.1002/9783527665662

Wei, Z., Qiao, H., Yang, H., Zhang, C., & Yan, X. (2009). Characterization of NiO nanoparticles by anodic arc plasma method. *Journal of Alloys and Compounds*,

479(1–2), 855–858. https://doi.org/10.1016/j.jallcom.2009.01.064

Werner, J., Niesen, B., & Ballif, C. (2018). Perovskite/Silicon Tandem Solar Cells: Marriage of Convenience or True Love Story? - An Overview. *Advanced Materials Interfaces*, *5*(1), 1700731. https://doi.org/10.1002/admi.201700731

Wolff, C. M., Zu, F., Paulke, A., Toro, L. P., Koch, N., & Neher, D. (2017). Reduced Interface-Mediated Recombination for High Open-Circuit Voltages in CH 3 NH 3 PbI 3 Solar Cells. *Advanced Materials*, *29*(28), 1700159. https://doi.org/10.1002/adma.201700159

Woo Leem, J., Guan, X.-Y., Choi, M., & Su Yu, J. (2015). Broadband and omnidirectional highly-transparent coverglasses coated with biomimetic moth-eye nanopatterned polymer films for solar photovoltaic system applications. *Solar Energy Materials and Solar Cells*, *134*, 45–53. https://doi.org/10.1016/j.solmat.2014.11.025

Wu, Y., Hermkens, P. M., van de Loo, B. W. H., Knoops, H. C. M., Potts, S. E., Verheijen, M. A., … Kessels, W. M. M. (2013). Electrical transport and Al doping efficiency in nanoscale ZnO films prepared by atomic layer deposition. *Journal of Applied Physics*, *114*(2), 024308. https://doi.org/10.1063/1.4813136

Wu, Yongzhen, Yang, X., Chen, H., Zhang, K., Qin, C., Liu, J., … Han, L. (2014). Highly compact TiO 2 layer for efficient hole-blocking in perovskite solar cells. *Applied Physics Express*, *7*(5), 052301. https://doi.org/10.7567/APEX.7.052301

Xu, X., Liu, Z., Zuo, Z., Zhang, M., Zhao, Z., Shen, Y., … Wang, M. (2015a). Hole Selective NiO Contact for Efficient Perovskite Solar Cells with Carbon Electrode. *Nano Letters*, *15*(4), 2402–2408. https://doi.org/10.1021/nl504701y

Xu, X., Liu, Z., Zuo, Z., Zhang, M., Zhao, Z., Shen, Y., … Wang, M. (2015b). Hole Selective NiO Contact for Efficient Perovskite Solar Cells with Carbon Electrode. *Nano Letters*, *15*(4), 2402–2408. https://doi.org/10.1021/nl504701y

Yakunin, S., Shynkarenko, Y., Dirin, D. N., Cherniukh, I., & Kovalenko, M. V. (2017).

Non-dissipative internal optical filtering with solution-grown perovskite single crystals for full-colour imaging. *NPG Asia Materials*, *9*(9), e431–e431. https://doi.org/10.1038/am.2017.163

Yan, W., Li, Y., Ye, S., Li, Y., Rao, H., Liu, Z., … Huang, C. (2016). Increasing open circuit voltage by adjusting work function of hole-transporting materials in perovskite solar cells. *Nano Research*, *9*(6), 1600–1608. https://doi.org/10.1007/s12274-016-1054-5

Yang, T. C.-J., Fiala, P., Jeangros, Q., & Ballif, C. (2018). High-Bandgap Perovskite Materials for Multijunction Solar Cells. *Joule*, *2*(8), 1421–1436. https://doi.org/10.1016/j.joule.2018.05.008

Yee, K. S. (1966). Numerical Solution of Initial Boundary Value Problems Involving Maxwell's Equations in Isotropic Media. *IEEE Transactions on Antennas and Propagation*. https://doi.org/10.1109/TAP.1966.1138693

Yin, W.-J., Shi, T., & Yan, Y. (2014a). Unusual defect physics in $CH_3NH_3PbI_3$ perovskite solar cell absorber. *Applied Physics Letters*, *104*(6), 063903. https://doi.org/10.1063/1.4864778

Yin, W.-J., Shi, T., & Yan, Y. (2014b). Unusual defect physics in CH 3 NH 3 PbI 3 perovskite solar cell absorber. *Applied Physics Letters*, *104*(6), 063903. https://doi.org/10.1063/1.4864778

Yin, X., Yao, Z., Luo, Q., Dai, X., Zhou, Y., Zhang, Y., … Lin, H. (2017). High Efficiency Inverted Planar Perovskite Solar Cells with Solution-Processed NiO x Hole Contact. *ACS Applied Materials & Interfaces*, *9*(3), 2439–2448. https://doi.org/10.1021/acsami.6b13372

Yoo, D.-G., Nam, S.-H., Kim, M. H., Jeong, S. H., Jee, H.-G., Lee, H. J., … Boo, J.-H. (2008). Fabrication of the ZnO thin films using wet-chemical etching processes on application for organic light emitting diode (OLED) devices. *Surface and Coatings Technology*, *202*(22–23), 5476–5479.

https://doi.org/10.1016/j.surfcoat.2008.06.064

Yoshikawa, K., Kawasaki, H., Yoshida, W., Irie, T., Konishi, K., Nakano, K., … Yamamoto, K. (2017a). Silicon heterojunction solar cell with interdigitated back contacts for a photoconversion efficiency over 26%. *Nature Energy*, *2*(5), 17032. https://doi.org/10.1038/nenergy.2017.32

Yoshikawa, K., Kawasaki, H., Yoshida, W., Irie, T., Konishi, K., Nakano, K., … Yamamoto, K. (2017b). Silicon heterojunction solar cell with interdigitated back contacts for a photoconversion efficiency over 26%. *Nature Energy*, *2*(5). https://doi.org/10.1038/nenergy.2017.32

You, J., Meng, L., Song, T.-B., Guo, T.-F., Yang, Y. (Michael), Chang, W.-H., … Yang, Y. (2016a). Improved air stability of perovskite solar cells via solution-processed metal oxide transport layers. *Nature Nanotechnology*, *11*(1), 75–81. https://doi.org/10.1038/nnano.2015.230

You, J., Meng, L., Song, T.-B., Guo, T.-F., Yang, Y., Chang, W.-H., … Yang, Y. (2016b). Improved air stability of perovskite solar cells via solution-processed metal oxide transport layers. *Nature Nanotechnology*, *11*(1), 75–81. https://doi.org/10.1038/nnano.2015.230

You, J., Meng, L., Song, T.-B., Guo, T.-F., Yang, Y., Chang, W.-H., … Yang, Y. (2016c). Improved air stability of perovskite solar cells via solution-processed metal oxide transport layers. *Nature Nanotechnology*, *11*(1), 75–81. https://doi.org/10.1038/nnano.2015.230

You, J., Yang, Y. (Michael), Hong, Z., Song, T.-B., Meng, L., Liu, Y., … Yang, Y. (2014). Moisture assisted perovskite film growth for high performance solar cells. *Applied Physics Letters*, *105*(18), 183902. https://doi.org/10.1063/1.4901510

Yu, Z., Raman, A., & Fan, S. (2010). Fundamental limit of nanophotonic light trapping in solar cells. *Proceedings of the National Academy of Sciences*, *107*(41), 17491–17496. https://doi.org/10.1073/pnas.1008296107

Yu, Z., Raman, A., & Fan, S. (2011). Nanophotonic light-trapping theory for solar cells. *Applied Physics A*, *105*(2), 329–339. https://doi.org/10.1007/s00339-011-6617-4

Yumnam, N., & Wagner, V. (2018). Controlled growth of ZnO nanorods via self-assembled monolayer. *Journal of Applied Electrochemistry*, *48*(1), 85–94. https://doi.org/10.1007/s10800-017-1134-6

Zardetto, V., Williams, B. L., Perrotta, A., Di Giacomo, F., Verheijen, M. A., Andriessen, R., … Creatore, M. (2017). Atomic layer deposition for perovskite solar cells: research status, opportunities and challenges. *Sustainable Energy & Fuels*, *1*(1), 30–55. https://doi.org/10.1039/C6SE00076B

Zhang, H., Wang, H., Chen, W., & Jen, A. K. Y. (2017). CuGaO2 : A Promising Inorganic Hole-Transporting Material for Highly Efficient and Stable Perovskite Solar Cells. *Advanced Materials (Deerfield Beach, Fla.)*, *29*(8). https://doi.org/10.1002/adma.201604984

Zhang, W., Ren, Z., Guo, Y., He, X., & Li, X. (2018). Improved the long-term air stability of ZnO-based perovskite solar cells prepared under ambient conditions via surface modification of the electron transport layer using an ionic liquid. *Electrochimica Acta*, *268*, 539–545. https://doi.org/10.1016/j.electacta.2018.02.103

Zhao, D., Wang, C., Song, Z., Yu, Y., Chen, C., Zhao, X., … Yan, Y. (2018). Four-Terminal All-Perovskite Tandem Solar Cells Achieving Power Conversion Efficiencies Exceeding 23%. *ACS Energy Letters*, *3*(2), 305–306. https://doi.org/10.1021/acsenergylett.7b01287

Zhao, Y., Belkin, M. A., & Alù, A. (2012). Twisted optical metamaterials for planarized ultrathin broadband circular polarizers. *Nature Communications*, *3*(1), 870. https://doi.org/10.1038/ncomms1877

Zhou, J., Meng, X., Zhang, X., Tao, X., Zhang, Z., Hu, J., … Yang, S. (2017). Low-temperature aqueous solution processed ZnO as an electron transporting layer

for efficient perovskite solar cells. *Materials Chemistry Frontiers*, *1*(5), 802–806. https://doi.org/10.1039/C6QM00248J

Zhou, Y., & Long, G. (2017). Low Density of Conduction and Valence Band States Contribute to the High Open-Circuit Voltage in Perovskite Solar Cells. *The Journal of Physical Chemistry C*, *121*(3), 1455–1462. https://doi.org/10.1021/acs.jpcc.6b10914

Zhu, J., Yu, Z., Fan, S., & Cui, Y. (2010). Nanostructured photon management for high performance solar cells. *Materials Science & Engineering R*, *70*(3–6), 330–340. https://doi.org/10.1016/j.mser.2010.06.018

Zhu, Z., Bai, Y., Zhang, T., Liu, Z., Long, X., Wei, Z., … Yang, S. (2014). High-performance hole-extraction layer of sol-gel-processed nio nanocrystals for inverted planar perovskite solar cells. *Angewandte Chemie - International Edition*, *53*(46), 12571–12575. https://doi.org/10.1002/anie.201405176

Zuo, C., Bolink, H. J., Han, H., Huang, J., Cahen, D., & Ding, L. (2016). Advances in Perovskite Solar Cells. *Advanced Science*, *3*(7), 1500324. https://doi.org/10.1002/advs.201500324

Zuo, C., & Ding, L. (2014). An 80.11% FF record achieved for perovskite solar cells by using the NH 4 Cl additive. *Nanoscale*, *6*(17), 9935. https://doi.org/10.1039/C4NR02425G

Zuo, C., Scully, A. D., Vak, D., Tan, W., Jiao, X., McNeill, C. R., … Gao, M. (2019). Self-Assembled 2D Perovskite Layers for Efficient Printable Solar Cells. *Advanced Energy Materials*, *9*(4), 1803258. https://doi.org/10.1002/aenm.201803258

Zuo, C., Vak, D., Angmo, D., Ding, L., & Gao, M. (2018). One-step roll-to-roll air processed high efficiency perovskite solar cells. *Nano Energy*, *46*, 185–192. https://doi.org/10.1016/j.nanoen.2018.01.037